

Beyond the Quantum Limit

—

A Squeezed-Light Laser in GEO 600

Von der Fakultät für Mathematik und Physik
der Gottfried Wilhelm Leibniz Universität Hannover
zur Erlangung des Grades

Doktor der Naturwissenschaften
– Dr. rer. nat. –

genehmigte Dissertation
von

Dipl.-Phys. Aleksandr Khalaidovski

geboren am 16. Januar 1982 in Kiev, Ukraine

2011

Referent:	Prof. Dr. Roman Schnabel
Korreferent:	Prof. Dr. Karsten Danzmann
Tag der Promotion:	21.12.2011

Abstract

Albert Einstein’s General Theory of Relativity predicts the existence of ripples in space-time, the so-called *gravitational waves* (GWs). In the past two decades, an international array of ground-based, kilometer-scale Michelson interferometers has been set up aiming at a first observation. These Earth-bound GW detectors target signals at audio frequencies in a band of ca. 10 Hz – 10 kHz. At Fourier frequencies above 1 kHz, their sensitivity is limited by quantum noise. This *shot-noise* arises from the zero-point fluctuations of the electromagnetic field, the so-called *vacuum fluctuations*, which enter the interferometer through its anti-symmetric signal port. Future generations of GW observatories will even be limited by quantum noise almost over their entire detection band [ET].

A ‘classical’ solution to further improve the signal-to-shot-noise ratio (SNR) of the observatories consists in an increase of the circulating light power. A higher optical load inside the interferometer will, however, lead to thermally-induced beam distortion as well as to an increased radiation pressure noise level. This will effectively result in an upper limit for the optical light power employable in future GW observatory generations. An alternative approach to improve the SNR is based on the injection of so-called *squeezed* states of light. Such a light field has a characteristic non-classical noise distribution in the field quadratures. Injected from the signal port, the squeezed state replaces the vacuum state, thereby reducing the interferometer’s quantum noise.

The first part of this thesis discusses the setup of a squeezed-light laser for the German-British GW observatory GEO 600. During characterization of the device, a noise reduction of up to 9.6 dB below the vacuum noise level was observed in the frequency band of 10 Hz – 10 kHz, setting a new benchmark for squeezing observed at audio frequencies. Corrected for detection losses, this value furthermore corresponds to more than 11 dB of squeezing available for injection into the dark port of GEO 600. Situated on a 1.15 m × 1.35 m optical breadboard, the device features transportability and can be operated independently of the GW interferometer. A key feature of the squeezed-light laser is its unprecedented long-term stability. The longest characterization measurements lasted for 20 h with an overall duty cycle of more than 99 %.

In the second part of this thesis, the implementation of squeezed light into GEO 600 is presented along with the results achieved. The observatory shot noise was reduced by up to 3.4 dB, corresponding to an improvement in sensitivity by a factor of up to 1.5. For isotropically distributed GW sources, this corresponds to an increase in detection probability by $1.5^3 \approx 3.4$. This makes GEO 600 the first large-scale GW interferometer with a non-classically enhanced sensitivity. Based on the performance of the squeezed-light laser, a sensitivity improvement by a factor of two, corresponding to an equivalent optical power increase by a factor of four, seems feasible in the near future.

Keywords: Interferometric gravitational-wave detector, squeezed light generation and injection, nonclassically enhanced sensitivity, low frequency squeezing

Kurzfassung

Im Jahre 1916 sagte Albert Einstein als Konsequenz der Allgemeinen Relativitätstheorie die Existenz von Gravitationswellen (GWs) voraus. Ihr bis heute ausstehender direkter Nachweis stellt eine der großen Herausforderungen der modernen Physik dar. In den vergangenen Jahrzehnten ist zu diesem Zweck ein weltweites Netzwerk von Laserinterferometern entstanden. Der Messbereich dieser erdgebundenen Detektoren erstreckt sich über den Audiofrequenzbereich von ca. 10 Hz bis 10 kHz, wobei die Messempfindlichkeit ab ca. 1 kHz durch Quantenrauschen limitiert wird. Dieses *Schrotrauschen* hat seinen Ursprung in den Nullpunktfluktuationen des elektromagnetischen Feldes, welche durch den Signalport ins Interferometer einkoppeln und so die Messempfindlichkeit begrenzen.

Der „klassische“ Ansatz zur Verbesserung des Signal-zu-Rausch-Verhältnisses (SNR) ist eine Erhöhung der in den Interferometerarmen zirkulierenden Lichtleistung. Dies führt jedoch auch zu einer Erhöhung der in den Substraten absorbierten Leistung sowie unausweichlich zu einer Vergrößerung des Strahlungsdruckrauschens. Einen alternativen Ansatz zur Verbesserung des SNR bietet sogenanntes *gequetschtes Licht*, welches weder zu einer Erhöhung der thermischen Last noch generell zu einem erhöhten Strahlungsdruckrauschen führt.

Das Ziel der vorliegenden Arbeit war der Aufbau eines Quetschlichtlasers für den deutsch-britischen Gravitationswellendetektor GEO 600 sowie die Demonstration einer nicht-klassisch verbesserten Messempfindlichkeit. Der experimentelle Aufbau des Quetschlichtlasers und seine Charakterisierung bilden den Schwerpunkt des ersten Teils dieser Dissertation. Dabei wurde im Frequenzband von 10 Hz–10 kHz eine Verringerung der Rauschleistung um bis zu 9.6 dB unter das Niveau des Vakuumrauschens beobachtet, was in diesem Frequenzintervall einen neuen Rekordwert darstellt. Für die Einkopplung in den Signalport von GEO 600 steht damit – nach Berücksichtigung der lediglich bei der Charakterisierung entstehenden optischen Verluste – ein Wert von über 11 dB zur Verfügung. Der Quetschlichtlaser stellt ein vom GW-Interferometer unabhängiges Gerät dar, das auf einem 1.15 m × 1.35 m großen optischen Breadboard Platz findet und damit transportabel ist. Ein Schlüsselmerkmal des Quetschlichtlasers ist seine Langzeitstabilität. Bei den längsten Charakterisierungsmessungen, welche sich über einen Zeitraum von 20 Stunden erstreckten, wurde ein effektiver duty cycle von weit über 99 % beobachtet.

Der zweite Teil der vorliegenden Arbeit diskutiert die Implementierung des Quetschlichtlasers in GEO 600 und die dabei erzielten Ergebnisse. Das Schrotrauschen des Interferometers wurde um bis zu 3.4 dB abgesenkt. Dies entspricht einer Empfindlichkeitsverbesserung um den Faktor 1.5 und damit einer Erhöhung der Detektionswahrscheinlichkeit um $1.5^3 \approx 3.4$ für isotrop verteilte Quellen von Gravitationswellen. Damit ist GEO 600 der weltweit erste Gravitationswellendetektor mit einer nicht-klassisch verbesserten Messempfindlichkeit.

Stichworte: Gravitationswellendetektor, gequetschtes Licht im Audiofrequenzbereich, nicht-klassische Verbesserung der Messgenauigkeit von Laserinterferometern

Acknowledgements

I would like to express my sincere gratitude to a large number of people who during the last years never ceased supporting me and without whom these years would never have been as exciting as they were.

First of all, I would like to thank Karsten Danzmann for giving me the opportunity to be a part of a really great institute and to make a humble contribution to the *opus magnum* called GEO 600.

A very special debt of gratitude I owe to my advisor, Roman Schnabel. It was his never fading enthusiasm that in the first place made the enterprise undertaken in the last years possible. The friendly and inspiring atmosphere he knows to create in his group, along with his outstanding mentoring at each and every occasion, made my doctoral studies a great and interesting time which I enjoyed a lot.

Legion are the things for which I am more than grateful to Henning Vahlbruch. Being a part of this particular project truly was like “standing on the shoulders of giants”. Without his innumerable contributions – beginning long before I joined the team and never ceasing – the results reported in this thesis would never have been possible. Henning, thank you so much for your advice and support, for your patience and for the cheerful working atmosphere. It really was a great pleasure to me!

To Hartmut Grote, Harald Lück, Benno Willke and the whole GEO 600 team I am very grateful for their belief in squeezing and for their support at innumerable occasions.

My very special thanks go to Philipp Schauzu, Stefan Bertram, Jan Diendrich and Hans Melching, who at all times supported us in designing new components as well as with the modifications of the existing ones that just did not want to fit any more in an experiment with a density approaching infinity more and more every day. Thank you guys, without you this device would never have worked in time.

The GEO 600 squeezed-light laser project participated as one of ten projects in the 2nd Science TV initiative of the DFG. This great scientific outreach was possible only through the work of Michael Britzger and Tobias Westphal. I also would like to thank Stefan Pfalz for his support.

I am indebted this way or another to many of my colleagues. My special thanks for introducing me to the world of optical laboratories and for extensive discussions throughout the years go to André Thüring. For implementing the digital control of the squeezed-light laser and for the nice working atmosphere I would like to thank Niko Lastzka and Christian Gräf. To Aiko Sambrowski I owe my gratitude for being a great roommate. I am obliged to Jessica Steinlechner for her support with TKSIm and for the fruitful discussions. To Andreas Freise and Stefan Hild I am very grateful for their FINESSE-support.

Without being able to use this very limited space to address everybody in person, I would like to thank all the people with whom I worked day by day at the AEI in the last five years.

To Nergis Mavalvala and Lisa Barsotti I am very grateful for enabling me to stay at LIGO-Hanford, as well as for the great number of interesting discussions we had. During this stay, I also enjoyed the opportunity to learn to know and to esteem Sheila Dwyer, Max Factourovich and Daniel Sigg. Working with you was an honor and a great pleasure, thanks a lot. I would also like to thank Keita Kawabe, Mike Landry and all the other people from LHO.

For proofreading of parts of this manuscript and for providing me with a variety of new ideas I am (in alphabetical order) indebted to Jöran Bauchrowitz, Michael Born, Michael Britzger, Tobias Eberle, Daniel Friedrich, Christian Gräf, Stefan Gossler, Vitus Händchen, Harald Lück, Holger Pletsch, Aiko Sambrowski, Sebastian Steinlechner, Henning Vahlbruch, Christina Vollmer and Benno Willke. Very special thanks for his patience in proofreading the complete manuscript go to Albrecht Rüdiger.

Finally, I would like to thank Anja & Frank Freund, Matthias Höh, Georg Kleine Büning and Johannes Will for their friendship and for their patience with the lack of time that, alas, became so chronic over the last years.

Dear reader, for the final few lines, please allow me to switch back to my mother tongue.

Я хотел бы поблагодарить моих родителей за их любовь и поддержку, за то, что – переехав в Германию – они открыли мне все возможности и за то, что они всегда верят в меня и в мои цели! И под конец, Ксения, разреши поблагодарить тебя за твою любовь, твоё терпение и твою поддержку. Без тебя, все достигнутое за последние годы осталось бы лишь мечтами.

Alexander Khalaidovski, November 7th 2011

Contents

Abstract	i
Kurzfassung	iii
Acknowledgements	v
List of Figures	xi
List of Tables	xv
Glossary	xvii
1. Introduction	1
1.1. A glimpse at gravitational waves	1
1.2. Approaches for a direct detection	3
1.3. Noise sources in interferometric GW observatories	5
1.4. Reducing the quantum noise	10
1.5. Experimental generation of squeezed light	12
1.6. Structure of the thesis	13
2. From classical light to quantum optics	15
2.1. Quantization of a single-mode electromagnetic field	15
2.2. Number or Fock states	17
2.3. Quadrature operators	20
2.4. Coherent states	21
2.5. Phase-space pictures of coherent states	23
2.6. Squeezed states	26
2.7. Basics of nonlinear optics	28
2.7.1. Nonlinear polarization	28

2.7.2.	Sum-frequency generation	30
2.7.3.	Phase matching - general considerations	32
2.7.4.	Phase matched second-harmonic generation in a LiNbO ₃ crystal	34
2.7.5.	Quasi phase matching	35
2.7.6.	Parametric amplification	36
2.8.	Generation of squeezed light	37
2.9.	Detection of squeezed light	38
2.10.	Influence of optical loss	40
3.	A squeezed-light laser for GEO 600	43
3.1.	Lessons learned from the past	43
3.2.	Preparation of the laser beams	45
3.3.	Second-harmonic generation	49
3.3.1.	Design of the SHG resonator	49
3.3.2.	Temperature stabilization	52
3.3.3.	Length stabilization	53
3.3.4.	Optical performance	53
3.4.	Ring mode-cleaner resonators	54
3.4.1.	Local oscillator beam for homodyne detection (1064 nm)	55
3.4.2.	532 nm squeezed-light source pump beam	56
3.5.	Squeezed-light source	57
3.6.	Squeezed-light cavity length control beam and pump beam alignment	58
3.6.1.	Alignment beam	59
3.6.2.	Cavity length control	60
3.6.3.	Controlling the squeezing angle - theoretical considerations	61
3.6.4.	Controlling the squeezing angle - experimental realization	64
3.7.	Control of the 1064 nm homodyne detector local oscillator field	65
3.8.	Pump power stabilization	69
3.8.1.	Theoretical considerations	69
3.9.	Experimental implementation of the pump power stabilization	80
3.10.	Conclusion	81
4.	Characterization of the squeezed-light laser	83
4.1.	Performance of the diagnostic homodyne detector	83
4.1.1.	Stray light elimination	84
4.1.2.	True quantum shot noise measurement	89
4.2.	Squeezing the vacuum noise	90
4.3.	Audio- and subaudio-frequency squeezing	93
4.4.	Remote control of the squeezed-light laser	95
4.4.1.	Connecting the experiment to the CDS	96
4.4.2.	Control automation	100

4.5. Long-term stability	101
4.5.1. Future CDS work	103
4.6. Conclusion	104
5. Squeezing the GEO 600 quantum noise	105
5.1. GEO 600 in a nutshell	105
5.2. Integration of the squeezed-light laser into the GEO 600 detection scheme	108
5.3. Loss estimation	113
5.4. Non-classically improved GEO 600 sensitivity	117
5.5. Future work	119
6. Summary and outlook	123
6.1. A glimpse into the future	124
A. Second-harmonic generation using PPKTP	127
B. Optical layout of the squeezed-light laser	129
Bibliography	131
List of publications	141
Curriculum Vitae	145

Contents

List of Figures

1.1. Effect of (+)- and (x)-polarized GWs on a ring of 8 test particles and on a Michelson laser interferometer	2
1.2. Photograph of the GEO 600 gravitational wave observatory	4
1.3. Status of the LIGO, Virgo and GEO 600 observatory sensitivities in the year 2010	6
1.4. Quantum noises in a Michelson interferometer without arm cavities and signal-recycling	8
1.5. Pictorial phase-space representation of a vacuum-state and of a squeezed vacuum state	10
1.6. Strain sensitivities of a Michelson interferometer with and without squeezed light injection	11
1.7. Schematic of a GW interferometer with squeezed light injection	12
2.1. Pictorial phase-space representation of a coherent state and of a vacuum state with $n = 0$	23
2.2. Wigner function of a vacuum state and of a Fock state with $n = 1$	25
2.3. Pictorial phase-space representation of a state squeezed in the \hat{X}^+ quadrature and in an arbitrary quadrature as well as a Wigner function for a squeezed vacuum state with $r = 0.7$ and $\theta = 0$	29
2.4. Sum-frequency generation in a $\chi^{(2)}$ nonlinear medium of length L	31
2.5. Conversion efficiency as a function of phase mismatch in the case of weak conversion	33
2.6. Ordinary and extraordinary indices of refraction of LiNbO_3 as a function of wavelength at room temperature and at $T = 316$ K. In the second case, the indices of refraction are equalized leading to an optimal phase-matching for the SHG process	35
2.7. Energy-level diagram for sum- and difference-frequency generation	36
2.8. Schematic of a balanced homodyne detector	38

2.9. Degree of squeezing as a function of the detection efficiency	41
3.1. Photograph of the squeezed-light laser	46
3.2. Schematic of the preparatory setup stage	48
3.3. Overview of possible linear resonator designs	50
3.4. CAD drawing and photograph of the optical resonators used for second-harmonic and squeezed light generation	50
3.5. Radius of the SHG beam waist as a function of the cavity length	51
3.6. Open-loop gain of the SHG temperature controller	52
3.7. Sketch of the travelling-wave ring mode-cleaner resonator	54
3.8. Open-loop gain of the cavity length control loop for the homodyne detection beam mode-cleaner	55
3.9. Photograph of the Invar mode-cleaner employed in the GEO 600 squeezed-light laser	56
3.10. Sketch and photograph of the squeezed-light source	58
3.11. Scheme of the squeezing control and detection stages	59
3.12. Resonance peaks of the p-polarized length control beam and the corresponding error signal after demodulation at $\nu_{\text{mod}}(\text{EOM}_3) = 44.44 \text{ MHz}$	61
3.13. Schematic of the squeezing angle control loop	64
3.14. Error signal for the squeezing angle control loop	66
3.15. Open-loop gain of the squeezing phase stabilization loop	66
3.16. Error signal for the homodyne readout quadrature control loop	68
3.17. Simulation of the frequency-dependent squeezed field assuming real experimental parameters and a detection loss of approximately 10.5 %	71
3.18. TKSIm simulation of the temperature change of the nonlinear crystal for a 532 nm pump power increase from 35 mW to 38.5 mW	72
3.19. Sketch of the setup employed to characterize the dependence of the degeneracy condition on the 532 nm beam power	73
3.20. Measurement of the alignment beam power transmitted through the squeezing resonator as a function of pump power	75
3.21. Phase rotation experienced by an optical field transmitted through the squeezing resonator in dependence of its detuning	76
3.22. Simulated degree of squeezing detected at a fixed homodyne angle, initially optimized for the nominal pump power of 34.5 mW, as a function of pump power	78
3.23. CAD drawing and photograph of the Mach-Zehnder-type interferometer used for 532 nm pump power stabilization	80
3.24. Photograph of the GEO 600 squeezed-light laser and a simplified sketch of the experimental layout	82
4.1. Shot noise spectrum measured after the experimental assembly was finished and prior to an additional stray light elimination using baffles and ND filters	85

4.2. Measurements of the balanced homodyne detector noise performed during stray light optimization, showing the effect of the stray light suppression measures	87
4.3. Photograph of the diagnostic homodyne detector	88
4.4. Measurement of the vacuum noise spectra using three different optical powers for the local oscillator beam	89
4.5. Degree of squeezing and anti-squeezing measured with different pump powers	90
4.6. Contour plot of the Wigner function of a lossless 10 dB squeezed state with different amounts of phase noise present	92
4.7. Measurement of a very pure squeezed state with -3.4 dB of squeezing and 4.2 dB of anti-squeezing at sideband frequencies extending over the entire GW wave detection band of 10 Hz– 10 kHz	93
4.8. Noise power of a squeezed state generated with an optical pump power of 45 mW. The noise level was reduced by up to 9.5 dB, being the maximal squeezing value achievable in the experiment. This corresponds to more than 11 dB of squeezing exiting the squeezing setup, because in this case the homodyne detector is by-passed and the total optical loss is reduced to 7% . The squeezing spectrum is white at audio frequencies	94
4.9. Schematic of the interface between the squeezed-light laser and the digital control system, exemplified at the example of the SHG	96
4.10. Squeezing spectrogram illustrating the long-term stability of the squeezing degree. The duty cycle was higher than 99.9% , merely 8 lock-losses were observed over 20 hours	102
5.1. Simplified optical layout of GEO 600 without squeezed light injection . . .	106
5.2. View into the GEO 600 central building containing the main interferometer optics and the squeezed-light laser	109
5.3. Sketch of the optical layout used to match the mode of the squeezed field to the eigenmode of the output mode-cleaner	110
5.4. Sketch of the optical layout of the GEO - HF detection stage with squeezing input	111
5.5. Measurement of the mode-matching of the squeezed beam to the interferometer and to the OMC	112
5.6. Estimation of the optical loss experienced by the squeezed field	113
5.7. FINESSE simulation of the signal-recycling cavity's frequency-dependent power reflectivity with the old and the new MSR	115
5.8. Current status: Simulated squeezing and anti-squeezing values prior to and after the injection in GEO 600	116
5.9. Main result: Non-classical reduction of the GEO 600 instrumental noise using squeezed vacuum states of light	118

List of Figures

5.10. Outlook: simulated squeezing and anti-squeezing values prior to and after the injection in GEO 600	120
A.1. Conversion efficiency of the PPKTP-SHG	128
B.1. Optical layout of the squeezed-light laser.	130

List of Tables

4.1. Overview over all CDS input channels	98
4.2. Overview over all CDS output channels	99
4.3. Re-lock times of the different subsystems, defined by the order of the automated locking sequence	101
5.1. Parameters of the GEO 600 optics and layout employed for the FINESSE simulation of the frequency-dependent loss introduced to the squeezed field by the signal-recycling cavity, as well as selected interferometer parameters	115

List of Tables

Glossary

List of abbreviations

AA	<u>anti-aliasing</u>
ADC	<u>analog-to-digital converter</u>
AEI	<u>Albert-Einstein-Institute</u> (Hannover and Golm, Germany)
AI	<u>anti-imaging</u>
AOI	<u>angle of incidence</u>
AOM	<u>acousto-optical modulator</u>
AR	<u>anti-reflective</u> (refers to dielectric coatings)
AUX1	<u>auxiliary laser beam</u> used to control the phase of the squeezed field
AUX2	<u>auxiliary laser beam</u> used to control the squeezed light source length
BAB	<u>bright alignment beam</u>
BS	<u>beam splitter</u>
BW	<u>bandwidth</u>
CAD	<u>computer-aided design</u>
CCF	<u>coherent control field</u>
CDS	<u>control and data system</u>
CLIO	<u>cryogenic laser interferometer observatory</u>
CMRR	<u>common-mode rejection ratio</u>
DAC	<u>digital-to-analog converter</u>
DBS	<u>dichroic beam splitter</u>
DDS	<u>direct digital synthesizer</u>
det	<u>detuning</u>
DFG	<u>difference-frequency generation</u>
EOM	<u>electro-optical modulator</u>
EPICS	<u>experimental physics and industrial control system</u>
ET	<u>Einstein Telescope</u>
FD	<u>fully-differential</u>

FFT	<u>F</u> ast- <u>F</u> ourier- <u>T</u> ransform
FI	<u>F</u> araday <u>i</u> solator
FR	<u>F</u> araday <u>r</u> otator
FSR	<u>f</u> ree <u>s</u> pectral <u>r</u> ange
FWHM	<u>f</u> ull <u>w</u> idth at <u>h</u> alf <u>m</u> aximum
GEO 600	German-British gravitational wave observatory located at Ruthe, Germany
GR	<u>G</u> eneral theory of <u>R</u> elativity
GUI	<u>g</u> raphical <u>u</u> ser <u>i</u> nterface
GW	<u>g</u> ravitational <u>w</u> ave
HF	<u>h</u> igh <u>f</u> requency
hmd	(balanced) <u>h</u> omodyne (detector)
HR	<u>h</u> ighly <u>r</u> eflective (refers to dielectric coatings)
HV	<u>h</u> igh <u>v</u> oltage
I/O	<u>i</u> nput- <u>o</u> utput
KTP	potassium titanyl phosphate, KTiOPO_4
LCGT	<u>l</u> arge-scale <u>c</u> ryogenic <u>g</u> ravitational wave <u>t</u> elescope
LIGO	<u>L</u> aser <u>I</u> nterferometer <u>G</u> ravitational Wave <u>O</u> bservatory
LiNbO ₃	lithium niobate
LO	<u>l</u> ocal <u>o</u> scillator
MC	<u>m</u> ode- <u>c</u> leaner, three mirror travelling-wave resonator
MCE/MCn	near interferometer steering mirrors (east/north arm)
MFe/MFn	far interferometer steering mirrors (east/north arm)
MM	<u>m</u> ode <u>m</u> atching
MPR	power-recycling mirror
MSR	signal-recycling mirror
MZ	<u>M</u> ach- <u>Z</u> ehnder
ND	<u>n</u> eutral <u>d</u> ensity
Nd:YAG	Neodymium-doped Yttrium Aluminium Garnet, $\text{Nd:Y}_3\text{Al}_5\text{O}_{12}$)
NL	<u>n</u> on- <u>l</u> inear
NPRO	<u>n</u> on- <u>p</u> lanar <u>r</u> ing <u>o</u> scillator
NTC	<u>n</u> egative <u>t</u> emperature <u>c</u> oefficient
OCXO	Oven controlled crystal oscillator
OMC	<u>o</u> utput <u>m</u> ode- <u>c</u> leaner
OPA	<u>o</u> ptical <u>p</u> arametric <u>a</u> mplification
OPO	<u>o</u> ptical <u>p</u> arametric <u>o</u> scillation
ORN	<u>o</u> ptical <u>r</u> eadout <u>n</u> oise
PBS	<u>p</u> olarizing <u>b</u> eam <u>s</u> plitter
PD	<u>p</u> hoto <u>d</u> etector
PDH	<u>P</u> ound - <u>D</u> rever - <u>H</u> all
PLL	<u>p</u> hase- <u>l</u> ocked <u>l</u> oop

POM	polyoxymethylen
PPKTP	potassium titanyl phosphate, KTiOPO_4
PRM	power-recycling mirror
PZT	piezo-electric actuator
QCF	quadrature control field
QE	quantum efficiency
RBW	resolution bandwidth
RF	radio frequency
ROC	radius of curvature
RP	radiation pressure noise
SE	single-ended
SFG	sum - frequency generation
SHG	second - harmonic generation
SN	shot noise or supernova
SNR	signal-to-noise ratio
SQL	standard quantum limit
SRC	signal-recycling cavity
TCO-C	vacuum chamber containing the GEO 600 OMC
TEM	transverse mode of the electromagnetic field
th	threshold
WF	Wigner function

List of symbols

This list is subdivided into a part originating from the latin alphabet and another part originating from the greek alphabet. Quantum mechanical operators and states are finally provided separately.

\vec{B}	magnetic field vector
c	speed of light
dB	decibel
d_{eff}	effective susceptibility value
$\vec{e}_{x,y,z}$	unit vectors
\vec{E}	electric field vector
E_n	energy eigenvalue
f	optical frequency
\vec{F}	force
\mathcal{F}	finesse of an optical cavity
g	optical gain
G	Newton's gravitational constant
h	gravitational wave amplitude

h_+ and h_x	orthogonal GW polarization modes
\hbar	reduced Planck constant
i	$\sqrt{-1}$
k	wave number ($k = \omega/c$)
l	optical round-trip length
L	length (e. g. arm length of a GW detector, crystal length and so on) or optical loss
M	mass
n	index of refraction or number of photons
n_o	ordinary index of refraction
n_e	extraordinary index of refraction
P	power
\vec{P}	polarization
$\vec{P}^{(1)}$	linear polarization
\vec{P}^{NL}	nonlinear polarization
r	squeeze parameter
R	mirror power reflectivity or degree of squeezing
T	mirror power transmission
V	variance
\mathcal{V}	fringe visibility
Δf_{FSR}	free spectral range
Δf_{FWHM}	full width at half maximum
Δk	wavevector mismatch
ϵ_0	vacuum permittivity ($8.85 \cdot 10^{-12}$ F/m)
$\epsilon_{(1)} = 1 + \chi^{(1)}$	relative permittivity
η	efficiency
θ	squeezing angle, phase or angle
κ	normalized frequency
λ	wavelength
Λ	coherence length
$\lambda/2, \lambda/4$	waveplates
μ	reduced mass
μ_0	vacuum permeability ($4\pi \cdot 10^{-7}$ Vs/Am in SI units)
ν	modulation frequency
ξ	propagation efficiency ($1 - \text{propagation loss}$)
ρ	cavity escape efficiency or amplitude reflectivity
τ	amplitude transmission of a mirror or of an optical resonator
ϕ	phase
$\chi^{(1)}$	linear susceptibility

$\chi^{(2)}$	2nd order susceptibility
χ^{NL}	nonlinear susceptibility
ω_0	angular carrier frequency
Ω	angular sideband frequency
$[,]$	commutator
\hat{a}	annihilation operator
\hat{a}^\dagger	creation operator
\hat{D}	displacement operator
\hat{H}	Hamiltonian
\hat{i}_c	current operator
\hat{n}	number operator
$\hat{\rho}$	density operator
$\hat{S}(r, \theta)$	squeeze operator
\hat{X}^+	amplitude quadrature operator
\hat{X}^-	phase quadrature operator
\hat{X}^θ	quadrature operator at angle θ
\hat{Y}^+, \hat{Y}^-	rotated quadrature operators
$ 0\rangle$	vacuum or ground state
$ n\rangle$	number or Fock state
$ \alpha\rangle$	coherent state

List of pictograms

The pictograms used throughout this thesis to visualize the experimental layouts were designed by Alexander Franzen to whom I owe a large debt of gratitude for kindly sharing his *Component Library* (componentlibrary by alexander franzen 2016).



laser



optical cavity containing a $\chi^{(2)}$ nonlinear crystal



spatial mode-cleaning travelling-wave resonator (mode-cleaner or MC)



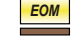
















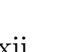


photo detector (1064 nm)



photo detector (532 nm)

Glossary

	quadrant photo detector (1064 nm)
	commercial PLL photo detector
	electro-optical modulator
	lens (AR-coated)
	waveplate (1064 nm and 532 nm, respectively)
	beam splitter
	polarizing beam splitter
	dichroic beam splitter
	highly reflective (HR) steering mirror
	piezo-actuated steering mirror
	Faraday rotator
	Faraday isolator
	optical fiber
	iris
	neutral density (ND) filter
	beam dump
	movable beam dump
	flip mirror
	aluminium tube (beam shielding)
	mixer
	signal generator

Introduction

1.1. A glimpse at gravitational waves

In his *Principia*, Isaak Newton described space and time as abstract parameters being independent one from each other [Newton87]. This concept has been revisited by Albert Einstein: As a consequence from the constancy of the speed of light, in his *special theory of relativity* [Einstein05] space and time are joined together into spacetime. A decade later, the *general theory of relativity* (GR) [Einstein15] dedicated to gravitation was published. One property addressed therein was the causality of gravity: A change in the gravitational field of an object is not observable instantly at an arbitrary distance, as implied by Newtonian gravity, but rather propagates at the speed of light. This means that, in analogy to electromagnetism, a ‘gravitational radiation’ exists. The first calculation of such radiation was published by Einstein himself [Einstein16, Einstein18] only a few months after the theory of GR and still constitutes the “leading-order quadrupole formula for the emission of *gravitational waves*” (GWs) [Flanagan+05]. As electromagnetic waves are emitted by accelerated charges, GWs are generated by accelerated masses and propagate through spacetime as transversal waves at the speed of light. An introduction to GR is e.g. provided by [Misner+73, Flanagan+05, Wald84, Schutz09] and the references therein.

From an experimentalist’s point of view, two questions are of particular interest: What is the effect of a gravitational wave and how strong is the expected interaction with a measurement apparatus? GWs are vibrations of spacetime. They manifest as a change ΔL in the proper distance L between two spacetime events that is also referred to as *strain*. The GW amplitude is described by the dimensionless quantity [Aufmuth+05]

$$h = 2\frac{\Delta L}{L}. \quad (1.1)$$

It is worth noting that every wave can be written as a superposition of two orthogonal polarization modes h_+ and h_x which go one into the other through a rotation of 45° .

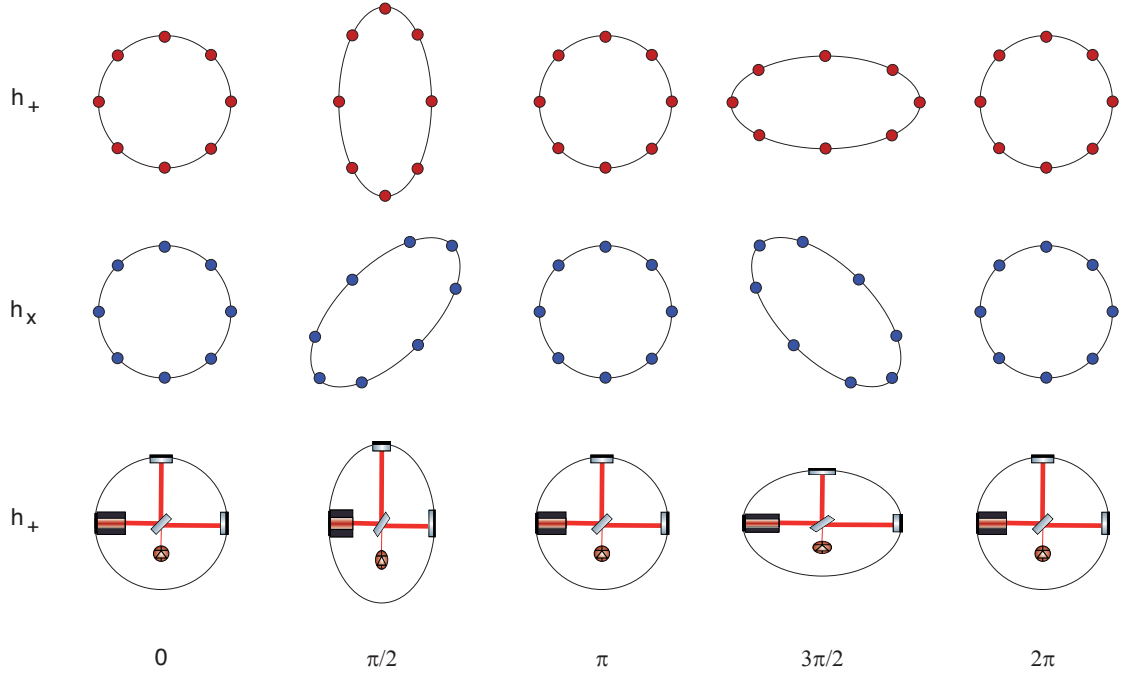


Figure 1.1.: The effect of a +-polarized (top) and a x-polarized (middle) gravitational wave propagating vertical to the image plane on a ring of 8 test particles. The illustration comprises one full cycle of the GW. Bottom: effect of a +-polarized GW on a Michelson-type laser interferometer.

In Fig. 1.1, the effect of the two polarizations on a ring of 8 free-falling test masses is illustrated, the direction of propagation is orthogonal to the image plane. Due to the quadrupolar nature of gravitational radiation, an asymmetry is introduced: While in one direction the distance between the masses is squeezed, it is stretched by the same amount in the orthogonal direction.

Though according to GR gravitational waves are omnipresent, the effects described are much too weak to be observed in everyday's life. The reason for this is the high elastic stiffness of spacetime. For an illustration, let us consider a possible laboratory experiment. Since GWs are emitted by accelerated objects whose motion is neither spherically nor cylindrically symmetric, a 'rotating dumbbell' is a good approach: Two masses $M_{1/2}$ are attached to a rod of length a and are spinning with the frequency Ω along the axis perpendicular to the rod. The gravitational wave amplitude produced by such a laboratory experiment is [Saulson94]

$$h_{\text{lab}} = \frac{4G}{c^4} \frac{\mu a^2 \Omega^2}{R}, \quad (1.2)$$

with G being Newton's gravitational constant, c the speed of light, $\mu = (M_1 M_2)/(M_1 + M_2)$ the reduced mass and R the distance to the observer. Even assuming extreme values like $\Omega/2\pi = 1$ kHz, $M_1 = M_2 = 10^3$ kg, $a = 1$ m and $R = 300$ km being the minimal distance of one wavelength, the resulting amplitude

$$h_{\text{lab}} \approx 10^{-39} \quad (1.3)$$

is incredibly small and far beyond the detection possibilities existing today. A laboratory source of GWs for dedicated experiments therefore appears very unlikely. More promising sources are massive astrophysical objects as e.g. coalescing binary neutron star (NS) or binary black hole systems, supernovae or pulsars. To give an example, a 'close-by' supernova at a distance of 10 kpc and hence well inside our galaxy is expected to result in a strain of $h_{\text{SN}} \approx 10^{-22}$ when measured on Earth [Ott09]. While still being fairly weak, this effect is nevertheless 17 orders of magnitude stronger than expected from the gedankenexperiment discussed above. Besides the *burst sources* corresponding to catastrophic events and *narrow-band sources* such as pulsars or binary systems far from coalescence, a *stochastic GW background*, resulting from the superposition of a large amount of weak sources, is expected to exist. Altogether, the emission spectrum covered by this variety of different source types extends from below 10^{-9} Hz up to kHz frequencies [Blair+12]. For an extensive discussion of different source types see [Thorne87, Saulson94, Cutler+02, Blair+12].

1.2. Approaches for a direct detection

The first attempt to directly measure GWs was undertaken almost half a century after the first prediction of their existence by Joseph Weber [Weber60]. His detector was designed as a large aluminium cylinder, forming a high-Q mechanical resonator. A gravitational wave was expected to excite the fairly sharp eigenresonance of this so-called *bar detector*. To measure the GW-induced elastic vibrations, piezoelectric transducers were attached to the bar. In 1969, Weber claimed a first detection of gravitational waves [Weber69, Weber70]. Though his results could never be confirmed by other research groups, it was this claim that encouraged several independent research groups to construct GW detectors. Until now, several resonant detectors have been operated worldwide. For an introduction to the single projects please refer to [ALLEGRO, AURIGA, EXPLORER/NAUTILUS, MiniGRAIL, NIOBE, Schenberg]. To reduce thermal noise which at room temperature would mask any GW signal, these detectors are operated at cryogenic temperatures. While reaching considerable strain sensitivities, a drawback of the resonant detectors is their low bandwidth of typically < 100 Hz.

The newly born field of gravitational wave detection experienced an enormous encouragement from the observation of the binary pulsar PSR 1913+16, reported by Hulse and Taylor in 1975 [Hulse+75]. General Relativity predicts such a binary system to emit gravitational radiation and due to this loss of energy to exhibit an orbital decay. Observations



Figure 1.2.: Photograph of the GEO 600 gravitational wave observatory (courtesy H. Lück).

over several years revealed the orbital decay to be in agreement with the GR predictions with an accuracy of better than 1% [Ju+12a]. Since then, other systems with a similar behaviour have been discovered [Deich+96, Stairs+02, Burgay+03, Faulkner+04]. For their discovery, which is generally considered an *indirect proof* of the existence of gravitational waves, Hulse and Taylor were awarded the Nobel Prize in 1993 [Hulse94, Taylor94].

An alternative approach for a measurement apparatus which was considered since the 1950s [Pirani56, Gertsenshtein+63, Weiss72, Forward78] is a laser interferometer. The effect of a gravitational wave on a Michelson-type interferometer is illustrated in the lower part of Fig. 1.1. For simplicity, the interferometer is oriented in an optimal way to a h_+ -polarized GW propagating perpendicular to the image plane. In this case, the GW strain changes the distance between the two interferometer mirrors (in the following referred to as *test masses*) and the beam splitter in an asymmetric way: While one arm of the interferometer is squeezed by the amount δl_{GW} , the other arm is stretched by exactly the same amount. This leads to an effective phase shift

$$\delta\phi_{\text{GW}} = \frac{4\pi}{\lambda} \delta L_{\text{GW}} = h_{\text{GW}}(t) \frac{2\pi L}{\lambda} \quad (1.4)$$

between the light fields propagating the two arms of the interferometer which can be detected as a change in the interference pattern. A Michelson-type interferometer therefore constitutes an optimal device for GW detection. A huge advantage when compared to resonant bar detectors is the broadband measurement sensitivity. It is worth stressing that the phase shift induced by the GW strain described by Eq. (1.4) depends on the arm length L as well as on the wavelength λ of the laser used. Additionally, the sensitivity increases with the amount of optical power stored in the arms. Following early prototype experiments [Livas+86, Newton+86, Spero+86, Shoemaker+88], several large-scale gravitational wave observatories have been constructed all over the world in the 1990s. This observatory network consists of:

Three **LIGO** interferometers [Fritschel+12] at two sites located in the states of Washington (Hanford) and Louisiana (Livingston) in the USA. While each site houses an interferometer with 4km arm length, at Hanford an additional 2km interferometer was built in the same vacuum system. To increase the storage time, the arms of the LIGO interferometers are constructed as Fabry-Perot resonators. This approach offers the advantage that the optical power at the interferometer beam splitter can be kept considerably low, thereby reducing thermal effects due to absorption of laser light inside the substrate.

Virgo [Acernese+08], a French-Italian project, is located near Pisa in Italy. It has an arm length of 3km and an optical layout very similar to the LIGO detectors.

GEO 600 [Grote+10] is a German-British project located in Ruthe near Hannover in Germany. Though the physical arm length is, as suggested by the name, indeed 600 m, the arms are folded once in the vertical plane, thereby yielding an effective optical path of 1200 m. GEO 600 does not possess arm cavities but uses the techniques of power-recycling and signal-recycling to resonantly enhance the circulating light power as well as the GW signal.

TAMA 300 [Takahashi+04] is a Japanese interferometer with 300 m arm length and Fabry-Perot arm cavities.

Over the last decade, the observatories completed several joint measurement campaigns, referred to as *science runs*. Figure 1.3 shows the observatory sensitivities (status summer 2010) in units of spectral density of the GW strain as well as of test mass displacement. In the following section, the different noise contributions which limit the measurement sensitivity are summarized.

1.3. Noise sources in interferometric GW observatories

The understanding of the different noises limiting the measurement sensitivity in various frequency bands is far from trivial. Several years of commissioning activities were required for the observatories to largely reach their design sensitivities and even after this time some noise sources are yet to be understood. In the following, merely the most

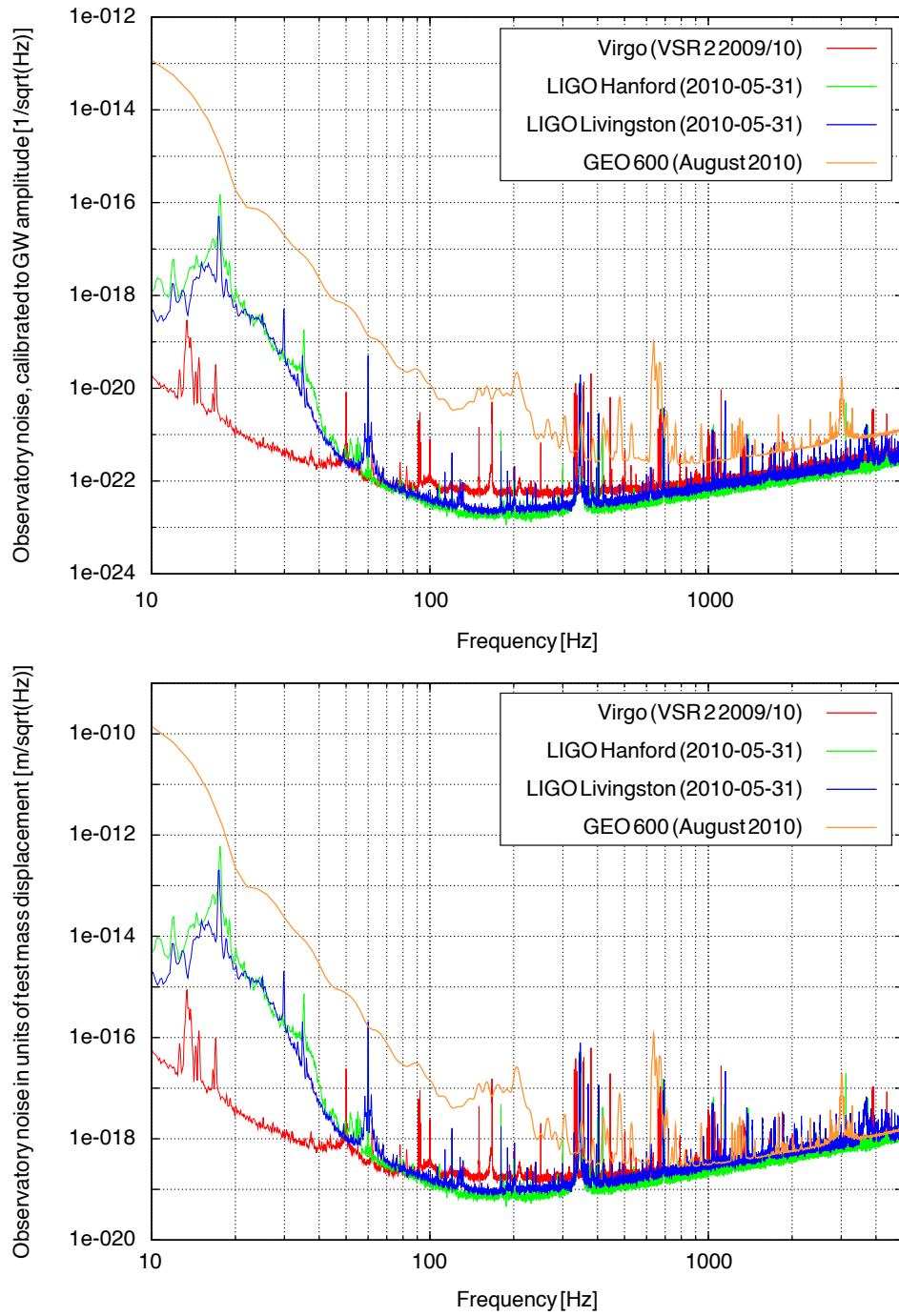


Figure 1.3.: Status of the observatory sensitivities in units of GW strain (top) and of test mass displacement (bottom) in the year 2010. The Virgo V2 sensitivity curve was chosen because it refers to the best Virgo sensitivity achieved by now at high frequencies where the observatory is limited by quantum noise (see discussion in Section 1.3). Source: [LIGO-Sens, Virgo-Sens, GEO-Sens].

fundamental noises limiting the sensitivity at low, intermediate and high frequencies are addressed.

Seismic noise

If vibrations of the terrestrial environment couple to the interferometer test masses, they will mask any potential GW signal. This seismic noise is due to a variety of causes that reach from human activities to the impact of ocean waves on continental coastlines. As a rule of thumb, the seismic noise spectrum can in first-order approximation be assumed to be white (frequency-independent) from 1 Hz to 10 Hz and to show a $1/f^2$ characteristics above 10 Hz [Saulson94]. A combination of active and passive filters along with multi-stage pendulum suspensions is used in the GW observatories for vibration isolation. Since the motion of a mass suspended from a pendulum is suppressed by a factor proportional to $1/f^2$ above the pendulum's resonance frequency (typically a few Hertz in case of the observatories), multiple suspensions can achieve an effective noise suppression by a factor of $10^7 - 10^8$ above some 10 Hz [Aufmuth+05]. Seismic noise is dominant at frequencies below about 50 Hz (with the exception of Virgo, where due to a sophisticated suspension system, the so-called *Virgo super attenuator*, measurements not limited by seismic noise down to frequencies of a few Hertz [Ballardin+01] are possible).

Thermal noise

Different noise sources that result from thermally excited motions are usually referred to as thermal noise. They can be sub-divided further into different categories [Rowan+05] as for example coating thermal noise [Crooks+04], substrate thermal noise [Liu+00], thermorefractive noise [Braginsky+01] or suspension noise. A broad overview discussion with further references is provided in [Ju+12b]. Generally, the thermal noise issue is addressed using materials with a high Q-factor and hence with a low mechanical loss for the test masses and the suspensions to concentrate the thermal energy in a discrete number of modes at frequencies outside the detection band. The test masses are designed to have the principal vibration modes above 5 kHz, while the modes of the pendulum suspensions are at seismic-noise dominated frequencies of a few Hertz [Aufmuth+05]. In current GW observatories operated at room temperature, the sensitivity is limited by thermal noise at frequencies between about 50 Hz and several hundred Hertz (again, with the exception of Virgo). Thermal noise is expected to limit the sensitivities of future generations of GW observatories. An approach to further reduce this noise is to operate the observatories at cryogenic temperature. Recently, the proposal for LCGT [Kuroda+10], a Japanese GW observatory where the final suspension stages are cooled to a temperature below 20 K, was approved. A GW laser interferometer operated at cryogenic temperatures was earlier demonstrated in the 100 m CLIO prototype experiment [Arai+09].

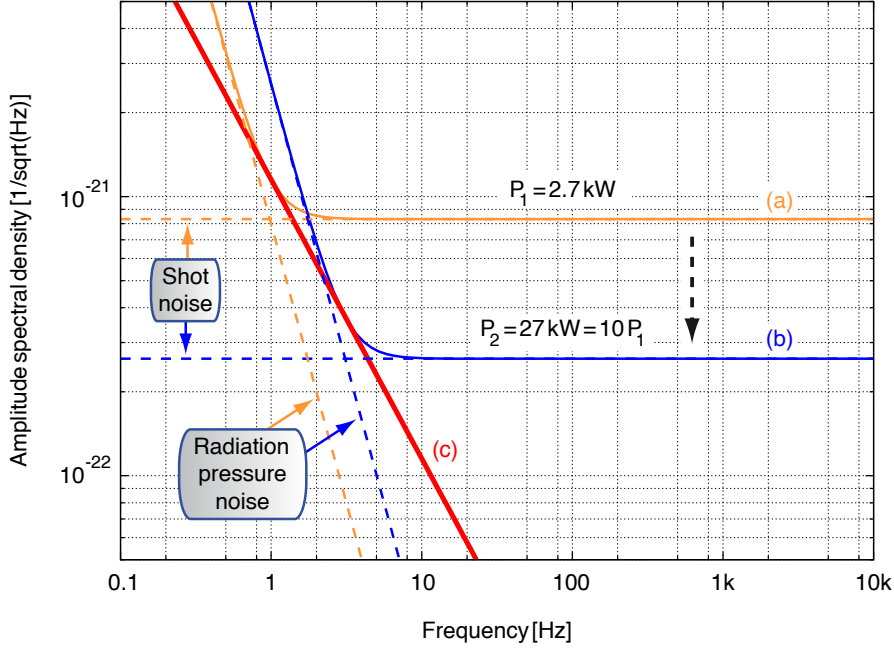


Figure 1.4.: Shot noise and radiation pressure noise in a Michelson interferometer without arm cavities and signal-recycling. (a) Assuming $P = 2.7 \text{ kW}$, $\lambda = 1064 \text{ nm}$, $m = 5.6 \text{ kg}$ and $L = 1200$ (corresponding to the GEO 600 parameters). (b) Same parameters with a laser power increased by a factor of 10. (c) Standard quantum limit showing the minimized optical readout noise value at any given frequency.

Quantum noise

A gravitational wave signal is ‘translated’ by the laser interferometer into a variation of the optical power at the signal output port. A fundamental limit for the possible measurement accuracy is set by the Poissonian distribution of the photon number

$$p(N) = \frac{\bar{N}^N \exp(-\bar{N})}{N!} \quad (1.5)$$

arriving within a time interval at the interferometric photo detector. Here, \bar{N} is the mean number per counting interval (when $\bar{N} \gg 1$, being a valid assumption for the laser interferometers, the Poissonian distribution can be approximated by a Gaussian distribution). Laser GW interferometers are operated close to their *dark fringe*, which means that due to destructive interference almost no light leaves the signal port and all optical power is reflected back to the laser. However, zero-point fluctuations of the electromagnetic field, in the following referred to as *vacuum fluctuations*, are coupled into the interferometer’s signal port and generate a signal that is not distinguishable from a GW signal. For a ‘simple’ Michelson-type interferometer without arm cavities or

signal-recycling, this effect is described by the frequency-independent signal-normalized amplitude spectral density [Rüdiger11]

$$h_{\text{Shot}}(f) = \frac{1}{\ell} \sqrt{\frac{\hbar c \lambda}{\pi P}}, \quad (1.6)$$

Here, $\ell = 2L$ is the total optical path, L is the arm length and P is the optical power inside the interferometer. Since this signal-normalized *quantum shot noise* is inversely proportional to the circulating power, in principle an arbitrarily precise measurement seems possible using more and more powerful lasers. In reality, a practical upper limit is given by the thermal effects which arise when laser light is absorbed by the interferometer optics. Currently, shot noise is the limiting contribution to the noise budget of the observatories at frequencies above several hundred Hertz (about 700 Hz in case of GEO 600).

Additionally, a back-action effect has to be considered: the system being measured is disturbed by the measurement process itself. The vacuum fluctuations coupled into the interferometer lead to a fluctuating radiation pressure force on the test masses and hence manifest as a displacement noise [Braginsky+92]. For a basic Michelson-type interferometer design, this *radiation pressure noise* contributes to the linear noise spectral density normalized to the GW amplitude as [Somiya11]

$$h_{\text{RP}}(f) = \frac{1}{m f^2 \ell} \sqrt{\frac{4 \hbar P}{\pi^3 c \lambda}}, \quad (1.7)$$

with m being the mirror mass. In contrast to shot noise, radiation pressure noise shows a $1/f^2$ characteristic and is hence dominant at lower frequencies. Furthermore, the radiation pressure noise contribution grows with increasing laser power. Both noise sources, which can be considered as “two faces of a single noise” [Saulson94], contribute to the total *optical readout noise* of a Michelson-type GW interferometer as

$$h_{\text{ORN}}(f) = \sqrt{h_{\text{Shot}}^2(f) + h_{\text{RP}}^2(f)}. \quad (1.8)$$

If we try to improve the sensitivity at low frequencies lowering the optical power, this will reduce the sensitivity at high frequencies and vice versa. For any given frequency, an optimal power value

$$P_{\text{opt}}(f) = \frac{\pi c \lambda m f^2}{2} \quad (1.9)$$

exists for which the readout noise contribution is minimized. Plugging Eq. (1.9) into Eq. (1.8) yields the expression

$$h_{\text{SQL}}(f) = \frac{1}{\pi f \ell} \sqrt{\frac{4 \hbar}{m}} \quad (1.10)$$

for the lowest possible optical readout noise at any given frequency, known as the *standard quantum limit* (SQL). The noise contributions derived are illustrated in Fig. 1.4.

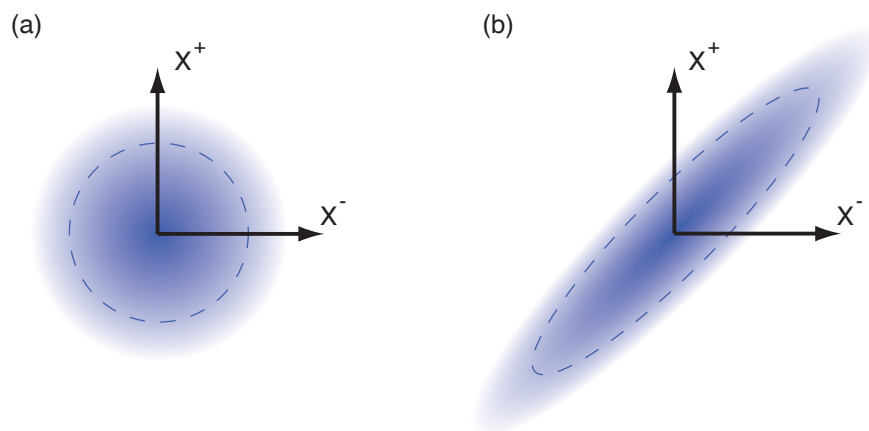


Figure 1.5.: (a) Pictorial phase-space representation of a vacuum state. The blue area represents a projection of the state's Wigner function, the quasi-probability value is encoded in the color density (the darker the color, the higher the quasi-probability value). The dashed line shows one contour line of the Wigner function. The quantum uncertainty is uniformly distributed in every field quadrature with X^+ and X^- denominating the amplitude and phase quadrature, respectively. (b) Representation of a squeezed vacuum state. The fluctuations are reduced in one field quadrature below the vacuum level at the expense of the orthogonal quadrature. The areas of the noise circle (a) and the noise ellipse (b) are identical.

1.4. Reducing the quantum noise

Although suggested otherwise by its name, the standard quantum limit does not constitute a fundamental limit. It assumes that the zero-point (vacuum) fluctuations which enter the interferometer's signal port are in a state of minimal uncertainty with equal noise in every quadrature of the electromagnetic field (Fig. 1.5 (a)). Because the interferometer is operated close to its dark fringe and thus constitutes a compound mirror, the vacuum noise is effectively reflected at the signal port and, arriving at the photo detector together with the signal, finally inhibits an arbitrarily precise measurement.

Heisenberg's uncertainty principle forbids the product of the uncertainties in two orthogonal quadratures of the electromagnetic field to drop below a certain value. It is, however, possible to generate a state of the light field whose uncertainty in one quadrature is reduced compared to a vacuum state, at the expense of an increased uncertainty in the orthogonal quadrature. Figure 1.5 (b) illustrates such a state in quadrature phase space. Due to the characteristic shape, it is usually denominated as a *squeezed (vacuum) state*.

It was Caves who in 1981 for the first time proposed to improve the signal-to-noise ratio (SNR) of a GW interferometer by utilizing squeezed states [Caves81]. This is especially

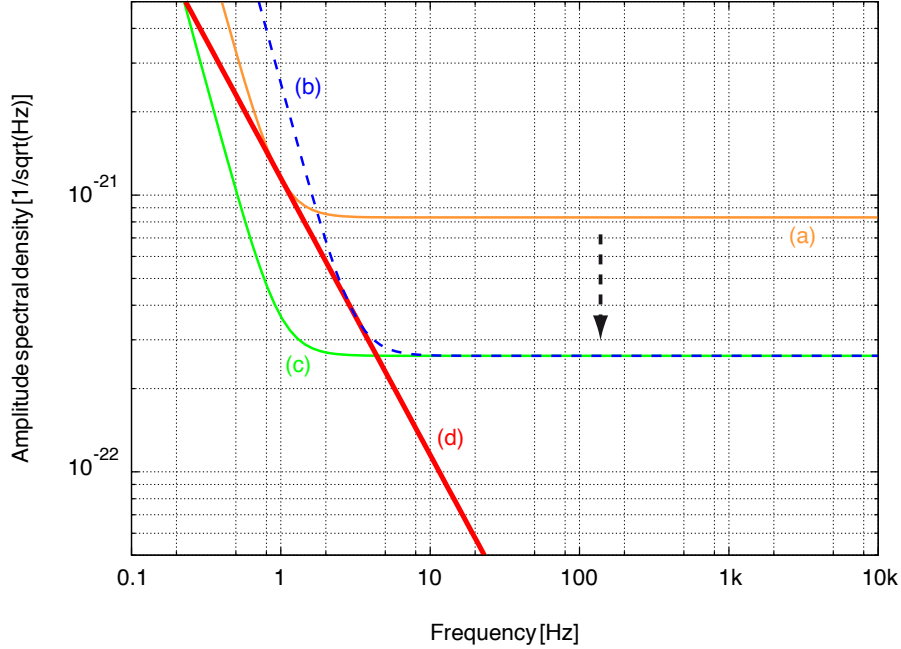


Figure 1.6.: Quantum-noise-limited strain sensitivities of a Michelson interferometer (compare to Fig. 1.4). (a) Assuming $P = 2.7$ kW, $\lambda = 1064$ nm, $m = 5.6$ kg and $L = 1200$ m (corresponding to the GEO 600 parameters). (b) Same parameters with a laser power increased by a factor of 10. (c) Same parameter as trace (a), but with 10 dB of squeezing injected into the signal port. The squeezing angle is optimized for a broadband sensitivity improvement [Jaeckel+90]. This is experimentally realized using an additional optical resonator to introduce a frequency-dependent orientation to the squeezing ellipse [Kimble+01]. (d) Standard quantum limit showing the minimized optical readout noise value at any given frequency for vacuum fluctuations entering the signal port.

remarkable considering that at this time interferometric GW detectors were yet to be constructed and squeezed light was also known merely as a theoretical concept. Later works extended the idea to a broadband sensitivity improvement that would allow to push the sensitivity below the SQL [Yuen83b, Unruh83, Jaeckel+90]. The basic idea is to substitute the vacuum state entering the signal port by an appropriately oriented squeezed vacuum. Where shot noise is dominant, the noise in the phase quadrature needs to be reduced as far as possible. At low frequencies it is, on the other hand, the noise in the amplitude quadrature that limits the sensitivity. The effect of squeezing injection is shown in Fig. 1.6. Therein, a squeezing factor of 10 dB, leading to a broadband sensitivity improvement by a factor of 3.3, was assumed. At shot-noise-dominated frequencies, the

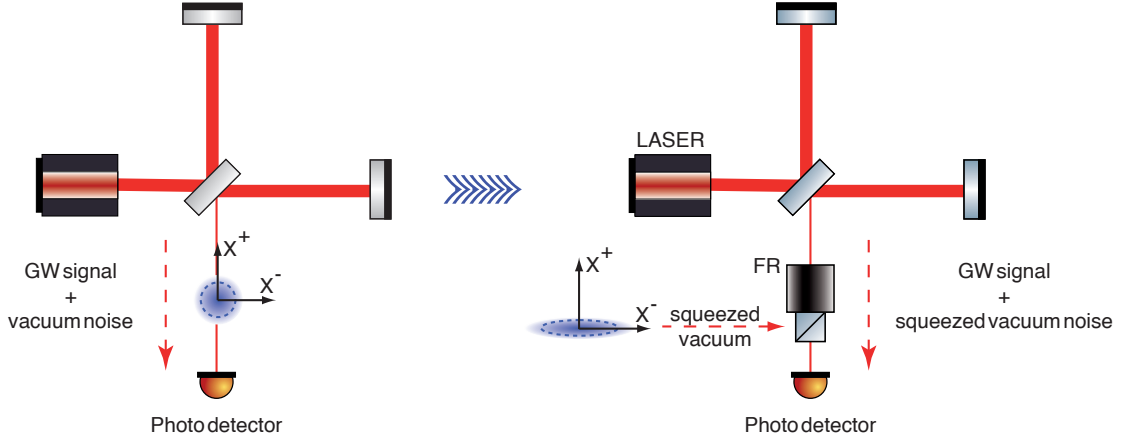


Figure 1.7.: Transition from a conventional Michelson-type GW interferometer (left) to an interferometer with squeezing injection (right).

same effects can be reached by a laser power increase by a factor of 10, however at the expense of a reduced sensitivity at low frequencies.

It is worth noting that the injection of squeezed states can only improve the interferometer sensitivity at frequencies where it is limited by quantum noise. Current observatory generations are limited by shot noise at frequencies above several hundred Hertz, while radiation pressure noise is not yet an issue. For noise reduction in only one quadrature (in this case the phase quadrature), the simple injection scheme shown in Fig. 1.7 is sufficient. It is realized using a Faraday rotator (FR) and a polarizing beam splitter (PBS). The squeezed field is reflected at the polarizer, experiences a 45 degree polarization rotation passing the FR and another 45 degree rotation in the same direction after having been reflected at the signal-recycling mirror of the interferometer. Due to the total polarization rotation of 90 degrees, the squeezed beam is transmitted by the PBS together with the output beam of the interferometer (carrying the GW signal) and arrives at the photo detector.

1.5. Experimental generation of squeezed light

The first experimental demonstration of squeezed states of light was achieved in the 1980s by Slusher *et al.* [Slusher+85], closely followed by other research teams [Wu+87, Pereira+88]. In the following two decades, interest moved away from proof of principle experiments to the construction of robust sources of squeezing with the main concern of improving the squeezing figures. For this purpose, below-threshold optical parametric oscillators proved to be very efficient squeezed-light sources. In these, squeezing is generated via parametrical down-conversion in a $\chi^{(2)}$ nonlinear crystal.

Strong squeezing at the carrier wavelength of the currently operated GW detectors, being 1064 nm, can e.g. be generated in MgO:LiNbO₃ [Vahlbruch+08, Mehmet+10] or periodically poled KTP (PPKTP) [Eberle+10], pumped by a second-harmonic 532 nm beam. Additional requirements on a squeezed-light source for GW detectors were imposed by their audio-frequency operation band. Proof of principle experiments included the development of novel control schemes to generate squeezing at audio frequencies [McKenzie+04, McKenzie+05, Vahlbruch+06, Vahlbruch+07, Chelkowski+07] as well as the demonstration of high degrees of squeezing [Mehmet+10, Eberle+10, Mehmet+11]. Finally, the implementation of squeezed light was tested in a suspended GW prototype detector [Goda+08b].

1.6. Structure of the thesis

The goal of the work presented in this thesis was the construction and characterization of a compact, transportable squeezed-light laser for the gravitational wave observatory GEO 600. Furthermore, a non-classically enhanced sensitivity of a large-scale GW observatory by squeezed light was to be demonstrated for the first time ever. The structure of this thesis basically follows the different stages of the experiment.

Chapter 2 provides a theoretical introduction to the concept of squeezed states as well as to the techniques necessary for squeezing generation and detection.

The layout of the GEO 600 squeezed-light laser is described in detail in Chapter 3. In particular the long-term stability of the squeezing output is addressed since the generated degree of squeezing has to remain stable on timescales of hours to days to ensure a non-varying observatory sensitivity.

In Chapter 4, a characterization of the squeezed-light laser is presented. Up to 9.6 dB of noise reduction was measured over the entire frequency band of Earth-bound GW observatories. The longest characterization measurements addressing the long-term stability lasted for 20 h, an overall duty cycle of more than 99 % was observed.

The integration of the squeezed-light laser in GEO 600 is discussed in Chapter 5. In the frequency range where the observatory sensitivity is limited by shot noise (above 700 Hz), a broadband noise reduction of up to 3.5 dB was achieved. This corresponds to an increase in detection rate for isotropically distributed GW sources in that frequency band by a factor of up to 3.4. Due to the application of squeezed light, GEO 600 has achieved its best ever sensitivity since the implementation of the DC readout scheme. Finally, an analysis of current optical loss sources is provided along with a discussion of the loss reduction feasible in the near future.

The results of the thesis are summarized in Chapter 6. Ultimately, an outlook to the squeezing contributions expected in future generations of GW observatories is provided.

From classical light to quantum optics

In this field (of physics), almost everything is already discovered, and all that remains is to fill a few holes.

Prof. P. von Jolly to Max Planck, 1874

With these words Philipp von Jolly, a friend of the Planck family, sought to dissuade the 17-years old Max Planck from dedicating his life to the field of physics [Lightman05]. Yet living in a ‘classical’ world, little did he know that a whole new theory of quantum mechanics was to emerge and that Planck’s ideas would contribute to it in an essential way.

Starting from Maxwell’s equations, in this chapter a quantized description of the electromagnetic field is derived. Thereupon, different states of the light field that are important for the work presented in this thesis, are discussed. Finally, basics of nonlinear optics required for the understanding of the generation of non-classical states of the light field are summarized. The discussions in Sections 2.1–2.6 follow the References [Gerry+06, Bachor+04].

2.1. Quantization of a single-mode electromagnetic field

A classical description of electromagnetic fields propagating in free space is given by Maxwell’s equations, which in SI units read as

$$\vec{\nabla} \cdot \vec{B} = 0 \qquad \vec{\nabla} \cdot \vec{E} = 0 \qquad (2.1 \text{ a, b})$$

$$\vec{\nabla} \times \vec{B} - \mu_0 \epsilon_0 \frac{\partial \vec{E}}{\partial t} = 0 \qquad \vec{\nabla} \times \vec{E} + \frac{\partial \vec{B}}{\partial t} = 0, \qquad (2.1 \text{ c, d})$$

2. From classical light to quantum optics

with \vec{E} and \vec{B} denominating the electric and the magnetic field vectors, respectively. Applying the rotation operator to Eq. (2.1 d) and considering Eqs. (2.1 a) and (2.1 c), after a short calculation yields the wave equation

$$\nabla^2 \vec{E} - \mu_0 \epsilon_0 \frac{\partial^2 \vec{E}}{\partial t^2} = 0 \quad (2.2)$$

that has *per definitionem* to be satisfied by any electric field. For simplicity, let us consider a single-mode field confined to a one-dimensional cavity that is oriented along the z -axis and has perfectly reflective mirrors. In addition, the polarization vector of the field is, without loss of generality, assumed to be parallel to the x -axis. A possible monochromatic solution satisfying Eq. (2.2) and the boundary conditions is given by

$$\vec{E}(\vec{r}, t) = \vec{e}_x E_x(z, t) = \vec{e}_x \left(\frac{2\omega^2}{V\epsilon_0} \right)^{1/2} q(t) \sin(kz), \quad (2.3)$$

with ω being the frequency of the field mode and \vec{e}_x being a unit polarization vector. For simplicity, the higher-order modes $2\omega, 3\omega, \dots$, likewise satisfying the boundary conditions, are omitted in the following. The wave number k is related to the frequency via $k = \omega/c$ and V denominates the effective volume of the cavity. The time-dependent factor $q(t)$ has the dimension of a length and will act as a canonical position as shown below. From Eq. (2.3) and Eq. (2.1 c), the magnetic field in the cavity is

$$\vec{B}(\vec{r}, t) = \vec{e}_y B_y(z, t) = \vec{e}_y \left(\frac{\mu_0 \epsilon_0}{k} \right) \left(\frac{2\omega^2}{V\epsilon_0} \right)^{1/2} \dot{q}(t) \cos(kz), \quad (2.4)$$

where \vec{e}_y is a unit polarization vector. In this model, the time derivative of the canonical variable $q(t)$ corresponds to the canonical momentum of a ‘particle’ of unit mass

$$\dot{q}(t) = p(t). \quad (2.5)$$

The *Hamiltonian*, describing the energy of the field mode, is given by the integral

$$H = \frac{1}{2} \int dV \left(\epsilon_0 E_x^2 + \frac{1}{\mu_0} B_y^2 \right) \quad (2.6)$$

over the cavity volume. Eq. (2.6) can be further simplified to

$$H(q, p) = \frac{1}{2} (p^2 + \omega^2 q^2). \quad (2.7)$$

Formally, a single-mode field is hence identical to a harmonic oscillator of unit mass with the electric and magnetic fields playing the role of canonical position and momentum. This allows us to identify the classical variables q and p with the operators \hat{q} and \hat{p} that satisfy the commutator relation

$$[\hat{q}, \hat{p}] = \hat{q}\hat{p} - \hat{p}\hat{q} = i\hbar. \quad (2.8)$$

This approach is known as *canonical quantization* [Cohen-Tannoudji+99]. Therewith, the electric and magnetic fields become operators as well, and the Hamiltonian can be expressed as

$$\hat{H}(\hat{q}, \hat{p}) = \frac{1}{2} (\hat{p}^2 + \omega^2 \hat{q}^2) . \quad (2.9)$$

It is worth noting that the canonical quantization constitutes an intuitive process which does not follow a precisely described mathematical rule.

Introducing the linear combinations

$$\hat{a} = \frac{1}{\sqrt{2\hbar\omega}} (\omega\hat{q} + i\hat{p}) \quad \text{and} \quad \hat{a}^\dagger = \frac{1}{\sqrt{2\hbar\omega}} (\omega\hat{q} - i\hat{p}) \quad (2.10)$$

with

$$[\hat{a}, \hat{a}^\dagger] = 1 , \quad (2.11)$$

the electric and magnetic field operators can be expressed as

$$\begin{aligned} \hat{E}_x(z, t) &= E_0 (\hat{a} + \hat{a}^\dagger) \sin(kz) , \\ \hat{B}_y(z, t) &= \frac{B_0}{i} (\hat{a} - \hat{a}^\dagger) \cos(kz) . \end{aligned} \quad (2.12)$$

Here $E_0 = (\hbar\omega/\epsilon_0 V)^{1/2}$ and $B_0 = (\mu_0/k) (\epsilon_0 \hbar\omega^3/V)^{1/2}$. This finally allows us to write the Hamiltonian as

$$\hat{H} = \hbar\omega \left(\hat{a}^\dagger \hat{a} + \frac{1}{2} \right) . \quad (2.13)$$

While the position and momentum operators are Hermitian and therefore correspond to observables, this is not the case for \hat{a} and \hat{a}^\dagger . They are usually referred to as the *annihilation* and the *creation* operator, respectively.

2.2. Number or Fock states

An understanding of the name convention for \hat{a} and \hat{a}^\dagger can be obtained from the analysis of the energy eigenstates $|n\rangle$ of the single-mode field with the energy eigenvalues E_n and hence with

$$\hat{H} |n\rangle = \hbar\omega \left(\hat{a}^\dagger \hat{a} + \frac{1}{2} \right) |n\rangle = E_n |n\rangle . \quad (2.14)$$

If Eq. (2.14) is multiplied by \hat{a} , we obtain the new eigenvalue equation

$$\hat{a}\hat{H} |n\rangle = \hbar\omega \left(\hat{a}\hat{a}^\dagger \hat{a} + \frac{1}{2}\hat{a} \right) |n\rangle = E_n \hat{a} |n\rangle . \quad (2.15)$$

Using the commutation relation from Eq. (2.11), Eq. (2.15) can be expressed as

$$\hbar\omega \left(1 + \hat{a}^\dagger \hat{a} + \frac{1}{2} \right) \hat{a} |n\rangle = E_n \hat{a} |n\rangle \quad (2.16)$$

2. From classical light to quantum optics

and thus as

$$\hat{H}(\hat{a}|n\rangle) = \hbar\omega \left(\hat{a}^\dagger \hat{a} + \frac{1}{2} \right) (\hat{a}|n\rangle) = (E_n - \hbar\omega) (\hat{a}|n\rangle) . \quad (2.17)$$

Eq. (2.17) describes the eigenvalue problem for $\hat{a}|n\rangle$, being an eigenstate of the Hamiltonian with the energy eigenvalue $E_n - \hbar\omega$. This explains the name ‘annihilation operator’. When \hat{a} is applied to a number state $|n\rangle$, a quantum of energy is ‘destroyed’:

$$\hat{a}|n\rangle = c_n |n-1\rangle , \quad (2.18)$$

with c_n being a normalization constant. Similarly, the application of \hat{a}^\dagger to $|n\rangle$ ‘creates’ a photon of energy $\hbar\omega$.

While an upper limit for the energy of a state $|n\rangle$ does not exist, a lower boundary is set by the fact that the energy of the harmonic oscillator must be positive. Therefore, a lowest energy state which satisfies the condition

$$\hat{a}|0\rangle \equiv 0 \quad (2.19)$$

with

$$\hat{H}(\hat{a}|0\rangle) = (E_0 - \hbar\omega) (\hat{a}|0\rangle) \equiv 0 \quad (2.20)$$

must exist. The eigenvalue problem for this state that is usually referred to as the *vacuum* or *ground* state is given by

$$\hat{H}|0\rangle = \hbar\omega \left(\hat{a}^\dagger \hat{a} + \frac{1}{2} \right) |0\rangle = \frac{1}{2}\hbar\omega |0\rangle , \quad (2.21)$$

where $\hbar\omega/2$ is the so-called zero-point energy of the electromagnetic field.

The energy eigenvalues E_n of the Hamiltonian are, due to the effect of the creation and annihilation operators discussed above, given by

$$E_n = \hbar\omega \left(n + \frac{1}{2} \right) \quad \text{with} \quad n = 0, 1, 2, \dots \quad (2.22)$$

The Hamiltonian can therefore also be written as

$$\hat{H} = \hbar\omega \left(\hat{n} + \frac{1}{2} \right) , \quad (2.23)$$

where $\hat{n} = \hat{a}^\dagger \hat{a}$ is the *number operator* with

$$\hat{n}|n\rangle = n|n\rangle . \quad (2.24)$$

To satisfy the identity $\langle n|n\rangle = 1$, the condition $c_n = \sqrt{n}$ for the normalization constant from Eq. (2.18) can be derived. This yields the useful relations

$$\hat{a}|n\rangle = \sqrt{n}|n-1\rangle \quad \text{and} \quad \hat{a}^\dagger|n\rangle = \sqrt{n+1}|n+1\rangle . \quad (2.25)$$

From this, we can immediately deduce that a state with an arbitrary number n of photons can be generated from the ground state by the repeated application of the creation operator \hat{a}^\dagger :

$$|n\rangle = \frac{(\hat{a}^\dagger)^n}{\sqrt{n!}} |0\rangle. \quad (2.26)$$

The number states $\{|n\rangle\}$ form a complete set of orthogonal vectors in Fock-space.

One interesting property of these states is that, while they have a well-defined energy given by Eq. (2.22), this is not the case for the electric field as directly follows from Eq. (2.12):

$$\langle n | \hat{E}_x(z, t) | n \rangle = E_0 \sin(kz) \left(\langle n | \hat{a} | n \rangle + \langle n | \hat{a}^\dagger | n \rangle \right) = 0. \quad (2.27)$$

The mean field of a number state therefore vanishes. The energy density of the field is given by

$$\begin{aligned} \langle n | \left(\hat{E}_x(z, t) \right)^2 | n \rangle &= E_0^2 \sin^2(kz) \langle n | \left((\hat{a})^2 + (\hat{a}^\dagger)^2 + \hat{a}\hat{a}^\dagger + \hat{a}^\dagger\hat{a} \right) | n \rangle \\ &= E_0^2 \sin^2(kz) \left(\langle n | 2\hat{a}^\dagger\hat{a} + 1 | n \rangle \right) \\ &= E_0^2 \sin^2(kz) \left(n + \frac{1}{2} \right) \end{aligned} \quad (2.28)$$

and is different from zero. The fluctuations of the field can be described by the *variance* that is defined as

$$\left\langle \left(\Delta \hat{E}_x(z, t) \right)^2 \right\rangle \equiv \left\langle \hat{E}_x^2(z, t) \right\rangle - \left\langle \hat{E}_x(z, t) \right\rangle^2 \quad (2.29)$$

or by the standard deviation

$$\Delta \hat{E}_x = \sqrt{\left\langle \left(\Delta \hat{E}_x(z, t) \right)^2 \right\rangle}. \quad (2.30)$$

For the Fock states, this so-called *uncertainty* is

$$\Delta \hat{E}_x = \sqrt{2} E_0 \sin(kz) \left(n + \frac{1}{2} \right)^{\frac{1}{2}}. \quad (2.31)$$

This expression describes a very important property: Even when $n = 0$, the fluctuations of the field do not vanish but reach a minimum value which is usually referred to as the *zero-point* or *vacuum* fluctuation.

2.3. Quadrature operators

So far the creation and annihilation operators, which are non-Hermitian and therefore do not correspond to real physical observables, were discussed. We can, however, introduce the linear combinations of \hat{a} and \hat{a}^\dagger

$$\hat{X}^+ \equiv \frac{1}{2} (\hat{a} + \hat{a}^\dagger) \quad (2.32)$$

$$\hat{X}^- \equiv \frac{1}{2i} (\hat{a} - \hat{a}^\dagger) . \quad (2.33)$$

They are Hermitian and therefore describe values that can be accessed in a measurement process (to be precise, \hat{X}^+ and \hat{X}^- essentially correspond to the position and momentum operators, but are scaled to be dimensionless). When we for clarity explicitly include the time dependence of the creation and annihilation operators as $\hat{a}(t) = \hat{a}(0) \exp(-i\omega t) \equiv \hat{a} \exp(-i\omega t)$ and $\hat{a}^\dagger(t) = \hat{a}^\dagger(0) \exp(i\omega t) \equiv \hat{a}^\dagger \exp(i\omega t)$, the operator for the electric field may be written as

$$\hat{E}_x(z, t) = 2E_0 \sin(kz) \left[\hat{X}^+ \cos(\omega t) + \hat{X}^- \sin(\omega t) \right] . \quad (2.34)$$

From this form it is obvious that \hat{X}^+ and \hat{X}^- are associated with the field amplitudes oscillating out of phase with each other by 90° . This explains the fact that they are usually referred to as *quadrature* operators.

From the commutation relation

$$\left[\hat{X}^+, \hat{X}^- \right] = \frac{i}{2} \quad (2.35)$$

and the well-known relation [Heisenberg27]

$$\Delta \hat{O}_1 \Delta \hat{O}_2 \geq \frac{1}{2} \left| \left\langle \left[\hat{O}_1, \hat{O}_2 \right] \right\rangle \right| \quad (2.36)$$

for any two operators $\hat{O}_{1/2}$, it directly follows that

$$\Delta \hat{X}^+ \Delta \hat{X}^- \geq \frac{1}{4} . \quad (2.37)$$

While obviously $\langle n | \hat{X}^+ | n \rangle = \langle n | \hat{X}^- | n \rangle = 0$, this is again not the case for the quadrature variations of a number state:

$$\begin{aligned} \langle n | \left(\hat{X}^+ \right)^2 | n \rangle &= \frac{1}{4} \langle n | \hat{a}^2 + (\hat{a}^\dagger)^2 + 2\hat{a}\hat{a}^\dagger + 1 | n \rangle = \frac{1}{4} (2n + 1) , \\ \langle n | \left(\hat{X}^- \right)^2 | n \rangle &= -\frac{1}{4} \langle n | \hat{a}^2 + (\hat{a}^\dagger)^2 - 2\hat{a}\hat{a}^\dagger - 1 | n \rangle = \frac{1}{4} (2n + 1) . \end{aligned} \quad (2.38)$$

The uncertainties are equally distributed over the two field quadratures. When $n = 0$, Heisenberg's uncertainty principle (Eq. (2.36)) is minimized and a state of minimum uncertainty is obtained.

2.4. Coherent states

A disadvantage of the number states $|n\rangle$ is that they have a uniform phase distribution, or, to put it in other words, do not have a well-defined phase. This makes them inappropriate for the description of real fields as for example laser beams. Even approaching the classical limit with $n \rightarrow \infty$, the mean field $\langle n | \hat{E}_x | n \rangle$ remains equal to zero. This does, however, not match a classical field that we know to oscillate sinusoidally in time at a fixed point in space. A set of states better suited to describe the ‘classical’ world of laser fields etc. is given by the eigenstates of the annihilation operator:

$$\hat{a} |\alpha\rangle = \alpha |\alpha\rangle . \quad (2.39)$$

The eigenvalues α may be complex since \hat{a} is a non-Hermitian operator. It is legitimate to expand $|\alpha\rangle$ as

$$|\alpha\rangle = \sum_{n=0}^{\infty} C_n |n\rangle , \quad (2.40)$$

since the number states form a complete set. Plugged into Eq. (2.39), this yields

$$\hat{a} |\alpha\rangle = \alpha \sum_{n=0}^{\infty} C_n |n\rangle = \sum_{n=1}^{\infty} C_n \sqrt{n} |n-1\rangle \quad (2.41)$$

and thus

$$C_n \sqrt{n} = \alpha C_{n-1} \quad (2.42)$$

after equating the coefficients of $|n\rangle$ on both sides. An iteration of the procedure results in the relation

$$C_n = \frac{\alpha}{\sqrt{n}} C_{n-1} = \frac{\alpha^2}{\sqrt{n(n-1)}} C_{n-2} = \dots = \frac{\alpha^n}{\sqrt{n!}} C_0 . \quad (2.43)$$

Eq. (2.40) may thus be rewritten as

$$|\alpha\rangle = C_0 \sum_{n=0}^{\infty} \frac{\alpha^n}{\sqrt{n!}} |n\rangle \quad (2.44)$$

and the constant C_0 can be determined from the normalization requirement $\langle \alpha | \alpha \rangle = 1$. The normalized expression for the so-called *coherent states* $|\alpha\rangle$ finally reads

$$|\alpha\rangle = e^{-\frac{1}{2}|\alpha|^2} \sum_{n=0}^{\infty} \frac{\alpha^n}{\sqrt{n!}} |n\rangle . \quad (2.45)$$

Writing α in polar coordinates as $\alpha = |\alpha| \exp(i\theta)$, it can be shown that the expectation value of the electric field operator

$$\langle \alpha | \hat{E}_x(\vec{r}, t) | \alpha \rangle = 2 |\alpha| \left(\frac{\hbar \omega}{2 \epsilon_0 V} \right)^{1/2} \sin(\omega t - \vec{k} \vec{r} - \theta) \quad (2.46)$$

2. From classical light to quantum optics

is similar to what would be expected from a classical field. The fluctuations in $\hat{E}_x(\vec{r}, t)$ are identical to those in a vacuum state. For this reason, the coherent state may be regarded as a nearly classical-like one. It is, in fact, the best quantum mechanical description of a laser field [Scully+02]. The absolute value of the complex parameter α is, as evident from Eq. (2.46), related to the amplitude of the field and furthermore equals the expectation value of the photon number operator:

$$\bar{n} = \langle \alpha | \hat{n} | \alpha \rangle = |\alpha|^2 \quad (2.47)$$

It hence simply describes the average photon number of the field. The fluctuation of the photon number

$$\Delta \hat{n} = \sqrt{\langle \hat{n}^2 \rangle - \langle \hat{n} \rangle^2} \quad (2.48)$$

can, using

$$\begin{aligned} \langle \alpha | \hat{n}^2 | \alpha \rangle &= \langle \alpha | \hat{a}^\dagger \hat{a} \hat{a}^\dagger \hat{a} | \alpha \rangle \\ &= \langle \alpha | \left(\hat{a}^\dagger \hat{a}^\dagger \hat{a} \hat{a} + \hat{a}^\dagger \hat{a} \right) | \alpha \rangle \\ &= |\alpha|^4 + |\alpha|^2 = \bar{n}^2 + \bar{n} \end{aligned} \quad (2.49)$$

be calculated to

$$\Delta \hat{n} = \sqrt{\bar{n}}. \quad (2.50)$$

This is characteristic for a Poissonian distribution. Correspondingly, the probability of detecting n photons is described by

$$P_n = |\langle n | \alpha \rangle|^2 = e^{-\bar{n}} \frac{\bar{n}^n}{n!}, \quad (2.51)$$

which is indeed a Poissonian distribution with a mean value of \bar{n} .

It is worth mentioning that different approaches can be followed to define coherent states. An alternative to the method described above is the application of the unitary *displacement* operator defined as

$$\hat{D}(\alpha) = \exp\left(\alpha \hat{a}^\dagger - \alpha^* \hat{a}\right) \quad \text{with} \quad \hat{D}^\dagger(\alpha) = \hat{D}(-\alpha) \quad (2.52)$$

to a vacuum state:

$$|\alpha\rangle = \hat{D}(\alpha) |0\rangle. \quad (2.53)$$

Using the disentangling theorem

$$\exp(\hat{A} + \hat{B}) = \exp(\hat{A}) \exp(\hat{B}) \exp\left(-\frac{1}{2} [\hat{A}, \hat{B}]\right), \quad (2.54)$$

Eq. (2.53) can be shown to be identical to Eq. (2.45).

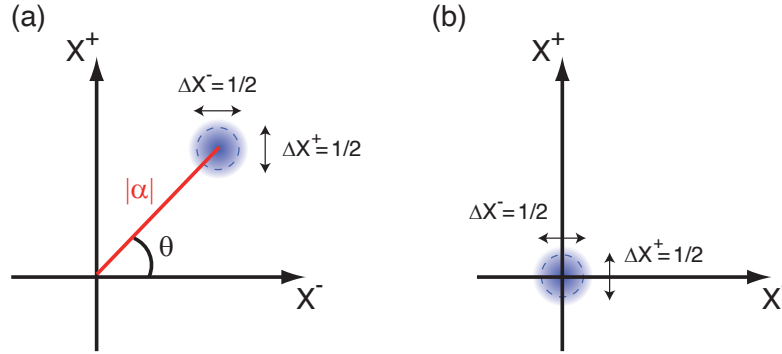


Figure 2.1.: (a) Pictorial phase-space representation of a coherent state of amplitude $|\alpha|$ and phase-angle θ . The fluctuations are uniformly distributed in every field quadrature with X^+ and X^- denominating the amplitude and phase quadrature, respectively. (b) Representation of a vacuum state with $n = 0$.

2.5. Phase-space pictures of coherent states

A coherent state $|\alpha\rangle$ with $\alpha = |\alpha|e^{i\theta}$ and

$$\begin{aligned}\langle \hat{X}^+ \rangle_\alpha &= \frac{1}{2}(\alpha + \alpha^*) = \text{Re}(\alpha), \\ \langle \hat{X}^- \rangle_\alpha &= \frac{1}{2i}(\alpha - \alpha^*) = \text{Im}(\alpha)\end{aligned}\tag{2.55}$$

can be represented pictorially in the complex α -plane as shown in Fig. 2.1 (a). The coherent amplitude is given by a phasor with the length $|\alpha| = \sqrt{n}$ while θ represents the phase angle. The ‘area of uncertainty’ is represented by the blue-shaded circle. It is worth stressing that the fluctuations are with

$$\Delta X^+ = \Delta X^- = \Delta X^\theta = \frac{1}{2}\tag{2.56}$$

equal in all directions of phase space and that the error circle is the same for all coherent states. Fig. 2.1 (b) shows the phase-space representation of a vacuum state. Though these pictures are qualitative only, they are useful to visualize the distribution of noise in the various field quadratures, as for example in case of the squeezed states discussed in Section 2.6.

In classical mechanics, the phase-space distribution constitutes a particularly important concept. A harmonic oscillator can e.g. be fully described by a function $P(q, p)$ providing the probability to find a particular pair of q and p values in a simultaneous measurement [O’Connell82, Leonhardt97]. From such a known probability distribution, all statistical quantities of the oscillator can be predicted. Per definition, such a function has to be normalized and positive.

2. From classical light to quantum optics

The situation is much more complex for a quantum mechanical state, where Heisenberg's uncertainty relation impedes a simultaneous and arbitrarily precise measurement of two non-commuting variables. It is, however, possible to define a similar distribution function $W(q, p)$. Due to the properties of quantum phase space, this 'probability distribution' can become ill-behaved, e. g. assuming negative values. Therefore, it is called a *quasiprobability distribution* (QPD). Although an arbitrary number of QPD-functions may be formulated, one of them proved to be particularly useful. It was introduced by E. P. Wigner in 1932 [Wigner32] as the earliest QPD and is known as the *Wigner function* (WF). For an arbitrary density operator

$$\hat{\rho} = \sum_i p_i |\psi_i\rangle \langle \psi_i|, \quad (2.57)$$

the Wigner function reads

$$W(q, p) \equiv \frac{1}{2\pi\hbar} \int_{-\infty}^{\infty} dx \exp(ipx/\hbar) \left\langle q - \frac{1}{2}x \left| \hat{\rho} \left| q + \frac{1}{2}x \right. \right. \right\rangle \quad (2.58)$$

with $|q + \frac{1}{2}x\rangle$ being the eigenkets of the position operator. Some basic properties of the Wigner function are that it is real for Hermitian operators $\hat{\rho}$:

$$W^*(q, p) = W(q, p) \quad (2.59)$$

and with

$$\int_{-\infty}^{\infty} dp \int_{-\infty}^{\infty} dq W(q, p) = 1 \quad (2.60)$$

normalized because of the normalization of the density operator. For a pure state with $\hat{\rho} = |\psi\rangle \langle \psi|$ it can be shown that integrating over the momentum yields the probability density for the position variable q

$$\int_{-\infty}^{\infty} W(q, p) dp = |\psi(q)|^2 \quad (2.61)$$

and vice versa. However, it must be kept in mind that for some non-classical states $W(q, p)$ can take negative values and may therefore not be mistaken with a true probability distribution.

The Wigner function offers a powerful tool to visualize in phase-space the quantum states discussed above. For example, the Wigner function of a vacuum state given by

$$W_0(q, p) = \frac{1}{\pi} \exp(-q^2 - p^2) \quad (2.62)$$

is shown in Fig. 2.2(a). It is formally identical to the Wigner function of a coherent state that merely represents a displaced vacuum (Eq. (2.53)) and can be written as the displaced Wigner function

$$W_0(q, p) = \frac{1}{\pi} \exp(-(q - q_0)^2 - (p - p_0)^2). \quad (2.63)$$

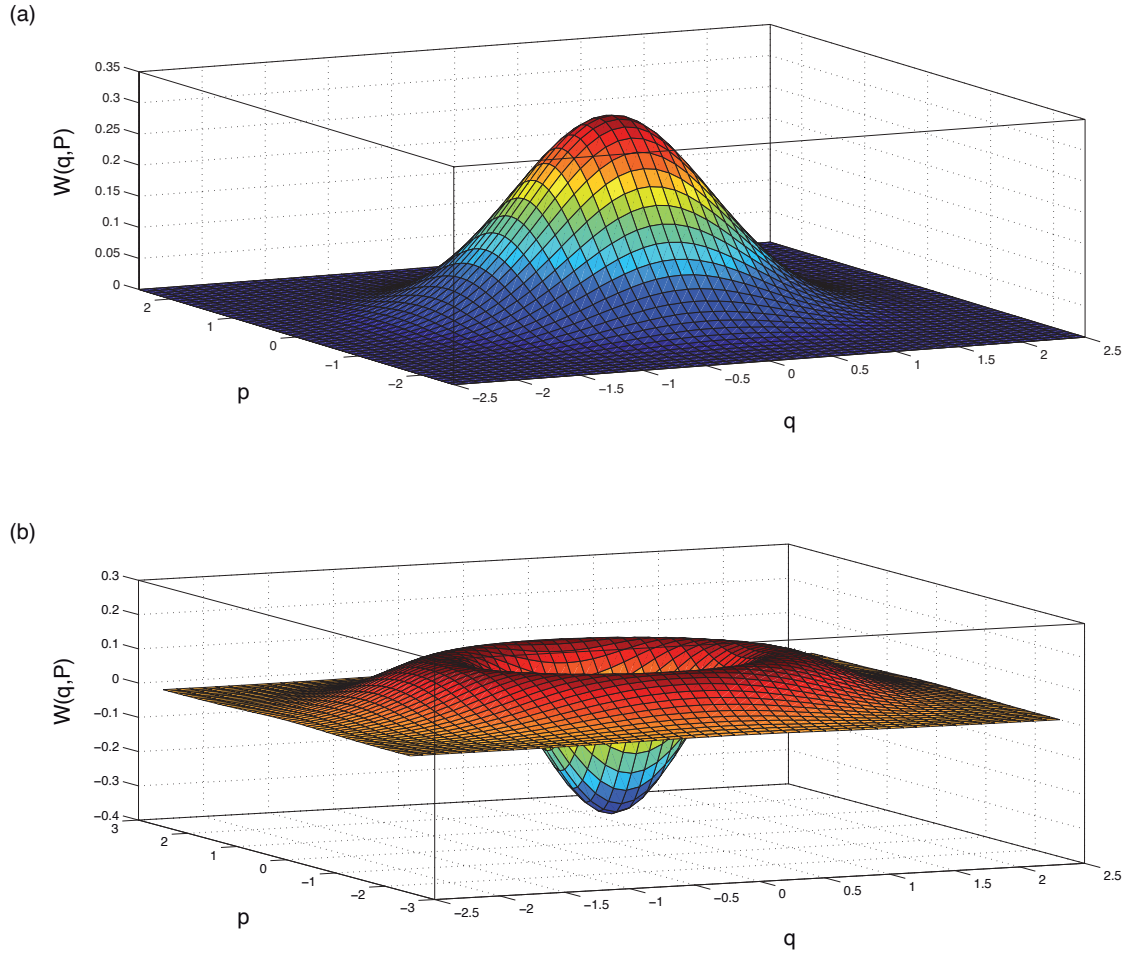


Figure 2.2.: Wigner function (a) for a vacuum state and (b) for a Fock state with $n = 1$.

Both are Gaussian distributions with a balanced amount of fluctuations in all quadratures. An example for the *quasi*-probability nature of the Wigner function, namely the WF of a single-photon Fock state

$$W_n(q, p) = \frac{2q^2 + 2p^2 - 1}{\pi} \exp(-q^2 - p^2), \quad (2.64)$$

is illustrated in Fig. 2.2 (b). It is clearly non-Gaussian and has negative values near the origin.

2.6. Squeezed states

For any three operators $\hat{O}_1, \hat{O}_2, \hat{O}_3$ that satisfy the commutation relation $[\hat{O}_1, \hat{O}_2] = i\hat{O}_3$, it can be shown that (see Eq. (2.36))

$$\left\langle (\Delta\hat{O}_1)^2 \right\rangle \left\langle (\Delta\hat{O}_2)^2 \right\rangle \geq \frac{1}{4} \left| \left\langle \hat{O}_3 \right\rangle \right|^2. \quad (2.65)$$

For the coherent states which are, as discussed above, minimum uncertainty states having

$$\left\langle (\Delta\hat{X}^+)^2 \right\rangle = \left\langle (\Delta\hat{X}^-)^2 \right\rangle = \frac{1}{4}, \quad (2.66)$$

this expression reduces to the equality

$$\left\langle (\Delta\hat{X}^+)^2 \right\rangle \left\langle (\Delta\hat{X}^-)^2 \right\rangle = \frac{1}{16}. \quad (2.67)$$

Equation (2.65) obviously sets a minimal limit to the amount of fluctuations present in two orthogonal quadratures. It does, however, not forbid the fluctuations in one of the quadratures to drop below the minimum uncertainty of a vacuum state at the expense of increased fluctuations in the orthogonal quadrature. States of the electromagnetic field which do with

$$\left\langle (\Delta\hat{X}^\theta)^2 \right\rangle < \frac{1}{4} \quad (2.68)$$

have such a non-classical noise distribution are known as *squeezed states*, in the following simply denominated as *squeezed states*.

In analogy to the displacement operator, a *squeeze* operator for mathematical generation of squeezed states can be defined as

$$\hat{S}(\zeta) = \exp \left[\frac{1}{2} (\zeta^* \hat{a} \hat{a} - \zeta \hat{a}^\dagger \hat{a}^\dagger) \right] \quad \text{with} \quad \zeta = r e^{i\theta}. \quad (2.69)$$

Usually, r is referred to as the *squeeze parameter*, while θ is the squeezing angle:

$$0 \leq r < \infty, \quad 0 \leq \theta \leq 2\pi. \quad (2.70)$$

If the squeeze operator acts on a vacuum state, it will create a sort of ‘two-photon coherent state’, since photons can be created or destroyed only in pairs by $\hat{S}(\zeta)$. To obtain the quadrature variances of a squeezed vacuum state, the expectation values of \hat{a}, \hat{a}^2 , etc. are required. It can be shown using the Baker-Hausdorf lemma that

$$\begin{aligned} \hat{S}^\dagger(\zeta) \hat{a} \hat{S}(\zeta) &= \hat{a} \cosh(r) - \hat{a}^\dagger e^{i\theta} \sinh(r) \\ \hat{S}^\dagger(\zeta) \hat{a}^\dagger \hat{S}(\zeta) &= \hat{a}^\dagger \cosh(r) - \hat{a} e^{-i\theta} \sinh(r). \end{aligned} \quad (2.71)$$

With these relations, the quadrature variances of the squeezed vacuum state can be calculated to

$$\begin{aligned}\langle (\Delta \hat{X}^+)^2 \rangle &= \frac{1}{4} [\cosh^2(r) + \sinh^2(r) - 2 \sinh(r) \cosh(r) \cos(\theta)] \\ \langle (\Delta \hat{X}^-)^2 \rangle &= \frac{1}{4} [\cosh^2(r) + \sinh^2(r) + 2 \sinh(r) \cosh(r) \cos(\theta)] .\end{aligned}\quad (2.72)$$

For $\theta = 0$, Eq. (2.72) reduces to

$$\begin{aligned}\langle (\Delta \hat{X}^+)^2 \rangle &= \frac{1}{4} e^{-2r} \\ \langle (\Delta \hat{X}^-)^2 \rangle &= \frac{1}{4} e^{2r} .\end{aligned}\quad (2.73)$$

The fluctuations in the \hat{X}^+ quadrature are for $r > 0$ hence ‘squeezed’ when compared with a vacuum state, while the \hat{X}^- variance increases correspondingly. In the following, this quadrature is referred to as *anti-squeezed*. The uncertainty product given in Eq. (2.67) is still satisfied and the squeezed vacuum state is thus also a state of minimum uncertainty.

It is evident from Eq. (2.72) that the choice $\theta = \pi$ will lead to squeezing in the \hat{X}^- quadrature. To simplify the discussion of squeezing for all other values of θ , it is useful to define the rotated quadrature operators \hat{Y}^+ and \hat{Y}^- as

$$\begin{pmatrix} \hat{Y}^+ \\ \hat{Y}^- \end{pmatrix} = \begin{pmatrix} \cos(\theta/2) & \sin(\theta/2) \\ -\sin(\theta/2) & \cos(\theta/2) \end{pmatrix} \begin{pmatrix} \hat{X}^+ \\ \hat{X}^- \end{pmatrix} .\quad (2.74)$$

This allows us to write Eq. (2.72) as

$$\begin{aligned}\langle (\Delta \hat{Y}^+)^2 \rangle &= \frac{1}{4} e^{-2r} \\ \langle (\Delta \hat{Y}^-)^2 \rangle &= \frac{1}{4} e^{2r}\end{aligned}\quad (2.75)$$

for any given squeezing angle.

In analogy with the coherent states, once again a more general description of a squeezed coherent state can be obtained applying the squeeze operator to Eq. (2.53):

$$|\alpha, \zeta\rangle = \hat{D}(\alpha) \hat{S}(\zeta) |0\rangle .\quad (2.76)$$

A consequence worth mentioning is that for a squeezed state the expectation value of the photon number operator

$$\langle \hat{a}^\dagger \hat{a} \rangle = |\alpha|^2 + \sinh^2(r)\quad (2.77)$$

increases when compared with a coherent state. This once more illustrates that by the squeezing process photons are generated. Their statistics is restricted to even values

(pairs) by the form of the squeeze operator as shown above.

A pictorial phase-space representation for a state squeezed in the \hat{X}^+ and in an arbitrary quadrature is shown in Fig. 2.3 (a) and (b), respectively. Later on, it is generally referred to as a *squeezing ellipse*. A more sophisticated description is given by the Wigner function of a squeezed vacuum state that can be shown to be [Leonhardt97]

$$W_s(q, p) = \frac{1}{\pi} \exp(-e^{2\zeta} q^2 - e^{-2\zeta} p^2). \quad (2.78)$$

It is, like for a normal vacuum state that is approached choosing $\zeta = 0$, a Gaussian distribution. The effect of quadrature squeezing manifests in the unbalanced variances. The Wigner function of a squeezed vacuum state is shown in Fig. 2.3 (c).

2.7. Basics of nonlinear optics

The considerations presented in Section 2.1 were based on Maxwell's equations for vacuum and treated only the states of the light field without any interactions with matter. It is, however, the nonlinear response of a material system to an optical field that is responsible for the generation of squeezed states. In the following, some basic concepts of nonlinear optics are presented. The discussions follow [Boyd08] that is also recommended to the dedicated reader for a detailed introduction to nonlinear optics.

2.7.1. Nonlinear polarization

If a homogenous electric field \vec{E} is applied to a dielectric material, a force $\vec{F} = q\vec{E}$ acts on the charge carriers, so that a separation of charges is induced. The separation strength is described by the *polarization* which gives the electric dipole moment induced per unit volume of the dielectric material. In the case of conventional optics, the induced displacement $|\vec{d}|$ is rather small and the restoring force is (according to Hook's law) proportional to $|\vec{d}|$. The polarization

$$\vec{P} = \epsilon_0 \chi^{(1)} \vec{E}(t) \quad (2.79)$$

thus depends linearly on the applied electric field. Here ϵ_0 is the vacuum permittivity and the constant of proportionality $\chi^{(1)}$ is the so-called *linear susceptibility*. This approximation is, however, no longer valid in case of intense electric fields. The generalized optical response can then be expressed by the power series

$$\vec{P} = \epsilon_0 \left[\chi^{(1)} \vec{E}(t) + \chi^{(2)} \vec{E}^2(t) + \chi^{(3)} \vec{E}^3(t) + \dots \right] \equiv \vec{P}^{(1)} + \vec{P}^{(\text{NL})} \quad (2.80)$$

with $\chi^{(i)}$ denoting the higher-order susceptibilities being $(i+1)$ -rank tensors. Herein, the linear polarization component describes the interactions known from 'classical' linear

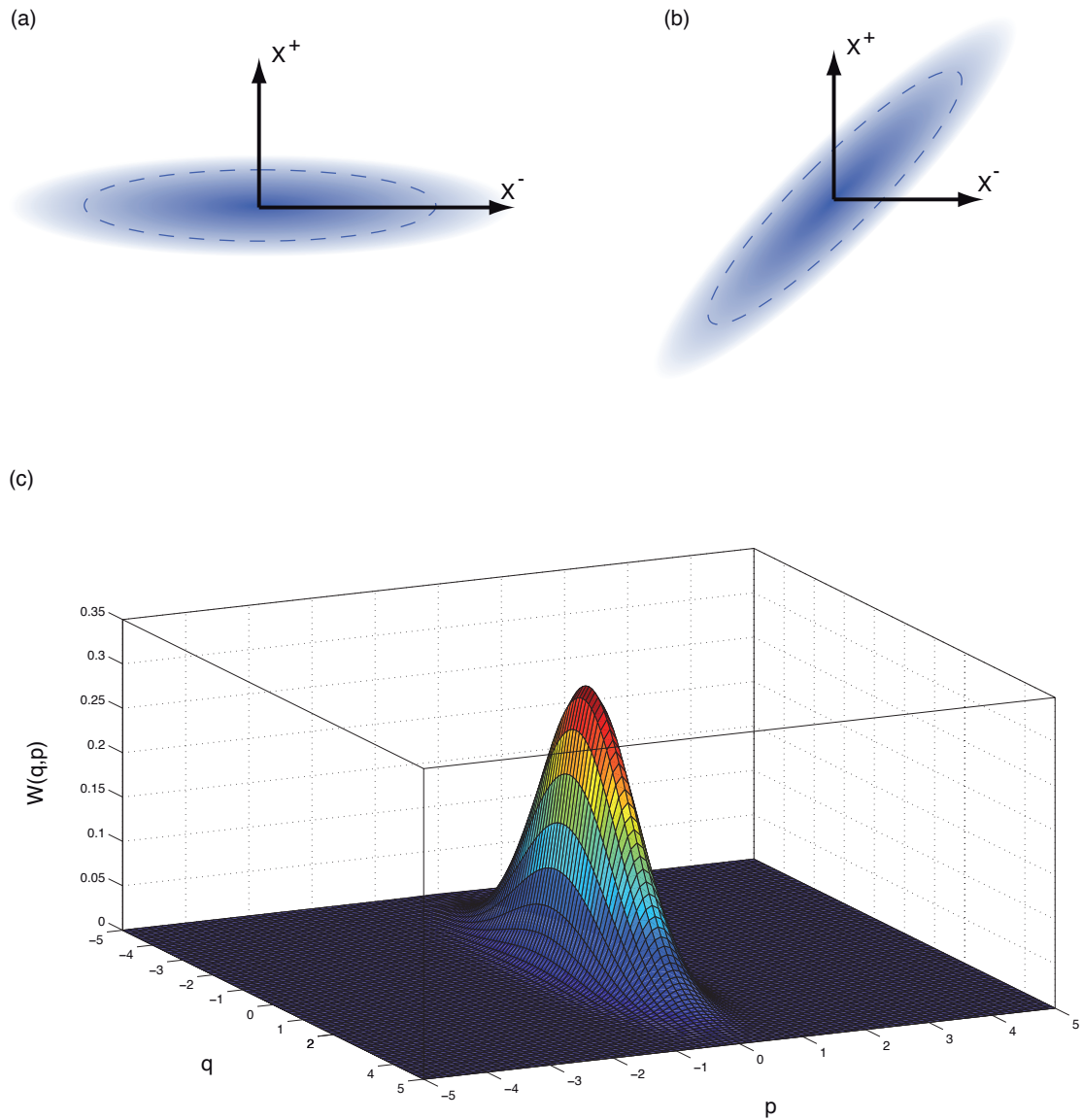


Figure 2.3.: Pictorial phase-space representation of a state (a) squeezed in the \hat{X}^+ and (b) in an arbitrary quadrature. The blue area represents a projection of the state's Wigner function, the quasi-probability value is encoded in the color density (the darker the color, the higher the quasi-probability value). The dashed line shows one contour line of the Wigner function. (c) Wigner function for a squeezed vacuum state with $r = 0.7$ and $\theta = 0$.

optics for which the frequency of the applied electric field is conserved. As shown below, already the second-order nonlinear interaction leads to the generation of additional frequency components. For a single-frequency field

$$E(t) = E_0 e^{-i\omega t} + \text{c. c.} \quad (2.81)$$

this means that due to the second-order polarization (Eq. (2.80))

$$P^{(2)} = 2\epsilon_0 \chi^{(2)} [E_0 E_0^* + E_0^2 e^{-2i\omega t}] + \text{c. c.} \quad (2.82)$$

an additional field at twice the frequency is generated. In the case that two or more frequencies are involved, the $\chi^{(2)}$ interaction correspondingly leads to the generation of sum and difference frequencies.

In the most general description, a huge variety of components of the susceptibility tensors have to be determined to fully describe any nonlinear interaction. This problem can fortunately be simplified considering the physical properties of electric fields as well as symmetry properties of nonlinear crystals. It can be shown that $\chi^{(2)}$ interactions like e. g. the sum-frequency generation

$$P^{(2)}(\omega_3 = \omega_1 + \omega_2) = 4\epsilon_0 d_{\text{eff}} E(\omega_1) E(\omega_2) \quad (2.83)$$

can be described by an effective susceptibility value d_{eff} [Boyd08]. It is finally worth mentioning that $\chi^{(2)}$ interactions can only occur in materials which do not display central symmetry. Therefore, in amorphous materials like glass as well as in many crystals, $\chi^{(2)}$ vanishes and no second-order nonlinear interactions can be observed. For the work described in this thesis, two different crystal species, namely LiNbO₃ and KTiOPO₄ (KTP), have been used as $\chi^{(2)}$ materials. In the following, a brief discussion of the second-order processes is provided.

2.7.2. Sum-frequency generation

Starting with Maxwell's equations in matter and assuming a medium which is free of sources and contains no free currents, the optical wave equation can be derived as

$$\nabla^2 \vec{E} - \frac{1}{c^2} \frac{\partial^2 \vec{E}}{\partial t^2} = \frac{1}{\epsilon_0 c^2} \frac{\partial^2 \vec{P}}{\partial t^2}. \quad (2.84)$$

In case of a lossless, dispersionless, isotropic medium the linear polarization component is parallel to \vec{E} and the wave equation can be simplified further to

$$\nabla^2 \vec{E} - \frac{\epsilon_{(1)}}{c^2} \frac{\partial^2 \vec{E}}{\partial t^2} = \frac{1}{\epsilon_0 c^2} \frac{\partial^2 \vec{P}^{(\text{NL})}}{\partial t^2} \quad (2.85)$$

where $\epsilon_{(1)} = 1 + \chi^{(1)}$ is the relative permittivity. Eq. (2.85) has the form of a driven wave

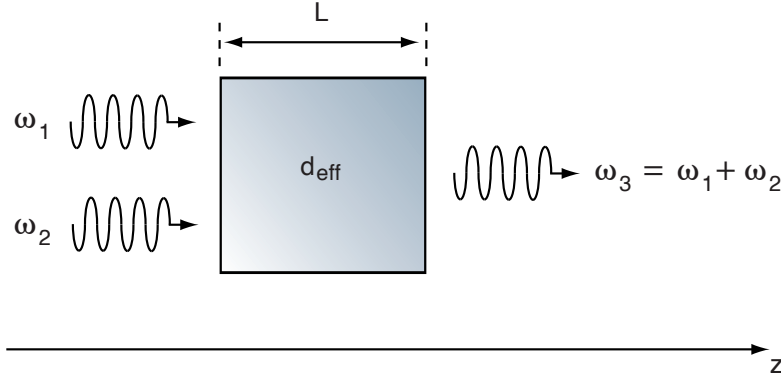


Figure 2.4.: Sum-frequency generation in a $\chi^{(2)}$ nonlinear medium of length L .

equation in which the nonlinear polarization component $\vec{P}^{(\text{NL})}$ drives the electric field. Whenever $\frac{\partial^2 \vec{P}}{\partial t^2} \neq 0$, charges are accelerated and emit energy in form of electromagnetic radiation.

To describe the process of sum-frequency generation (SFG), let us assume collimated, monochromatic, continuous-wave input beams at the frequencies $\omega_{1/2}$ to be coupled at normal incidence into a $\chi^{(2)}$ nonlinear medium as shown in Fig. 2.4. Eq. (2.85) holds separately for each frequency component. For the sum-frequency component generated at $\omega_3 = \omega_1 + \omega_2$ by the nonlinear interaction, the solution to the wave equation is

$$E_3(z, t) = A_3(z)e^{i(k_3z - \omega_3t)} + \text{c. c.}, \quad (2.86)$$

where

$$k_3 = \frac{n_3\omega_3}{c} \quad \text{and} \quad n_3 = \sqrt{\epsilon^{(1)}(\omega_3)}, \quad (2.87)$$

thus being a plane wave at frequency ω_3 propagating in the $+z$ -direction. Due to the nonlinear source term in Eq. (2.85), the field amplitude $A_3(z)$ is a slowly varying function of z . In the marginal case of a linear wave equation with $P^{(\text{NL})} \rightarrow 0$, this variation disappears and A_3 becomes a constant.

Representing the incident light fields in a manner similar to Eq. (2.86) as

$$E_j(z, t) = E_j(z)e^{-i\omega_jt} + \text{c. c.} \equiv A_j e^{i(k_jz - \omega_jt)} + \text{c. c.} \quad \text{where} \quad j = 1, 2, \quad (2.88)$$

the amplitude of the nonlinear polarization can be written as (see Eq. (2.83))

$$P_3(z, t) = P_3 e^{i\omega_3t} + \text{c. c.}, \quad (2.89)$$

where

$$P_3 = 4\epsilon_0 d_{\text{eff}} E_1 E_2 = 4\epsilon_0 d_{\text{eff}} A_1 A_2 e^{i(k_1 + k_2)z}. \quad (2.90)$$

2. From classical light to quantum optics

Substituting Eq. (2.86) and Eq. (2.90) into the wave equation and assuming the field amplitudes to vary slowly as discussed above, a set of *coupled-amplitude* equations can be derived:

$$\frac{dA_1}{dz} = \frac{2id_{\text{eff}}\omega_1^2}{k_1c^2} A_3A_2^*e^{-i\Delta kz} \quad (2.91)$$

$$\frac{dA_2}{dz} = \frac{2id_{\text{eff}}\omega_2^2}{k_2c^2} A_3A_1^*e^{-i\Delta kz} \quad (2.92)$$

$$\frac{dA_3}{dz} = \frac{2id_{\text{eff}}\omega_3^2}{k_3c^2} A_1A_2e^{i\Delta kz}. \quad (2.93)$$

Therein, $\Delta k = k_1 + k_2 - k_3$, usually referred to as the *wavevector mismatch*, describes the phase relation between the polarization and the electric field. This set of coupled differential equations fully describes the interaction of the three electric fields inside a lossless medium.

To derive a solution for Eq. (2.93), let us first consider the special case of a *weak conversion* and thus $A_1 = A_2 = \text{const.}$ This allows us to write the amplitude of the sum-frequency field as

$$A_3(L) = \frac{2id_{\text{eff}}\omega_3^2 A_1 A_2}{k_3 c^2} \int_0^L e^{i\Delta kz} dz = \frac{2id_{\text{eff}}\omega_3^2 A_1 A_2}{k_3 c^2} \left(\frac{e^{i\Delta kL} - 1}{i\Delta k} \right), \quad (2.94)$$

where L denominates the length of nonlinear interaction. From Eq. (2.94), the intensity of the wave generated at the sum-frequency can be calculated to

$$I_3 = 2n_3c|A_3|^2 = \frac{8d_{\text{eff}}^2\omega_3^2 I_1 I_2}{n_1 n_2 n_3 \epsilon_0 c^2} L^2 \text{sinc}^2 \left(\frac{\Delta k L}{2} \right), \quad (2.95)$$

where

$$\text{sinc}^2 \left(\frac{\Delta k L}{2} \right) \equiv \frac{\sin^2(\Delta k L/2)}{(\Delta k L/2)^2}. \quad (2.96)$$

Evidently, in the case of perfect phase matching ($\Delta k = 0$ for a plane wave and $\Delta k > 0$ for Gaussian beams, for a detailed discussion see [Lastzka-PhD]) the conversion is maximal. On a microscopic scale this means that the individual atomic dipoles are properly phased and that the field emitted by each of them constructively adds to the generated field propagating in $+z$ -direction. Figure 2.5 shows the conversion efficiency as a function of the phase-mismatch.

2.7.3. Phase matching - general considerations

Up to now, the depletion of the two input fields was neglected assuming a weak conversion. It can, however, be shown that in the case of significant conversion leading to a depletion of the input fields, the condition $\Delta k = 0$ has to be maintained to maximize the conversion

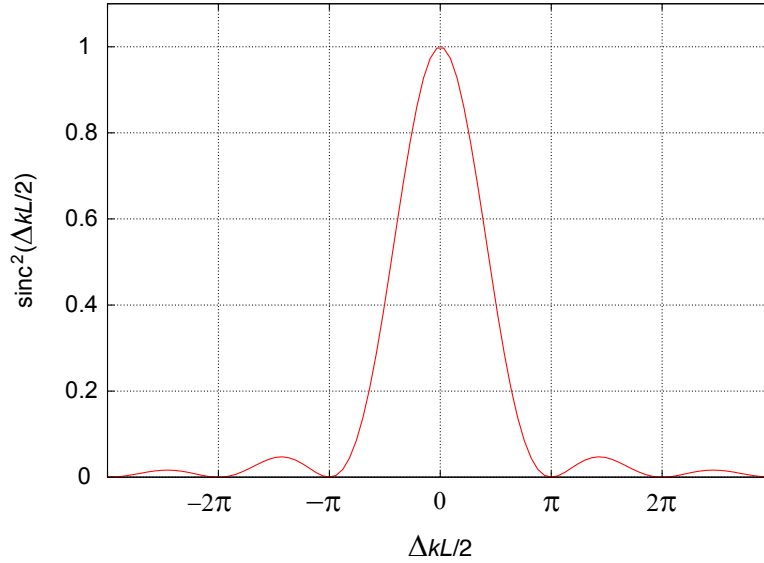


Figure 2.5.: Conversion efficiency as a function of phase mismatch in the case of weak conversion.

efficiency (here and in the following again, for simplicity, regarding plane waves). The demand

$$\Delta k = k_1 + k_2 - k_3 \stackrel{!}{=} 0 \quad (2.97)$$

can be alternatively expressed as

$$n_1(\omega_1) \cdot \omega_1 + n_2(\omega_2) \cdot \omega_2 = n_3(\omega_3) \cdot \omega_3. \quad (2.98)$$

In the particular case of second-harmonic generation with $\omega_1 = \omega_2$ and hence $n_1(\omega_1) = n_2(\omega_2)$, Eq. (2.98) can be further simplified to

$$n_1(\omega_1) = n_3(\omega_3). \quad (2.99)$$

Unfortunately, the refractive index of lossless materials is usually a monotonically increasing function of frequency, an effect known as *normal dispersion*. Evidently, no optimal phase matching can be achieved in such a medium. In principle, this problem could be circumvented making use of the decrease of the refractive index that occurs near an absorption feature. This solution, however, bears the drawback of an increased absorption loss so that in the end an efficient frequency conversion is not possible.

A more elegant phase-matching technique uses the fact that the refractive indices of many crystals changes with the direction of polarization of the applied electric fields. This effect is known as *birefringence* and depends on the crystal structure, so that not all crystals display birefringence. For this thesis, especially uniaxial crystals like LiNbO_3

or KTP are important. In general, this classification includes crystals with a trigonal, a tetragonal and a hexagonal lattice system. Uniaxial crystals can be characterized by the so-called *crystal-* or *c-axis*. A wave with wavevector \vec{k} propagating through the crystal is called *ordinary* if it is polarized orthogonally to the plane that is spanned by \vec{k} and \vec{c} . Light polarized in the plane containing the wave vector and the crystal axis is in contrast called *extraordinary*. Both waves experience the ordinary and extraordinary refractive indices n_o and n_e , respectively. The extraordinary refractive index is a function of the angle θ between \vec{k} and the crystal axis. The limit $\theta \rightarrow 0$ equalizes the two indices of refraction.

2.7.4. Phase matched second-harmonic generation in a LiNbO₃ crystal

Typically phase matching can be accomplished using either the temperature dependence of the refractive index or tuning the angle between the crystal axis and the propagation direction of the laser beam. A disadvantage of the angle-tuning method is that in the case $\theta \notin \{0, \pi/2\}$, the Poynting vector and the propagation vector \vec{k} are not parallel for extraordinary rays. The ordinary and the extraordinary beams therefore quickly diverge from one another, thus limiting the achievable conversion efficiency. For this reason, in the following the temperature-tuning method is discussed.

Figure 2.6 shows the ordinary and extraordinary indices of refraction of pure LiNbO₃, described by the relations [Hobden+66]

$$\begin{aligned} n_o^2 &= 4.9130 + \frac{1.173 \cdot 10^5 + 1.65 \cdot 10^{-2} T^2}{\lambda^2 - (2.12 \cdot 10^2 + 2.7 \cdot 10^{-5} T^2)^2} - 2.78 \cdot 10^{-8} \lambda^2, \\ n_e^2 &= 4.5567 + \frac{0.970 \cdot 10^5 + 2.70 \cdot 10^{-2} T^2}{\lambda^2 - (2.01 \cdot 10^2 + 5.4 \cdot 10^{-5} T^2)^2} - 2.24 \cdot 10^{-8} \lambda^2 \\ &\quad + 2.605 \cdot 10^{-7} T^2, \end{aligned} \quad (2.100)$$

with T being the crystal temperature in degrees K and λ being the wavelength in nm. Such crystals are per convention called *negative uniaxial* because $n_o(\omega)$ is always larger than $n_e(\omega)$. In the case of second-harmonic generation (SHG), $\omega_1 = \omega_2 = \omega_3/2$. To achieve phase-matching, the second-harmonic field thus needs to have extraordinary polarization, while the harmonic field is ordinarily polarized. The concrete example given in Fig. 2.6 treats the up-conversion of 1064 nm light (which is the standard wavelength in current GW interferometers) to 532 nm. This type of phase-matching in which the two input fields (in the case of the SHG given by a single field interacting with itself) have the same polarization and are orthogonally polarized to the field generated at frequency ω_3 is called *Type I*.

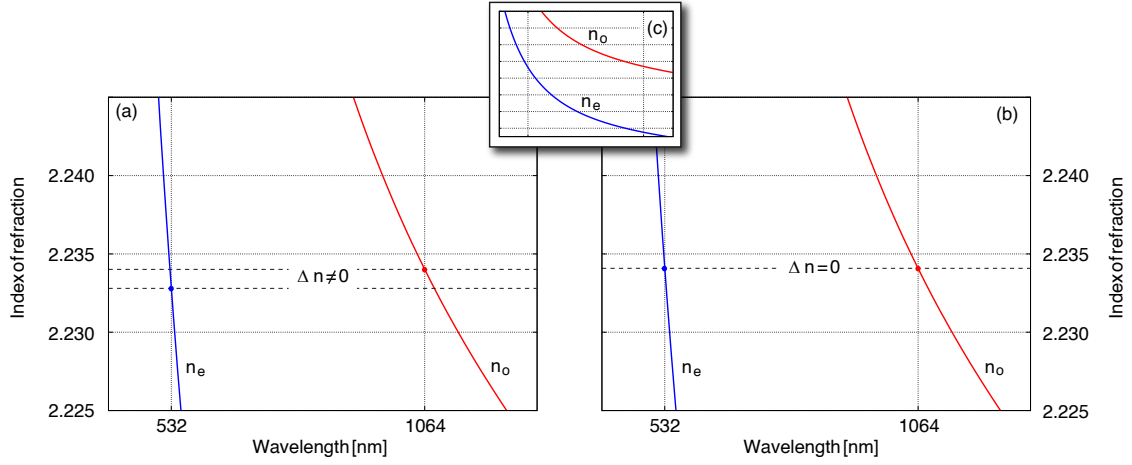


Figure 2.6.: Ordinary and extraordinary indices of refraction of LiNbO₃ as a function of wavelength. (a) at room temperature with $n_o(1064 \text{ nm}) \neq n_e(532 \text{ nm})$ and thus with $\Delta n \neq 0$. (b) at $T = 316 \text{ K}$, the indices of refraction are equalized leading to an optimal phase-matching for the SHG process. (c) Zoom-out showing the characteristic dependence of the two indices of refraction on the wavelength.

From Eq. (2.100) and its visualization in Fig. 2.6 it is evident that the two indices of refraction depend on the temperature. The condition for an optimal frequency conversion, $n_e(532 \text{ nm}) = n_o(1064 \text{ nm})$, can thus be reached by tuning the crystal temperature.

2.7.5. Quasi phase matching

In the case of perfect phase matching, the power is constantly converted from the input field to the generated second-harmonic field. If a phase mismatch is present, after a certain interaction length the output wave will get out of phase with its driving polarization and power will flow back to the fundamental ω_1 field. The coherent build-up length of the interaction is defined as

$$L_{\text{coh}} = \frac{2}{\Delta k} \quad (2.101)$$

and evidently approaches ∞ for $\Delta k \rightarrow 0$. This power oscillation can be used to achieve phase matching in *periodically poled crystals*, being crystals with a periodically inverted optical axis as a function of position along the direction of propagation. An inverted orientation of the c -axis also inverts the sign of the effective nonlinear coefficient d_{eff} and thus can compensate for $\Delta k \neq 0$. For a quasi-phase-matched structure, an optimal period length

$$\Lambda = 2L_{\text{coh}} = \frac{2\pi}{k_1 + k_2 - k_3} \quad (2.102)$$

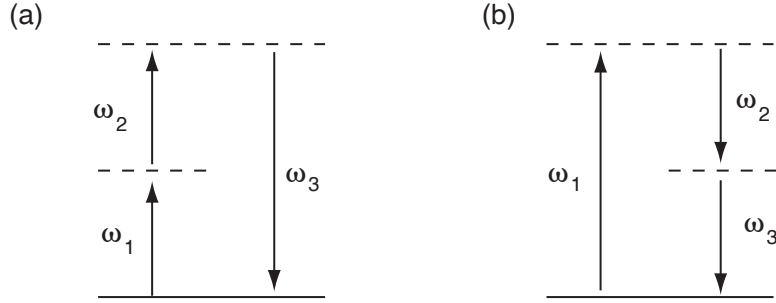


Figure 2.7.: Energy-level diagram of (a) sum-frequency generation and (b) difference-frequency generation.

can be derived. To provide a concrete example, L_{coh} can be shown to be about $3.4 \mu\text{m}$ for the second-harmonic generation in LiNbO_3 using 1064 nm light. The fabrication of periodically poled crystals employs a static electric field to periodically invert the orientation of the ferroelectric domains of a ‘common’ crystal [Yamada+93]. A big experimental advantage of periodically poled media is that they make it possible to reach higher effective nonlinearities and furthermore do not pose as strict constraints on the required temperature stabilization as does the phase-matching procedure based on temperature-tuning.

2.7.6. Parametric amplification

Up to now we have considered only the sum-frequency generation and the particular case of the SHG. Another possible nonlinear effect is the *difference-frequency generation* (DFG) described by

$$P^{(2)}(\omega_3 = \omega_1 - \omega_2) = 2\epsilon_0\chi^{(2)}E_1E_2^*. \quad (2.103)$$

While this process at the first glance appears to be very similar to the sum-frequency generation, an important difference can be deduced from the description of the two processes in a photon energy-level diagram as illustrated in Fig. 2.7. In the case of DFG, for every photon created at the frequency ω_3 , a photon with frequency ω_1 must be annihilated and an additional photon with ω_2 must be created due to energy conservation. This effect can be employed for optical amplification: If a strong (*pump*) field at the frequency ω_1 and a weak (*signal*) field at ω_2 are injected into the nonlinear medium, the signal field is amplified by the nonlinear interaction. For this reason, the process of difference-frequency generation is also referred to as *optical parametric amplification* (OPA). Here ‘parametric’ means that in this process the initial and the final quantum mechanical states of the system are identical. Considering the OPA process on the atomic level, an atom absorbs a photon with energy $\hbar\omega_1$ and jumps to a virtual level. This is followed by a decay that happens as a stimulated two-photon process. If no field at the

frequency ω_2 is present, spontaneous processes will also lead to the generation of photons at the difference frequency. This effect, known as parametric fluorescence, is however much weaker than in the case of stimulated emission.

If the nonlinear crystal is placed inside an optical resonator, the length of interaction is considerably increased so that high amplification factors can be reached. In the case that the nonlinear amplification denoted by g exceeds the total optical loss κ ($g > \kappa$), oscillation can occur so that even without a bright input field at frequency ω_2 , two fields at the frequencies ω_2 and ω_3 are created from a pump field at ω_1 . Such a device is known as an *optical parametric oscillator* (OPO) and constitutes a useful source of frequency-tunable laser radiation. The special case of $g = \kappa$ is referred to as *OPO threshold*. Below-threshold oscillators are denominated as *optical parametric amplifiers* (OPAs) and can be used to amplify or to deamplify an input field, depending on the phase relation between the pump and the signal fields. This process also leads to a coupling of the quantum noise present in the two field quadratures and thus makes it possible to generate squeezed states of light. In the following section, a quantum mechanical description of the squeezing process is provided.

2.8. Generation of squeezed light

Most schemes for squeezed light generation are based on a parametric process inside some kind of nonlinear medium. A detailed review over a variety of schemes is provided in [Bachor+04]. Reference [Franzen-PhD] presents a selection of 74 milestone-experiments in the field of squeezed states preparation. For the work discussed in this thesis, the parametric down-conversion process discussed above was chosen for squeezed light generation. The nonlinear crystal was pumped with a field at the frequency ω_p . Thus, pairs of photons at the frequency $\omega = \omega_p/2$ were created. The Hamiltonian for this process can be expressed as [Gerry+06]

$$\hat{H} = \hbar\omega\hat{a}^\dagger\hat{a} + \hbar\omega_p\hat{b}^\dagger\hat{b} + i\hbar\chi^{(2)} \left(\hat{a}\hat{a}\hat{b}^\dagger - \hat{a}^\dagger\hat{a}^\dagger\hat{b} \right), \quad (2.104)$$

where \hat{a} is the mode of the signal field and \hat{b} refers to the pump field. Let us assume the interaction to be weak enough for the pump field not to be depleted of photons, like for the derivation of the sum frequency amplitudes given above in Section 2.7.2. Furthermore, the pump field is assumed to be in a coherent state $|\beta\rangle$. The operators \hat{b} and \hat{b}^\dagger can be approximated by

$$\hat{b} \rightarrow \beta e^{-i\omega_p t} \quad \text{and} \quad \hat{b}^\dagger \rightarrow \beta^* e^{i\omega_p t}. \quad (2.105)$$

This leads to the parametric approximation to Eq. (2.104)

$$\hat{H} = \hbar\omega\hat{a}^\dagger\hat{a} + i\hbar\chi^{(2)} \left(\beta^*\hat{a}\hat{a}e^{i\omega_p t} - \beta\hat{a}^\dagger\hat{a}^\dagger e^{-i\omega_p t} \right). \quad (2.106)$$

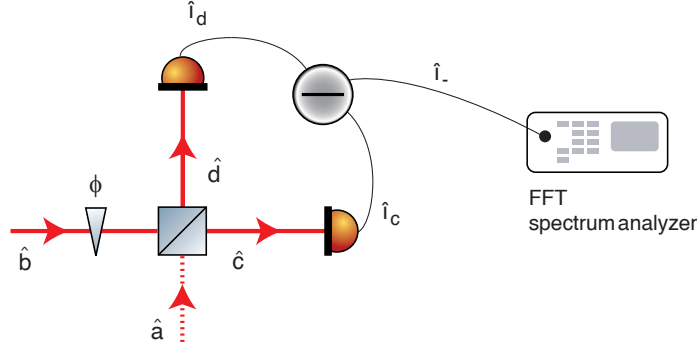


Figure 2.8.: Schematic of a balanced homodyne detector. The signal field \hat{a} interferes with a strong local oscillator field \hat{b} at a balanced beam splitter. The difference of the photo currents generated with the photo detectors in the two beam splitter ports is processed by a Fast Fourier Transform spectrum analyzer.

For the interaction of the two field modes, this yields the time-dependent Hamiltonian

$$\hat{H}(t) = i\hbar\chi^{(2)} \left(\beta^* \hat{a} \hat{a} e^{i(\omega_p - 2\omega)t} - \beta \hat{a}^\dagger \hat{a}^\dagger e^{-i(\omega_p - 2\omega)t} \right). \quad (2.107)$$

Considering the fact that the pump frequency was chosen to be twice the signal frequency, Eq. (2.107) finally simplifies to

$$\hat{H}(t) = i\hbar\chi^{(2)} \left(\beta^* \hat{a} \hat{a} - \beta \hat{a}^\dagger \hat{a}^\dagger \right). \quad (2.108)$$

The evolution operator associated with the described parametric process is

$$\hat{U}(t, 0) = \exp(-i\hat{H}t/\hbar) = \exp(\chi^{(2)} \beta^* t \hat{a} \hat{a} - \chi^{(2)} \beta t \hat{a}^\dagger \hat{a}^\dagger). \quad (2.109)$$

Evidently, it has the same form as the squeeze operator introduced in Eq. (2.69). Thus, squeezed states of the light field discussed in Section 2.6 can be generated by parametric down-conversion inside a $\chi^{(2)}$ nonlinear medium.

2.9. Detection of squeezed light

Beyond any doubt, a key instrument in optical experiments is the photo detector. It converts photons to freely moving electrons and thus produces a photo current proportional to the incident light power. To properly measure squeezed states, it is, however, necessary to obtain information about the quantum noise distribution in the different field quadratures. An appropriate method to measure quadrature squeezing is given by *balanced homodyne detection*, first proposed for squeezed states in 1983 by Yuen and Chan [Yuen+83a]. The basic setup is illustrated in Fig. 2.8. The squeezed field interferes

with a reference laser beam having the same frequency at a 50/50 beam splitter (BS) and the two BS outputs are thereupon measured with photo detectors. For simplicity, the BS splitting ratio is assumed to be perfectly balanced and optical loss is neglected. We can represent the two input beams as

$$\hat{a} = \alpha + \delta\hat{a} \quad \text{and} \quad \hat{b} = e^{i\phi} (\beta + \delta\hat{b}). \quad (2.110)$$

This approach is known as *linearization* and is valid as long as the fluctuations can be assumed to be small [Bachor+04]. In Eq. (2.110), ϕ refers to the relative phase difference between the signal (\hat{a} , squeezed) and the local oscillator field (\hat{b}). In the experiment, the phase difference can be controlled by a phase shifter device (for example by a steering mirror mounted on a piezo-electric element). The BS output fields are

$$\hat{c} = \frac{1}{\sqrt{2}} (\hat{a} + \hat{b}) \quad \text{and} \quad \hat{d} = \frac{1}{\sqrt{2}} (\hat{a} - \hat{b}). \quad (2.111)$$

From these, the photo currents – that are proportional to the photon numbers – can be calculated via

$$\hat{i}_c \propto \hat{c}^\dagger \hat{c} \quad \text{and} \quad \hat{i}_d \propto \hat{d}^\dagger \hat{d}. \quad (2.112)$$

Thus, the photo current measured at port c can be expressed as

$$\begin{aligned} \hat{i}_c &\propto \hat{c}^\dagger \hat{c} \\ &= \frac{1}{2} \left[\alpha^2 + \beta^2 + 2\alpha\beta \cos(\phi) + 2\alpha \left(\delta\hat{X}_a^+ + \cos(\phi)\delta\hat{X}_b^+ - \sin(\phi)\delta\hat{X}_b^- \right) \right. \\ &\quad \left. + 2\beta \left(\delta\hat{X}_b^+ + \cos(\phi)\delta\hat{X}_a^+ + \sin(\phi)\delta\hat{X}_a^- \right) \right] + \mathcal{O}(\delta^2). \end{aligned} \quad (2.113)$$

Here, all higher-order fluctuation terms have been neglected in accordance with the linearization. Similarly, the other photo current can be calculated to

$$\begin{aligned} \hat{i}_d &\propto \hat{d}^\dagger \hat{d} \\ &= \frac{1}{2} \left[\alpha^2 + \beta^2 - 2\alpha\beta \cos(\phi) - 2\alpha \left(\cos(\phi)\delta\hat{X}_b^+ - \sin(\phi)\delta\hat{X}_b^- - \delta\hat{X}_a^+ \right) \right. \\ &\quad \left. - 2\beta \left(\cos(\phi)\delta\hat{X}_a^+ + \sin(\phi)\delta\hat{X}_a^- - \delta\hat{X}_b^+ \right) \right] + \mathcal{O}(\delta^2). \end{aligned} \quad (2.114)$$

A very interesting result follows when we now analyze the difference of the two photo currents and require the local oscillator to dominate the output and thus to be much more intense than the signal beam:

$$|\beta|^2 \gg |\alpha|^2. \quad (2.115)$$

This allows us to drop all terms proportional to α in first-order approximation and to express the difference photo current as

$$\hat{i}_- \propto \hat{i}_c - \hat{i}_d \propto \beta \left(\cos(\phi)\delta\hat{X}_a^+ + \sin(\phi)\delta\hat{X}_a^- \right) \propto \beta\delta\hat{X}_a^\phi. \quad (2.116)$$

The fluctuations of the signal beam in the quadrature X^ϕ are amplified by the coherent amplitude β of the local oscillator, while the LO noise is completely suppressed. Thus, the noise of the LO beam can be much higher than the minimal uncertainty of an ideal technical-noise-free beam without affecting the measurement result. In reality, an upper limit for the tolerable LO noise is set by the balancing of the homodyne detector. An arbitrary quadrature can be accessed by the homodyne detector measurement using the phase-shifter device.

In the experiments discussed in this thesis, the variance [Bachor+04]

$$V(\hat{i}_-) \propto \beta^2 V(\hat{X}_{\text{sqz}}^\phi) \quad (2.117)$$

of the difference photo current was measured and the noise distribution analyzed in the frequency-domain using a Fast-Fourier-Transform (FFT) spectrum analyzer. Please note that the measured variance scales quadratically with the LO amplitude and thus linearly with the intensity of the LO beam.

In experimental publications, the measured degree of squeezing is usually provided in Decibel (dB). A simple but useful relationship that allows the reader to convert dB values into squeeze factors and vice versa is given by

$$r = \frac{\ln\left(10^{\frac{V[\text{dB}]}{10}}\right)}{2} \quad \text{and} \quad V[\text{dB}] = -10 \log_{10}\left(e^{-2r}\right), \quad (2.118)$$

where ‘V [dB]’ is the reduction in noise power with respect to a vacuum state measured by the spectrum analyzer.

2.10. Influence of optical loss

In a ‘classical’ experiment, any optical loss can be compensated for by increasing the intensity of the light source. This is no longer the case for experiments involving squeezed light. Any optical loss will reduce the degree of squeezing. A simple model to describe this problem can be derived using a beam splitter as follows: An optical loss ϵ (e. g. arising from absorption, scattering or a detection efficiency smaller than unity) is equivalent to a beam splitter with power reflectivity $R \equiv \epsilon$ and power transmission $T \equiv \eta = (1 - \epsilon)$. Through the second BS port, vacuum fluctuations couple into the squeezed field. This results in an increased noise in the squeezed quadrature, while the noise in the anti-squeezed quadrature is hardly affected. Mathematically, the problem can be described using the BS transfer matrix [Bachor+04]. It can be shown that the optical loss acts on the fluctuations of an input field as

$$\delta\hat{X}_{\text{out}}^\phi = \sqrt{\eta}\delta\hat{X}_{\text{in}}^\phi + \sqrt{1-\eta}\delta\hat{X}_{\text{vac}}. \quad (2.119)$$

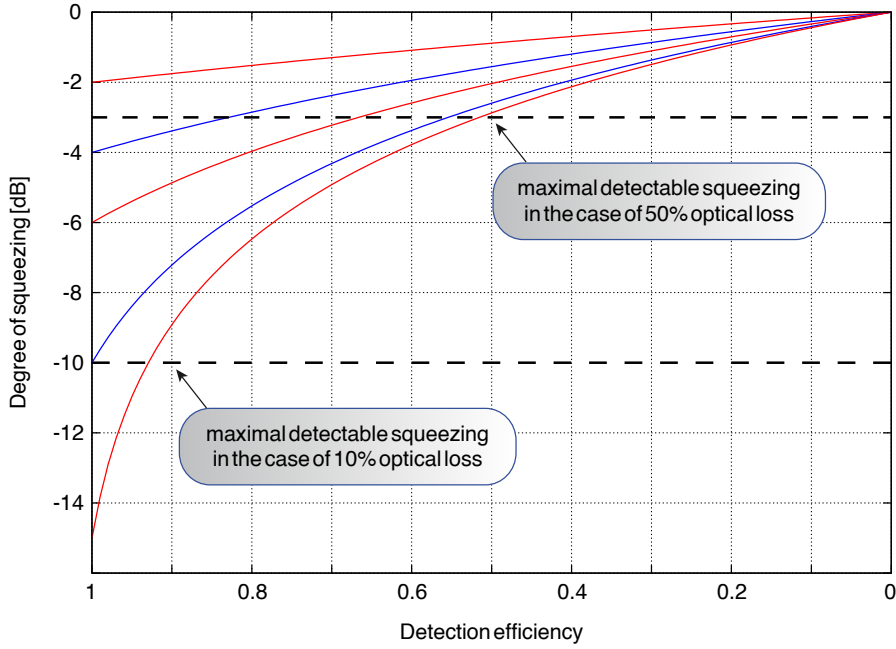


Figure 2.9.: Influence of a decreasing detection efficiency on the detected degree of squeezing, illustrated at the example of various initial squeezing values (2 dB–16 dB). The higher the initial squeezing value, the stronger the degradation. Two theoretical limits worth mentioning are a maximal detected squeezing value of 10 dB in the case of a total optical loss of 10 % and a maximal level of 3 dB for 50 % loss.

This calculation can be performed independently for each angle ϕ . Since the vacuum fluctuations do not show an angle dependence, the squeezing angle remains unchanged but the degree of squeezing is reduced. Using Eq. (2.118), the relation

$$V' [\text{dB}] = -10 \log_{10} \left(\eta 10^{\frac{V [\text{dB}]}{10}} + (1 - \eta) \right) \quad (2.120)$$

can be derived. Here, V [dB] is the variance of the squeezed state (measured in dB) prior to an optical loss, while the post-loss variance is given by V' [dB]. The effect of optical loss is visualized in Fig. 2.9. The higher the initial degree of squeezing, the stronger the degradation at a fixed loss value. From Eq. (2.120), it immediately follows that even in the case of infinite initial squeezing a loss of 10 % restricts the squeezing degree to 10 dB and a loss of 50 % reduces the maximal squeezing value down to 3 dB. In the marginal case of a vacuum input state, the quantum noise is obviously not affected at all.

A particular loss source in the balanced homodyne detection scheme worth mentioning is a non-perfect contrast of the two fields. The contrast can be evaluated measuring the *fringe visibility*

$$\mathcal{V} = \frac{I_{\max} - I_{\min}}{I_{\max} + I_{\min}} \quad (2.121)$$

2. From classical light to quantum optics

at one of the homodyne detector photo diodes (for an experimental discussion of the visibility measurement, see Section 3.7). Here, $I_{\min/\max}$ refer to the minimal and maximal photo current values, respectively, that can be obtained. In the case of perfect interference the fringe visibility approaches unity. The visibility contributes quadratically to the detection efficiency which thus can be expressed as

$$\eta_{\text{tot}} = \eta_{\text{prop}} \cdot \eta_{\text{PD}} \cdot \eta_{\text{VIS}}. \quad (2.122)$$

Here, η_{prop} addresses the total optical propagation loss, η_{PD} accounts for imperfect photo detectors and $\eta_{\text{VIS}} = \mathcal{V}^2$ finally addresses the homodyne mode-mismatch.

A squeezed-light laser for GEO 600

Though the idea to improve interferometric GW detectors by squeezed light is considerably old [Caves81], more than twenty years of research and development were necessary before a concrete implementation could finally be undertaken. Since the first observation in 1985 [Slusher+85], the degree of squeezing has been constantly improved, recently reaching a value of almost 13 dB [Eberle+10]. In the GW detection band, the generation of squeezing remained an unsolved problem for a long time. It was not until 2004 that squeezing at audio frequencies down to 280 Hz could be generated for the first time [McKenzie+04], soon followed by the creation of a coherent control scheme [Vahlbruch+06, Chelkowski+07] that allowed the observation of frequency-independent squeezing over the entire Earth-bound gravitational wave detection band from 10 Hz to 10 kHz [Vahlbruch+07]. The same experiment also demonstrated that the sensitivity of a table-top Michelson-type interferometer could be improved by squeezed light injection at kHz-frequencies. Finally, in 2008 a conceptual design considering the concrete application at the GEO 600 detector site was proposed [Vahlbruch-PhD]. In this chapter, the experimental setup of the GEO 600 squeezed-light laser is presented.

3.1. Lessons learned from the past

The goal of the GEO 600 squeezed-light laser project was to combine the lessons learned from previous setups and to construct a stable and compact experiment that would provide high squeezing values in the GW detection band in a permanent operation mode in which it is to be used in GEO 600. The two most important insights concerning audio frequency squeezing are that it is highly sensitive to

1. control beam noise at the fundamental squeezing frequency [Bowen+02] as well as
2. to any scattered light [Vahlbruch+07].

3. A squeezed-light laser for GEO 600

The coherent control scheme described below is based on the fact that no light at exactly the same frequency as the generated squeezed field enters the squeezed-light source. Therefore, no technical noise (predominant at audio frequencies) is introduced into the system. Unfortunately, such noise is carried not only by a control beam but also by scattered photons. If such photons, scattered for instance from the main beam of the squeezed-light laser and being in exactly the same mode as the squeezed field, enter the squeezed-light source and interfere with the squeezed field, this will mask squeezing at audio Fourier frequencies in a very efficient way. Even marginal amounts of scattered light are sufficient to degrade the performance of the squeezed-light source [McKenzie+04].

An issue even more important is that usually multiple scattering processes at components constantly moving due to acoustic and thermal excitations and having very different frequency-response characteristics, are experienced by the scattered photons. As discussed in [Vahlbruch-PhD, Vahlbruch+07], each movement creates optical sideband fields at the corresponding frequencies and harmonics, which are later on read out by the homodyne detector and thus impede a quantum shot-noise limited measurement. Scattered light has therefore been shown to result in a continuous noise level monotonically increasing with decreasing frequency and making itself noticeable already at kHz-frequencies. To achieve a flat (white) squeezing level over the entire GW detection band of 10 Hz – 10 kHz, it is therefore necessary to

1. suppress stray light generation as effectively as possible,
2. to avoid re-scattering by identifying and blocking all residual light beams arising from imperfect AR or HR-coatings and
3. to minimize the acoustically and thermally excited motion of all mechanical parts.

It is worth stressing that in principle one of the three approaches is sufficient, since it is of no relevance whether no stray light is created, whether it is created and subsequently dumped and so on. In practice, however, a combination of all measures is required.

Regarding the generation of stray light and its avoidance, the following mechanisms were addressed:

- contamination of the optical surfaces (e.g. by dust)
- imperfection of the surface itself (namely the surface micro-roughness as well as damages)
- reflections from imperfect anti-reflection (AR) coatings as well as residual transmission of highly reflective mirrors

To deal with the first mechanism, it appeared convenient to construct the squeezed-light laser in a class 100 cleanroom facility at the AEI in Hanover. The class is defined according to the US FED STD 209E Cleanroom Standards and denotes the number of particles of 0.5 μm size or larger permitted per cubic foot of air. For the class 100 lab, this practically resulted in maximally several tens of particles even when several persons

worked inside simultaneously; the particle concentration dropped to zero as soon as the lab was abandoned.

The second issue addressed was the surface quality of the optics used. The highly reflective (HR) steering mirrors were produced by the manufacturer ATFilms [ATF] and had a super-polished reflective surface (resulting in an rms surface roughness of approximately 0.5 \AA) with a scratch/dig ratio of 10/5. The power reflectivity was specified to be $R_{s,p} \geq 99.995\%$, measurements have shown that even higher values of $R_{s,p} \geq 99.9987\%$ were achieved, thereby further reducing the amount of stray light. To balance the stress applied to the optics by the dielectric coating as well as to minimize stray light propagating close to the original beam, the other side of the mirrors was AR-coated ($R_{s,p} < 0.2\%$).

The lenses and dichroic beam splitters used (both also from ATFilms), as well as all resonator optics, were specified to have a comparably low surface roughness. The only optics with ‘conventional’ surfaces were the Faraday rotators, beam splitters, polarizing beam splitters and waveplates (along with some 532 nm optics, which are, however not as critical for the stray light considerations). To clean the surfaces, the polymer solution [First Contact] was employed.

Setting the working environment to the AEI imposed the constraint of portability on the squeezed-light laser. Therefore, the experiment is set up on an optical breadboard. The board dimensions of $1.35 \text{ m} \times 1.13 \text{ m}$ were determined by the maximal amount of space available on the GEO 600 detection bench, an optical table inside the main GEO 600 building where the designated squeezed-light laser position is. To maintain the requirement of transportability by manpower resulting from the limited clearance inside the building and thus to keep the weight low, the GEO squeezer board produced by [TMC] is made of aluminium. It uses a honeycomb core structure with a cell profile of 3.2 cm^2 as well as a black anodized aluminium top plate (to absorb potential stray light). The bottom plate consists of stainless steel, the board is specified to be used in a cleanroom environment and has a weight of only about 70 kg. The long-term performance of the experiment proved the breadboard to have the required high mechanical stability. To protect the experiment from residual dust particles as well as from laminar air flow, the breadboard is covered by a case made of opaque acrylic glass. Another advantage is that thereby the experiment is additionally shielded against external stray light sources. Figure 3.1 shows a photograph of case and breadboard.

3.2. Preparation of the laser beams

The experiment is driven by a monolithic non-planar Nd:YAG ring laser (NPRO) with 2 W single-mode output power at 1064 nm, produced by the company InnoLight [InnoLight], in the following referred to as *Mephisto* or as *main laser*. The monolithic implementation of the laser cavity leads to a high mechanical stability and

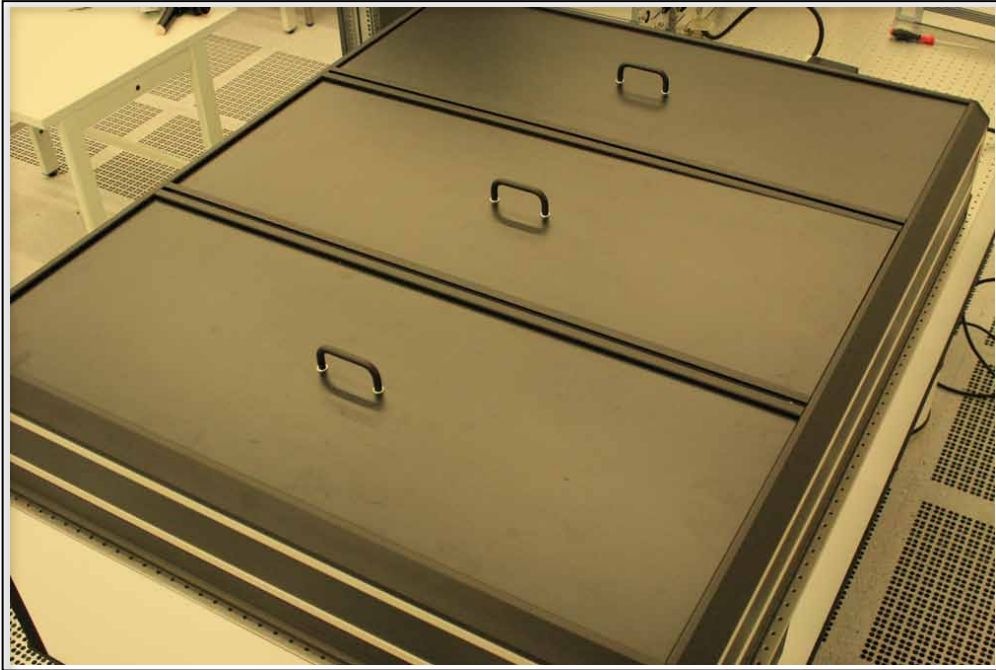


Figure 3.1.: Photograph of the optical breadboard covered by a protective case made of opaque acrylic glass. Thereby, the experiment inside is shielded against residual dust particles, external stray light as well as against laminar air flow disturbing the measurements at low frequencies.

consequently to a high stability of the optical frequency. The pump radiation for the lasing process is provided by two pump diode arrays at 808 nm. Fluctuations in pump power (as well as any other non-equilibrium state) lead to relaxation oscillations which can be observed as an increased intensity noise around the oscillation frequencies. To reduce this noise, a fraction of the generated laser light is detected with a PIN photo diode inside the laser head and an error signal for pump power stabilization is generated. This feedback loop, the so-called *noise eater*, allows, especially at the relaxation oscillation frequencies, a suppression of the intensity noise by typically 30–40 dB.

The laser crystal temperature is internally stabilized to improve the long-term stability (with a specified frequency drift of less than 1 MHz per minute). The set point of the stabilization loop can, however, be changed to allow for a fast frequency tuning of the laser field. The tuning range extends over 30 GHz with a thermal tuning coefficient of -3 GHz/K and a response bandwidth of 1 Hz. Additionally, a piezoelectric transducer (PZT) is attached to the laser crystal. A change in the voltage results in a change of the mechanical stress applied to the laser cavity and thus changes the laser frequency. This tuning possibility has a much higher bandwidth (of 100 kHz) and makes it possible to

cover a tuning range of approximately 100 MHz with a tuning coefficient of ca. 1 MHz/V. Both tuning ports are essential for locking the frequency of the main laser to the GEO 600 master laser (see Section 5.2). The same ports are available for the auxiliary units to be locked to the main squeezing laser, as described below.

An implementation of the coherent control scheme (explicitly discussed in [Vahlbruch+06, Vahlbruch-PhD, Vahlbruch+07, Chelkowski-PhD]) requires two additional auxiliary optical frequencies. The basic idea is to remove all noisy fields that could by means of interference introduce noise to the squeezed field at audio frequencies. To control the length of the squeezer cavity, a beam polarized orthogonally to the squeezed field is used. Just as the index of refraction of a birefringent crystal depends on the polarization, so does the optical length of the squeezing resonator. To adjust a simultaneous resonance for the two polarizations, the control field has to be frequency-shifted. Furthermore, the squeezing angle control is done with another independent beam of different frequency as discussed below in Section 3.6.3. The two control fields are provided by NPRO lasers of approximately 190 mW output power at 1064 nm each (Mephisto OEM series), in the following denominated as *AUX1* and *AUX2*. They have specifications similar to the Mephisto unit and possess the same frequency tuning possibilities.

As mentioned earlier, one main constraint of the setup was a long-term mechanical stability, since after the implementation in GEO 600 every beam misalignment will lead to a degradation of the squeezing value and thus will affect the detector sensitivity. To reduce a misalignment of the laser beams over long time scales, mostly rigid optics mounts as well as monolithic flexure mounts for steering mirrors were employed.

Figure 3.2 shows the setup of the preparatory stage that contains the phase-locked loops (PLLs) of the three lasers as well as the generation of the second-harmonic pump field. Since light back-reflected from optical surfaces or resonators might cause the noise eater electronics to oscillate or even damage the pump diodes [Heurs-PhD], a Faraday isolator (LINOS FI-1060-5SI with an isolation of approx. 40 dB) is used to suppress back-reflected light. The power behind the FI was measured to be about 2 W (using an OPHIR 3A thermal power sensor and an OPHIR Nova II power meter with a total accuracy of 3%). Finally, collimator lenses placed close to the laser aperture allow fairly collimated beams with similar beam parameters to optimize the optical beat at the PLL photo detectors.

The PLLs are a commercial solution offered by the manufacturer InnoLight GmbH. They are used to lock the frequency of the auxiliary lasers (slave) to the one of the main (master) laser with a pre-defined frequency offset. The PLLs consist of two parts: a photo detector (PLL PDs, containing an InGaAs photo diode) and the control electronics. All controllers include two actuator outputs: A slow ramp signal is used to scan the slave laser's crystal temperature, while a fast ramp signal is connected to the laser crystal PZT. The electronics provide an auto-lock mode: in the case of lock-loss, the lock is restored without external software control.

3. A squeezed-light laser for GEO 600

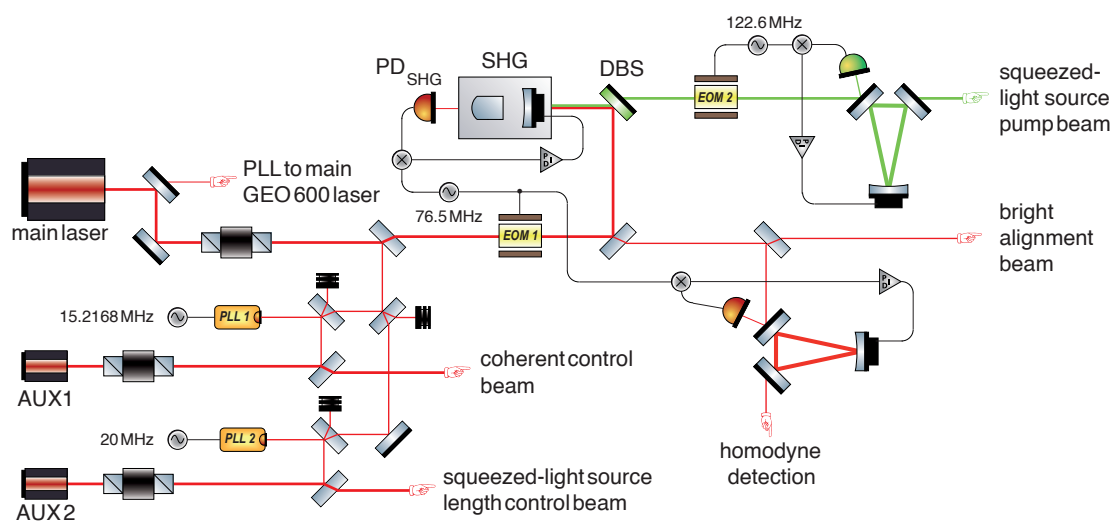


Figure 3.2.: Schematic of the preparatory setup stage, including the phase-locked loops (PLLs) of the auxiliary lasers to the main laser and the frequency-up-conversion of the main laser beam in the second-harmonic generator (SHG). For clarity reasons, mode-matching lenses and steering mirrors are omitted. Details are provided in the text.

To stabilize the length of the squeezing resonator, the AUX2-beam was used. The frequency offset between the two polarization modes required for simultaneous resonance was 20 MHz (for details see Section 3.5). This external frequency reference was provided by an AD9959 direct digital synthesizer (DDS) [AD-DDS]. It consists of 4 cores that allow independent frequency, phase and amplitude control on each channel. All channels share a common system clock and are therefore inherently synchronized. The DDS is supplied with an external reference clock frequency chosen to be 500 MHz. If required, a synchronization of several devices is possible.

The control beam to stabilize the angle of the squeezing ellipse is provided by the AUX1-laser. The frequency offset has been chosen to a value of 15.2168 MHz owing to favorable conditions at the GEO 600 detector site (namely for the control field to be anti-resonant inside the GEO 600 signal-recycling cavity, for details see Section 5.2). Since the coherent control scheme requires a demodulation at twice the offset frequency, an ultra low noise OCXO (Oven Controlled Crystal Oscillator) manufactured by Wenzel Associates [Wenzel] with a phase noise between 132 dBc/Hz and 175 dBc/Hz at 10 Hz and 10 kHz, respectively, and an output frequency $\nu_{\text{Wenzel}} = 30.4336$ MHz is used. The device is complemented by an ultra low noise power splitter and an ultra low noise regenerative divider (division by a factor of two) to provide all the signals necessary for the coherent control scheme.

The optical powers required at the PLL photo detectors were merely several μW . A small fraction of the main laser beam (approx. 18 mW) was tapped off behind the FI and distributed to the coherent control PLLs, while the remaining power was used for second-harmonic generation (Section 3.3), a local oscillator for the on-board homodyne detector (Section 3.7) as well as for a bright alignment beam mode-matched into the squeezer cavity (Section 3.6). Additionally, 3.1 mW were tapped off directly behind the laser and used for an external PLL to the GEO 600 laser as described in Section 5.2. Similarly, a small fraction of the auxiliary laser beams was used for interference at the PLL detectors while the rest was either used for the coherent control applications or dumped.

3.3. Second-harmonic generation

The squeezed-light source for GEO 600 is based, like all squeezers constructed at the AEI, on the principle of optical parametric down-conversion in a nonlinear $\chi^{(2)}$ crystal. As described in Section 2.7, this process requires a strong pump field at twice the frequency of the squeezed field. This pump beam is generated via the physically very similar process of second-harmonic generation (SHG). The SHG is a self-interaction process and therefore requires high optical power densities. To achieve such in an experiment using continuous-wave laser radiation and moderate laser powers, the nonlinear medium is placed in a Fabry-Perot resonator. In the following, the mechanical and optical design of the resonator as well as the electronic control are discussed.

3.3.1. Design of the SHG resonator

Two main degrees of freedom must be controlled to achieve an optimal frequency up-conversion, namely the length of the resonator as well as the crystal temperature. Fig. 3.3 provides a brief overview over several possible and commonly used resonator designs. A ‘hemilithic’ design, as in Fig. 3.3 (b), which offers the advantage of a movable coupling mirror and thereby of an adjustable resonator length, is preferable for second-harmonic generation. A CAD drawing of the mechanical housing (design by Christian Gräf [Gräf-Diploma]) is shown in Figure 3.4. For thermal isolation as well as to protect the cavity from air flow perturbation, the crystal is situated in a housing which is in the following referred to as the *oven*. The temperature actuation is realized via a Peltier element [Telemeter]. For temperature sensing, a negative temperature coefficient (NTC) thermistor [Hygrosens] was placed inside the L-shaped copper plate that separates crystal and Peltier. The crystal is wrapped in indium foil to ensure good temperature coupling. On the top side, the stack is completed by another L-shaped element made of Macor ceramics which is supposed to ensure thermal isolation and to reduce the formation of a temperature gradient inside the crystal. The entire stack is situated in an U-shaped block made of polyoxymethylen (POM). An aluminium plate holds the coupling mirror which

3. A squeezed-light laser for GEO 600

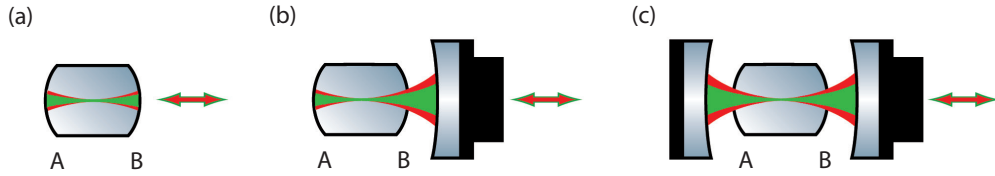


Figure 3.3.: Possible linear resonator designs. (a) Monolithic resonator. Facet A is highly-reflective (HR) coated for both, 1064nm and 532 nm light, while the coating of facet B can be chosen according to the explicit requirements (e.g. singly resonant with a high escape efficiency for a squeezed-light source). The laser frequency is stabilized to the cavity length. (b) Semi-monolithic (hemilithic) resonator: A is still HR-coated, while B is anti-reflective (AR) coated for the two wavelengths. A coupling mirror situated on a ring piezo-electric transducer completes the resonator. This design offers the benefit of cavity length tunability while the internal loss is still kept low. (c) Nonlinear crystal placed in a linear resonator. The two crystal facets are now AR-coated.

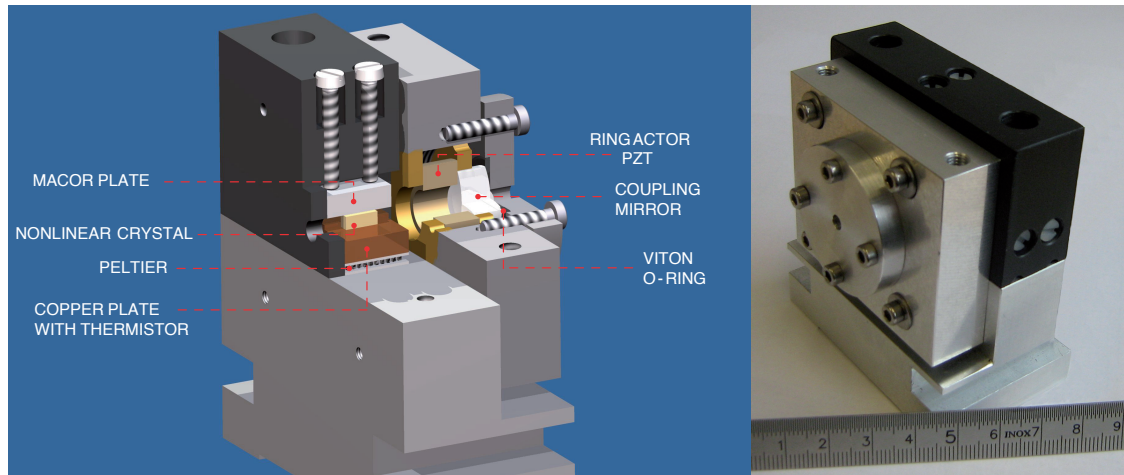


Figure 3.4.: **Left:** CAD drawing of the nonlinear resonator. The designs of the second-harmonic generator and the squeezed light source are identical. Crystal and coupling mirrors are shown in false colors for clarity, a detailed description is given in the text. **Right:** Photograph of the fully assembled oven for second-harmonic generation.

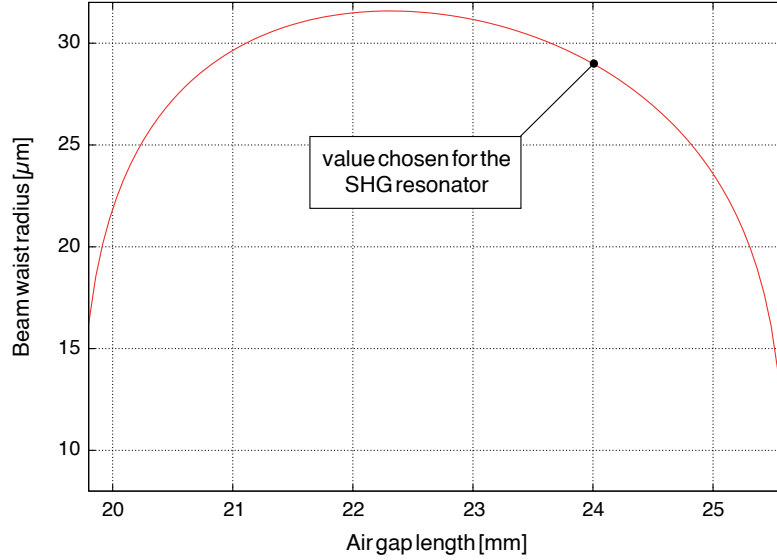


Figure 3.5.: Radius of the SHG beam waist as a function of the optical cavity length, determined by the air gap between the coupling mirror and the AR-coated crystal facet. The cavity stability range extends from 19.8 mm to 25.6 mm. Parameters: crystal length: 6.5 mm, $n(\text{LiNbO}_3, 1064 \text{ nm}) = 2.232$, crystal radii of curvature: 8 mm, coupling mirror radius of curvature: 25 mm.

is mechanically pressed on the ring actor PZT (outer diameter: 16 mm, inner diameter: 8 mm, thickness: 7 mm, range: $1.75 \mu\text{m}$ at 350 V [PIa]).

The nonlinear medium is a 7% MgO:LiNbO₃ crystal measuring $2 \times 2.5 \times 6.5 \text{ mm}^3$. One surface has a radius of curvature (ROC) of 8 mm and is HR-coated for both, 1064 nm and 532 nm light, the other surface is plano and AR-coated for both wavelengths. The coupler is a meniscus mirror with a diameter of 12.7 mm. The inner facet has a radius of curvature of 25 mm and a power reflectivity of $R_{1064} = 90\%$ and $R_{532} \leq 2\%$, respectively. The outer facet is AR-coated ($R_{1064} < 0.1\%$ and $R_{532} < 0.2\%$) and has an ROC of 20 mm. All values are specified for an angle of incidence (AOI) of 0° . This results in a finesse of $\mathcal{F} \approx 59$ for the fundamental 1064 nm field.

One last tunable parameter is the length of the air gap between the planar crystal surface and the inner mirror facet. The results of a [FINESSE] simulation of the cavity stability are shown in Fig. 3.5. For a stable operation, the air gap can extend from 19.8 mm to 25.6 mm. For the SHG cavity, an air gap of 24 mm has been chosen, resulting in an expected beam waist radius of $29.0 \mu\text{m}$ situated at a distance of 3.5 mm from the HR-coated facet. Taking into account the refractive index of LiNbO₃ at 1064 nm, $n = 2.232$, the optical cavity length is $L = 77 \text{ mm}$, which leads to a linewidth (full width half maximum, FWHM) of $\Delta f_{\text{FWHM}} \approx 66 \text{ MHz}$ and a free spectral range of $\Delta f_{\text{FSR}} \approx 3.9 \text{ GHz}$.

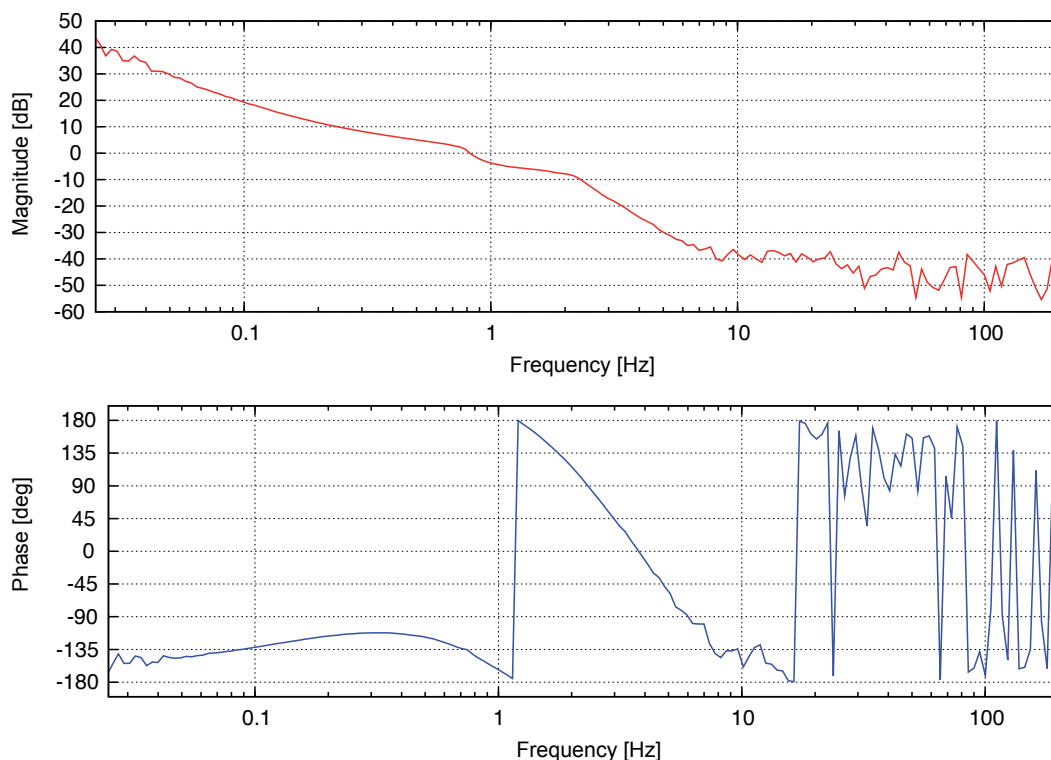


Figure 3.6.: Open-loop gain of the SHG temperature controller, measured with a SR785 dynamic signal analyzer. The unity-gain frequency is approximately 800 mHz.

3.3.2. Temperature stabilization

The conversion efficiency of the fundamental 1064 nm light to the 532 nm pump wavelength strongly depends on the phase matching of the two fields. In our case, the phase matching is optimized using the temperature dependence of the refractive indices. For thermal stabilization, the crystal is put into indirect thermal contact with a NTC thermistor (over a layer of indium foil and the L-shaped copper plate). The NTC is a resistor with a large negative temperature coefficient and serves as a sensor. Its resistance value is compared with an external reference resistor (usually a potentiometer) that acts as a set value. Any deviations from the set value result in a proportional voltage signal which is amplified, converted into a proportional current and then applied to the Peltier element as a control signal. The temperature controller has an integrator with a cut-off frequency of 120 mHz and two differentiators with cut-off frequencies of 400 mHz and 700 mHz, as well as a low-pass filter at 8 Hz ($Q = 0.577$) before the Peltier input. The open-loop gain of the system is shown in Figure 3.6, a detailed circuit diagram of the temperature controller is given in Appendix B of reference [Vahlbruch-PhD]. From the

set resistance value, the temperature of maximal conversion efficiency was calculated to approximately 55 °C, the maximal output power was 187 mW.

3.3.3. Length stabilization

To stabilize the length of the resonator, the Pound-Drever-Hall (PDH) technique was utilized [Drever+83] (a common modulation-demodulation technique, see [Black01] for a detailed description). To avoid electrical beat signals at audio frequencies which might introduce excess noise to the squeezed field, a modulation frequency of 76.5 MHz has been chosen (considering the frequencies utilized at the GEO 600 site). A custom-made electro-optical modulator (EOM), consisting of a MgO:LiNbO₃ crystal placed in a resonance circuit, was constructed with a reflection of < 1 % for the electric modulation field. Due to the residual transmittance of the HR-coated facet of the SHG crystal, a fraction of the intra-cavity field could be detected in transmission by PD_{SHG} (see Fig. 3.2). For the photo detector, a V4TUF design was chosen (designed by H. Vahlbruch, circuit board in B.10 of reference [Vahlbruch-PhD]). It possesses an input port for an electrical local oscillator (LO) signal as well as an on-board mixer, so that a demodulated error signal is readily provided. This signal is processed by a servo control electronics (circuit diagram published in B.3- B.5 of reference [Vahlbruch-PhD]) which is equipped with two integrators (at 8940 Hz and 400 Hz), a notch-filter at 8.3 kHz and a low-pass filter at 10 kHz. The unity-gain frequency of the control loop is approximately 5 kHz. To supply EOM_I and PD_{SHG} (Fig. 3.2) with the LO frequency of 76.5 MHz, channel 0 of the AD9959 DDS was used, the output power is ca. -2.2 dBm.

3.3.4. Optical performance

The shape of the cavity eigenmode is completely determined by the optical and mechanical resonator parameters described above. To mode-match the Mephisto laser beam to the SHG cavity, three superpolished lenses (with ROCs of 25mm, 50mm and 100mm, respectively) have been employed. Only 385 mW of 1064 nm light were used to pump the SHG while most of the remaining power was dumped. This resulted in a 532 nm output power of ca. 187 mW. Taking into account the non-perfect mode-matching of $\approx 92\%$ to the SHG cavity, a conversion efficiency of

$$\eta_{\text{conv}} = \frac{P_{\text{out}}}{P_{\text{in}}} = \frac{n_{\text{out}} f_{\text{out}}}{n_{\text{in}} f_{\text{in}}} \approx 0.53 \quad (3.1)$$

could be derived, with $P_{\text{out/in}}$ denoting the measured optical powers at 532 nm and 1064 nm, respectively, and $n_{\text{out/in}}$ referring to the photon numbers involved. While this value is sufficient in the present experiment, further applications for the second and third generation of GW detectors may require higher η_{conv} values. Values greater 90 % can be reached making periodically poled potassium titanyl phosphate (PPKTP) the nonlinear material of choice as described in Appendix A.

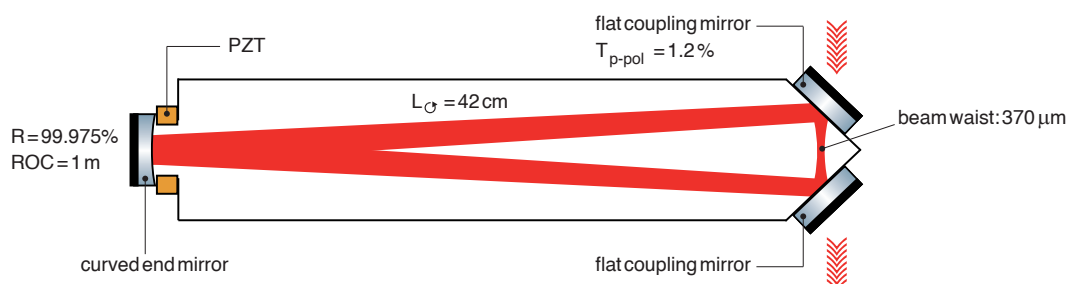


Figure 3.7.: Sketch of the travelling-wave Fabry-Perot resonator used as a mode-cleaner in the local oscillator path. The beam waist radius of $370\ \mu\text{m}$ (for $1064\ \text{nm}$ light) was determined by the cavity round-trip length of $42\ \text{cm}$ as well as by the ROC of the curved end mirror. The mode-cleaner employed for the $532\ \text{nm}$ squeezed-light source pump beam has an identical design, only the mirror parameters vary as discussed in the text.

3.4. Ring mode-cleaner resonators

Before being injected into the squeezed-light source, the $532\ \text{nm}$ pump beam is transmitted through a spatial mode-cleaning travelling-wave resonator, in the following referred to as a *mode-cleaner* or *MC*. Another MC is used to filter the local oscillator beam utilized for homodyne detection. Such filter cavities, first proposed in [Willke+98, Uehara97], offer several advantages. First, they act as a low-pass filter for laser amplitude and phase noise. At the frequency $\Delta f_{\text{FWHM}}/2$, the amplitude noise of the transmitted laser field is attenuated by a factor of 2, at Fourier frequencies much larger than the MC cavity linewidth merely quantum shot-noise is present. Second, an effective spatial mode-filtering is provided; the cavity eigenmode is determined by the geometric parameters described below. The result is a transmitted beam with a high power content in the TEM_{00} mode, while all higher-order-mode light is reflected from the MC. The measurements reported in [Willke+98] actually have shown the higher-order mode content of the transmitted beam to be lower than $0.1\ \%$ for the design used. Third, and actually being most important for the reported experiment, the RF-modulation applied to the laser beams for the PDH cavity locks leads to high-frequency phase noise on the employed beams. This phase fluctuations, leading to a reduced overlap of the squeezed field with the local oscillator beam at the homodyne detector, have been shown to diminish the maximal degree of squeezing achievable [Franzen+06, Takeno+07]. The mode-cleaners serve as low-pass filters for the high-frequency phase noise and thereby make it possible to reach higher squeezing values, as demonstrated in Ref. [Vahlbruch+08]. Furthermore, the MC used for the squeezed-light source pump beam is a crucial component for alignment purposes as described in Section 3.6.

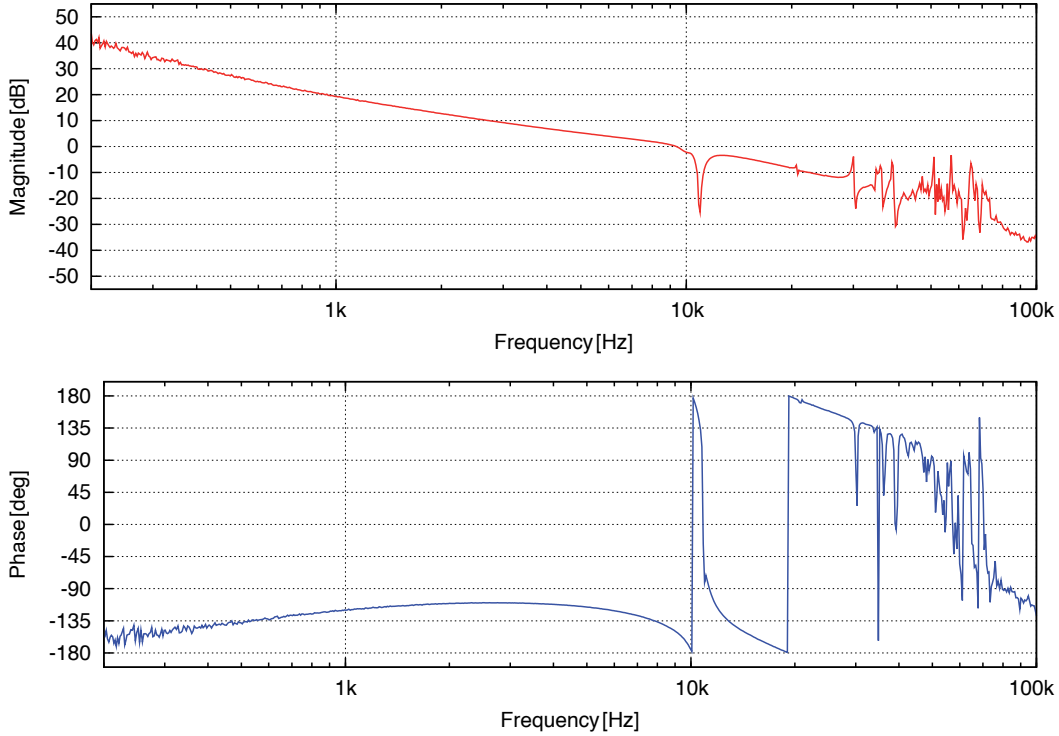


Figure 3.8.: Open-loop gain of the cavity length control loop for the homodyne detection beam mode-cleaner cavity (MC_{1064}). The unity-gain frequency is 9 kHz.

3.4.1. Local oscillator beam for homodyne detection (1064 nm)

The two mode-cleaners are constructed as travelling-wave Fabry-Perot ring cavities with a round-trip length of 42 cm. Figure 3.7 shows a sketch of the design, the values are given for a wavelength of 1064 nm. The cavity is formed by three mirrors. Two of them serve as cavity couplers, they have planar surfaces and a power transmittance of $T_{p-pol} = 1.2\%$ for p-polarized light. The third mirror is plano/curved with a ROC of 1.0 m and has a residual transmittance of 100 ppm. All mirrors have super-polished surfaces and are AR-coated at the facet averted from the cavity. To maximize the mechanical stability, the mirrors are glued with epoxy to an Invar spacer, thereby resulting in a quasi-monolithic cavity design. The material is chosen for the very low thermal expansion coefficient of only about $2.0 \times 10^{-6} \text{ K}^{-1}$ at room temperature (compared with aluminium with about $23.0 \times 10^{-6} \text{ K}^{-1}$). The intra-cavity field determined in its shape by the mirror curvature and the round-trip length has its waist centrally between the two flat coupling mirrors with a waist radius of $370 \mu\text{m}$. Further important cavity parameters are

$$\Delta f_{\text{FSR}} \approx \frac{c}{L} = 714 \text{ MHz}, \quad \mathcal{F} \approx \frac{\pi \sqrt{\rho_1 \rho_2 \rho_3}}{1 - \rho_1 \rho_2 \rho_3} = 259, \quad \Delta f_{\text{FWHM}} = \frac{\Delta f_{\text{FSR}}}{\mathcal{F}} \approx 2.76 \text{ MHz}$$

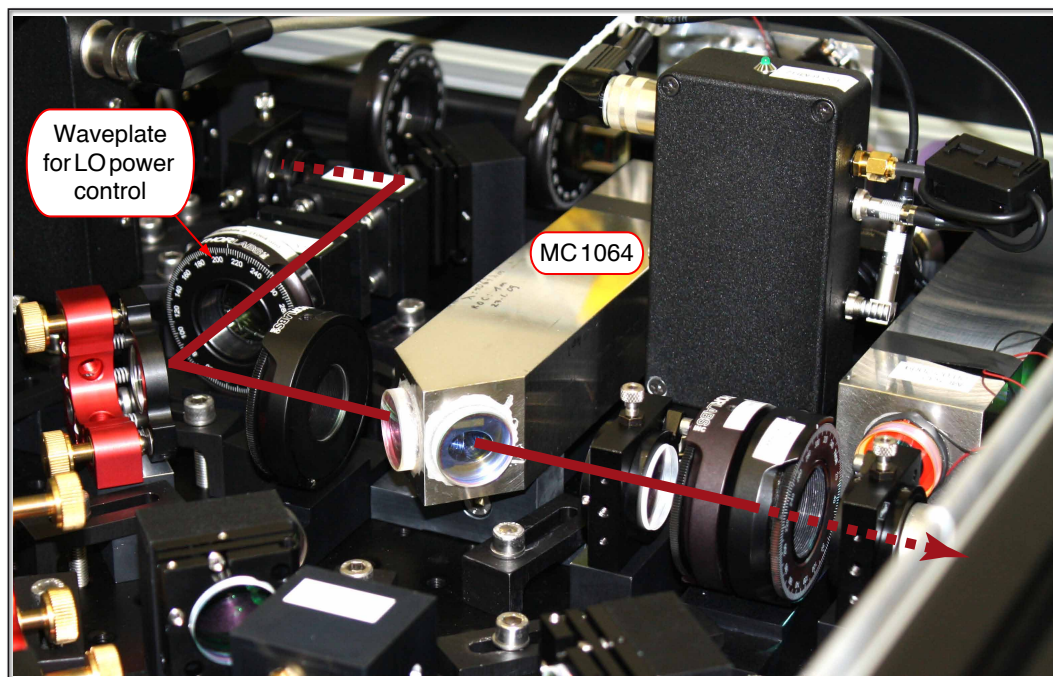


Figure 3.9.: Photograph of the Invar mode-cleaner employed in the GEO 600 squeezed-light laser. To reduce residual phase noise and beam pointing fluctuations, the mode-cleaner is situated as close to the diagnostic homodyne detector (not shown) as possible.

with $\rho_i = \sqrt{R_i}$ being the amplitude reflectivities.

To keep the cavity on resonance with the laser field, the PDH technique was employed. The required phase modulation was, again, provided by EOM_1 with $\nu_{\text{mod}}(\text{EOM}_1) = 76.5 \text{ MHz}$. A fraction of the field reflected by the cavity was detected, demodulated at $\nu_{\text{mod}}(\text{EOM}_1)$ and processed by a servo electronics equipped with two integrators (at 492 Hz and 9.4 kHz), a notch-filter at 10.890 kHz and a low-pass filter at 13 kHz. This design resulted in the open-loop transfer function of the system shown in Figure 3.8. The unity-gain frequency is about 9 kHz. Figure 3.9 shows a photograph of the mode-cleaner. A $\lambda/2$ waveplate situated in front of the cavity allows an adjustment of the optical power of the local oscillator beam.

3.4.2. 532 nm squeezed-light source pump beam

While the cavity design and geometry is identical to the one described above, the mirror parameters vary slightly. The coupling mirrors have a power transmission of $T_{\text{p-pol}} = 5500 \text{ ppm}$ for p-polarized light, the curved end mirror a value of $T = 150 \text{ ppm}$. This results in a calculated finesse value of $\mathcal{F} = 562$ and in a calculated cavity linewidth of

$\Delta f_{\text{FWHM}} = 1.27$ MHz. For cavity length stabilization, the 532 nm beam is transmitted through another custom-made EOM driven at a power of -2.6 dBm. The modulation frequency is 122.6 MHz. The beam reflected by the cavity is detected by PD_{MC532} and processed by a servo identical to the one described above. The open-loop transfer function of the system is not shown since it is similar to the one plotted in Fig. 3.8.

3.5. Squeezed-light source

The core of the entire experiment is a $9.3 \text{ mm} \times 1.5 \text{ mm} \times 1.0 \text{ mm}$ crystal of periodically poled potassium titanyl phosphate (KTiOPO_4 , PPKTP). This choice of material, first proposed for GW observatory squeezed-light sources in [Goda+08a], offers several advantages when compared with LiNbO_3 which was used in previous experiments.

First, the phase-matched-condition does not as strongly depend on the crystal temperature as is the case for lithium niobate. As shown in Ref. [McKenzie-PhD], the phase-matched temperature for PPKTP is approximately 35°C with a FWHM of 5°C , while it is approximately 64°C with a FWHM of 1.3°C for lithium niobate. Therefore, PPKTP imposes less strict conditions for the temperature stabilization of the squeezed-light source. Furthermore, the operation temperature is closer to room temperature.

Second, the effective nonlinear coefficient $d_{\text{eff, PPKTP}}$ is several times larger than $d_{\text{eff, LiNbO}_3}$ as summarized in [Goda-PhD] (with $|d_{\text{eff, PPKTP}}| \approx 10.8 \text{ pm/V}$). This means that less 532 nm power is required to reach the same squeezing values.

Third, the optical absorption of PPKTP at the wavelength of 532 nm is supposed to be smaller than the one of lithium niobate. This reduces the sensibility of the system and hence of the squeezing degree to pump power fluctuations, when no pump power stabilization scheme is implemented (see Section 3.8). The optical loss at 1064 nm is, on the other hand, similarly large for both media, so that the intra-cavity loss does not increase when PPKTP is used. The results reported in this work as well as in [Eberle+10] showed PPKTP to be superior to LiNbO_3 as nonlinear squeezing medium at 1064 nm and 1550 nm in every respect at moderate pump powers.

Figure 3.10 shows a sketch of the squeezing resonator. Like in the case of the SHG, it is composed of a HR-coated crystal surface ($R = 99.975\%$, $\text{ROC} = 12 \text{ mm}$) and a meniscus coupling mirror ($R_{1064} = 92\%$, $R_{532} = 20\%$), while the intra-cavity crystal facet is AR-coated for the two wavelengths. The air gap between the AR crystal surface and the coupling mirror is 22.5 mm long which results in an optical round-trip cavity length of 79 mm, taking into account the crystal's refractive index $n_{\text{PPKTP}}^{1064 \text{ nm}} = 1.8302$. The beam waist radius predicted by a FINESSE simulation is $33 \mu\text{m}$. Further important cavity parameters were calculated to be

$$\Delta f_{\text{FSR}} \approx 3.80 \text{ GHz}, \quad \mathcal{F}(1064 \text{ nm}) \approx 75, \quad \Delta f_{\text{FWHM}}(1064 \text{ nm}) \approx 50 \text{ MHz}.$$

3. A squeezed-light laser for GEO 600

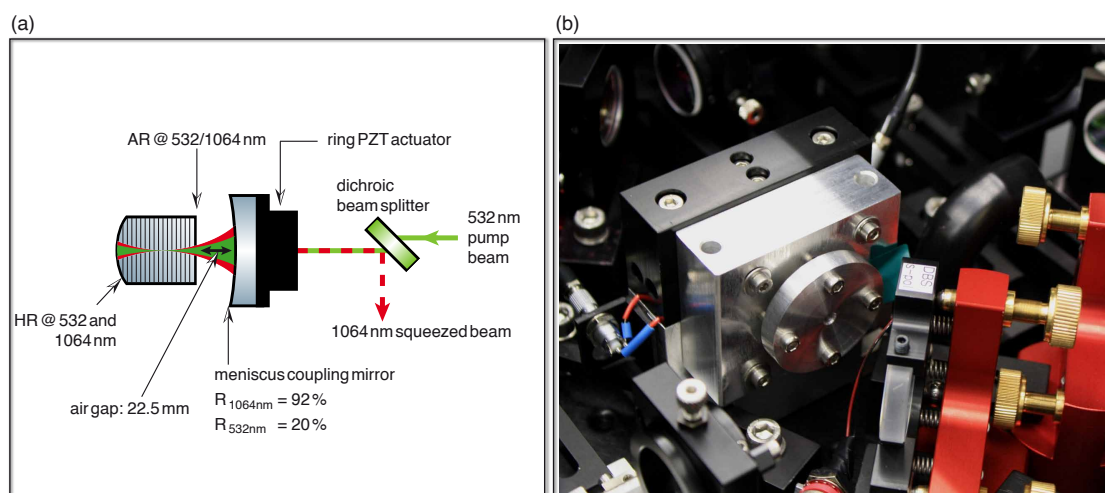


Figure 3.10.: (a) Sketch of the squeezed-light source. A 9.3 mm long PPKTP crystal is used as nonlinear medium. The cavity has a finesse of 75, a linewidth of 50 MHz and a FSR of 3.8 GHz. (b) Photograph of the GEO 600 squeezed-light source. The crystal housing is similar to the one used for the second-harmonic generator.

The mechanical design of the squeezed-light source is identical to the one used for the SHG. Again, the crystal is temperature-stabilized inside an oven housing to ensure the phase-matched condition between the fundamental (squeezed) and the second-harmonic (pump) field. The operating temperature is, however, significantly lower. A value of $34^{\circ}\text{C} - 35^{\circ}\text{C}$ could be estimated, assuming a typical performance of the temperature sensor. No absolute calibration was performed since the absolute value is of no relevance for the experiment. The temperature stabilization loop is similar to the one described in Section 3.3 and allowed a control bandwidth of about 1 Hz. In the following sections, the coherent control scheme used for the cavity length and for the squeezing phase stabilization (schematically shown in Figure 3.11) is described.

3.6. Squeezed-light cavity length control beam and pump beam alignment

To generate squeezing at MHz-frequencies, one single laser source can be used for SHG, control and homodyne detection purposes (as e.g. described in detail in [Chelkowski-PhD]). A part of the laser light is frequency up-converted and used to pump the squeezed-light source. Along with this 532 nm pump beam, a fraction of the 1064 nm beam with phase-modulation sidebands for control purposes is injected into the squeezed-light cavity. This beam has exactly the same mode and polarization as the

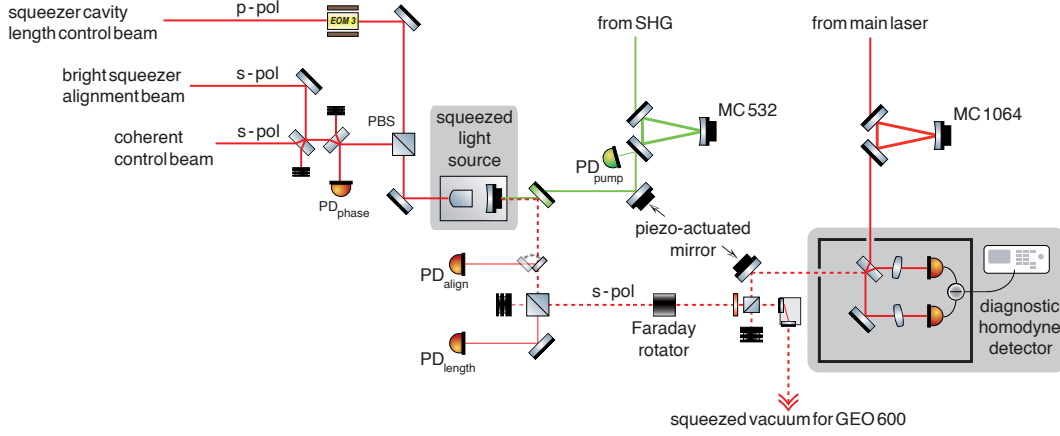


Figure 3.11.: Scheme of the squeezing control and detection stages. Two additional laser beams, phase-locked to the main laser, are used to stabilize the squeezer cavity length as well as the squeezing phase. Furthermore, a bright alignment beam can be injected into the cavity to allow a mode-matching of the 532 nm pump beam into the squeezed-light source. An on-board diagnostic balanced homodyne detector finally allows for a characterization of the squeezed-light laser. For clarity reasons, only the main components are shown, details are provided in the text.

generated squeezed field and thus allows a control of the cavity length as well as of the phase of the squeezed field. Unfortunately, this beam also carries technical noise at frequencies up to several MHz which completely masks squeezing at audio frequencies and makes such a control scheme unusable for GW observatory purposes.

In the following, the alignment procedures and the coherent control scheme ([Vahlbruch+06, Vahlbruch-PhD, Vahlbruch+07, Chelkowski-PhD]) for generation of squeezing at audio Fourier frequencies are presented.

3.6.1. Alignment beam

The so-called *bright alignment beam* (BAB) with frequency $\omega_0^{\text{s-pol}}$ originates from the main Mephisto laser and has a power of 20.9 mW. This auxiliary field is injected into the squeezed-light source through the HR-coated facet and the transmitted field is monitored by the photo detector PD_{align} . The BAB was employed for several purposes as discussed in the following.

In the first place, the beam was used to properly align the coupling mirror of the nonlinear resonator. As long as no control scheme was implemented, the alignment beam could also be used for cavity length stabilization due to the RF-sidebands applied by EOM_1 . Finally, after implementation of the control scheme, the $\omega_0^{\text{s-pol}}$ -beam was used for a reversed alignment of the 532 nm pump beam path. A spatial overlap between the

pump field and the squeezer cavity eigenmode is very important, not only to reach high parametric gain values (which are easily reached with PPKTP in any case), but also to avoid an interaction of the pump field with any higher-order 1064 nm modes inside the cavity. Such an interaction could lead to squeezing or even to anti-squeezing of other spatial modes which would result in an additional noise contribution to the squeezed TEM_{00} mode and thus reduce the amount of squeezing achievable. When the bright 1064 nm alignment beam was injected into the squeezed-light source, it was partially frequency up-converted to produce a weak 532 nm alignment beam. Even though the conversion efficiency was quite poor due to the high under-coupling of the squeezer cavity, the obtained beam power was sufficient to allow a mode-matching to the 532 nm mode-cleaner cavity and thereby to perform a reversed mode-matching procedure. PD_{pump} , optimized for the detection of very weak beams with merely some μW light power, was used to monitor the field reflected by MC_{532} . Furthermore, the BAB is necessary for the alignment of the squeezed beam with respect to GEO 600 as discussed in Section 5.2.

While the bright alignment beam can be used to optimize the experimental alignment at any time, it has, however, to be dumped whenever the squeezed-light source is operated targeting squeezing at audio frequencies. Otherwise it would obscure any squeezing at frequencies up to several MHz.

3.6.2. Cavity length control

The first parameter addressed by the coherent control scheme by means of the AUX2-laser beam with an optical power of 63 mW is the length of the squeezing resonator. The control field is p-polarized and thus has a polarization orthogonal to the one of the squeezed field. Due to the crystal's birefringence, the cavity resonance condition is different for each polarization. The bright alignment beam was used to determine the resonance conditions, simultaneously injecting the $\omega_0^{\text{s-pol}}$ beam and the AUX2 beam into the squeezing resonator and monitoring the resonant curves of the cavity in transmission using PD_{align} . When no 532 nm light is injected into the squeezing resonator, we found the frequency offset necessary to allow for a simultaneous resonance to be 12.6 MHz. This value, however, slightly changes due to the power absorbed by the crystal when a pump beam is injected. Therefore, the frequency offset was chosen to be 20 MHz. It is controlled by PLL_2 as described above, the frequency reference is provided by the AD9959 digital signal generator. A fine-tuning of the polarization degeneration can be performed by slightly changing the squeezer crystal temperature, thereby compensating for the cavity length change induced by optical power absorption. A drawback of this approach is that the control scheme is relatively sensitive to pump power fluctuations. Long-term operations therefore required the implementation of a pump power stabilization scheme as discussed in Section 3.8.

Like the SHG and the mode-cleaners, the squeezed-light source cavity length is also stabilized with a PDH lock. The required phase modulation was provided by EOM_3

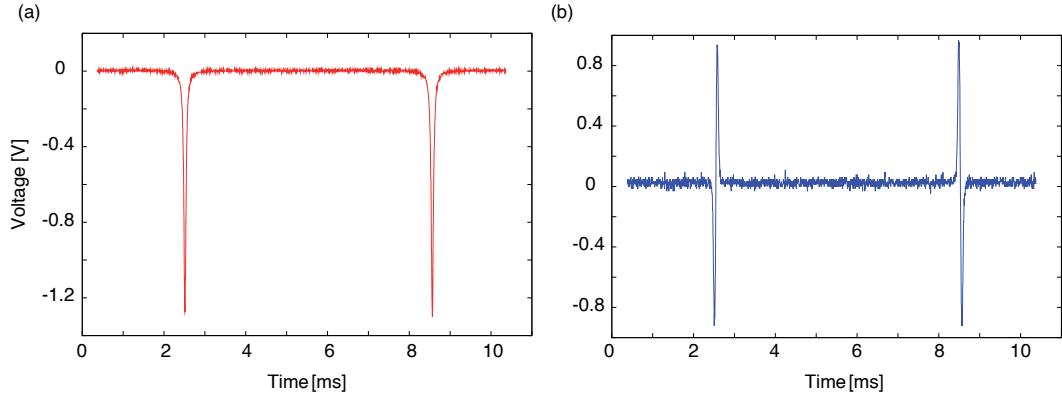


Figure 3.12.: (a) Resonance peaks of the p-polarized length control beam transmitted by the squeezing resonator and detected at $\text{PD}_{\text{length}}$. The mode-matching to the cavity was in the order of 99% and is similar to the values achieved for the other resonators employed throughout the experiment. (b) Corresponding error signal after demodulation at $\nu_{\text{mod}}(\text{EOM}_3) = 44.44$ MHz. The signal-to-noise ratio (SNR) was 37.

with $\nu_{\text{mod}}(\text{EOM}_3) = 44.44$ MHz. The beam transmitted by the squeezed-light source is separated from the s-polarized squeezed field at a polarizing beam splitter and detected by $\text{PD}_{\text{length}}$. Figure 3.12 shows one free spectral range of the squeezer cavity as well as the error signal generated by demodulation at $\nu_{\text{mod}}(\text{EOM}_3)$. The error signal was processed by a servo equipped with two integrators (492 Hz and 7.2 kHz) and a low-pass filter at 6 kHz. The unity-gain frequency of the control loop was 5 kHz.

3.6.3. Controlling the squeezing angle - theoretical considerations

While the squeezer cavity length control is independent from the nonlinear process, a beam that senses the nonlinearity is required to stabilize the phase of the squeezed field with respect to the pump field as well as to the local oscillator field employed for homodyne detection. The control field used must be coherent with the squeezed field, which is, in the reported experiment, solved by an independent but phase-locked laser beam. In the following, the theoretical principles derived in [Chelkowski-PhD] are summarized.

The goal of the enterprise is to derive an expression for the field exiting the squeezing resonator when a control field shifted by a frequency Ω with respect to the fundamental squeezing frequency ω_0 is injected into the squeezed-light source. Following the notation used in Ref. [Chelkowski-PhD], this field is denominated as *QCF = Quadrature Control Field*. Prior to any nonlinear interaction, the QCF, which can be described by the real-valued amplitude α_Ω , represents a single-sideband field with respect to the fundamental

3. A squeezed-light laser for GEO 600

field at ω_0 . Hence, the expectation values of the annihilation operators for the upper ($\omega_0 + \Omega$) and lower ($\omega_0 - \Omega$) sideband frequency fields are

$$\langle \hat{a}_+ \rangle \equiv \langle \hat{a}(\omega_0 + \Omega) \rangle = \alpha_\Omega \quad \text{and} \quad \langle \hat{a}_- \rangle \equiv \langle \hat{a}(\omega_0 - \Omega) \rangle = 0. \quad (3.2)$$

With the formalism derived by Caves and Schumaker [Caves+85], the quadrature amplitudes can be written as

$$\hat{a}_1 = \frac{1}{\sqrt{2}}(\hat{a}_+ + \hat{a}_-^\dagger) \quad \text{and} \quad \hat{a}_2 = \frac{1}{i\sqrt{2}}(\hat{a}_+ - \hat{a}_-^\dagger), \quad (3.3)$$

with the indices 1 and 2 referring to the amplitude and the phase quadrature, respectively. The optical parametric amplification and deamplification of the single quadratures can be described as a transformation

$$\bar{\mathbf{b}} \equiv \begin{pmatrix} \hat{b}_1(\Omega) \\ \hat{b}_2(\Omega) \end{pmatrix} = \hat{S}(r, \theta) \bar{\mathbf{a}} \hat{S}^\dagger(r, \theta) \equiv \hat{S}(r, \theta) \begin{pmatrix} \hat{a}_1(\Omega) \\ \hat{a}_2(\Omega) \end{pmatrix} \hat{S}^\dagger(r, \theta), \quad (3.4)$$

where

$$\hat{S}(r, \theta) = e^{r(\hat{a}_+ \hat{a}_- - \exp(-2i\theta) - \hat{a}_+^\dagger \hat{a}_-^\dagger \exp(2i\theta))} \quad \text{with} \quad \hat{S}^\dagger(r, \theta) = \hat{S}(-r, \theta) \quad (3.5)$$

is the *squeezing operator* known from Section 2.6. The values

$$0 \leq r < \infty \quad \text{and} \quad 0 \leq \theta \leq 2\pi \quad (3.6)$$

describe the degree of squeezing and the squeezing phase, respectively [Caves+85]. Considering the relations

$$\hat{S}(r, \theta) \hat{a}_\pm \hat{S}^\dagger(r, \theta) = \hat{a}_\pm \cosh(r) + \hat{a}_\mp^\dagger e^{2i\phi} \sinh(r) \quad (3.7)$$

$$\hat{S}(r, \theta) \hat{a}_\pm^\dagger \hat{S}^\dagger(r, \theta) = \hat{a}_\pm^\dagger \cosh(r) - \hat{a}_\mp e^{-2i\phi} \sinh(r) \quad (3.8)$$

that can be obtained from application of the Baker-Hausdorff lemma [Gerry+06], the expression

$$\bar{\mathbf{b}} = \begin{pmatrix} \cosh(r) + \sinh(r) \cos(2\theta) & \sinh(r) \sin(2\theta) \\ \sinh(r) \sin(2\theta) & \cosh(r) - \sinh(r) \cos(2\theta) \end{pmatrix} \begin{pmatrix} \hat{a}_1 \\ \hat{a}_2 \end{pmatrix} \quad (3.9)$$

follows as the most general description for the squeezed quadrature vector after the nonlinear $\chi^{(2)}$ interaction. The two orthogonal squeezed quadratures can then in a further step be employed to obtain any arbitrary quadrature θ through linear combination. Considering Eq.'s (3.2) and (3.3), the expectation values

$$\langle \hat{b}_1(\Omega) \rangle = \frac{\alpha_\Omega}{\sqrt{2}} [\cosh(r) + \sinh(r) \cos(2\theta)] + \frac{\alpha_\Omega}{i\sqrt{2}} [\sinh(r) \sin(2\theta)] \quad (3.10)$$

$$\langle \hat{b}_2(\Omega) \rangle = \frac{\alpha_\Omega}{\sqrt{2}} [\sinh(r) \sin(2\theta)] + \frac{\alpha_\Omega}{i\sqrt{2}} [\cosh(r) - \sinh(r) \cos(2\theta)] \quad (3.11)$$

for the squeezed quadrature amplitudes follow directly from Eq. (3.9). A Fourier transform

$$\hat{b}_1(t) = \hat{b}_1(\Omega)e^{-i\Omega t} + \hat{b}_1^*(\Omega)e^{i\Omega t}, \quad (3.12)$$

$$\hat{b}_2(t) = \hat{b}_2(\Omega)e^{-i\Omega t} + \hat{b}_2^*(\Omega)e^{i\Omega t}, \quad (3.13)$$

regarding, as the entire consideration, only a single frequency Ω , finally transfers the squeezed quadrature amplitude values into the time domain and thus directly allows us to derive an expression for the electric field

$$E^{\text{QCF}} \propto \langle \hat{b}^+(t) + \hat{b}^-(t) \rangle \quad \text{with} \quad \hat{b}^\pm(t) \equiv \frac{1}{2} \left[\hat{b}_1(t) \pm i\hat{b}_2(t) \right] e^{\mp i\omega_0 t}, \quad (3.14)$$

namely

$$E^{\text{QCF}} \propto \frac{1+g}{\sqrt{2g}} \alpha_\Omega \cos(\omega_0 t + \Omega t) - \frac{1-g}{\sqrt{2g}} \alpha_\Omega \cos(\omega_0 t - \Omega t - 2\theta) \quad (3.15)$$

with $g = e^{2r}$ being the nonlinear gain for a single-path $\chi^{(2)}$ interaction. Equation (3.15) instantly allows us to deduce the effect of the nonlinear $\chi^{(2)}$ interaction on the single-sideband control field: While the injected field possesses only the frequency component Ω , the field exiting the squeezing resonator is composed of the two sidebands $\omega_0 \pm \Omega$. It thus contains information on the squeezing phase, being the relative phase between the two generated sidebands.

An intuitive understanding of this effect can be gained from the optical down-conversion process. Due to the $\chi^{(2)}$ interaction, the single-sideband field experiences a parametric amplification with the 532 nm beam serving as the pump. The single-sideband field cannot be deamplified, due to energy conservation, since no field is present at $\omega_- = \omega_0 - \Omega$. In the course of the amplification process, two 1064 nm photons are generated from one 532 nm photon. Again, energy conservation enforces the production of a photon at $\omega_- = \omega_0 - \Omega$, when the $\omega_+ = \omega_0 + \Omega$ is amplified, effectively resulting in the generation of the lower sideband.

The generated double-sideband field allows a direct control of the squeezing angle. The only experimental condition for low-frequency squeezing is that Ω has to be large enough to not introduce by interference technical laser noise at the frequencies of interest and still small enough for the field to sense a significant parametric gain inside the nonlinear resonator. In our case, this has been solved by choosing $\Omega/2\pi = 15.2168$ MHz. To generate an adequate control signal, the detected photo current

$$I^{\text{QCF}} \propto |E^{\text{QCF}}|^2 \propto \frac{\alpha_\Omega^2}{2g} [(1+g) \cos(\omega_0 t + \Omega t) - (1-g) \cos(\omega_0 t - \Omega t - 2\theta)]^2 \quad (3.16)$$

has finally to be mixed down with an electrical local oscillator signal

$$I^{\text{demod}} \propto \alpha_{\text{demod}} \cos(2\Omega t + \chi), \quad (3.17)$$

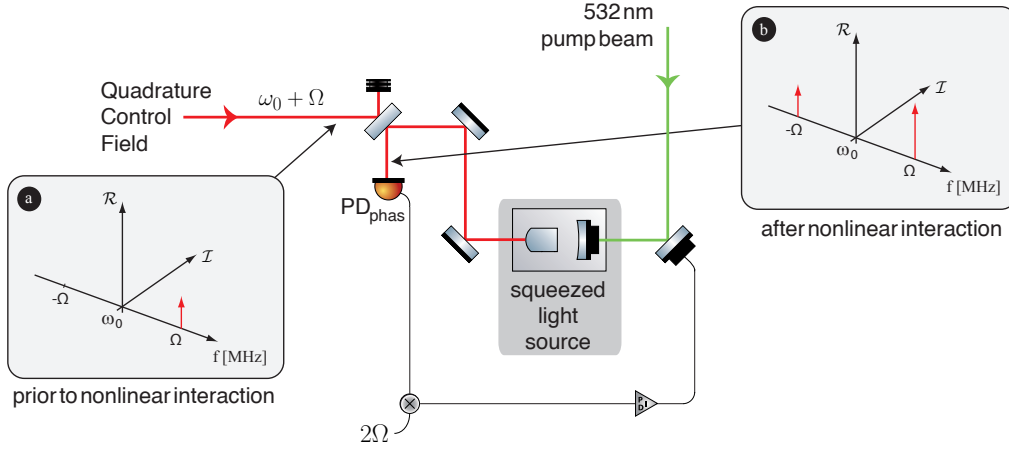


Figure 3.13.: Schematic of the squeezing angle control loop. The quadrature control field injected as a single sideband into the squeezed-light source (illustrated by box (a) in which ω_0 is chosen as the central frequency) is turned into a field with sidebands at $\omega_0 \pm \Omega$ (box (b)) by the nonlinear interaction. When the detected photo current is demodulated at the frequency 2Ω , a sinusoidal error signal is obtained which is used to stabilize the length of the 532 nm pump beam path.

that has twice the optical offset frequency, while χ denotes the demodulation phase and α_{demod} is the field amplitude. A lengthy but simple calculation results in the clear expression

$$\epsilon_{\text{phase}}^{\text{QCF}} \propto I^{\text{QCF}} I^{\text{demod}} \propto -\frac{\alpha^2(1-g^2)}{4g} \cos(\chi - 2\theta) + \mathcal{O}(4\Omega) + \mathcal{O}(2\omega_0) \quad (3.18)$$

for the error signal with $\alpha^2 = \alpha_{\Omega}^2 \alpha_{\text{demod}}$. The high frequency (HF) components can be removed electronically through low-pass filtering, and the demodulation phase can be chosen in the experiment, which finally leads to the sinusoidal error signal

$$\epsilon_{\text{phase}}^{\text{QCF}} \propto \frac{(g^2 - 1)}{4g} \alpha^2 \cos(2\theta). \quad (3.19)$$

This signal depends only on the phase of the squeezed field and thus can be directly used to stabilize the angle of the squeezing ellipse.

3.6.4. Controlling the squeezing angle - experimental realization

From the experimental point of view, the stabilization of squeezing ellipse angle is identical to the stabilization of the 532 nm pump beam path length, since the phase offset between this pump field and the generated squeezed field directly determines the

squeezing angle. Therefore, a phase-shifting device is placed into the 532 nm beam path. The PZT employed therein has a high dynamic range, the maximal displacement available is 11 μm when the device is operated at 370 V (length: 27 mm, max. range 30 μm at 1000 V [PIb]). Such a dynamic range is required to compensate for large low-frequency drifts (e. g. thermally induced). Since the effect of the large PZT on the beam alignment is significant, it is placed in the path between SHG and MC₅₃₂. Thus, any fluctuation in pointing of the 532 nm beam onto the squeezed-light resonator, which would considerably deteriorate the degree of squeezing, is excluded. Pointing fluctuations will result only in a reduced mode-matching of the 532 nm beam to MC₅₃₂ and hence in a pump power change, which can be compensated for by a power stabilization scheme as discussed in Section 3.8.

The control field, provided by the AUX1 laser, with an optical power of 25 μW , is injected into the squeezed-light source at the HR-coated facet, as illustrated in Fig. 3.13. It experiences the nonlinear $\chi^{(2)}$ interaction, in the course of which a second sideband at $\omega_0 - \Omega$ is generated. The resulting field is detected in reflection from the squeezing resonator at the photo detector PD_{phas}. After demodulation at the frequency 2Ω that is provided by the ultra low noise Wenzel OCXO, the error signal shown in Fig. 3.14 is obtained and is fed back to the phase shifter. The unity gain frequency is several kHz. In case a higher bandwidth should be required at any time (e. g. due to different laboratory conditions at the detection site), a second phase-shifter is available in the setup. It is constructed as a $6 \times 6 \times 8 \text{ cm}^3$ brass block with a weight of ca. 2.5 kg. Inside the block, the steering mirror is clamped to a ring PZT in a very stiff way. This stiff construction, together with the high mass, allows an effective suppression of the eigenresonances at low frequencies and thus makes it possible to achieve a control bandwidth of about 7 kHz as shown in Fig. 3.15, however at the expense of the microscopic dynamic range of the PZT. When required, the two actuators can be used for a single control loop and addressed through a frequency-separating filter. Thereby, one part of the control loop with low bandwidth but a high actuation range would address large low-frequency drifts, while the other part would allow a compensation of the HF jitter.

3.7. Control of the 1064 nm homodyne detector local oscillator field

Before the squeezed field is injected into GEO 600, a characterization of the squeezed-light laser output was necessary. For that purpose, an on-board diagnostic homodyne detector was set up. The detection scheme is shown in the right part of Fig. 3.11. The s-polarized squeezed field emitted by the squeezed-light source is separated from the p-polarized length control field at a polarizing beam splitter and is guided to the signal port of the homodyne detector through a $\lambda/2$ -PBS set. At a later stage, when operated in GEO 600, the waveplate is rotated by 90° , thereby closing the diagnostic port.

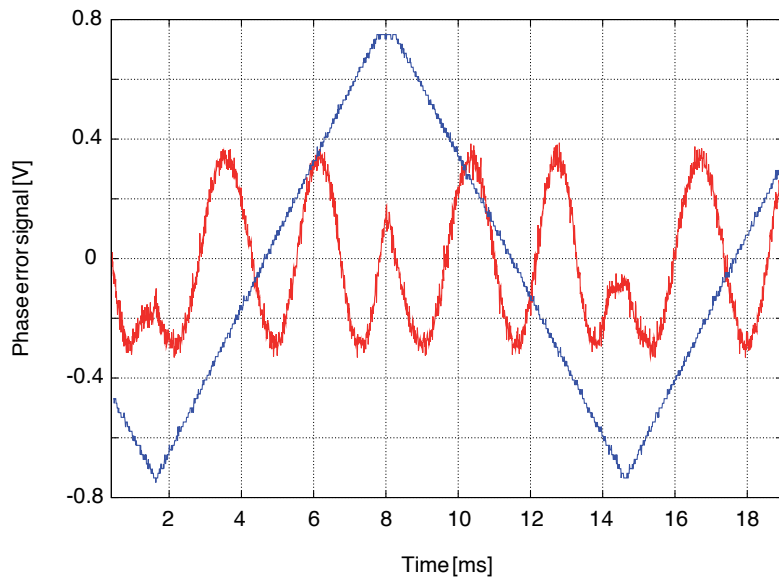


Figure 3.14.: Error signal for the squeezing angle control loop, generated by demodulating the quadrature control field at twice the offset frequency Ω .

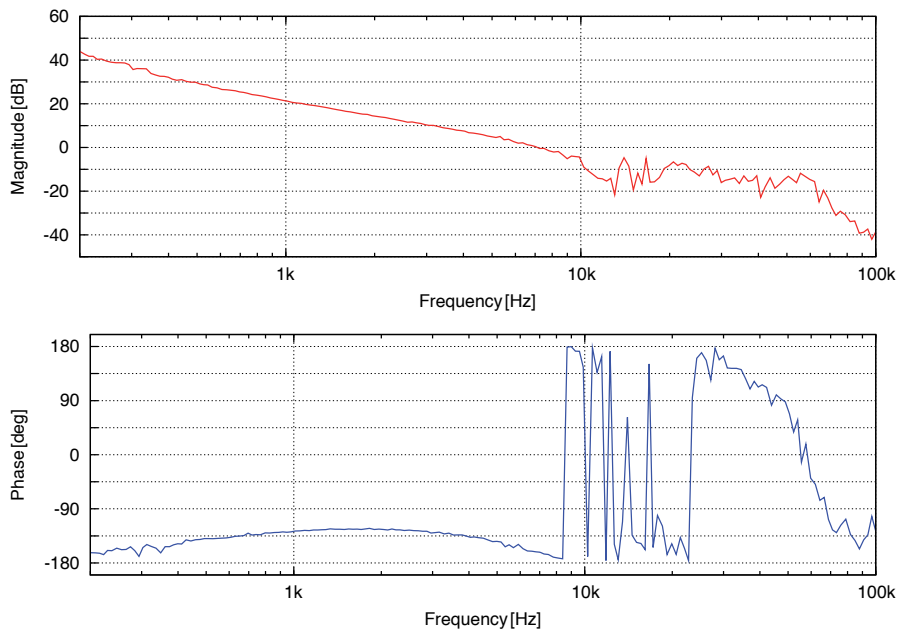


Figure 3.15.: Open-loop gain of the squeezing phase stabilization loop. The phase-shifter PZT is clamped to a massive brass holder. The unity-gain frequency is about 7 kHz.

The main functional principle of a homodyne detector was presented in Section 2.9. The squeezed vacuum field contains only a few photons, so that in the case of a direct detection any signal produced at the photo detector would be completely obscured by the dark noise of the detector itself. Therefore, this weak field is interfered with a strong local oscillator beam at a 50/50 beam splitter. In consequence, the signal (or, to be precise, one single field quadrature) undergoes a strong optical amplification. To eliminate the technical noise inherent to the LO beam, the difference of the two photo currents is generated. In a balanced detector, this signal does in first-order approximation not contain LO noise contributions and provides information on the quantum noise in the observed field quadrature. The homodyne output signal is monitored using a fast Fourier transform (FFT) spectrum analyzer. For measurements in the audio frequency band, long integration times (of several minutes when measuring down to mHz frequencies) are required. Therefore, a stabilization of the measurement quadrature of the homodyne detector is necessary.

The signal for a homodyne angle stabilization is, once again, obtained from the quadrature control field. In Eq. (3.15), the expression for the QCF after nonlinear interaction was derived. This field, copropagating with the squeezed beam (about 1 μ W is transmitted through the squeezing resonator), is overlapped with the optical LO field $E^{\text{LO}} \propto \alpha_{\text{LO}} \exp(-i(\omega_0 t + \phi)) + \text{c. c.}$ at the homodyne beam splitter. The fields at the two beam splitter outputs read

$$\begin{aligned} E^{\text{H1/2}} &= \frac{1}{\sqrt{2}} [E^{\text{LO}} \pm E^{\text{QCF}}] \\ &\propto \frac{1}{\sqrt{2}} \left[\alpha_{\text{LO}} e^{-i(\omega_0 t + \phi)} \right. \\ &\quad \left. \pm \left\{ \frac{1+g}{\sqrt{2g}} \alpha_{\Omega} \cos(\omega_0 t + \Omega t) - \frac{1-g}{\sqrt{2g}} \alpha_{\Omega} \cos(\omega_0 t - \Omega t - 2\theta) \right\} \right] + \text{c. c.} . \end{aligned} \quad (3.20)$$

The difference of the photocurrents measured at the two ports is given by

$$\begin{aligned} I^{\text{diff}} &\propto |E^{\text{H1}}|^2 - |E^{\text{H2}}|^2 \\ &\propto \frac{4\sqrt{2}}{\sqrt{g}} \alpha_{\text{LO}} \alpha_{\Omega} \cos(\omega_0 t + \phi) \\ &\quad \times [(1+g) \cos(\omega_0 t + \Omega t) - (1-g) \cos(\omega_0 t - \Omega t - 2\phi)] \\ &\propto \sqrt{\frac{8}{g}} \alpha_{\text{LO}} \alpha_{\Omega} [(1+g) \cos(-\Omega t + \phi) - (1-g) \cos(\Omega t + 2\theta + \phi) + \mathcal{O}(2\omega_0)] . \end{aligned} \quad (3.21)$$

Experimentally, the subtraction is realized in a compact electronic circuit (the circuit board design is published in [Vahlbruch-PhD] Fig. B8-9, page 153-4). A low-pass filtering stage which is followed by a demodulation at the frequency Ω leads to the signal

$$\begin{aligned} \epsilon_{\text{hmd}}^{\text{QCF}} &\propto I^{\text{diff}} I^{\text{demod}} \\ &\propto \sqrt{\frac{2}{g}} \alpha [(1+g) \cos(\chi + \phi) - (1-g) \cos(\chi - \phi - 2\theta) + \mathcal{O}(2\Omega)] \end{aligned} \quad (3.22)$$

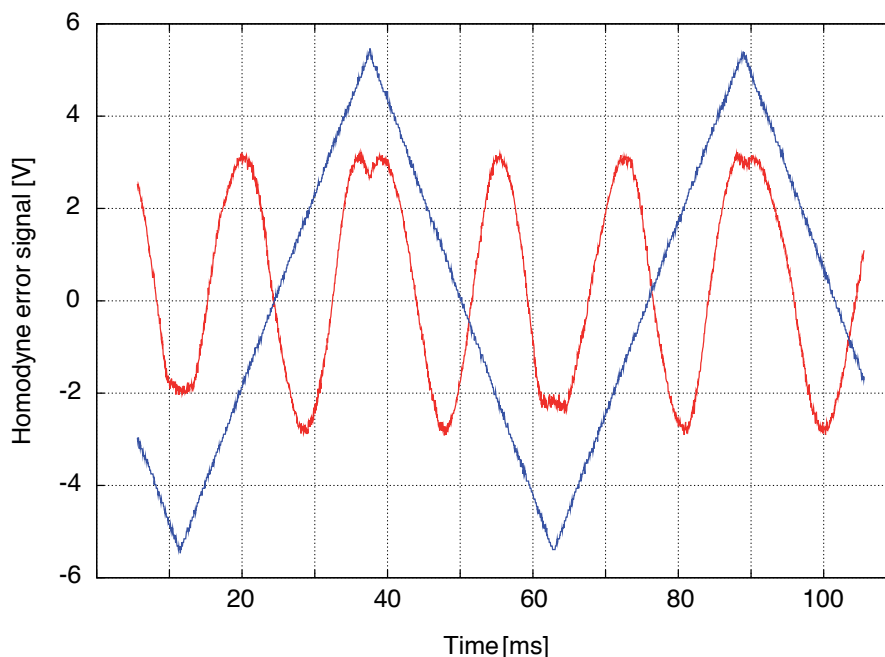


Figure 3.16.: Red trace: error signal for the homodyne readout quadrature control loop, generated by demodulating the quadrature control field at the QCF offset frequency. Blue trace: triangle waveform applied to the phase-shifter PZT.

where $\alpha = \alpha_{\Omega}\alpha_{\text{LO}}\alpha_{\text{demod}}$. A last low-pass filtering finally leaves us with an error signal depending on the squeezing angle θ as well as on the local oscillator phase ϕ , while the demodulation phase χ can be chosen. After the squeezing angle is stabilized using the – completely independent – pump path control loop, the homodyne error signal depends merely on ϕ and thereby can be directly employed to stabilize the homodyne detection angle.

For the experimental realization, another high-mass brass phase-shifter holder is placed in the squeezing path. This is completely equivalent to the actuation of the local oscillator beam phase. Again, a control bandwidth of several kHz could be achieved, the obtained error signal is shown in Fig. 3.16.

To minimize pointing effects, the phase-shifter is located in close proximity to the homodyne beam splitter. Any pointing fluctuation would lead to a reduced fringe visibility (in the following simply abbreviated as *visibility*) at the homodyne detector. To maximize the visibility and to reduce phase noise, the local oscillator beam is transmitted through the mode-cleaning resonator discussed in Section 3.4. On the other side, the beam parameters of the squeezed beam are matched to the LO beam. For this purpose, the bright alignment beam was employed. It has, apart from the optical power, exactly

the same parameters as the squeezed beam and therefore allowed an adjustment of the homodyne visibility. The realized fringe visibility was

$$\mathcal{V} = \frac{V_{\max} - V_{\min}}{V_{\max} + V_{\min}} \approx 0.9875, \quad (3.23)$$

where $V_{\max/\min}$ are the maximal/minimal voltages of a single homodyne photo diode measured while the relative phase between the homodyne local oscillator beam and the bright alignment beam is varied. This leads to a homodyne detection efficiency of

$$\eta_{\text{hmd,vis}} = \mathcal{V}^2 \approx 0.975 \quad (3.24)$$

and thus corresponds to a detection loss of 2.5% due to non-perfect interference of the two beams. This value was sufficient for the application as a diagnostic homodyne detector. For a further visibility improvement, an additional diagnostic cavity providing a beam parameter reference would be helpful. While crucial for other experiments, the detected value of squeezing is of minor relevance in this special case, since the homodyne detector is by-passed in any case when the squeezed-light laser is operated in GEO 600.

3.8. Pump power stabilization

A permanent employment in a GW observatory imposed an additional demand on the GEO 600 squeezed-light laser: the generated degree of squeezing has to remain stable on timescales of hours to days (in the following referred to as *long-term*) in order to ensure a non-varying observatory sensitivity. During the characterization of the long-term performance of the system, the stability of the squeezing degree was, however, found to depend on the power stability of the 532 nm pump beam. In the following, the effects of a time-dependent pump power value on the squeezing degree are discussed. Finally, the extension of the coherent control scheme by a pump power stabilization scheme is presented.

3.8.1. Theoretical considerations

The squeezing output in several ways depends on the 532 nm pump beam power. Pump power fluctuations will change the degree of squeezing and anti-squeezing, as well as the angle of the squeezing ellipse, as shown below. One reason for the varying pump power is that the power of the 1064 nm laser beam used to pump the SHG device is not stabilized. The fluctuations of the 1064 nm laser power therefore directly couple into the 532 nm power value. Please note that the nonlinear coupling mechanism can – due to the power dependence of the SHG conversion efficiency – furthermore lead to an even greater relative power change for the second-harmonic beam. Furthermore, degradation of beam alignment into the SHG (being a weeks- or month-timescale effect) will also

lead to a slowly changing pump power level. This time-dependence of the 532 nm pump power is not compensated by the control loops described above. A first characterization of the degree of squeezing has shown that it slowly degrades without a pump power stabilization employed. Though a detailed analysis of the power fluctuation has not been performed, values of several percent have been observed. For the calculations presented in the following, a worst-case scenario of $\pm 5\%$ has been assumed. To account for a long-term alignment degradation, additionally a value of -10% is considered. Please note that both are arbitrary values employed to visualize the effect on the degree of squeezing.

Squeezing as a function of pump power

The fluctuation of the pump beam power will result in two different effects. First, the anti-squeezing and squeezing variances

$$R_{a/s} = 1 \pm \eta_{\text{tot}} \frac{4\sqrt{P/P_{\text{th}}}}{(1 \mp \sqrt{P/P_{\text{th}}})^2 + 4\kappa^2} \quad (3.25)$$

depend on the pump power P [Takeno+07]. In this expression a and s and the upper and lower signs denote the anti-squeezing and the squeezing, respectively, η describes the total detection efficiency and P_{th} is the OPO threshold power. The normalized frequency

$$\kappa = \frac{2\pi f}{\gamma} \quad \text{with} \quad \gamma = \frac{c(T+L)}{l} \quad (3.26)$$

is a function of cavity parameters, where T is the power transmittance of the output coupling mirror, L is the intra-cavity loss and l the optical cavity round-trip length, while f is the frequency as measured with a spectrum analyzer. Please note that the frequency dependence is provided in a wrong way in reference [Takeno+07], where the factor 2π is omitted. The total detection efficiency

$$\eta_{\text{tot}} = \rho \xi \mathcal{V}^2 \eta_{\text{hmd}} \quad (3.27)$$

depends on the cavity escape efficiency $\rho = T/(T+L)$, the total propagation loss $(1-\xi)$, the fringe visibility \mathcal{V} and finally on the quantum efficiency of the homodyne photo detectors η_{hmd} . Finally, for some calculations it might be useful to express Eq. (3.25) in terms of the optical gain

$$g = \frac{1}{(1 - \sqrt{P/P_{\text{th}}})^2} \quad (3.28)$$

of the squeezer cavity.

The direct dependence of the squeezing degree on the pump power is relatively weak. When we assume realistic parameters

$$\eta_{\text{hmd}} = 0.99, \quad \mathcal{V} = 0.985, \quad \xi = 0.98, \quad \rho \approx 0.95, \quad \text{and} \quad \frac{P}{P_{\text{th}}} = 0.5,$$

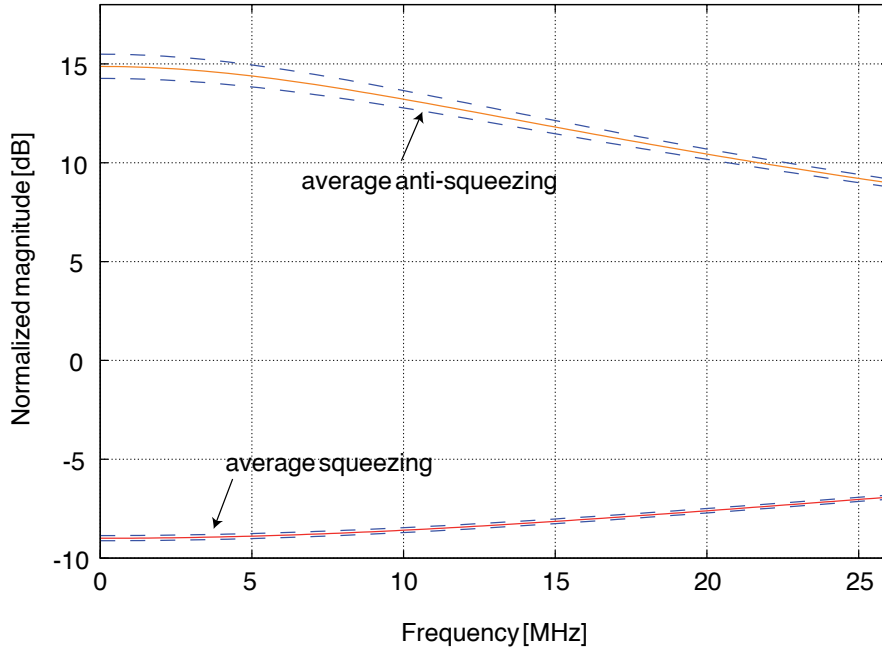


Figure 3.17.: Simulation of the frequency-dependent squeezed field assuming real experimental parameters (see text). The total assumed detection loss is approximately 10.5%. The squeezing (red line) and anti-squeezing (orange line) is shown as a function of frequency. The FWHM of the squeezer cavity is 51.5 ± 0.5 MHz. The blue dashed lines indicate the expected effect of a $\pm 10\%$ pump power fluctuation. With $\approx \pm 0.13$ dB it is negligible for the squeezing and therefore is not expected to affect the experimental performance.

the detected level of squeezing

$$V_{a/s} = 10 \log_{10}(R_{a/s}) \quad (3.29)$$

in our hypothetical system would be 9 dB at frequencies much smaller than the cavity linewidth. A pump power change even by $\pm 10\%$ would lead to a deviation of merely $+0.135$ dB or -0.124 dB, respectively. The anti-squeezing would vary by approximately 0.5 dB as shown in Fig. 3.17. At this point, an ideal system without phase noise contributions is described. It is, however, obvious that the direct dependence of the squeezing and anti-squeezing values on the pump power alone is not significant for the long-term stability considerations.

Thermal effects

The thermally-induced mechanism is much more severe for the employed coherent control scheme. Since the nonlinear crystal has a non-vanishing absorption coefficient for 532 nm light, any pump power change results in a change of the absorbed power and thus in a

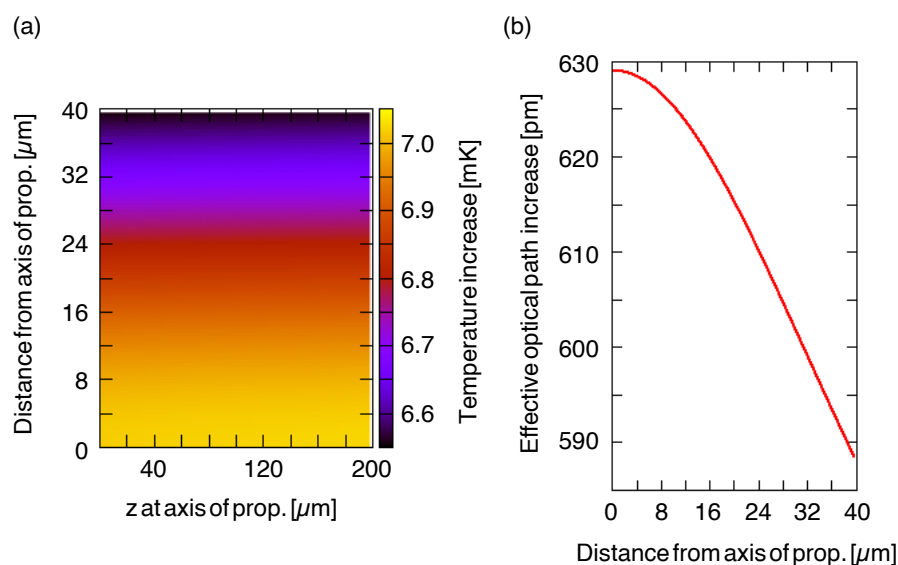


Figure 3.18.: TKSIm [Lastzka-PhD] simulation of the temperature change of the nonlinear crystal for a 532 nm pump power increase from 35 mW to 38.5 mW. (a) Lateral cut parallel to the axis of beam propagation at an arbitrary position inside the crystal (the gaussian beam properties are not considered by the simulation). (b) Cross-section perpendicular to the axis of propagation. The y -axis shows the effective optical path increase due to the created temperature gradient. Since an implementation of the complete system consisting of crystal and copper plate was not possible with TKSIm, the results are shown merely to visualize the temperature gradient, while exact numbers could not be derived. Values of $t = 1$ ms and $\alpha_{\text{PPKTP}} = 2.4\%/cm$ were used for the observation time and the absorption coefficient, respectively.

change of the crystal temperature. The reported absorption coefficients cover a range of $0.5\%/cm$ to $4.5\%/cm$, a detailed discussion is provided in Ref. [Meier-PhD], where a value of $2.4\%/cm$ was observed.

Figure 3.18 shows the simulated effect of a pump power increase by 10% from 35 mW to 38.5 mW on the temperature distribution inside the crystal. The result is a temperature gradient with the highest temperature change at the axis of propagation. The simulation was performed with the program *TKSIm* by N. Lastzka [Lastzka-PhD]. Please note that the simulation relies on a set of material parameters not known exactly for the nonlinear crystal employed in the squeezer cavity and is provided here to visualize the qualitative effect rather than to derive exact numbers. Nonetheless, the results obtained support the model for the influence of the 532 nm pump power change on the coherent control scheme derived below. Coming back to the simulation, one drawback worth mentioning is that it does not account for the different materials employed in the oven. Furthermore, the temperature coupling between the crystal and the copper plate as well as between the

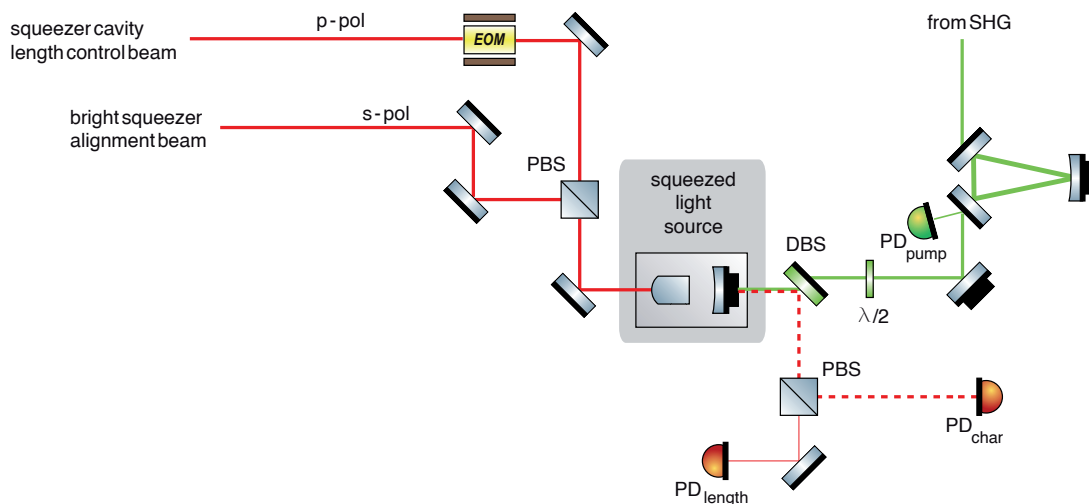


Figure 3.19.: Sketch of the setup employed to characterize the dependence of the degeneracy condition on the 532 nm beam power. The cavity length was stabilized via the p-pol length control beam, the QCF was not injected. The s-polarized bright alignment beam was injected and detected in transmission by PD_{char} as a function of the pump power employed. The polarization of the pump field ensured the optical gain to be close to 1 for the measurement. PBS: polarizing beam splitter, DBS: dichroic beam splitter, PD: photo detector.

copper plate and the NTC sensor is unknown. It was thus not possible to calculate the temperature change expected to be sensed by the NTC. It may, however, be expected to be considerably smaller than the increase at the optical axis due to the relatively big volume of the copper plate.

A measurement on another (similar) squeezer cavity showed the NTC value to change by approximately $3\ \Omega$ for a pump power increase from 35 mW up to 38.5 mW. This corresponds to a value of $\approx 0.8\ \text{mK}$.

The changed temperature gradient inside the crystal is not sensed in an efficient way by the implemented temperature stabilization loop and therefore cannot be compensated for. Please note that this problem is not fundamental and in principle can be solved by a calibrated temperature stabilization scheme. The alternative pump power stabilization solution presented later on is, however, both, simpler and more precise. Due to the temperature dependence of the refractive index, a pump power variation results in a change of the optical cavity length.

To evaluate the expected effect for the squeezed-light laser, let us assume the following starting condition: The length of the squeezing resonator is stabilized using the p-polarized control beam and the degeneracy condition between the s- and the frequency-shifted p-polarized light is adjusted using the crystal temperature as a fine-adjustment

tool. When operated in this way, the temperature is optimized with regard to the phase-matching condition and the squeezing resonator delivers the maximal amount of squeezing possible at the chosen pump power. Now the pump power increases and the higher thermal load leads to a cavity length increase. While the resonator is still held on resonance with the PDH control loop, the polarization degeneracy is no longer fulfilled to 100%. Thus, the increased power results in a cavity that is perfectly resonant for p-polarized light but slightly detuned from resonance for the s-polarized squeezed field.

A separate characterization measurement was performed in order to obtain quantitative results for the detuning of the squeezing resonator to be expected at a certain pump power deviation from the set value. For this, the bright alignment beam and the setup shown in Figure 3.19 were used. The length of the squeezing resonator was stabilized using the p-polarized field, and a pump power of $P_{532\text{ nm}} = 34.5\text{ mW}$ was injected into the squeezing resonator, while the coherent control field was blocked. The crystal temperature was optimized for a polarization degeneration and the pump beam polarization shifted by 90° . This ensured that lowest nonlinear conversion took place while the 532 nm power was still present and absorbed inside the crystal. Now the pump power was varied and the change in the alignment beam power (being proportional to the intracavity power and hence to the cavity's resonant curve) recorded by the diagnostic photo detector PD_{char} . This measurement directly allowed deducing the resonator detuning as a function of the relative pump power change. The normalized results are shown in Fig. 3.20. The measured data (red crosses) are in good agreement with the simulation of the cavity resonant curve (blue line). From the known cavity parameters given above, it is directly possible to deduce that a pump power fluctuation of only 1% will already lead to a detuning of 0.3 MHz for the s-polarized quadrature control beam. A pump power change of 5% will result in a detuning of 1.5 MHz and 10% even in a detuning by ca. 3 MHz.

Considering the cavity FSR of $\approx 3.8\text{ GHz}$, a detuning by 3 MHz corresponds to an optical path length change by about 0.42 nm. Taking into account the temperature dependence of the refractive index as well as of the crystal length [Wiechmann+93]

$$\left. \frac{\Delta n}{\Delta T} \right|_{1064\text{ nm}} \approx 6.14 \times 10^{-6} \frac{1}{\text{K}} \quad \text{and} \quad \frac{\Delta L}{\Delta T} \approx 6 \times 10^{-7} \frac{1}{\text{K}}, \quad (3.30)$$

the increase of the crystal temperature at the optical axis could be estimated to approximately 3.7 mK. This value, together with the 0.8 mK sensed at the NTC in a similar system, allows a rough estimate of the changed temperature gradient inside the nonlinear crystal. Both results are in good agreement with the TKSIm simulation shown in Fig. 3.18.

Expected squeezing degradation

When the squeezing resonator is detuned from resonance, the generated squeezed field is affected in several ways.

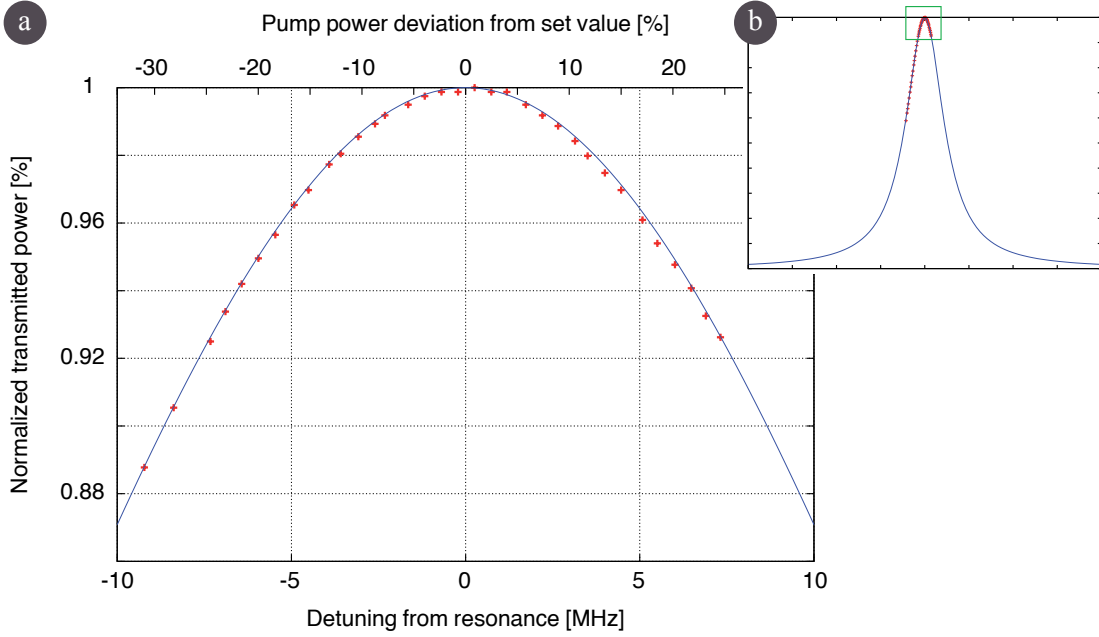


Figure 3.20.: (a) Measurement of the alignment beam power transmitted through the squeezing resonator as a function of pump power (upper x -axis). A power of 34.5 mW, corresponding to the envisioned GEO 600 operations condition, was employed as set value. The measured data (red crosses) are in good agreement with the simulation of the cavity resonant curve (blue line) employing experimental parameters. From this, a calibration of the cavity detuning corresponding to the pump power change was calculated (lower x -axis) (b) Frequency zoom-out showing the location of the measured data with respect to the resonant curve.

1. First, the coherent control scheme is based on a single-sideband field used for stabilization of the squeezing ellipse angle. The other sideband at the frequency $\omega_0 - \Omega$ is generated by the nonlinear $\chi^{(2)}$ interaction. The phase relation between the two sidebands is then used as reference in the control scheme. To provide an intuitive understanding of the detuning effect, Fig. 3.21 shows the phase shift

$$\Phi(f) = \arg \left(\frac{\tau_1 \tau_2 e^{\frac{i l 2 \pi f}{c}}}{1 - \rho_1 \rho_2 e^{\frac{2 i l 2 \pi f}{c}}} \right) \quad (3.31)$$

experienced by an optical field transmitted through the squeezing resonator. Here, $\tau_{1/2}$ and $\rho_{1/2}$ denote the amplitude transmittances and reflectivities, respectively, of the resonator coupling mirrors. In the coherent control scheme, the optical phase difference $\Delta_0 = \Phi(f_{\text{QCF}}) - \Phi(-f_{\text{QCF}})$ of the two sidebands is used as reference to stabilize the phase of the squeezed field. When the cavity is now detuned from

3. A squeezed-light laser for GEO 600

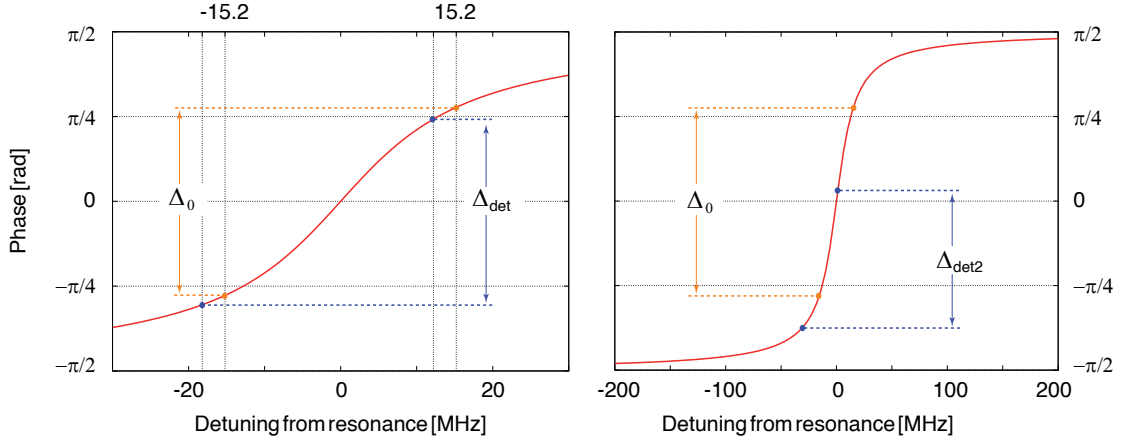


Figure 3.21.: Left: Phase rotation experienced by an optical field transmitted through the squeezing resonator in dependence of its detuning. The phase difference between the two QCF sidebands, serving as reference for the squeezed field phase stabilization, is always larger for a resonant (Δ_0) than for a detuned (Δ_{det}) cavity. The difference $\Delta_0 - \Delta_{det}$ is small for detunings much smaller than the cavity linewidth and reaches a constant maximal value for frequencies much larger than the linewidth. The shown frequency offset was chosen to be 3 MHz, corresponding to the effect of a 10% variation of the 532 nm pump power. Right: Zoom-out at large detuning values for a visual illustration of the effect described with an arbitrary example frequency offset of 15 MHz.

resonance by f_{det} , the two sidebands experience a phase rotation different from the previous condition, which results in

$$\Delta_{det} = \Phi(\Omega \pm f_{det}) - \Phi(-\Omega \pm f_{det}) \neq \Delta_0, \quad (3.32)$$

as illustrated on the right side of Fig. 3.21. As a consequence, the squeezing ellipse experiences a rotation by an angle

$$\begin{aligned} \Theta(f_{det} = -1.5 \text{ MHz}) &\approx -5.6 \text{ mrad} \approx -0.32 \text{ deg}, \\ \Theta(f_{det} = -3.0 \text{ MHz}) &\approx -22.5 \text{ mrad} \approx -1.29 \text{ deg} \end{aligned}$$

depending on the detuning and hence on the pump power variation. This rotation directly translates into the degree of squeezing detected at the diagnostic homodyne detector as

$$V'_{a/s,\Theta} = V_{a/s} \cos^2 \Theta + V_{s/a} \sin^2 \Theta. \quad (3.33)$$

$V_{s/a}$ denominates the values of squeezing and anti-squeezing, respectively, while Θ is the rotation angle. Trace (a) of Fig 3.22 shows the simulated degradation of squeezing under a fixed readout angle ($V'_{a/s,\Theta}$) that was initially optimized for the

highest squeezing at the nominal pump power. For the simulation, a state with 9.3 dB of squeezing and 16.75 dB of anti-squeezing was assumed.

2. The homodyne angle stabilization loop is affected by the resonator detuning in the same way. In this case, however, the optical beat of the double-sideband QCF field and the LO field at frequency f_0 is employed for stabilization. It is hence the average value of the phase differences between the f_0 field and the two sideband fields that serves as reference. Depending on the detuning, the homodyne readout quadrature is rotated by

$$\begin{aligned}\phi(f_{\text{det}} = -1.5 \text{ MHz}) &\approx -2.8 \text{ mrad} \approx -0.16 \text{ deg}, \\ \phi(f_{\text{det}} = -3.0 \text{ MHz}) &\approx -11.3 \text{ rad} \approx -0.65 \text{ deg}.\end{aligned}$$

Thus, the readout quadrature is co-rotating with the squeezed field quadrature and therefore to some extent compensates for the squeezing degradation as shown in trace (b) of Fig. 3.22.

3. An additional parameter is the detuning-dependent nonlinear gain experienced by the two sidebands which will result in a change of the sideband amplitudes and hence in a further effect on the resulting phase difference. Please note that this effect is not accounted for by the simulation results shown in Fig. 3.22. Quantitative results on the gain contribution may be obtained by solving Eq. (3.14) for the quadrature control field transmitted by the squeezing resonator as a function of sideband frequency. Equally omitted is the effect of the nonlinear gain on the cavity bandwidth, which will result in a dependence of the effective linewidth on the gain value as well as on the phase relation between the fundamental and the pump fields inside the squeezer cavity.
4. The magnitude of the error signal used for the homodyne angle stabilization loop (given in Eq. (3.19)) depends on the intensity of the coherent control beam transmitted through the squeezing resonator as well as on its nonlinear gain. Both values will change when a detuning is introduced. Here, the QCF intensity change is mainly due to a different nonlinear gain experienced by the two sidebands. Additionally, a small contribution (0.2% for a 3 MHz detuning when no gain is considered) will arise from the changing cavity transmittance $|\tau(f_{\text{det}})|^2$.

In case the zero-crossing point of the error signal is chosen as operation point, an intensity change does not have an effect on the detection angle. Since in the homodyne locking scheme an electronic offset is added to the error signal in order to adjust the desired ellipse orientation, an operation at the mid-point of the sinusoidal error signal will usually not be the case. Depending on the operation point, a changing error signal magnitude will result in a rotation of the readout quadrature, which is the stronger the closer the operation point is to the turning point of the error signal.

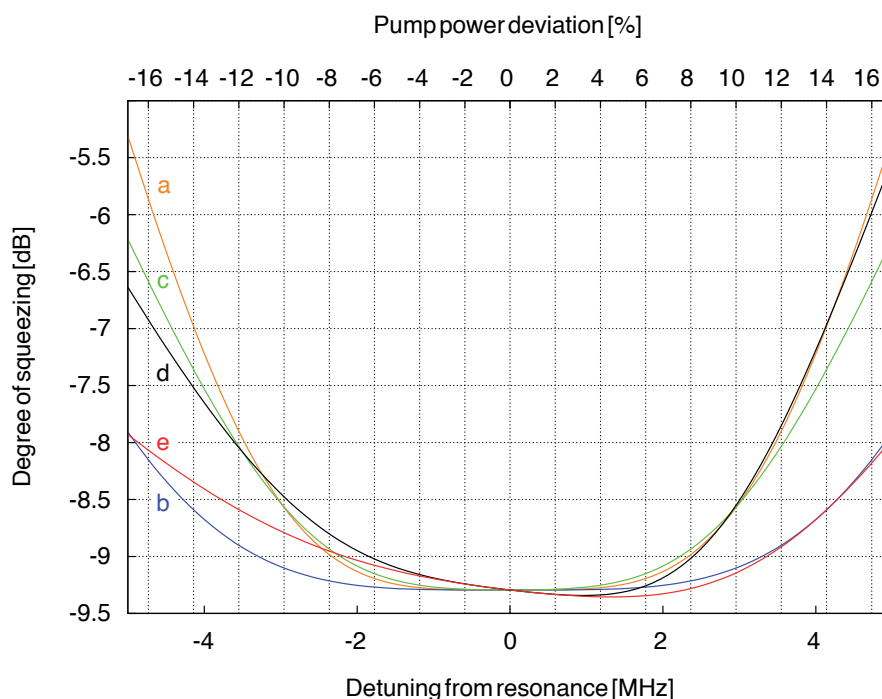


Figure 3.22.: Simulated degree of squeezing detected at a fixed homodyne angle, initially optimized for the nominal pump power of 34.5 mW. The upper x -axis shows the pump power deviation in percent, the lower x -axis gives the resulting cavity detuning for s-polarized light. (a) only considers the rotation of the squeezing ellipse induced by the detuning. (c) additionally takes into account the reduced squeezing output of a detuned cavity. (d) additionally accounts for the optical gain changing with pump power. (e) finally takes into account the detuning-induced rotation of the homodyne readout quadrature. Additionally, (b) shows the effect of the co-rotation of the readout quadrature on trace (a) disregarding the effects of a changing nonlinear gain.

It is worth mentioning that the same kind of effect will also arise from a power fluctuation of the auxiliary laser beam used as the QCF. For operation in GEO 600, the mid-point of the sinusoidal error signal is therefore chosen as operation point.

5. The amount of squeezing produced is no longer the highest possible value as can be seen from Fig. 3.17. This effect is not particularly strong as long as the detuning values are significantly smaller than the cavity linewidth. A detuning by several MHz can, however, result in a measurable effect which is shown in Fig. 3.22.
6. As long as the cavity is held on resonance, the phase shift experienced by the squeezed field is equal in magnitude (with an opposite sign) for the sidebands at the upper and the lower Fourier frequencies. This results in a frequency-independent orientation of the squeezing ellipse in phase space. When the resonance condition is

no longer fulfilled, the phase shifts experienced by the upper and the lower sidebands of the squeezed field are no longer equal, which leads to a frequency-dependent rotation of the squeezing ellipse, as was shown in [Chelkowski+05]. In the discussed case, this effect is, however, negligible in a first-order consideration since frequencies far smaller than the cavity linewidth are considered.

Summarizing, pump power fluctuations result in an alteration of the squeezing strength as well as in a rotation of the squeezing ellipse. While the first effect is a lasting one, the second one can be compensated for by manipulating either the squeezing phase or the homodyne readout angle. An experiment relying on a long-term stability of the squeezing angle will, however, suffer severe degradation of the squeezing strength detected by the homodyne detector at one fixed readout angle.

Figure 3.22 illustrates how the changing pump power affects the frequency-dependent squeezing level, as far as this is accessible by the simple model given above. Trace (a) shows the simple case where the varying optical gain is not considered at all and the squeezing ellipse is merely rotated. This rotation is partially compensated by the co-rotating homodyne readout quadrature, as shown by trace (b). Traces (c) and (d) again neglect this compensation and show merely the phase of the squeezing ellipse. Trace (c) takes into account that a detuning of the squeezing resonator reduces the effective optical gain experienced by the s-polarized field. Though the squeezing level decreases minimally, so does even more the anti-squeezing value. Because the rotation of the ellipse introduces a coupling of the anti-squeezing into the squeezing via Eq. (3.33), at the end the squeezing level at a fixed readout angle is not as strongly affected as it would be when the anti-squeezing decrease was not considered. Trace (d) furthermore accounts for the change of the pump power itself which leads to an asymmetric gain change. A higher pump power leads to a higher anti-squeezing and thereby to a further reduction of the squeezing value detected, while the effective squeezing value increases slightly for lower pump powers. Trace (e), again, considers the co-rotation of the readout quadrature, constituting the most complete result achievable by the derived model. Please note that the effect of the changing nonlinear gain on the QCF sidebands as well as on the error signal itself is not considered by the simulation. Additionally, other degrees of freedom as e.g. the power in the QCF laser beam will also influence the control scheme. The simulation results are therefore merely shown to derive a more intuitive understanding of some of the different effects connected to a changing pump power level, rather than to derive exact predictions for squeezing values. The considerations given above, along with the experimental observation of a time-dependent degree of squeezing, however indicated a pump power stabilization scheme to be mandatory for any long-term operations.

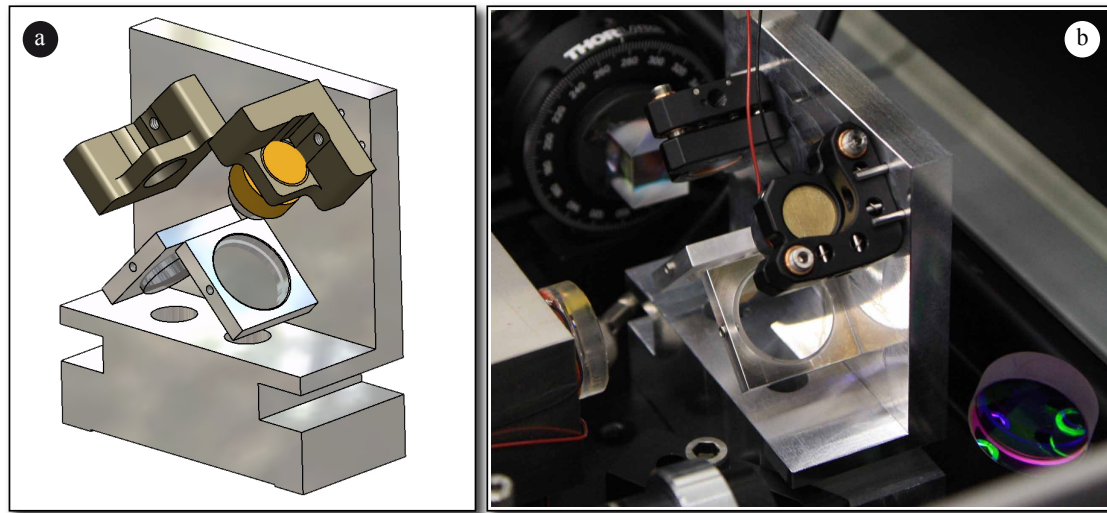


Figure 3.23.: (a) CAD drawing of the Mach-Zehnder-type interferometer. While the beam splitters are housed in monolithic mounts, the mirror orientations may be adjusted. One mirror is attached to a PZT actuator to control the relative length of the two interferometer arms. (b) Photograph of the compact Mach-Zehnder-type interferometer used to stabilize the optical power of the 532 nm squeezing pump beam.

3.9. Experimental implementation of the pump power stabilization

The most straightforward stabilization approach employs an electro-optical amplitude modulator. This device is based on the Pockels effect and consists of a nonlinear crystal, usually $\text{MgO}:\text{LiNbO}_3$, placed in an electrical condensator. Depending on the voltage applied, the polarization of the linearly polarized input beam is rotated by a certain value. When the device is combined with a PBS, one PBS port can be used to set up a control loop while the other port emits the stabilized optical field. Unfortunately, neither commercially available nor custom devices did work at the wavelength of 532 nm. Any polarization rotation induced by an external HV field was compensated for on a seconds-timescale. The strength of the compensation effect depended on the optical power used. A possible reason for this effect could be that the optical field led to microscopic charge separation which compensated the externally-applied electric field.

The implemented pump power stabilization (which does not rely on nonlinear effects) is realized via a Mach-Zehnder type interferometer. The device was constructed vertically, to keep it as compact as possible and the spatial requirements low. Figure 3.23 shows a CAD drawing as well as a photograph. One of the steering mirrors is mounted on a

PZT actuator, thereby making it possible to change the optical power transmitted by the interferometer. For the stabilization scheme, a small fraction of the 532 nm pump beam is tapped off close to the squeezed-light source and monitored with a photo detector. The recorded voltage value is compared with a reference voltage. The unity gain frequency was 1 kHz.

This stabilization scheme made it possible to remove long-term pump power fluctuations and thereby to stabilize the degree of squeezing. Another advantage of the setup is that different squeezing values can be adjusted after a first calibration: The monitor photo detector provides a relative measurement of the pump power employed and thereby allows for a reproducibility being higher than when relying on power meter measurements. The implemented power stabilization improved the long-term stability of the squeezed-light laser output. The results achieved are discussed in Section 4.5.

3.10. Conclusion

The squeezed-light laser for GEO 600 was set up in a cleanroom environment on a 135 cm × 113 cm optical breadboard. For squeezing observation at audio Fourier frequencies, the coherent control scheme was implemented. This scheme relies on two auxiliary laser beams with a polarization and/or frequency different from the one of the squeezed field. The two auxiliary lasers are frequency-locked to the main squeezing laser which in turn can be locked to the GEO 600 laser system. To improve the long-term stability of the squeezing degree, the 532 nm pump beam power is stabilized using a Mach-Zehnder interferometer. Figure 3.24 shows a photograph of the squeezed-light laser as well as a simplified sketch of the experimental layout. A detailed schematic including all optical components is provided in Appendix B.

3. A squeezed-light laser for GEO 600

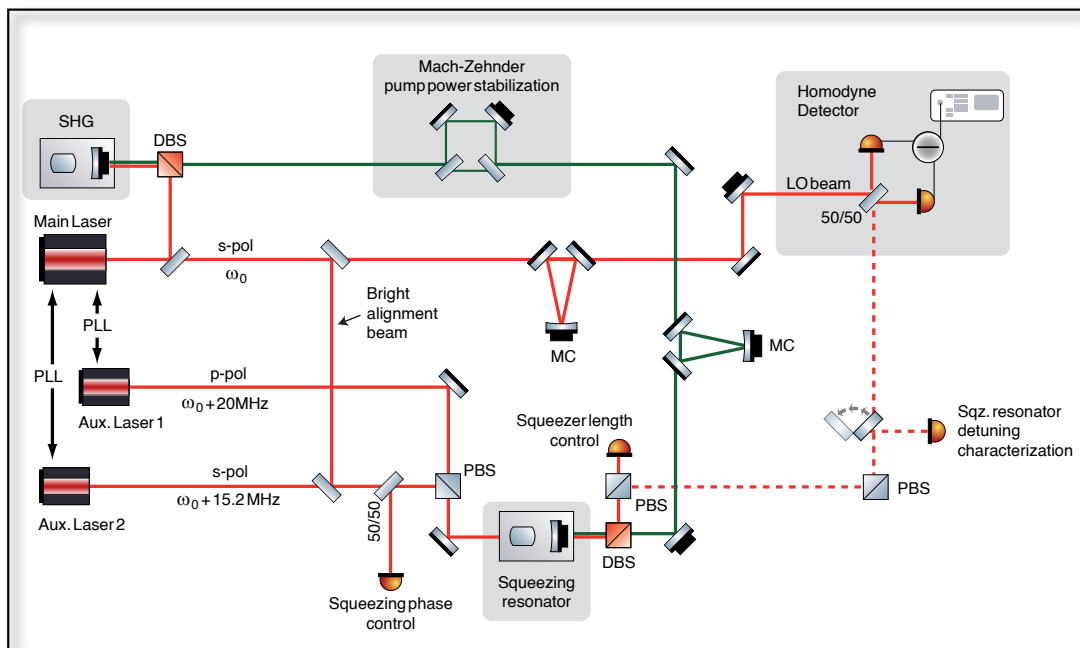
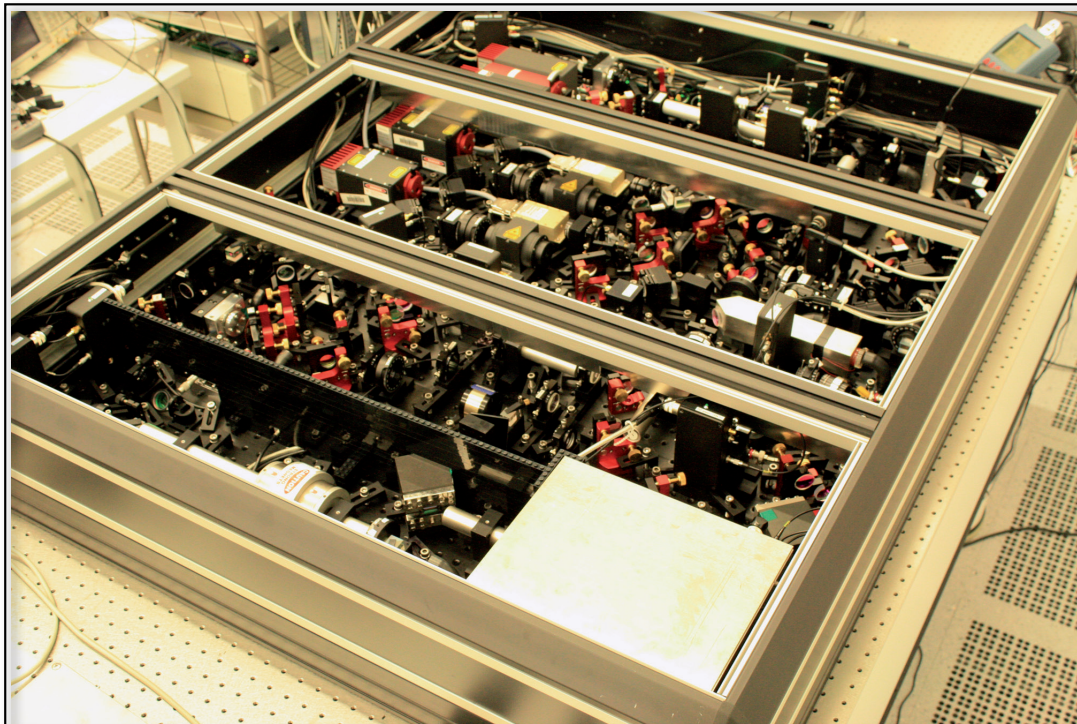


Figure 3.24.: **Top:** Photograph of the GEO 600 squeezed-light laser.
Bottom: Simplified sketch of the experimental layout.

Characterization of the squeezed-light laser

Not later than in the third generation of GW observatories will squeezed-light lasers constitute a standard component to reduce quantum shot noise as well as radiation pressure noise. Before such a component is, however, implemented in the detection scheme, it must be thoroughly characterized to make sure no additional noise is sent to the detector, thereby corrupting the sensitivity instead of improving it. For this purpose, the squeezed-light laser breadboard is equipped with a diagnostic homodyne detector. This chapter discusses the performance of the homodyne detector as well as the squeezing output generated by the squeezed-light laser. Finally, the long-term stability of the system, necessary for permanent GW observatory operations, is presented.

4.1. Performance of the diagnostic homodyne detector

A successful squeezing measurement down to audio frequencies crucially depends on the common-mode rejection ratio (CMRR) of the homodyne detector. A perfect CMRR is equivalent to the maximal suppression of any classical noise inherent to the 1064 nm local oscillator beam. To maximize the CMR ratio, it is necessary to match the photocurrents measured by the individual photo diodes of the homodyne detector. Perfect photo detectors have a quantum efficiency of

$$\text{QE} = \frac{\text{photoelectrons/sec}}{\text{photons/sec}} = 1 \quad (4.1)$$

over the entire detection surface and are thus automatically perfectly matched. In reality, this is not the case since the quantum efficiencies are smaller than unity and differ between photo diodes. Fortunately, it is sufficient to match the photocurrents detected by the two

homodyne photo diodes. To achieve this goal, the local oscillator beam is used, because it is the noise of the LO beam that would by interference mask the squeezing and hence disturb the measurement. Since the power reflectivity and transmittance values of the beam splitter depend on the angle of incidence (AOI), the AOI can be adjusted such that the difference of the two photocurrents equals zero. For the LO beam, such a procedure automatically compensates a possibly non-perfect splitting ratio deviating from the ideal 50/50 value as well as differences in photo detector quantum efficiency. The required changes in the AOI are small (of the order of $\pm 1^\circ$), so that no significant change in the AR-coating reflectivity values and hence no additional loss is introduced. To optimize the balancing procedure, the homodyne beam splitter is mounted on a precision rotation stage which makes μrad AOI adjustments possible.

Another crucial component is an electronic circuit able to amplify the weak homodyne signal without introducing electronic noise even at low audio frequencies. For this purpose, a custom amplifier electronics, which allowed measurements over the entire GW detection band and below, has been designed by H. Vahlbruch.

Furthermore, the fringe visibility at the two photo detectors must be as high as possible to minimize detection loss. After leaving the squeezed-light source, the squeezed beam is guided through mechanically rigid components to minimize any misalignment effects. To optimize the visibility, the alignment of the local oscillator beam can be adjusted. A permanent monitoring of the squeezing degree would additionally require the extension of the present experimental setup by an auto-alignment loop for the local oscillator beam. Such a permanent monitoring, using a 95/5 beam splitter to send a small fraction of the squeezed field to the homodyne detector, was considered in the initial design published in [Vahlbruch-PhD]. While this additional loss would degrade the squeezing value available for injection in GEO 600 by about 2 dB, it would provide merely about 0.2 dB of squeezing for monitoring purposes. This value is, however, too low to allow a reasonable validation of the squeezed-light laser output. A higher BS transmission value would, on the other hand, introduce too much optical loss to the squeezed field to reach the science goal of the experiment. Thus, the permanent monitoring concept was omitted in the experimental setup.

4.1.1. Stray light elimination

One particular topic, the stray light suppression, has not been discussed by now though it was crucial for low-frequency squeezing measurements [Vahlbruch+07]. In fact, the decision to work with super-polished optical surfaces in a cleanroom has proven to be an excellent approach to reduce the stray light problem from the beginning on. Figure 4.1 shows a first measurement which was performed after the experimental setup was completed but before any residual stray light issues were addressed. It revealed a flat (white) quantum noise spectrum down to a frequency of 10–20 Hz. Below this frequency, the measured spectrum showed a monotonic roll-up, reported already in

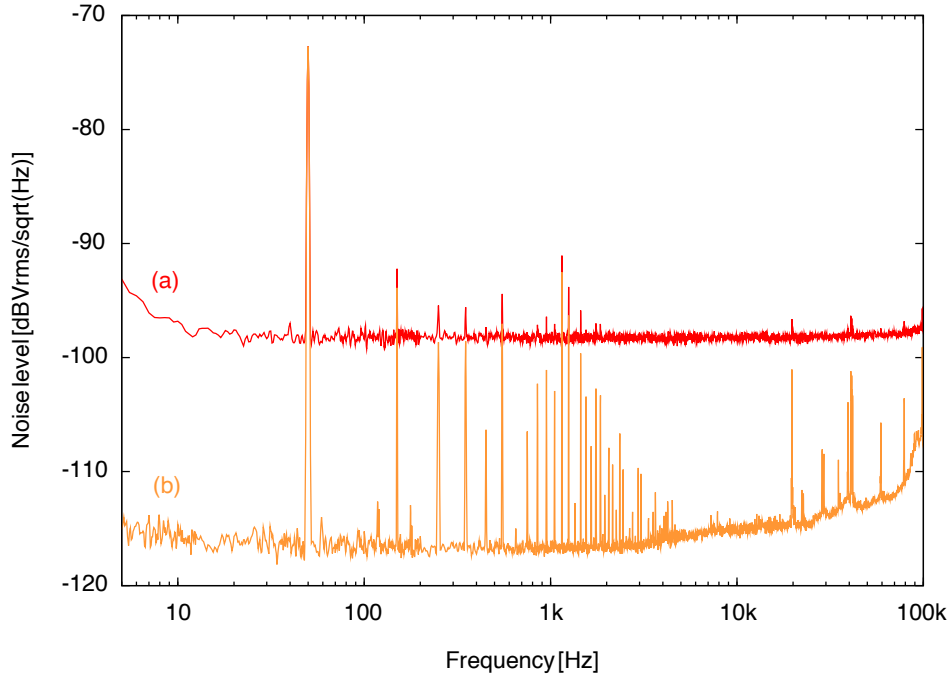


Figure 4.1.: (a) Quantum noise spectrum measured after the experimental assembly was finished and prior to any stray light countermeasures. At frequencies above 20 Hz, the spectrum was flat, below a ‘roll-up effect’ due to parasitic optical interference was observed. The LO power was $570 \mu\text{W}$. The electronic dark noise (trace b) was not subtracted from the measured data, the dark noise clearance was 18 dB in the interval of 10 Hz – 10 kHz. Both traces were pieced together from 9 FFT frequency windows: 5–200 Hz, 200–800 Hz, 800–1600 Hz, 1.6–3.2 kHz, 3.2–6.4 kHz, 6.4–12.8 kHz, 12.8–25.6 kHz, 25.6–51.2 kHz, 51.2–102.4 kHz.

Reference [Vahlbruch-PhD] and identified there to originate from parasitic interference. The electronic dark noise clearance was 18 dB at the frequencies of interest, the shown data were not corrected for dark noise.

Next, the performance at lower audio frequencies was optimized. During the experimental assembly, the following measures have already been taken:

- The experiment was shielded against diffuse stray light originating from the laboratory environment by an opaque case made of black acrylic glass. While this case could be opened for experimental assembly, for the measurement time the lids were closed thereby protecting the experiment not only against stray light but also against air flow turbulences and dust.
- The light power provided by the three laser sources exceeded the required power many times over. Therefore, at various locations throughout the experiment excess

4. Characterization of the squeezed-light laser

light was dumped inside custom-made beam sinks (colored black to maximize the absorption). Those locations were situated as far as possible from the homodyne detector and the squeezed-light source to minimize the stray light input.

- As described in Section 3.3, the conversion efficiency inside the SHG was approximately 50 %. When not properly filtered, 1064 nm photons would co-propagate with the 532 nm pump beam and directly enter the squeezed-light source. A combination of three dichroic beam splitters was used to eliminate any remaining 1064 nm light from the pump beam.
- The lenses used to focus the two beams onto the homodyne detector photo diodes had super-polished surfaces and were tilted by a small angle for additional stray light mitigation. The AR-coating quality was measured by the manufacturer to $R \leq 0.003\%$ for s- and p-polarized light at an AOI of 5° .
- The homodyne detector photo diodes were not equipped with protective windows. Such windows are usually not anti-reflectively coated and thus lead to an increased detection loss as well as to photons back-scattered into the squeezed-light source through the signal port. Additionally, the semiconductor wafer from which the photo diodes have been manufactured was AR-coated for the wavelength of 1064 nm and for an angle of incidence of 20° . Residual scattered photons were thus guided in the direction of the optical breadboard and dumped there by neutral-density (ND) filters.

After the first characterization shown in Figure 4.1, the following steps have been gradually applied until a satisfactory performance of the experiment was achieved.

- The temporary homodyne detector enclosure was replaced by an opaque and light-proof version. This new box is made of aluminium and is equipped with light-proof cable feedthrough possibilities. After all adjustments are finished, the box is closed with a cover plate. Merely two 10 mm holes allow the input of the signal and the local oscillator beams.
- Stray light spots originating from imperfect AR-coatings were identified and dumped using absorptive neutral-density glass filters (ND filters). In the high-power optical paths, ND filters were also placed behind the HR steering mirrors to eliminate residual transmitted light.
- Inside the homodyne detector, the residual AR reflection spots from the photo diodes as well as from all other optics were dumped individually with ND filters. The effect of such action is shown in Figure 4.2. The difference of traces (a) and (b) is due to a single ND filter added to block the residual AR reflection of a homodyne photo diode. A photograph of the final homodyne detector design is shown in Figure 4.3.

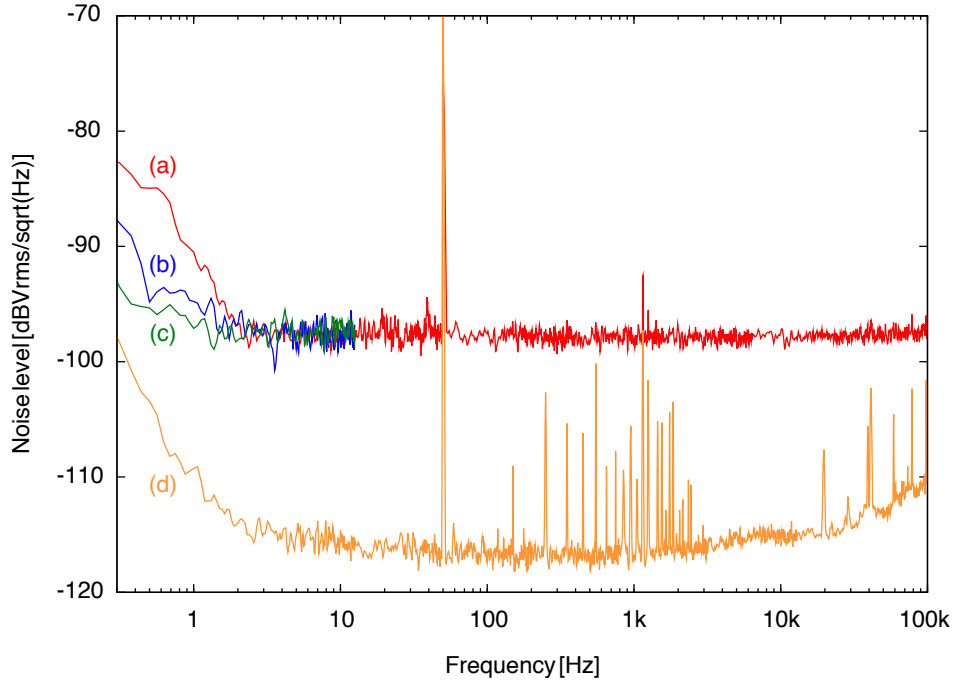


Figure 4.2.: Measurements of the balanced homodyne detector noise performed during stray light optimization. Traces (a–c) show vacuum noise measurements. Trace (a) was recorded with the new opaque homodyne detector enclosure in place, procuring an improvement compared to trace (a) of Fig. 4.1. Both detection ports were open, no squeezing was generated. In trace (b), the residual light reflected by the AR-coated homodyne photo diodes was blocked using an ND filter. When the squeezing port was blocked, a further improvement could be achieved as shown by trace (c). Such behaviour is an indicator that residual stray light is still propagating inside the experimental enclosure and has to be eliminated. The LO power was $570 \mu\text{W}$. The electronic dark noise (d) was not subtracted from the measured data. All traces were pieced together from 7 FFT frequency windows: 0.3–12.5 Hz, 12.5–50 Hz, 50–200 Hz, 200–800 Hz, 0.8–3.2 kHz, 3.2–12.8 kHz, 12.8–102.4 kHz.

- Stray light generation is especially high in the proximity of the lasers. These regions were shielded by several aluminium baffles to separate the individual experiment parts as far as possible.
- The last experimental stage containing the squeezed beam propagating to the homodyne detector was additionally shielded using thin bricks made out of black plastic. A comparison of different colors has proven the black ones to cause the smallest scattering of 1064 nm light. The advantage of such bricks is a high modularity which allows an adaption of the baffles to the experimental layout and thus an incorporation of the existing structures.

4. Characterization of the squeezed-light laser

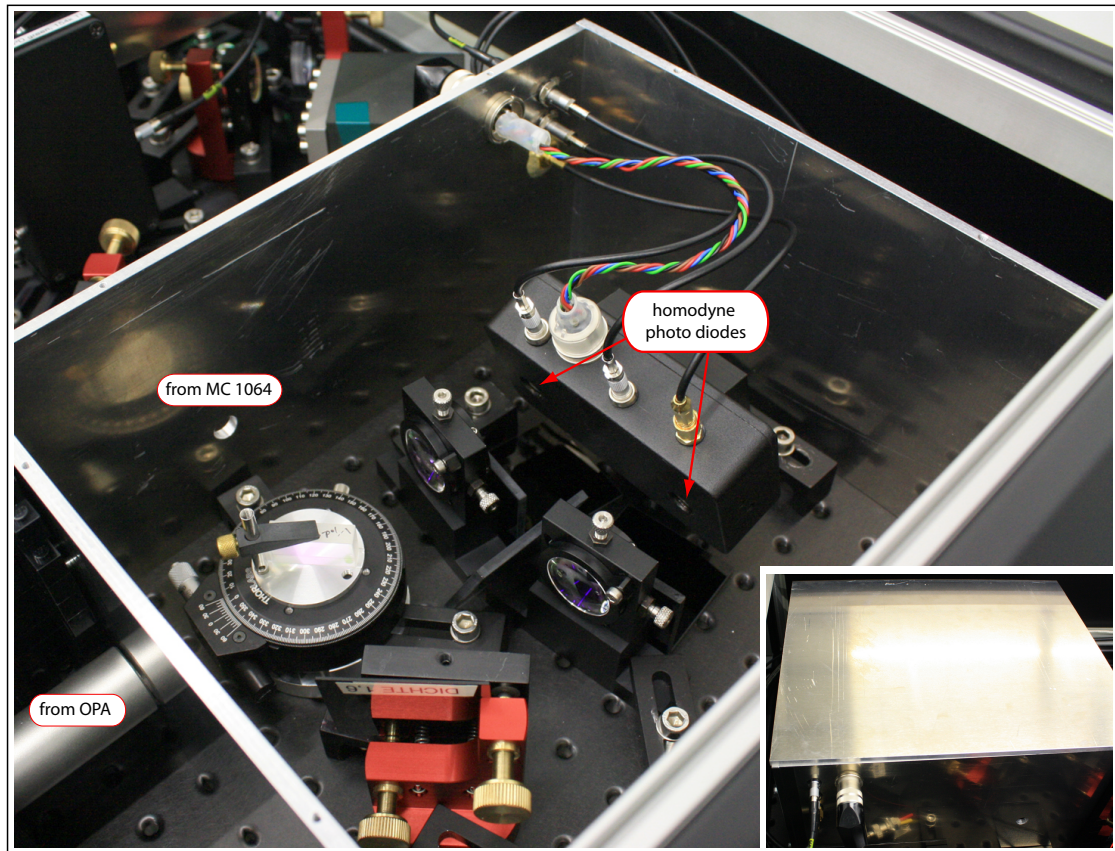


Figure 4.3.: Photograph of the diagnostic homodyne detector. The black case contains two custom-made photo diodes with a quantum efficiency of 99% together with the electronics necessary for photocurrent subtraction. The photo diodes do not possess protective windows while the wafer itself is AR-coated. ND-filters absorb the residual stray light originating from the AR-coated surfaces. The beam splitter is placed on a precision rotation stage to optimize the common-mode rejection. Inset: Closed homodyne detector ready for measurements. Merely two 10 mm holes allow the two beams to enter the detector, for electronic supply and readout light-proof feedthroughs are provided.

- Where possible, free-propagating beams were shielded by aluminium tubes. This impeded stray light entering these beams and hence being injected with them into the squeezing resonator and/or the diagnostic homodyne detector. Additionally, convection was reduced due to the shielding.

These measures allowed the observation of a flat vacuum shot noise spectrum down to frequencies below 1 Hz.

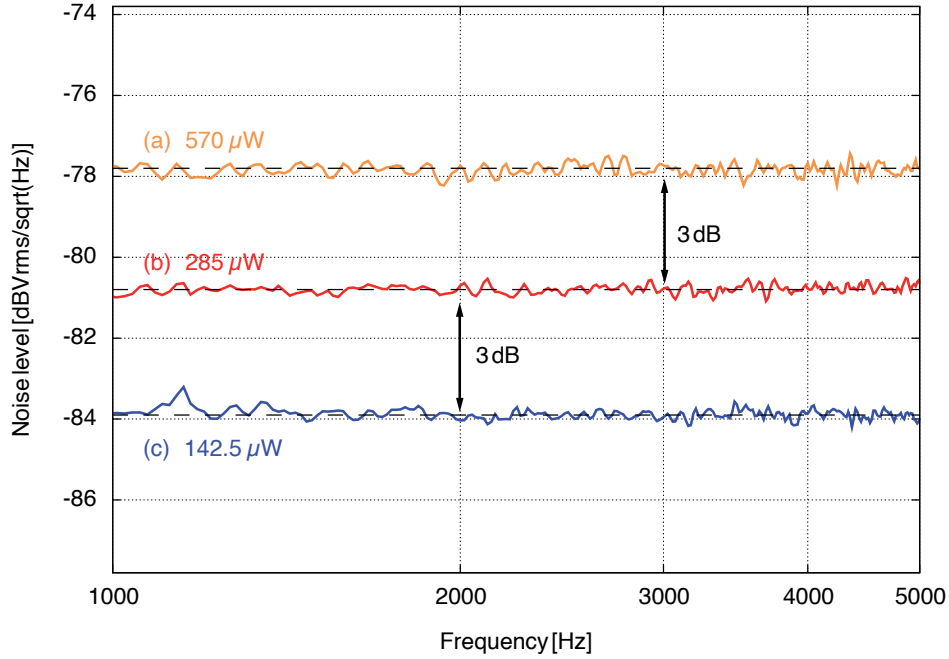


Figure 4.4.: Measurement of the vacuum noise spectra using three different optical powers for the local oscillator beam. The linear behaviour proves that purely quantum noise was detected and no technical noise contaminated the measurement. The electronic dark noise was approximately 12 dB below and thus was not subtracted from the measured data. All traces originate from a single FFT window.

4.1.2. True quantum shot noise measurement

A first measurement necessary for the detection of squeezed light concerns a reference value, namely the shot noise of a pure vacuum state. For this purpose the squeezing input port of the homodyne detector must be blocked, so that merely the noise of a vacuum state is measured. A linear dependence of the measured spectral noise power on the optical local oscillator beam power is, as discussed in Section 2.9, a necessary criterion for a shot-noise-limited measurement. Figure 4.4 shows the spectral noise powers measured by the diagnostic homodyne detector for three different optical LO powers. The corresponding power levels were $570 \mu\text{W}$, $285 \mu\text{W}$, and $143 \mu\text{W}$, respectively. The value of $570 \mu\text{W}$ corresponded to the power of the alignment beam that is used for fringe visibility optimization. As required, the measured noise levels scaled linearly with the LO power confirming the homodyne detector to be limited by quantum noise only and thus suited for further squeezing measurements.

4. Characterization of the squeezed-light laser

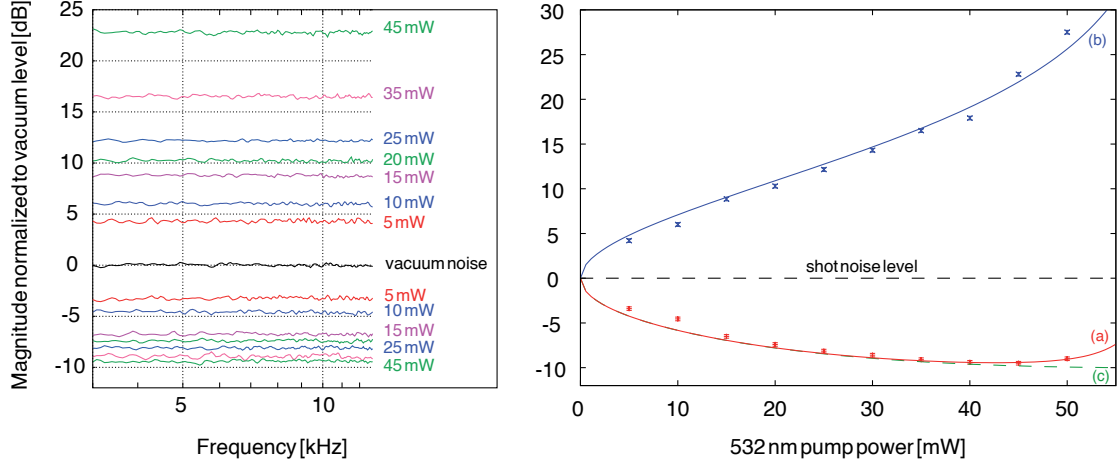


Figure 4.5.: **Left:** Degree of squeezing and anti-squeezing measured with different pump powers. For clarity, only a small frequency range of 3 kHz – 12.8 kHz is shown. **Right:** the blue and red points show the degree of squeezing and anti-squeezing measured at 5 kHz, as shown in the left graph. Traces (b) and (c) show the theoretical prediction of the expected anti-squeezing and squeezing, respectively, taking into account an overall loss of 10.5 %. A threshold power of 61 mW was estimated from the measurement. In trace (a), the model is extended by phase noise of $0.5^\circ \approx 9$ mrad.

4.2. Squeezing the vacuum noise

The results of a first characterization measurement, namely the degree of squeezing and anti-squeezing as a function of the 532 nm pump power, are shown in the left part of Figure 4.5. It is worth noting that very low 532 nm pump powers are sufficient to produce a high degree of squeezing. At a power of 5 mW (corresponding to about 15 mW intra-cavity power), the quantum noise was reduced by more than 3 dB, equivalent to a factor of two in noise power reduction. The degree of squeezing reached a maximal value of 9.5 dB at a pump power of 45 mW. This value is more than an order of magnitude below the pump power levels necessary to reach corresponding squeezing values with similar cavity designs using $\text{MgO}:\text{LiNbO}_3$ as nonlinear medium.

In the right part of Figure 4.5, the measured values (taken at a frequency of 5 kHz) are compared with the theoretical expectations. The degree of squeezing

$$V_{a/s} = 10 \times \log_{10}(R_{a/s}). \quad (4.2)$$

can be calculated using Eq. (3.25) to account for the dependence on the pump power P as well as for the frequency dependence of the squeezing. In the present case, the latter may be omitted since the considered frequencies are much smaller than the cavity linewidth.

Another parameter entering Eq. (4.2) is the optical loss. A rather simple model for a visualization of the mechanism how squeezing is affected by losses can be derived from the reflection at a beam splitter as discussed in Chapter 2. The higher the loss, the higher is also the contribution of the vacuum noise that interferes with the squeezed field and degrades the degree of squeezing. Furthermore, the higher the initial degree of squeezing, the stronger the degradation. The different loss sources during the generation and detection processes are:

- The escape efficiency $\rho = T/(T + L)$ of the squeezed-light resonator. The transmission of the coupling mirror was chosen to a value of $T = 0.08$. The total loss per round-trip, due to the non-perfect AR-coating of the crystal facet as well as to the residual power absorption of the nonlinear crystal, can be estimated to $L \approx 0.04$, thereby resulting in $\rho \approx 0.95$.
- The total propagation loss suffered by the squeezed field on the way from the squeezing resonator to the homodyne detector. The critical components in this path are three polarizing beam splitters as well as a Faraday rotator, while the contribution of the super-polished lenses is negligible. In an independent measurement, the propagation efficiency was estimated to be $\xi \approx 0.98$.
- The fringe visibility \mathcal{V} at the homodyne detector, contributing quadratically, was measured to range between 0.985 and 0.9875.
- The quantum efficiency of the homodyne photo diodes. To minimize this loss, custom-made high-efficiency diodes were used. The diameter of the active area is 500 μm . Equivalent diodes have already been used in high-level squeezing experiments, as e.g. reported in [Vahlbruch-PhD], and have been estimated to have a quantum efficiency of $\eta_{\text{hmd}} > 0.99$.

A consideration of all possible sources results in a total detection efficiency of $\eta_{\text{tot}} \approx 0.895$. This value perfectly corresponds to the measured squeezing and anti-squeezing levels, as shown in Figure 4.5. The deviation at very low pump powers is probably due to a non-perfect calibration of the pump power measurement. The OPO threshold power of $P_{\text{th}} \approx 61 \text{ mW}$ was estimated from the measurements. Please note furthermore that the homodyne detector is merely a diagnostic device which is by-passed when the squeezed-light laser is used in the GEO 600 detection scheme. Hence, the homodyne visibility loss is not relevant for a later operation and has to be corrected for. Since a photo diode from the same manufacturer is used in GEO 600, the detection loss will remain the same. It is nevertheless corrected for at this stage to facilitate a separation of the different experimental stages in a later loss consideration. Thus, a total loss of merely 7% can be deduced. This means that more than 11 dB of squeezing are available for the injection into the dark GEO 600 port when using a considerably high pump power of 45 mW, which also gives approximately 23 dB of anti-squeezing. To keep the latter at a more moderate value, the device may be operated at a pump power of 35 mW, still yielding more than 10 dB of squeezing but only 17 dB of anti-squeezing.

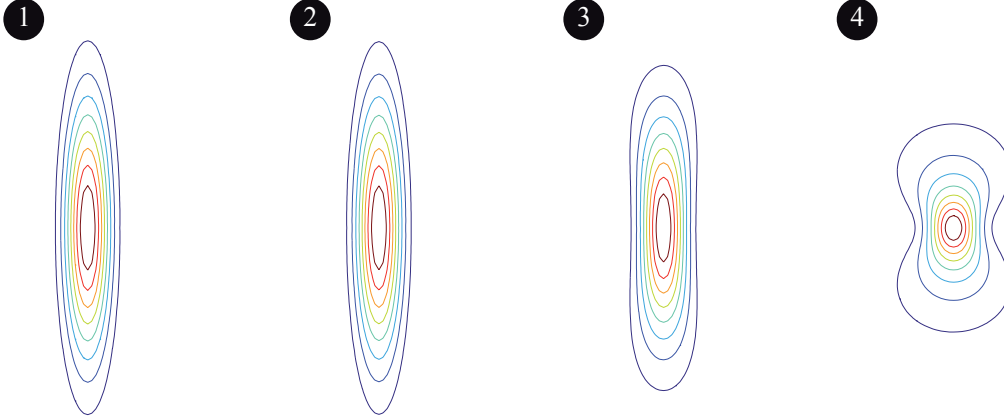


Figure 4.6.: Contour plot of the Wigner function of a lossless 10 dB squeezed state. From (1) to (4), the assumed phase noise increases from 0 via 10 mrad and 100 mrad up to a value of 500 mrad. This jitter leads to an increased projection onto the squeezed quadrature and hence to a decreased squeezing. As discussed in the text, the residual phase noise in our case is of the order of 10 mrad and thereby does not significantly affect the squeezing strength. The calculation was performed with a MATLAB code kindly shared by B. Hage.

So far, we have regarded a perfect system that is only limited by optical loss. In reality, any phase noise of the pump field leads to a jitter of the squeezing ellipse and thereby to a degradation of squeezing as illustrated in Figure 4.6. Although a ring-cavity mode-cleaner is employed to reduce the amount of phase noise (mainly due to the HF modulation fields used for the PDH stabilization loops), the presence of residual phase jitter may not be excluded. As discussed in Reference [Takeno+07], the phase noise effect on the degree of squeezing can be described as

$$R'_{a/s} = R_{a/s} \cos^2(\theta) + R_{s/a} \sin^2(\theta), \quad (4.3)$$

where θ describes the phase jitter. The separate contributions of optical loss and phase jitter can not be definitely identified from the measured spectra, since both mechanisms in the end lead to a very similar effect, namely to a degraded squeezing value. However, the simulation results shown in trace (b) of Figure 4.5 indicate the presence of a residual phase noise with $\theta \lesssim 10$ mrad. Neither the optical loss nor the residual phase jitter do, however, affect the goals formulated for the GEO 600 squeezed-light laser. On the contrary, the goal injection value of 10 dB is even exceeded. In current GW observatories, the different loss sources appearing at various stages of the squeezed light injection (as e.g. non-perfect mode-matching between the detector and the output mode-cleaner (OMC), loss inside the OMC and others) are far more dominant and in the end limit the maximal sensitivity improvement achievable with squeezed light. This case is addressed in the Sections 5.3, 5.5 and 6.1.

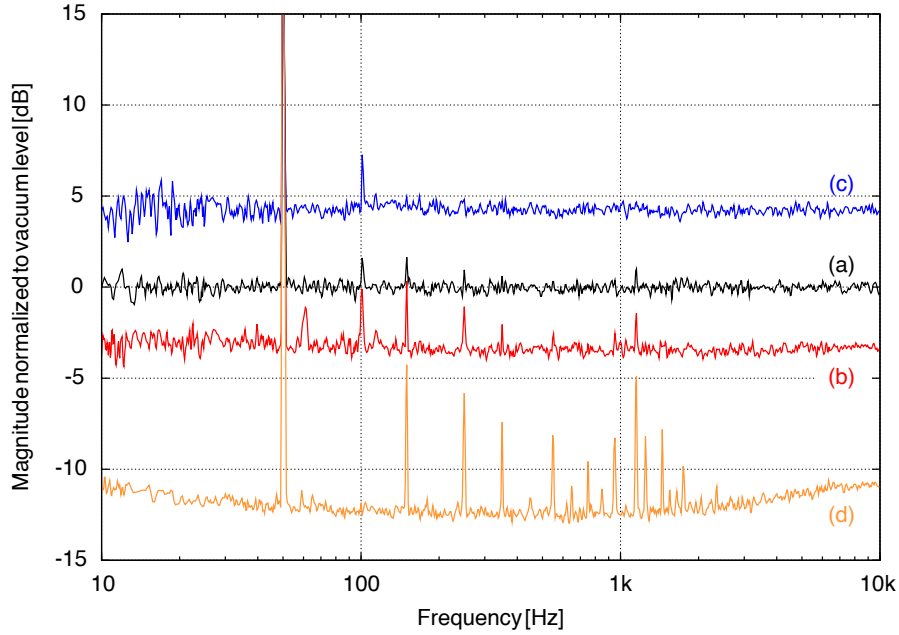


Figure 4.7.: (a) Quantum noise power of a vacuum state, measured with a local oscillator power of $570 \mu\text{W}$. (b) Noise power of a squeezed state generated with an optical pump power of 5 mW and detected at the same LO power as trace a. (c) Corresponding anti-squeezing noise power spectrum. With a non-classical noise reduction of -3.4 dB and a corresponding anti-squeezing value of 4.2 dB , a very pure state is generated at sideband frequencies extending over the entire GW wave detection band. Please note the flat spectra as well as the very low pump power employed. (d) Electronic dark noise, not subtracted from the data. FFT frequency windows: $5 \text{ Hz} - 12.5 \text{ Hz}$, $12.5 \text{ Hz} - 25 \text{ Hz}$, $25 \text{ Hz} - 50 \text{ Hz}$, $50 \text{ Hz} - 100 \text{ Hz}$, $100 \text{ Hz} - 200 \text{ Hz}$, $200 \text{ Hz} - 400 \text{ Hz}$, $400 \text{ Hz} - 800 \text{ Hz}$, $800 \text{ Hz} - 1.6 \text{ kHz}$, $1.6 \text{ kHz} - 3.2 \text{ kHz}$, $3.2 \text{ kHz} - 6.4 \text{ kHz}$, $6.4 \text{ kHz} - 12.8 \text{ kHz}$. Corresponding RBWs: 62.5 mHz , 125 mHz , 250 mHz , 500 mHz , 1 Hz , 2 Hz , 4 Hz , 8 Hz , 16 Hz , 32 Hz , 64 Hz .

4.3. Audio- and subaudio-frequency squeezing

The second requirement for a GW-observatory squeezed-light laser is a flat (white) squeezing spectrum in the entire frequency band of Earth-bound instruments extending from 10 Hz up to 10 kHz . This requirement is in fact the most crucial one and required all the described measures to impede any stray light photons to enter either the squeezed-light source or the homodyne detector. An additional component not necessary to achieve a flat shot noise level but crucial for a flat squeezing is a Faraday isolator placed between the squeezed-light source and the homodyne detector [McKenzie-PhD]. Thereby, any light back-reflected to the OPA was eliminated. The inevitable drawback was that an in-

4. Characterization of the squeezed-light laser

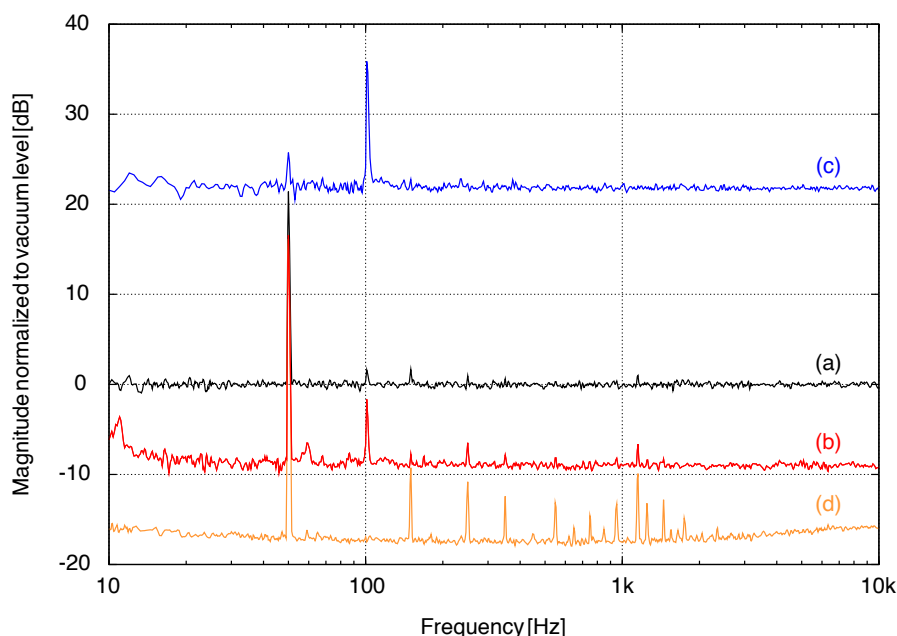


Figure 4.8.: (a) Quantum noise power of a vacuum state, measured with a local oscillator power of $570 \mu\text{W}$. (b) Noise power of a squeezed state generated with an optical pump power of 45 mW and detected at the same LO power as trace (a). The noise level was reduced by up to 9 dB . Please note that this does, however, correspond to more than 11 dB of squeezing exiting the squeezing setup, because in this case the homodyne detector is by-passed and the total optical loss reduces to 7% . The squeezing spectrum is, again, white at audio frequencies. At lower frequencies the performance is slightly constrained by the air-conditioning system of the laboratory. (c) Corresponding anti-squeezing noise power of 23 dB . The structures at 102.5 Hz are due to parasitic electronic pick-up. (d) Electronic dark noise, not subtracted from the data. FFT frequency windows: $12.5 \text{ Hz} - 25 \text{ Hz}$, $25 \text{ Hz} - 50 \text{ Hz}$, $50 \text{ Hz} - 100 \text{ Hz}$, $100 \text{ Hz} - 200 \text{ Hz}$, $200 \text{ Hz} - 400 \text{ Hz}$, $400 \text{ Hz} - 800 \text{ Hz}$, $800 \text{ Hz} - 1.6 \text{ kHz}$, $1.6 \text{ kHz} - 3.2 \text{ kHz}$, $3.2 \text{ kHz} - 6.4 \text{ kHz}$, $6.4 \text{ kHz} - 12.8 \text{ kHz}$. Corresponding RBWs: 125 mHz , 250 mHz , 500 mHz , 1 Hz , 2 Hz , 4 Hz , 8 Hz , 16 Hz , 32 Hz , 64 Hz .

creased isolation also led to a higher optical loss (increased by approximately 1.5%). Figure 4.7 shows the measurement of a very pure squeezed state generated at 5 mW of 532 nm pump power. The squeezing and anti-squeezing levels (of -3.4 dB and 4.2 dB , respectively) are flat over the entire frequency band of interest and even below. The electronic dark noise was not subtracted from the measured data.

Figure 4.8 shows the experimental performance recorded with a pump power of 45 mW . This value corresponds to the maximal squeezing generation and thereby constitutes the maximal pump power at which the squeezed-light source would possibly be operated in

the GEO 600 detection scheme. The generated squeezing and anti-squeezing levels were -9 dB and 23 dB, respectively. The slightly lower squeezing value compared to the results shown in Fig. 4.5 is due to a fringe visibility decrease from 0.985 to 0.978 . Again, white noise levels could be observed over the entire frequency band. We assume the features in the frequency band of 10 Hz – 20 Hz to be due to excess noise generated by the laboratory air conditioning system which was not shut down for the presented measurement. The structure at 102.5 Hz, visible in trace (c) of Figure 4.8, does not originate from the experimental setup and is probably generated through parasitic electronic pick-up from close-by experiments which could not be avoided for all measurements. It will, however, not appear at the GEO 600 detection site. Again, the measured data was not corrected for electronic dark noise. Such a correction would result in a squeezing level of 10 dB but violate the spirit of this thesis in which only directly recorded data without corrective post-processing shall be shown.

The measurements reported in this work characterized the constructed squeezed-light laser to be suitable for GW detection operations. The device allows the generation of pure states with a correspondingly low anti-squeezing value as well as strong squeezing injection exceeding the value of 10 dB. In the noise spectra shown, merely the frequency band of Earth-bound GW detectors (10 Hz – 10 kHz) was considered. Though the GEO 600 squeezed-light source is also capable of generating significant squeezing below the lower limit of 10 Hz (and even below 1 Hz), those results are of no relevance for the work in hand. For the first and second generation of GW observatories, the sensitivity at those frequencies will not be dominated by quantum noise, so that no additional reduction will be possible with squeezed light injection. It is, however, worth mentioning that even the third generation observatories which will probably be limited by quantum noise at frequencies below 10 Hz (e.g. about 5 Hz in case of the Einstein Telescope design sensitivity), can already today count on quantum noise reduction techniques available over their entire detection frequency band. Squeezing will thus most likely constitute a key technology to reach the envisioned detection sensitivity values as discussed in Section 6.1.

4.4. Remote control of the squeezed-light laser

A routine operation of the squeezed-light source as part of a gravitational wave observatory requires an automated control of the squeezed-light laser. To maximize the experimental compatibility with the existing GEO 600 control scheme, the automation is implemented using the LIGO Control and Data System (CDS) [LIGO-CDS] incorporating the Experimental Physics and Industrial Control System (EPICS) [EPICS]. Though the core GEO 600 slow digital control is implemented in LabView, recently added systems as e.g. the output mode-cleaner are controlled using EPICS and LIGO CDS. Up to now, the squeezed-light laser is controlled by a separate system, as described below. The two systems can, however, be joined together if need arises.

4. Characterization of the squeezed-light laser

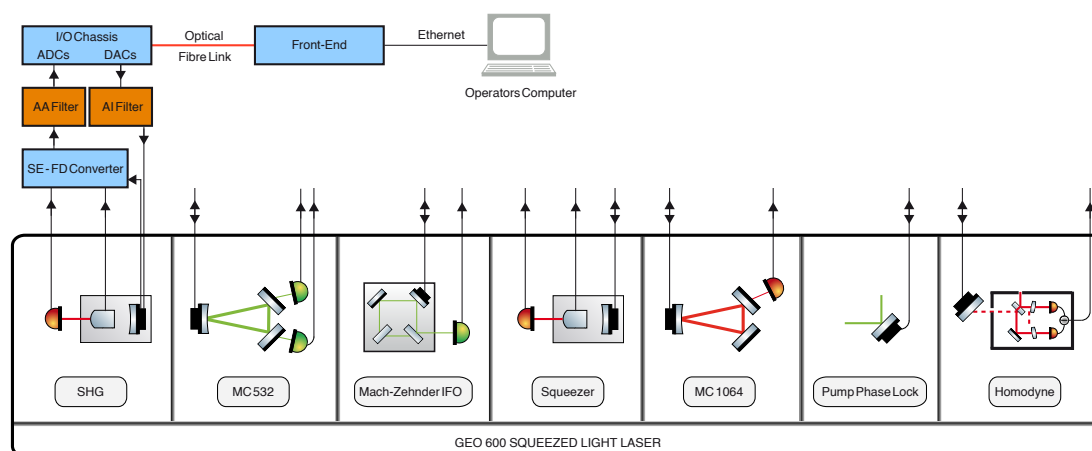


Figure 4.9.: Schematic of the interface between the squeezed-light laser and the digital control system, exemplified at the SHG (left hand side). All other locking loops are likewise digitally interfaced as illustrated by the open connection ports. FD: fully differential, SE: single ended, AA: anti-aliasing, AI: anti-imaging, ADC: analog-to-digital converter, DAC: digital-to-analog converter, I/O: input/output.

4.4.1. Connecting the experiment to the CDS

The following section offers a very brief description of the implemented infrastructure and of the locking procedures. A more detailed discussion as well as the underlying Python code are provided in [Lastzka-PhD], the hardware implementation will be described in details in the PhD thesis of Christian Gräf. Basically, the electronic control of the experiment is still performed with the analog electronics discussed throughout Chapter 3, while the lock (re)acquisition and set point control is executed by the CDS. Therefore, all experimental channels necessary for control purposes are interfaced with the CDS via the EPICS system. A general scheme is shown in Figure 4.9, taking the length control loop of the SHG as a concrete example. The single-ended error signal provided at the output of PD_{SHG} is converted to a fully-differential (FD) signal to reduce electronic pick-up. This error signal is still used by the SHG servo described before for cavity length stabilization. Additionally, its copy is monitored by the CDS, while the lock acquisition itself is realized by monitoring the DC power level of PD_{SHG} . To remove aliasing artefacts, LIGO-design AA filters [LIGO-Fil01, LIGO-Fil02] are used.

The digitization is performed by an analog-to-digital converter (ADC, 32 channel 16-bit PCI-X card [General Standards Corporation]). The ADC/DAC cards are housed in an *I/O chassis*. In the digital data acquisition, every mV of an input signal corresponds to 3 count units, later on simply referred to as *counts*. The PCI-X bus of the I/O chassis is connected to a *front-end computer* via a fiber link. Inside the front-end, all the main operations are performed. It runs the real-time system and can, however not in the

present case, contain digital filters for a fully or partially digital control. Please note that currently only control bandwidths up to about 1 kHz are available, this value may, however, be extended by about an order of magnitude in the future. Another important part is the *frame builder* that permanently stores the data to a hard disk and also allows an access of the stored data via Ethernet. The front-end is finally connected to a separate operator's computer, the experiment is controlled via a graphical user interface (GUI).

Turning again to the SHG example, the filtered and digitized DC power level is monitored by the control system. When a lock is requested via the GUI, a triangular ramp signal is generated digitally and applied to the HV amplifier of the SHG PZT. As soon as the resonance is approached and a certain threshold value of the optical power recorded by PD_{SHG} is exceeded, the corresponding voltage value is held and the lock sequence begins. The loop is closed by means of a trigger signal applied to the servo via the I/O chassis and an AI filter. From then on, the control is executed in the traditional way by the analog electronics whose output voltage is added to the voltage generated by the CDS. The DC power level is monitored constantly with a bandwidth of 256 Hz. In case of lock-loss, an automatic re-lock is performed.

An overview over all implemented input channels is shown in Table 4.1. The data acquisition frequency determined by the hardware used is currently 2^{16} Hz = 65536 kHz. At the input port, the data rate is reduced by a factor of two using software-implemented down-sampling. The resulting value of 32768 kHz is, however, used only for the squeezing value monitoring channel, while all other channels are further down-sampled to 256 Hz. This frequency is sufficient for monitoring and lock purposes, while the amount of recorded data is reduced.

The other three cavities are stabilized with control loops similar to the one for the SHG. The same is true for the Mach-Zehnder interferometer: A triangular ramp applied to its PZT generates a sinusoidal signal at the corresponding photo detector which is used as an error signal. An electronic offset, added by additional analog electronics, allows the adjustment of the optical power level in transmission of the interferometer. The operation levels were determined in an independent calibration. A photo detector signal of 700 mV, corresponding to 2930 counts of the CDS, constitutes the normal operation state with 35 mW power at 532 nm.

For pump phase and homodyne angle stabilization, no sophisticated routine is required. When the remaining systems are locked and the sinusoidal error signals are generated, it is sufficient to remotely activate the lock switch of the servo along with the corresponding integrators. The error signal level is monitored by a separate control loop, so that a re-lock procedure is initiated in case of lock-loss.

More input channels are provided for data acquisition and monitoring purposes. First, the lock status of all three phase-locked loops is monitored. This information is provided by the diagnostic port of the PLL controller itself. A remote re-lock is not possible, the information is merely recorded for duty-cycle calculation and for data quality flags.

4. Characterization of the squeezed-light laser

Another channel, also usable for data quality flag purposes, records the lock status of the entire experiment. Finally, the homodyne detector output is also recorded, constituting the only high-bandwidth channel.

The output channels are summarized in Table 4.2. For every subsystem, three electronic switches are available. Additionally, a triangular ramp signal to approach the operating points of the cavities is provided. It is applied to the HV amplifiers as described above. In case of the sinusoidal error signals, again a HV input is provided to bring the subsystems into a well-defined mid-fringe initial state after every lock-loss.

Subsystem	Channel	Employment	Sampling freq. [Hz]
SHG	PD DC Level	Control	256
	Error Signal	Monitoring	256
	PZT HV Level	Monitoring	256
Squeezing resonator	PD DC Level	Control	256
	Error Signal	Monitoring	256
	PZT HV Level	Monitoring	256
MC ₅₃₂	PD DC Level	Control	256
	Error Signal	Monitoring	256
	PZT HV Level	Monitoring	256
MC ₁₀₆₄	PD DC Level	Control	256
	Error Signal	Monitoring	256
	PZT HV Level	Monitoring	256
Mach-Zehnder	PD DC Level	Control	256
	Error Signal	Monitoring	256
	PZT HV Level	Monitoring	256
Pump beam phase	PD DC Level	Monitoring	256
	Error Signal	Control	256
	PZT HV Level	Monitoring	256
Homodyne detector	Error Signal	Control	256
	PZT HV Level	Monitoring	256
	Squeezing Level	Monitoring	32768 ¹
GEO PLL	PLL status	Monitoring	256
Length control PLL	PLL status	Monitoring	256
Squeezing control PLL	PLL status	Monitoring	256
Total experiment	Lock status	Monitoring	256

¹ The effective bandwidth is about 10 kHz due to the 4th order low-pass filter in the AA filter electronics.

Table 4.1.: Overview over all input channels implemented in the digital control system.

Subsystem	Channel	Type
SHG	Lock	Switch
	Integrator 1	Switch
	Integrator 2	Switch
	Ramp (frequency: 0.5 Hz)	Triangular
Squeezing resonator	Lock	Switch
	Integrator 1	Switch
	Integrator 2	Switch
	Ramp (frequency: 1 Hz)	Triangular
MC ₅₃₂	Lock	Switch
	Integrator 1	Switch
	Integrator 2	Switch
	Ramp (frequency: 0.2 Hz)	Triangular
MC ₁₀₆₄	Lock	Switch
	Integrator 1	Switch
	Integrator 2	Switch
	Ramp (frequency: 1 Hz)	Triangular
Mach-Zehnder	Lock	Switch
	Integrator 1	Switch
	Integrator 2	Switch
	HV Input	Level Reset
Pump beam phase	Lock	Switch
	Integrator 1	Switch
	Integrator 2	Switch
	HV Input	Level Reset
Homodyne detector	Lock	Switch
	Integrator 1	Switch
	Integrator 2	Switch
	HV Input	Level Reset

Table 4.2.: Overview over all output channels implemented in the digital control system. The bandwidth of every channel is 32768 Hz.

4.4.2. Control automation

In a last step, the lock acquisition and re-acquisition of the entire experiment was completely automated for permanent operation. The following sequence has been implemented.

1. Main GEO 600 laser PLL status check
2. Squeezing angle control laser PLL status check
3. Squeezing resonator cavity length control laser PLL status check
4. Squeezing resonator cavity length stabilization
5. SHG cavity length stabilization
6. MC₅₃₂ cavity length stabilization
7. Mach-Zehnder interferometer length stabilization
8. Stabilization of the squeezing ellipse angle
9. MC₁₀₆₄ cavity length stabilization
10. Stabilization of the homodyne detection angle

The goal of the chosen sequence was to maximize the duty cycle of the experiment. In the case of lock-loss of a certain component, all subsystems depending on the responsible one automatically unlocked. Thereafter the sequential locking scheme is executed starting with the subsystem that had lost lock in the first place. Since the squeezing resonator has demonstrated a particularly stable lock performance, it is situated at the beginning of the sequence right after the PLL status check. The homodyne angle lock is, on the other hand, the most sensitive subsystem. In contrast to the squeezing angle stabilization, where a high dynamic range is available through a large PZT, the phase shifter device of the homodyne loop offers only a small dynamic range. In the AEI cleanroom, this led to an average operation time of 60–90 minutes, after which a re-lock was required. At the GEO 600 detector site, on the other hand, much longer operation times were achieved as described below. Please note that this loop in any case does not constrain the performance of the GEO 600 squeezed-light laser since the homodyne detector constitutes merely an additional diagnostic component which is disabled during operation in the GW observatory. Therefore, no additional optimization was performed. The re-lock times of the different subsystems are provided in Table 4.3. In the case of a total loss of lock, the squeezing output is restored within 14 seconds. This value can, if desired, be reduced, since up to now a soft re-lock with considerably long DC-level check times after the lock of each subsystem is implemented. The digitally controlled system reached a very high total duty cycle of $> 99\%$.

When GEO 600 is operated in science mode, the duty cycle is of the order of 90% [Grote+10] with typical lock durations ranging from several hours up to 40–60 hours, being larger than for the squeezed-light laser. This difference should, however, not significantly affect the duty cycle of a squeezed-input GEO 600. In the case of lock-loss

Subsystem	Lock (re-)acquisition time
Squeezing resonator	14 s
SHG	12 s
MC ₅₃₂	10 s
Mach-Zehnder	8 s
Squeezing phase lock	6 s
MC ₁₀₆₄	4 s
Homodyne detection angle	2 s

Table 4.3.: Re-lock times of the different subsystems, defined by the order of the automated locking sequence. These values were chosen for a soft re-lock and can, if necessary, be reduced even further.

the squeezing beam input path will be automatically blocked, thereby ensuring that the detector sensitivity is not degraded due to anti-squeezing input. Hence, the detection sensitivity will be improved by squeezing most of the time and be equal to the classical sensitivity when the squeezed-light laser is not locked. A lock-loss of GEO 600, on the other hand, may also lead to a lock-loss of the squeezed-light source. Because the lock acquisition time of the latter is with max. 15 seconds much shorter than the approximately 10 minutes of GEO 600, no additional performance degradation is expected.

4.5. Long-term stability

To validate the long-term performance of the experiment, the recorded homodyne detector output can be analyzed employing an FFT script described in detail in Reference [Lastzka-PhD]. The upper part of Fig. 4.10 shows the long-term behaviour of the squeezed-light source observed during characterization at the GEO 600 detector site. The spectrogram provides the squeezing strength in dependence of the Fourier frequency and time. The time resolution was chosen to be 15 min. Not shown in the plot is the dark noise of the converter card which was more than 15 dB below the dark noise of the homodyne amplifier electronics.

For this measurement, the main squeezing laser was phase-locked to the GEO 600 laser. The squeezed-light source was operated with a 532 nm pump power of 35 mW, resulting in a measured squeezing value of up to 9.3 dB. A histogram analysis of the measurement is shown in the lower part of Fig. 4.10. Such operation conditions on average correspond to a squeezing value of 10.5 dB available for the injection into GEO 600. The longest quasi-continuous squeezing observation extended over 20 hours, the test run was terminated by maintenance work at GEO 600. The longest total lock of the squeezed-light laser extended over 8.5 hours, the overall duty cycle exceeded the value of 99.9% .

4. Characterization of the squeezed-light laser

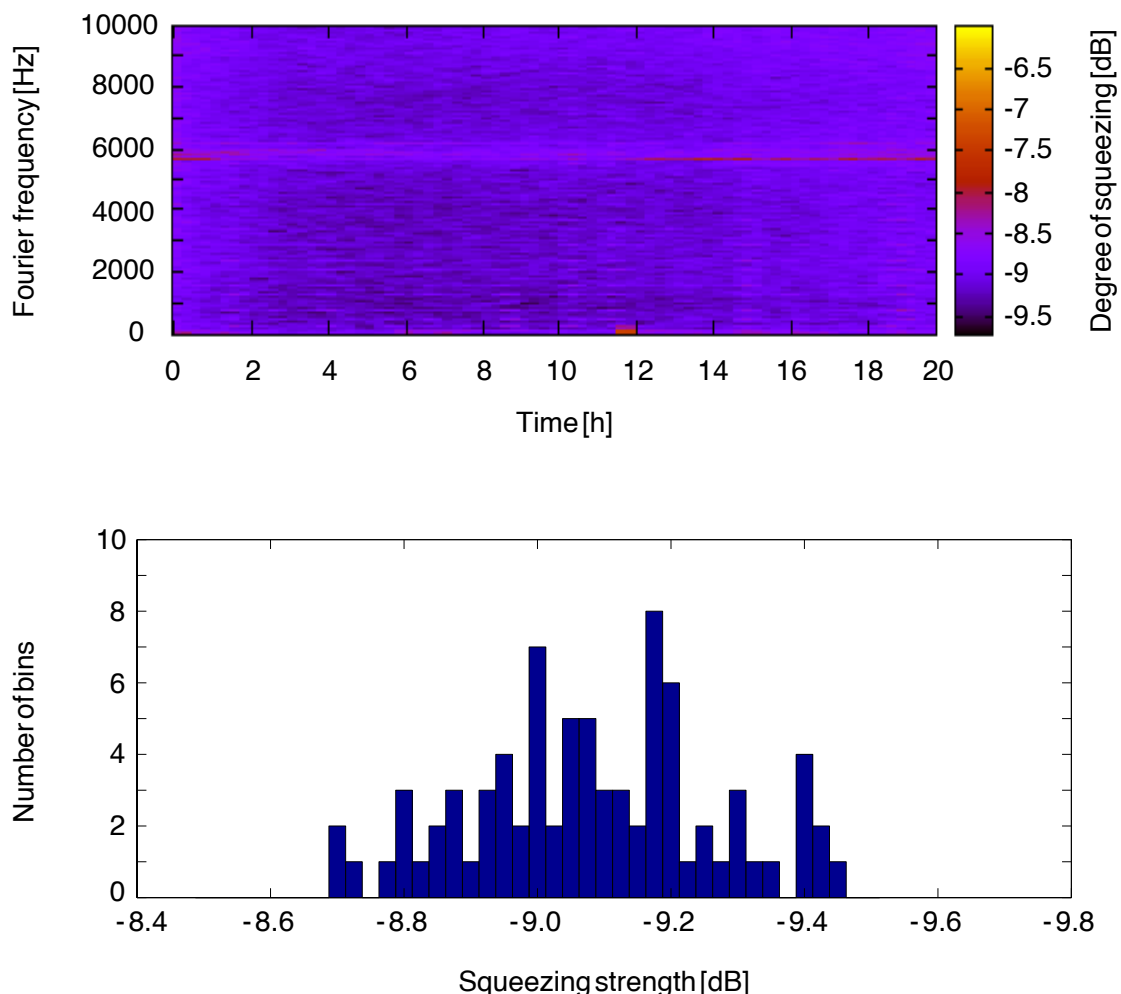


Figure 4.10.: **Top:** Squeezing spectrogram generated by the *dump_spectra.py* Python script developed by N. Lastzka [Lastzka-PhD]. The time resolution is 15 minutes, each time bin was generated by the application of an FFT to a 60 sec long dataset. The data were recorded continuously at the output of the homodyne detector through a fast CDS channel. The duty cycle of the squeezed-light laser for this long-term characterization exceeded 99.9%, merely 8 lock-losses were observed over 20 hours. They are "hidden" randomly in the spectrogram since the analyzed data segments are equidistant and no particular starting time was selected. The longest continuous lock lasted over 8.5 hours. The lower squeezing value around 6 kHz originates from electronic pick-up at the GEO 600 detector site.

Bottom: Histogram analysis of the data shown above. The frequency of 3 kHz was arbitrarily chosen from the frequency band where the observatory noise is dominated by quantum shot noise.

4.5.1. Future CDS work

Up to now, the goal of the digital experimental control was to substitute an operator and thus to enable a stable long-term operation without the requirement for a manual re-lock. Therefore, digital control was implemented only where it was crucially necessary for locking loop automation. There are, however, other components and applications that will benefit from a remote access in the near future:

- The nonlinear crystal temperature of SHG and squeezed-light source is controlled via an entirely analog device. A monitor channel can be implemented to read out the resistance value of a second NTC thermistor placed in the oven for monitoring purposes. Furthermore, it is convenient to substitute the current temperature controller by a fully digital loop. Since a high control bandwidth is not required, this can be implemented without any obstacles. In the case of the squeezed-light source, a digital crystal temperature control offers the major advantage of enabling to maintain an optimal resonance condition for both polarizations, thereby maximizing the degree of squeezing. As a monitor channel for the squeezing quality, a copy of the GEO 600 $h(t)$ signal can be employed.
- For long-term operations, an auto-alignment of the squeezed beam into the GEO 600 interferometer must be implemented, as is discussed in Section 5.5.
- In the case of lock-loss of the squeezing phase orientation, the quadrature that is injected into the dark port is no longer well-defined. Such a noisy state will, with a high probability, disturb the detector performance and in the worst case lead to a lock-loss of the entire observatory. This can be avoided if the squeezing input port is blocked automatically as soon as a lock-loss is detected. Additionally, data quality flags can be created marking the time intervals when the system operated without squeezed input as well as the times of lock-loss and lock re-acquisition with a possibly disturbed performance.
- If desired, the diagnostic homodyne detector can be accessed remotely. Such a loop would allow a direct monitoring of the squeezing strength at any time. It would, however, require experimental modifications:
 - The $\lambda/2$ -waveplate leading the squeezed beam either to the homodyne detector or to the output port must be replaced by a motorized one.
 - A remote optimization of the homodyne visibility is required, therefore two steering mirrors have to be replaced by mirrors attached to motorized mounts.
 - Automatic control is also required for the shutter of the bright alignment beam, the implementation of another automated shutter in the 532 nm pump beam is furthermore advisable for safety reasons.

In the intermediate and far future, a fully digital control scheme of the entire experiment may be implemented. It does, at the current stage, however not offer significant advantages since an analog control scheme is already in place and functioning satisfactorily.

4.6. Conclusion

Summarizing the descriptions given above, the GEO 600 squeezed-light laser constitutes the prototype of a compact, transportable, fully automated and long-term stable audio-frequency squeezed-light source. With a total size of only 1.5 m^2 the setup is suitable for experiments with restricted spatial conditions. The area may be reduced even further, if necessary, e. g. applying even more compact setup procedures such as optical bonding of the components or separating the laser and the squeezing stages.

The key feature of the reported squeezed-light source is the high long-term stability along with a high squeezing value. At the nominal operation conditions for a long-term employment in the GW observatory, 9 dB of squeezing, corresponding to 10.5 dB directed to GEO 600, could be observed over up to 20 hours. The longest total lock of the entire system extended over 8.5 hours. Due to the GEO-HF upgrade program and to the works conducted at the detector site, no undisturbed extended long-term characterization of the system could be performed. A permanent observatory operation with squeezing input after the end of the GEO-HF upgrade will allow deducing the stability of the generated squeezing degree on a timescale of weeks or months. The results reported in this Chapter let us, however, expect that the performance of the squeezed-light laser will not significantly affect the duty cycle of GEO 600, while more than 10 dB of squeezing will be available for injection over most of the time. These results furthermore do, to the best of our knowledge, set a new benchmark for the longest continuous operation of a squeezed-light source along with the highest degree of squeezing reported at audio- and subaudio frequencies.

Squeezing the GEO 600 quantum noise

GEO 600 is one of the world's most sensitive optical measurement devices that during the last decade has been permanently developed and improved to reach the current performance. In the course of the GEO-HF upgrade [Willke+06, Lück+10], several additional modifications have been or are still to be implemented. One of them was the integration of squeezed light. In principle, the squeezing injection constitutes a completely independent upgrade. However, some of the changes performed during the GEO-HF upgrade (like the installation of an output mode-cleaner or the switch to a new readout scheme) do have a beneficial effect on the squeezed-input GEO 600. Therefore, this chapter presents a short description of the initial optical GEO 600 layout and of the changes during the GEO-HF program that are related to the squeezed-light laser. Thereupon, the integration of the squeezing into the GEO detection scheme is discussed and the results achieved are presented.

5.1. GEO 600 in a nutshell

GEO 600 is a Michelson-type laser interferometer with a physical arm length of about 600 m each. A simplified schematic of the GEO 600 optical layout is shown in Fig. 5.1. Detailed descriptions and discussions of subsystems, which are briefly summarized in this Chapter, are provided by [Willke+02, Winkler+07, Grote+08, Grote+11] and the references given therein. The input laser field at the wavelength of 1064 nm is generated by an injection-locked laser-diode-pumped Nd:YAG master-slave system. Therein, the 800 mW output power of the NPRO master laser is amplified in a four-mirror slave ring cavity to a value of maximal 12 W. The laser output is subsequently filtered by two ring mode-cleaner resonators with suspended optics (having a finesse of 2700 and 1900, respectively) in order to reduce the amount of spatial fluctuations and thereafter injected into the interferometer. In contrast to the LIGO and Virgo detectors, GEO 600 does not

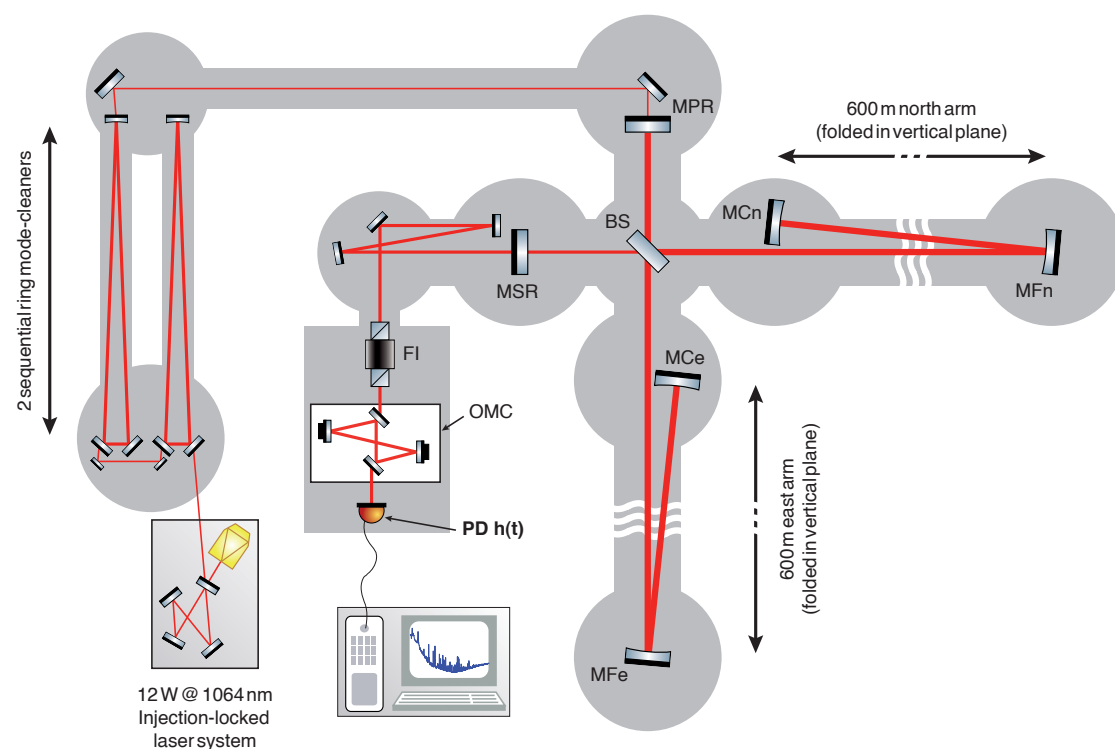


Figure 5.1.: Simplified optical layout of GEO 600 without squeezed light injection. A detailed discussion is given in the text. BS: beam splitter, FI: Faraday isolator, MPR: power-recycling mirror, MSR: signal-recycling mirror, MFe/MFn: far interferometer steering mirrors (east/north arm), MCe/MCn: near interferometer end mirrors (east/north), OMC output mode-cleaner, PD $h(t)$: photo detector for interferometer signal measurement. Please note: The near mirrors in the drawing are shown displaced in the horizontal plane for a clearer illustration.

possess Fabry-Perot arm cavities. The interferometer arms are, however, folded once in the vertical plane to achieve an optical arm length of approximately 1200 m. Selected interferometer parameters are summarized in Table 5.1. All main interferometer optics are suspended from triple cascaded pendulums in a vacuum in the upper 10^{-9} mbar region. The last, quasi-monolithic suspension stage furthermore minimizes thermal noise contributions in the suspensions.

The operation point of GEO 600 is, like for the other GW detectors, close to the so-called *dark fringe*, being the state where due to destructive interference at the beam splitter the optical power at the signal port of the interferometer is minimal. Due to energy conservation, almost the entire incident light is back-reflected by the interferometer which acts as a compound mirror. This fact makes it possible to resonantly increase the circulating optical power by placing a mirror between the input mode-cleaners and

the interferometer beam splitter. This so-called *power-recycling mirror* (MPR) has a power reflectivity of 99.91% and leads to a power buildup factor of about 1000. The increased power leads to an improved detector sensitivity at frequencies where shot noise is the limiting factor. During the measurements reported in this thesis, the output of the master-slave laser system was chosen such that the optical power at the beam splitter was 2.7 kW. Another mirror with a power reflectivity of 98.1% is employed to enhance the gravitational wave signal output of the interferometer. In analogy to the MPR it is called *signal-recycling mirror* (MSR).

It is worth noting that the length of the *signal-recycling cavity* (SRC) formed by the interferometer end mirrors and the MSR can, during operations, be deliberately changed, thereby introducing a detuning from carrier resonance. Such a detuning makes it possible to shape the response function of the detector and thus to increase the sensitivity at certain frequencies at the expense of deterioration in the remaining frequency band. For the LSC S5 science run, a detuning value of 550 Hz was employed throughout the run, leading to a GEO 600 peak sensitivity centered around this frequency [Grote+08]. A detuned operation, however, also has several disadvantages [Hild+07]. With regard to the squeezing input, it introduces a frequency dependence for the phase of the upper and lower sidebands of the squeezed field, thereby leading to a frequency-dependent orientation of the squeezing ellipse inside the interferometer. To allow a broadband sensitivity improvement of a GW detector by squeezed light, an additional optical resonator that counter-rotates the squeezing ellipse appropriately would be required. This so-called *filter cavity* needs to have the same resonator parameters as the signal-recycled interferometer and a detuning in the opposite direction. While an implementation of frequency-dependent squeezed light is theoretically possible [Harms+03, Schnabel+04, Chelkowski+05], the addition of a filter cavity to the optical GEO 600 layout is not feasible in the course of the GEO-HF upgrade. Therefore, as well as to get rid of other disadvantages, the squeezed-input GEO-HF is operated with a SRC tuned to resonance. The bandwidth of the SRC is 220 Hz. A quantitative analysis of the frequency-dependent loss introduced to the squeezed field by the SRC is provided in Section 5.3. In the course of the GEO-HF upgrade, a reduction of the MSR reflectivity from 98.1% down to 90% is planned. As discussed in [Lück+10], this will allow to increase the interferometer sensitivity at shot-noise limited frequencies by up to a factor of 2, while the sensitivity at frequencies below 800 Hz (dominated by thermal noise) will be affected only marginally.

In the initial design, heterodyne readout was used for GEO 600. This means that RF sidebands modulated onto the input laser beam at 14.9 MHz serve as local oscillator for the gravitational wave signal at the $h(t)$ photo detector [Schnupp88]. Experimental experience has, however, shown a series of problems, which are discussed in detail in [Hild+09], to arise from heterodyne readout. A more convenient alternative is offered by the so-called *DC-readout* which is a special case of a homodyne readout scheme. Due to a slight dark fringe offset, a fraction of the carrier light leaves the interferometer at the dark port, is transmitted by the MSR and serves as a local oscillator. With regard to the

squeezing, this scheme offers two main advantages. First, for tuned signal-recycling the overall detected shot noise decreases and therefore the sensitivity at shot-noise-limited frequencies increases by a factor between $\sqrt{1.5}$ and $\sqrt{2}$ [Hild+09]. Second, the squeezing has to be generated only in the GW detection frequency band and not also at twice the RF modulation frequency [Chickarmane+98]. This would be the case for heterodyne readout in order to avoid an effective loss of 50%.

In theory, only light in the TEM_{00} mode should exit the interferometer at the MSR. However, thermal lensing effects at the beam splitter (resulting from the optical power absorbed inside the substrate) as well as unequal radii of curvature of the interferometer mirrors reduce the interferometer contrast below the theoretically achievable value of unity. Though these effects are addressed and partially compensated for by dedicated compensation systems, the field exiting the interferometer through the signal port contains mainly higher-order spatial modes (with approximately 6–7 mW out of about 40 mW in the TEM_{00} mode). This light does not contain any signal information accessible by the readout scheme, but may lead to an increased shot noise contribution. For DC-readout, where a dominant TEM_{00} mode content is needed, additional modifications to the used modulation indices and to the operation point of the interferometer are required. To fully benefit from the new readout scheme, an output mode-cleaner (OMC) was included into the optical layout during the GEO-HF upgrade [Degallaix+09]. It is constructed as a four-mirror cavity with a finesse of about 150 and a FWHM of ca. 3 MHz. The alignment of the interferometer output beam on the OMC is controlled by an auto-alignment system. With regard to the squeezing, the OMC introduces the mode-matching of the squeezed field to it as an additional degree of freedom and as a possible loss mechanism. Another loss source arises from the intracavity loss in the OMC as discussed in Section 5.3.

Finally, in the course of the GEO-HF upgrade the circulating light power inside the interferometer will be increased by a factor of about 10. For this, an E-LIGO 35 W laser will substitute the current 12 W system. Further modifications to interferometer optics and the control system will also be necessary. Though an increased light power will not directly affect the squeezed light input, it will additionally improve the interferometer sensitivity at shot-noise limited frequencies. All modifications described above shall, together with the implementation of squeezed light addressed in the following, yield a sensitivity improvement by about one order of magnitude compared to the sensitivity achieved during the S5 science run at kHz-frequencies.

5.2. Integration of the squeezed-light laser into the GEO 600 detection scheme

After characterization and commissioning in the AEI cleanroom, the squeezed-light laser was transported to the GEO 600 detector site. One of the initial design criteria was

5.2. Integration of the squeezed-light laser into the GEO 600 detection scheme

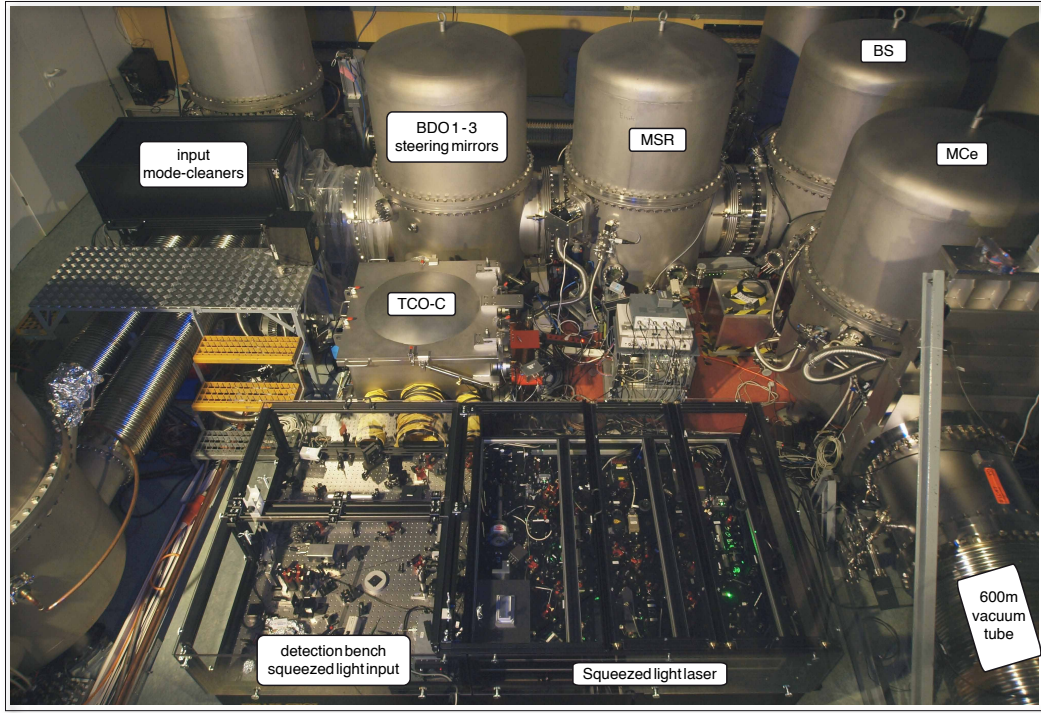


Figure 5.2.: View into the GEO 600 central building containing the main interferometer optics. Centered in the front is the detection bench with the squeezed-light laser, shielded by a double enclosure. The squeezed beam is guided over the detection bench into the TCO-C vacuum chamber containing the OMC and the $h(t)$ photo detector.

a compact setup. This requirement arose from spatial restrictions at the so-called *detection bench*, an optical table located close to the vacuum chamber that contains the squeezing input PBS, the OMC and the $h(t)$ photo detector (this vacuum chamber is denominated *TCO-C* in the following). With 113 cm x 135 cm being vacant, the detection bench offered the sole space large enough to house the squeezed-light laser available in the GEO 600 central building. Another requirement resulting from the limited clearance inside the building was a desired transportability by manpower. Situated on an aluminium breadboard and having a total weight of about 100–120 kg, the GEO 600 squeezed-light laser meets both requirements. The transport in a truck was carried out in a custom-made flight case to protect the components from contamination. Merely the control electronics have been disconnected for transport purposes, no optical dis- and reassembly was performed. This made it possible to reach the same performance as at the AEI in about 1–2 weeks which were required to create the infrastructure for the control electronics. Figure 5.2 shows a view into the GEO 600 central building with the squeezed-light laser located at the front on the detection bench.

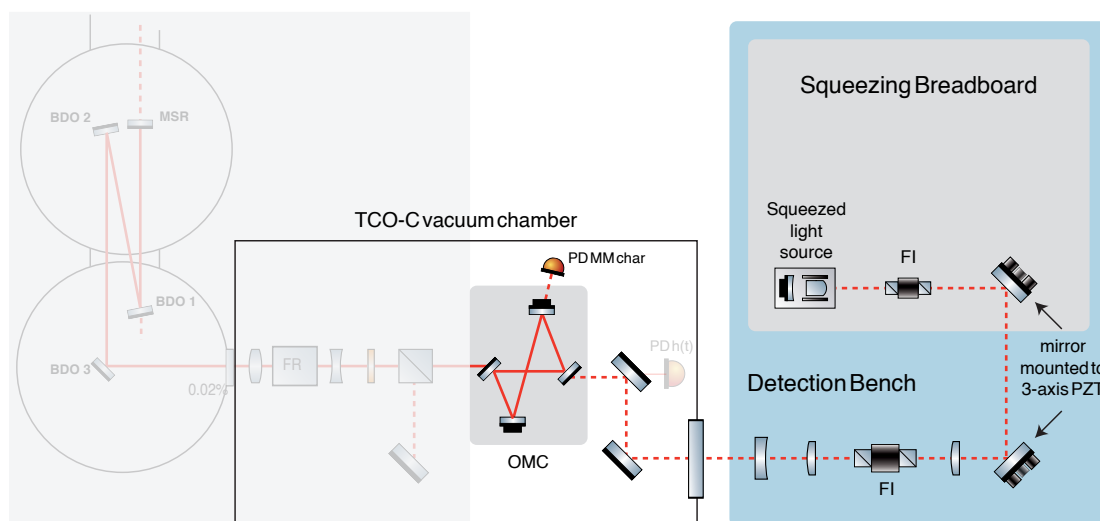


Figure 5.3.: Sketch of the optical layout used to match the mode of the squeezed field to the eigenmode of the output mode-cleaner (OMC). For clarity reasons, the auxiliary photo detector $PD_{MM\ char}$ is drawn inside the vacuum chamber, though in reality it is situated on the detection bench. Steering mirrors and auxiliary optics are omitted. Details are provided in the text. The PZT-mounted mirrors as well as the Faraday rotator are shown for completeness and were not relevant at this stage. The whole optical layout of the GEO - HF detection stage (between MSR and PD h(t)) is shown in Fig. 5.4.

To ‘connect’ the squeezed-light laser to GEO 600, the frequency of the main squeezing laser was locked to the GEO 600 laser using a commercial Innolight PLL, which is described in more detail in Section 3.2. A weak beam of a few mW was tapped off from the GEO master laser output and guided through a fiber-coupled AOM and a polarization-maintaining fiber to the detection bench. It was overlapped with a pickoff beam from the main squeezing laser outside the breadboard enclosure. The intensity of the two beams was about 3 mW each. To lock the lasers with a zero frequency offset, the beam from GEO 600 was frequency-shifted by 80 MHz with the AOM and the PLL was operated at exactly the same frequency offset.

As discussed in Chapter 1, the final squeezing injection scheme is realized through the combination of a Faraday rotator (FR) and a polarizing beam splitter: The squeezed field is reflected at the PBS between the OMC and the MSR, experiences a 45 degree polarization rotation passing the FR and another 45 degree rotation after having been reflected at the signal-recycling mirror of the interferometer. The total polarization rotation of 90 degrees allows the squeezed beam to be transmitted by the PBS together with the output beam of the interferometer (carrying the GW signal) and to arrive at

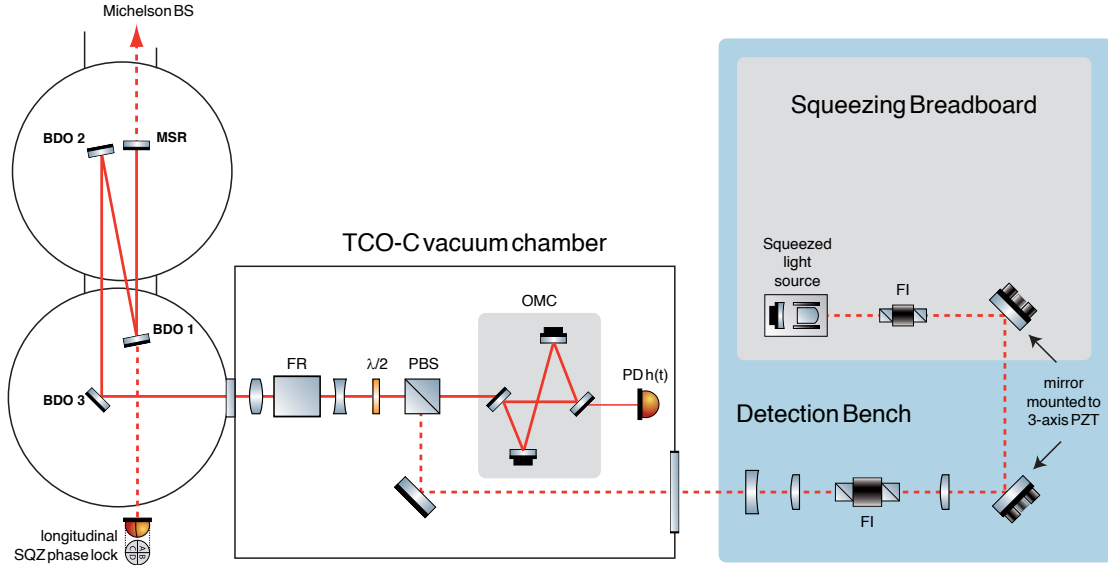


Figure 5.4.: Sketch of the optical layout of the GEO-HF detection stage with squeezing input. Auxiliary optics are omitted for clarity reasons. Details are provided in the text.

the OMC at what is in the following called the *input port*. From the *output port* it is directly guided to the $h(t)$ photo detector.

The mode-matching of the squeezed field to the eigenmode of the interferometer was separated into two steps. Before injecting the squeezing into the SRC, a pre-mode-matching procedure was performed to match the mode of the squeezed field to the OMC, thereby already choosing the correct lens positions on the detection bench. For this, the bright alignment beam (BAB), which apart from the power has the same properties as the squeezed beam, was utilized. On the squeezing breadboard, the diagnostic homodyne detector was bypassed and the alignment beam was guided onto the detection bench. The setup employed is sketched in Fig. 5.3. The bright alignment beam was injected into the OMC from the output port. The OMC length was scanned with the PZT-mounted end mirror and the mode content monitored with the auxiliary photo detector $PD_{MM \text{ char}}$. The optical path of the alignment beam was ensured to be of exactly the same length as if the BAB was injected through the correct input port. A mode-matching of 98% to the OMC eigenmode was realized adapting the lens positions on the detection bench.

A sketch of the final optical layout of the GEO-HF detection stage with squeezing input is shown in Fig. 5.4. Because of the high higher-order mode content of the beam exiting the MSR, a quantification of the mode-matching of the interferometer beam to the OMC is difficult. Measurements in different configurations (tuned DC and detuned heterodyne) furthermore yielded different results for the MM quality. Therefore, after optimizing

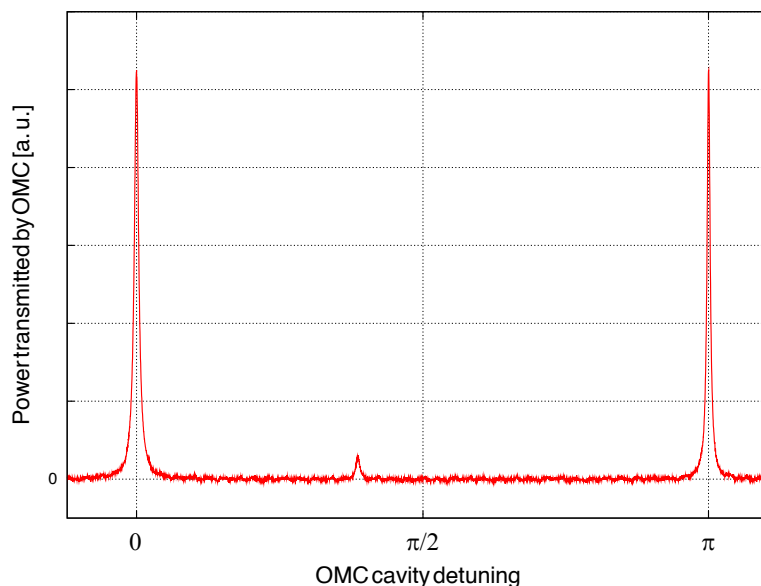


Figure 5.5.: Free spectral range of the GEO 600 output mode-cleaner, measuring the bright alignment beam reflected off the signal-recycling mirror and transmitted through the OMC. The mode-matching of the squeezed beam to the interferometer and to the OMC was estimated to a value of 94.5 % from this measurement.

the lens positions inside TCO-C for the detuned heterodyne configuration, the bright alignment beam was employed to validate the mode-matching of the squeezed beam to the interferometer and subsequently to the OMC. GEO 600 was unlocked and one of the arm mirrors deliberately misaligned for this measurement, so that MSR acted as a normal mirror ($R = 98.1\%$) without the complication of an intra-cavity interferometer. Just as during squeezed-input operations, the alignment beam was reflected by the MSR and sent back to the OMC, where a length scan was used to evaluate the mode spectrum employing directly the $h(t)$ photo detector. While a coarse alignment was performed by conventional steering mirrors, the fine-tuning was done with the two mirrors mounted on three-axis PZT actuators as illustrated in Fig. 5.4. These mirrors are also used to stabilize the phase of the squeezed field with respect to the interferometer as discussed later. Figure 5.5 shows the mode content of the bright alignment beam power reflected by MSR and transmitted by the OMC. The scanning frequency was 1 Hz. From this measurement, the TEM_{00} mode content was calculated to about 94.5%. Please note that this value also includes the mode-matching from the squeezed-light source to the OMC, so that the mode-matching from the interferometer to the OMC alone will be even slightly better.

For the operation of a squeezed-input GEO 600, the bright alignment beam needs to be blocked so as to not to introduce excess noise at the frequencies of interest. Furthermore,

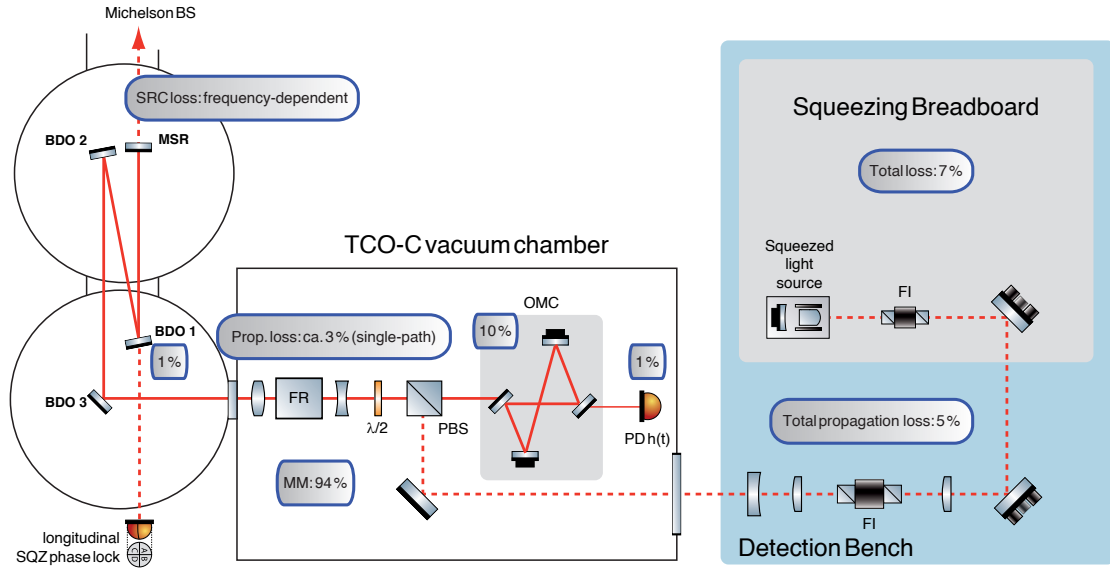


Figure 5.6.: Estimation of the losses experienced by the squeezed field, including the squeezed-light laser itself as well as the contributions from the GEO - HF detection stage.

another control loop is required to stabilize the phase of the squeezed field with respect to the field exiting the interferometer. For this purpose, the coherent control field is employed again. The signal transmitted at BDO_1 , being the beat of the GEO 600 carrier field with the CCF, is demodulated at the CCF offset frequency of 15.2168 MHz. In this way, an error signal for the longitudinal phase lock is generated. It is processed digitally by the CDS system and fed back to the 3-axis PZTs as well as to the suspended BDO_2 steering mirror. Thus, the slow drifts are compensated by the suspended optic (having a cut-off frequency of 1 Hz) allowing a high actuation range, while the control at higher frequencies is done with the PZTs. The unity-gain frequency of the longitudinal phase control loop was a few hundred Hz.

5.3. Loss estimation

From the measurements of squeezing and anti-squeezing levels discussed in Section 4.2, a total optical loss on the squeezing breadboard of approximately 10.5% was calculated. In this value, a loss at the homodyne detector (due to a non-perfect fringe visibility and due to photo detector losses) of ca. 3.5% is already included. This loss can be subtracted if the squeezed beam is directly guided into the GEO 600 signal port. Thus, a residual optical loss value of 7% is obtained, which means that up to 11.3 dB of squeezing is available at the output of the squeezing breadboard for injection into GEO 600. Due to the residual

optical loss this value is, however, connected to a much higher anti-squeezing of about 22 dB. Therefore, the squeezed-light source is operated at 35 mW pump power, which only insignificantly reduces the squeezing output to about 10.6 dB, while the anti-squeezing value is, with about 17 dB, much lower (Traces (a–b) in Fig. 5.8). In the following, the optical losses experienced by the squeezed field are summarized:

- The total loss on the squeezer breadboard is, as stated above, about 7%, taking into account an estimated escape efficiency of 95% and a propagation loss of 2%. The latter arises mainly from a Faraday isolator necessary to suppress light back-reflected from the interferometer into the squeezed-light source. This light would interfere with the squeezed field and mask squeezing at audio frequencies.
- During the implementation of squeezing, it was discovered that an additional Faraday isolator was required to protect the interferometer from back-scattering as well as the squeezed-light source from an interferometer bright beam. Without this isolation, about 0.5 μ W of light are injected into the squeezing resonator (estimating 50 mW incident from MSR at the squeezing input PBS, a PBS extinction ratio of 1/100 and an isolation of 30 dB by the Faraday isolator on the squeezing breadboard). The additional Faraday isolator adds 44 dB of isolation but contributes 4% to the propagation loss. The total propagation loss on the detection bench is therefore about 5%. A discussion of how this and other losses will be reduced in the future is presented in Section 5.5.
- The expected single-path propagation loss inside TCO-C, due to imperfect AR-coatings and absorption, can be estimated to be about 3%. The individual contributions are illustrated in Fig. 5.6.
- 1% is transmitted at BDO₁ for error signal generation (This loss also contributes twice due to the double-path of the squeezed beam).
- A frequency-dependent loss is introduced by the signal-recycling cavity. While at frequencies outside the SRC linewidth it acts as a mirror, at low frequencies the squeezed field is coupled into the interferometer and experiences the intra-cavity loss. Figure 5.7 shows the expected power reflectivity of the SRC for the squeezed field obtained from a FINESSE simulation [FINESSE]. For this, the FINESSE file of GEO 600 published in [Hild-PhD] was used. Trace (b) additionally shows the expected effect for a decreased MSR reflectivity, leading to an increased SRC bandwidth of about 1.1 kHz and therefore to a higher loss at kHz-frequencies. Selected interferometer parameters used in the simulation are given in Table 5.1.
- The best mode-matching to the signal-recycling cavity and to the output mode-cleaner measured was about 94%.
- From the design parameters, the optical loss for a single transmission through the OMC was estimated to be below 1%. During characterization, however, a much higher value of about 10% was measured. This loss could not be reduced further

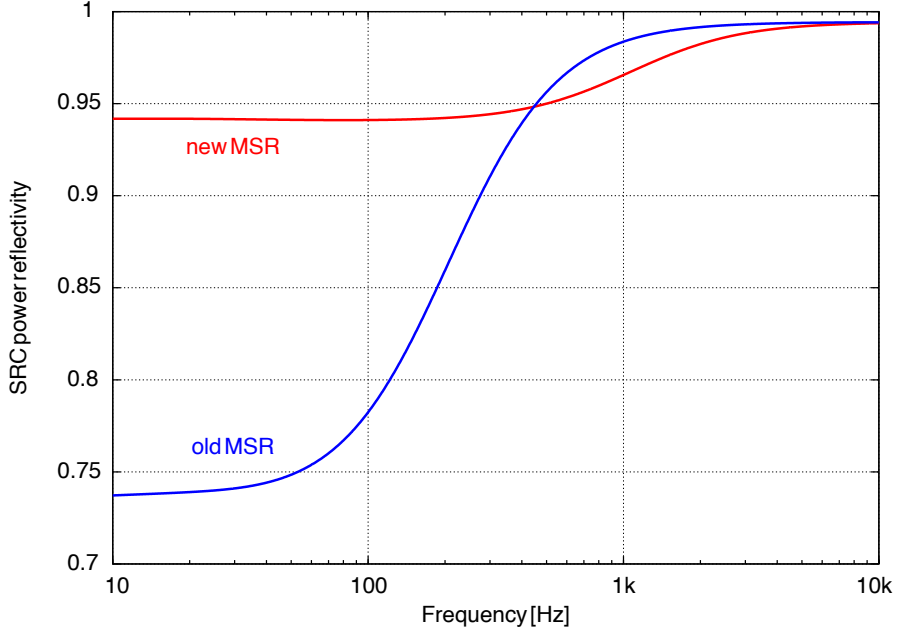


Figure 5.7.: FINESSE simulation of the signal-recycling cavity’s frequency-dependent power reflectivity with the old (blue trace) and new (red trace) MSR. The parameters used for the simulation are provided in Table 5.1.

parameter	value
length north arm	1196.72 m
length east arm	1196.80 m
power at BS	2.7 kW
loss at BS AR-coating	60 ppm
scattering loss per optical surface	100 ppm
reflectivity of MPR	0.9991
reflectivity of old MSR	0.9805
reflectivity of new MSR	0.90
beam waist at MPR and MSR	8.764×10^{-3} m
SRC BW with old MSR	ca. 220 Hz
SRC BW with new MSR	ca. 1100 Hz

Table 5.1.: Parameters of the GEO 600 optics and layout employed for the FINESSE simulation of the frequency-dependent loss introduced to the squeezed field by the signal-recycling cavity, as well as selected interferometer parameters.

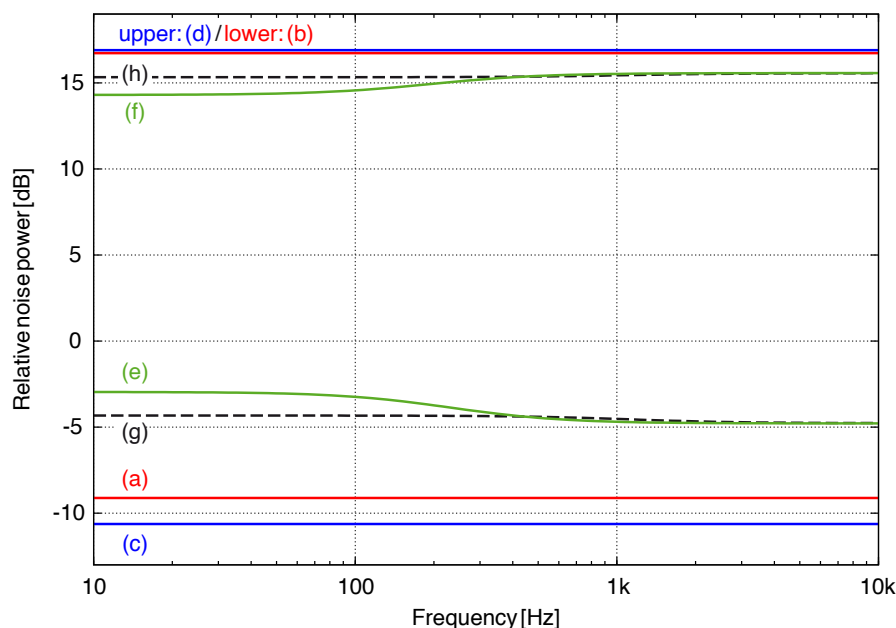


Figure 5.8.: Simulated squeezing and anti-squeezing values prior to and after the injection in GEO 600. A value of 35 mW was assumed for the 532 nm pump power. Traces (a–b): measuring at the diagnostic homodyne detector. Traces (c–d): squeezing and anti-squeezing available at the output of the squeezer breadboard, corrected for the homodyne detector losses. Traces (e–f): frequency-dependent squeezing and anti-squeezing values at the h(t) photo detector with the old MSR. Traces (g–h): same with the new MSR.

by cleaning and probably arises from a combination of imperfect optical surfaces and dielectric coatings deviating from the design specifications.

- Before the GEO-HF upgrade, a Perkin Elmer C30642 photo diode was used for h(t) signal detection. It was substituted by a custom-made high-efficiency photo diode, as already used in the diagnostic homodyne detector. The diameter of the active area is 3 mm. The quantum efficiency was measured to be 8% higher than for the Perkin Elmer PD and is expected to be similar to the 500 μm diodes used in previous experiments, namely about 99%.
- The dark noise clearance at shot-noise-limited frequencies is approximately a factor of 5–6.

The total loss for the squeezing, being a product of all contributions mentioned above, is therefore estimated to a value of 32% at kHz-frequencies and up to 50% at frequencies much lower than the SRC linewidth. With 220 Hz the latter is, however, already in the frequency range where the interferometer sensitivity is no longer limited by quantum

noise. Figure 5.8 shows the expected squeezing and anti-squeezing values for the squeezed-light laser operated with a pump power of 35 mW. Traces (a–b) refer to the squeezing and anti-squeezing measured at the diagnostic homodyne detector. Traces (c–d) correct those values for the homodyne detector loss and therefore show the squeezing or anti-squeezing available for injection at the squeezing breadboard output. Traces (e–f) finally give an estimation of the amount of squeezing or anti-squeezing present at the $h(t)$ photo detector. Trace (g) illustrates the effect of the MSR exchange, leading to an increased SRC linewidth (see discussion in Section 5.5).

5.4. Non-classically improved GEO 600 sensitivity

The main result, a non-classical improvement of the GEO 600 sensitivity with squeezed light injection, is presented in Fig. 5.9. Therein, the left y -axis shows the observatory noise given in units of the GW amplitude, while on the right y -axis the noise is calibrated to the test mass displacement. Trace (a) shows the ‘classical’ observatory noise, recorded with 2.7 kW optical power at the BS and with the old signal-recycling mirror. In trace (b), about 10.5 dB of squeezing is injected into the signal port of GEO 600 (this value refers to the output of the squeezed-light laser inferred from the calculations given above in Section 5.3). The squeezed-light laser was operated at 35 mW pump power. In the frequency range where the observatory sensitivity is limited by shot noise (above 700 Hz), a broadband noise reduction by up to 3.5 dB was achieved. At 3 kHz (being a frequency arbitrarily chosen from a range where shot noise is the dominant limiting contribution and no calibration lines are present), the quantum noise was reduced from $1.0 \times 10^{-21} \text{ Hz}^{-1/2}$ down to $6.7 \times 10^{-22} \text{ Hz}^{-1/2}$. This corresponds to a factor $1.5^3 \approx 3.4$ increase in detection rate for isotropically distributed GW sources in that frequency band. Due to the application of squeezed light, GEO 600 has achieved its best ever sensitivity since the implementation of the DC readout scheme. As expected, at Fourier frequencies below 700 Hz, squeezed light does neither reduce nor increase the current displacement noise level.

The calculated loss value of 32% derived above does not include the dark noise contribution from the $h(t)$ photo detector electronics. Subtracting this contribution from the measured data shown in Fig. 5.9 leads to an inferred squeezed light sensitivity enhancement by about 3.7 dB. This value is about 1 dB lower than the maximal squeezing contribution expected from the known loss parameters. Such a deviation would correspond to additional 10% loss not considered in Section 5.3. The discussion therein does, however, neither account for phase noise nor for a misalignment of the squeezed beam with respect to the interferometer. At the current implementation stage, both effects are, however, expected to be present. An auto-alignment procedure of the squeezed field to the interferometer is yet to be implemented. Without this control loop, the suspended interferometer optics, though locked with respect to each other, are free swinging with

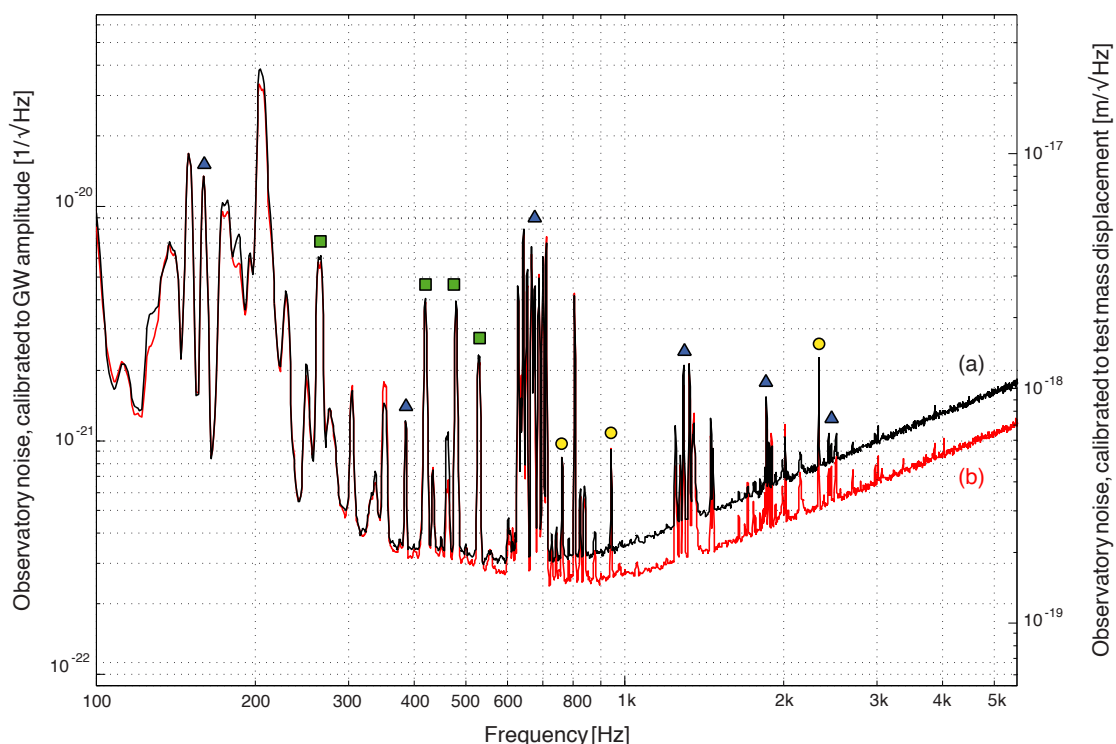


Figure 5.9.: Non-classical reduction of the GEO 600 instrumental noise using squeezed vacuum states of light, calibrated to GW amplitude (left y -axis) and to differential mirror displacement (right y -axis). Trace (a) shows the observatory noise spectral density without the injection of squeezed light. At frequencies above 700 Hz, the noise is dominated by quantum shot-noise. An injection of squeezed vacuum states into the interferometer leads to a broadband noise reduction of up to 3.5 dB in the shot-noise limited frequency band, as shown in trace (b). The spectral features are caused by excited violin modes of the suspensions (600–700 Hz and harmonics, blue triangles) as well as by calibration (160 Hz–2.5 kHz, yellow circles) and OMC alignment control (250–550 Hz, green squares) lines. Both traces were averaged over 4 minutes. The resolution bandwidth is 1 Hz for frequencies below 1 kHz, and 2 Hz at higher frequencies. Published in [Abadie+11].

respect to the squeezed beam injection path. This introduces a time-dependent, unknown effective loss for the squeezing injection. Additionally, phase jitter, leading to a degrading squeezing level as illustrated in Fig. 4.6, may arise from the longitudinal phase lock of the squeezed field to the interferometer output as well as from the PLL to the GEO 600 laser. Furthermore, regarding the optical loss contributions, the mode-matching quality of the squeezed field to the interferometer and to the OMC remains the most speculative factor, known at best with a certainty of several percent. It is therefore probably a contribution from all the discussed effects that impedes the observation of a higher squeezing value

that could be expected from a consideration basing merely on the sum of all known optical losses.

Up to now, the squeezing enhancement has been successfully operated for several consecutive hours. The long-term behaviour of the squeezed-light source has been addressed in detail in Section 4.5. In a first characterization, up to 9.3 dB were observed at the homodyne detector for up to 20 hours, corresponding to an injection value of about 10.5 dB. During this measurement, the longest lock lasted for 8.5 hours, the duty cycle was higher than 99.9%. Subsequent observations during the 2011 joint GEO 600 – Virgo science run, which are to be published elsewhere, included much longer lock durations of several tens of hours. Therefore, the 8.5 hours reported above may in good conscience be addressed rather as a typical behaviour than as an exception. When GEO 600 is operated in science mode, its duty cycle is in the order of 90% [Grote+10] with typical lock durations extending from several hours up to 40–60 hours, being larger than for the squeezed-light laser. This difference should, however, not significantly affect the duty cycle of a squeezed-input GEO 600. In case of a lock-loss of the squeezed-light laser, a shutter automatically blocks the squeezing beam input path, thereby ensuring that the detector sensitivity is not degraded due to anti-squeezing input. Hence, the detection sensitivity will be improved by squeezing most of the time and be equal to the classical sensitivity when the squeezed-light laser is unlocked. A lock-loss of GEO 600, on the other hand, may also lead to a lock-loss of the squeezed-light source. Because the lock acquisition time of the latter is with max. 15 seconds much shorter than the approximately 10 minutes of GEO 600, no additional performance degradation is expected.

5.5. Future work

The long-term goal to be achieved with squeezed light injection is a desired reduction of the observatory noise by 6 dB at quantum-noise limited frequencies and a permanent squeezing contribution during the operation of GEO-HF. After the first successful enhancement of the observatory sensitivity by squeezed light, the achievement of both intents seems to be feasible in the near future. Regarding the squeezing factor, the following loss sources can be addressed:

- The optical loss during beam propagation on the detection bench is mainly due to the currently used Faraday isolator with a suboptimal performance in this respect as well as to polarization optics. The use of a high-throughput Faraday rotator identical to the one already used in the squeezed-light laser setup in combination with hand-picked polarizing beam splitters will allow a reduction of the propagation loss. Apart from the Faraday isolator, merely super-polished optics with a high-performance AR-coating (as used on the squeezer breadboard) will be used, thereby reducing loss due to surface scattering and to residual AR-coating reflection. An overall loss value of 2% seems feasible for the detection bench propagation loss.

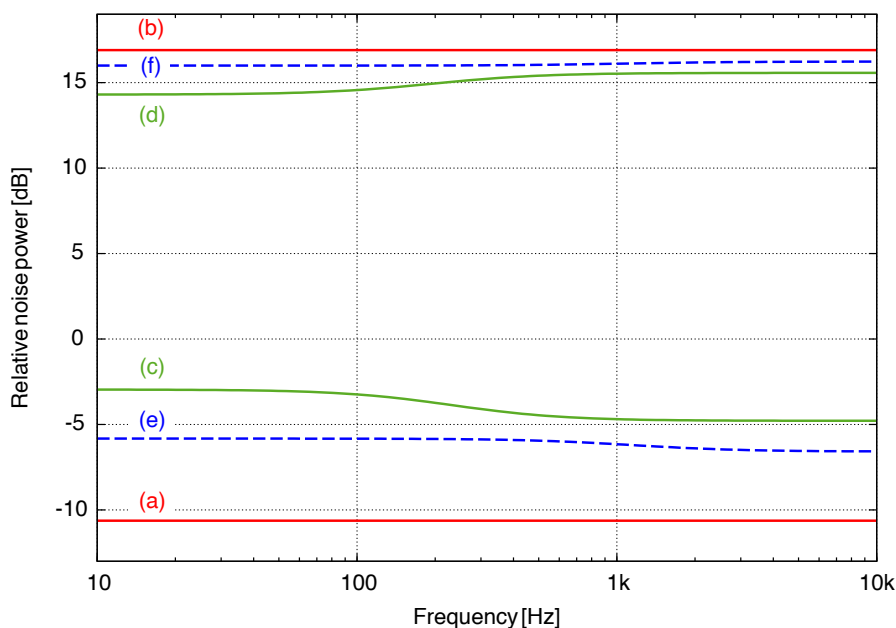


Figure 5.10.: Simulated squeezing and anti-squeezing values prior to and after the injection in GEO 600. A value of 35 mW was assumed for the 532 nm pump power. Traces (a–b): squeezing and anti-squeezing available at the output of the squeezing breadboard, corrected for the homodyne detector losses. Traces (c–d): frequency-dependent squeezing and anti-squeezing values at the $h(t)$ photo detector with the old MSR and the current optical losses as discussed in Section 5.3. Traces (e–f): same, taking into account the new MSR and the optical loss reduction feasible in the near future.

- Lenses with a super-polished surface and a low residual reflection at the AR-coating (as already used in the squeezed-light laser setup) will be used inside TCO-C. Furthermore, the residual transmission at BDO_1 can be reduced to a value of 0.5 %, thereby lowering the effective loss for the squeezed field reflected twice at this optics to 1 %.
- Up to now, the largest single loss contribution arises from the transmission through the output mode-cleaner. In the future, the OMC optics will be exchanged. From the specifications of the single optics, the total transmission loss (mainly due to coating and surface imperfections and to a 100 ppm residual transmission of one of the mirrors for monitoring purposes) was estimated to be below 1 %. This value is therefore assumed as an upper limit in this paragraph.
- The exchange of the signal-recycling mirror will slightly increase the loss at kHz-frequencies as can be seen from Fig. 5.7 (g). While at frequencies below 500 Hz the effective SRC loss decreases and the squeezing value hence increases, at frequencies between 500 Hz and 7 kHz the expected squeezing value slightly degrades by up to

0.2 dB. This effect is not significant compared with the sensitivity improvement of GEO 600 expected to arise from the exchange of the signal-recycling mirror discussed above.

- Finally, the mode-matching of the squeezed field to the interferometer and to the output mode-cleaner can be improved further. At this point, a precise estimation of the achievable value seems, however, rather difficult. While no theoretical reason that would impede a perfect mode-matching exists, the experimental realization may require several iterations, so that at a certain point a trade-off between the work load and the achievable effect will have to be made. Nevertheless, a value of 98 % seems quite realistic and an even better value might be achievable.

Modifying the loss discussion from Section 5.3 for these considerations yields a total residual loss of about 19 % at kHz-frequencies. Therewith, the possible squeezing enhancement of the observatory noise is almost 7 dB at shot-noise limited frequencies as illustrated in Fig. 5.10. As far as the optical loss is concerned, an observatory noise reduction by 6 dB therefore seems a realistic goal for a squeezing-enhanced GEO-HF.

An important issue to be addressed is the automatic alignment of the squeezed beam to the interferometer. To generate error signals, the beam transmitted through BDO₁ can be employed. The error signal will be processed digitally by the CDS system with an appropriate weighting matrix and fed back to the three-axis PZT-actuators, thereby allowing an alignment of the spatial x and y (tip/tilt) degrees of freedom. The z component will still be used for the fast part of the longitudinal phase lock. The generation of auto-alignment error signals is currently under investigation.

Due to the GEO-HF upgrade program and to the works conducted at the detector site, no undisturbed extended long-term characterization of the system could be performed. A permanent observatory operation with squeezing input after the end of the GEO-HF upgrade will allow deducing the stability of the generated squeezing on a timescale of weeks or months.

Summary and outlook

The measurement sensitivity of the first generation of gravitational wave observatories is limited by quantum shot noise at frequencies above several hundred Hertz. In future observatory generations, quantum noise may even become the limiting factor over the entire frequency band observed. Since the signal-to-noise ratio of the observatories depends on the optical powers employed in the interferometers, a power increase is a possible solution to improve the SNR. This will, however, also increase the thermal load to the interferometer optics, so that finally an upper limit for the optical light power employable in future GW observatory generations will be reached [ET].

In the last decade, a vast amount of proof-of-principle experiments has been performed to demonstrate that squeezed light constitutes an appropriate alternative method to improve the SNR of GW observatories. The purpose of this thesis was, basing on those insights, to construct a squeezed-light laser for the GW observatory GEO 600.

The optical layout of the device was discussed in Chapter 3 along with the implemented control schemes. The designated permanent employment in GEO 600 imposed on the squeezed-light laser the demand of long-term stability: the generated degree of squeezing had to remain stable on timescales of hours to days in order to ensure a non-varying observatory sensitivity. During the characterization of the long-term performance of the system, the stability of the squeezing degree was found to depend on the power stability of the 532 nm pump beam for the coherent control scheme employed. A description of the coupling mechanism was derived. Finally, the extension of the coherent control scheme by a pump power stabilization was discussed.

In Chapter 4, a characterization of the squeezed-light laser was presented. The generated squeezing spectrum was flat (white) over the entire frequency band of Earth-bound GW observatories extending from 10 Hz to 10 kHz. With a noise reduction of up to 9.6 dB below the vacuum noise level, a new benchmark was set. Corrected for detection losses, this value corresponds to more than 11 dB of squeezing available for injection into the

dark port of GEO 600. The longest characterization measurements lasted for 20 h with an overall duty cycle of more than 99 %.

The first operation of a GW observatory ‘beyond the quantum limit’ was finally presented in Chapter 5. In the frequency range where the GEO 600 observatory sensitivity is limited by shot noise (above 700 Hz), a broadband noise reduction of up to 3.5 dB, corresponding to a factor of about 1.5, was achieved. At 3 kHz, the quantum noise was reduced from $1.0 \times 10^{-21} \text{ Hz}^{-1/2}$ to $6.7 \times 10^{-22} \text{ Hz}^{-1/2}$. This corresponds to a factor $1.5^3 \approx 3.4$ increase in detection rate for isotropically distributed GW sources in that frequency band. Due to the application of squeezed light, GEO 600 has achieved its best ever sensitivity since the implementation of the DC readout scheme. As expected, at Fourier frequencies below 700 Hz, squeezed light did neither reduce nor increase the current displacement noise level. Finally, the present sources of optical loss – which impedes an even stronger sensitivity improvement by squeezed light – were discussed. An analysis of possible loss reduction shows that an improvement of the GEO 600 sensitivity by a factor of two seems feasible in the near future. This effect is equivalent to an increase of the circulating optical power by a factor of four. Since squeezed light injection is completely independent from the optical power employed in the interferometer, it constitutes a valuable alternative or additional technique to enhance the observatory sensitivity at detection frequencies where quantum noise is the limiting factor.

6.1. A glimpse into the future

The aim of the first and second generation of Earth-bound GW interferometers was and still remains a first direct observation of gravitational waves. Based on the current models of GW sources along with the design sensitivities of Advanced LIGO and Advanced Virgo, a first observation can be considered to be likely in the course of the next five to ten years [ET]. For most of the events, the expected signal-to-noise ratios are, however, too low for precise astrophysical studies. A sensitivity improvement of about one order of magnitude over the entire GW detection band will be required to detect events on a daily basis with a SNR sufficiently high to extract astrophysical information and hence to usher in the era of routine gravitational wave astronomy. On (or much more below) the ground, this goal is aimed at by the *Einstein Telescope* (ET), a European project for a 3rd generation GW observatory. The (recently completed) ET design study among other topics investigated the question how a sensitivity improvement by a factor of ten with respect to the 2nd detector generation may be realized. One of the techniques included in the final design proposal as necessary to achieve this ambitious goal is squeezed light; a reduction of the observatory quantum noise by 10 dB is envisioned. Thereby, an upper limit of 10 % is set for the total optical loss which may be experienced by the squeezed field.

Such a restriction constitutes a challenge for the design of the GW observatory as well as for the squeezed-light laser to be employed. On the observatory side, additional optical loss will be introduced by the filter cavities required for a broadband sensitivity improvement by squeezed light. The resulting restrictions have been addressed in detail in Ref. [ET]. The calculations presented therein used conservative parameters for the filter-cavity specifications and found the science goal to be feasible in case of a total optical loss (besides the contribution by the filter cavities) of 9%. This value, which accounts for loss inside the squeezed-light laser as well as for injection loss, is more than a factor of two below the value predicted for the near future in GEO-HF in Section 5.5.

Though being ambitious, the ET requirements seem feasible considering the present state of research in the field of non-classical light. Currently, the highest squeezing degree reported is 12.7 dB at a wavelength of 1064 nm [Eberle+10] and 12.3 dB at the wavelength of 1550 nm [Mehmet+11] that is proposed as operation wavelength for the Einstein Telescope.

Another factor that should not be neglected is the additional loss introduced by the Faraday rotator(s) in the squeezing injection path. This optical isolation is necessary to protect the squeezed-light source from light coming out of the interferometer as well as to protect the interferometer from the same light back-scattered by the squeezing resonator. The required degree of isolation depends on the observatory sensitivity as well as on the microscopic movement of the back-scattering surface, namely the coupling mirror of the squeezing resonator. Since every additional Faraday isolator employed currently adds 1–2% of optical loss, an alternative approach may be given by suspending the squeezing resonator in one of the interferometer's vacuum chambers. This would lead to a reduction of the acoustic and to some extent also of the seismic excitations and thereby possibly reduce the amount of back-scattered light.

Summing up, the results reported in this thesis confirmed the feasibility of a GW observatory with a non-classically enhanced sensitivity. Considering current results in the field of non-classical light, squeezing seems to be well on its way to become a 'standard' technique for the 3rd and possibly even already for the 2nd generation of gravitational wave observatories.

6. *Summary and outlook*

Second-harmonic generation using PPKTP

Up to this work, MgO:LiNbO_3 was usually employed as nonlinear medium for second-harmonic-generation in the experiments conducted at the AEI. A crystal with a higher second-order nonlinear susceptibility is potassium tytanyl phosphate (KTP) [Goda-PhD]. Therefore, initially a periodically poled KTP (PPKTP) crystal was used in the GEO 600 squeezed-light laser for second-harmonic generation. The very promising results shown in Fig. A.1 have demonstrated that an SHG conversion efficiency of greater than 90% is generally feasible with PPKTP crystals. The measurement was done with an *Ophir NOVA II* with a $3A$ thermal power sensor, a maximal deviation of $\pm 3\%$ was specified by the manufacturer. Please note that the results shown in Fig. A.1 are corrected for a non-perfect mode-matching of the 1064 nm beam to the SHG cavity, the mode-matching quality was measured to 95%. The highest directly measured conversion efficiency was $88 \pm 6\%$, corresponding to a corrected value of $92.5 \pm 6\%$.

While of no primary interest for the current setup, this result is very interesting for future low-frequency squeezed-light lasers: Since the squeezed-light source (likewise employing PPKTP, see Section 3.5) required only 45 mW of 532 nm pump power to generate 9.5 dB of squeezing, a 2 W Mephisto laser is no longer required in future setups. The 200 mW output power of an auxiliary laser are completely sufficient to generate a sufficiently high second-harmonic power, to drive the PLLs and to provide a local oscillator beam for homodyne detection. This, again, results in a significant cost reduction for future low-frequency squeezed-light lasers for GW detectors.

Unfortunately, the PPKTP crystal employed in the SHG showed an intrinsic defect that grew larger with time and finally required a replacement of the crystal. The precise nature of the defect is currently unknown. A visual inspection has shown a milky structure inside the crystal that does not seem to coincide with grey tracking effects to which

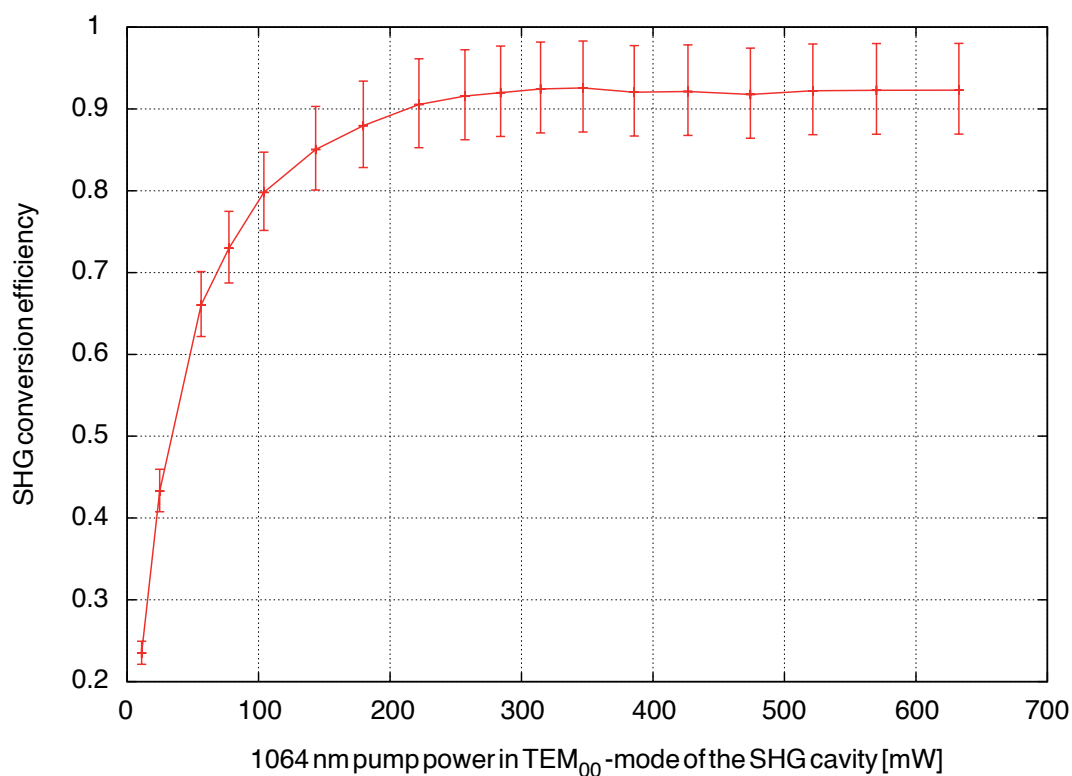


Figure A.1.: Conversion efficiency of the PPKTP-SHG as a function of 1064 nm pump power. The results shown are corrected for a mode-mismatch of the 1064 nm beam.

PPKTP is known to be sensitive (see [Meier-PhD]). Nevertheless, a long-term analysis in a separate experiment is required to prove that PPKTP crystals are suitable for the use in SHG at 1064 nm before this material can be considered in the planning of future long-term experiments. For the work presented here, the defect crystal was replaced by a ‘conventional’ MgO:LiNbO₃ crystal, as described in Section 3.3.

Optical layout of the squeezed-light laser

Figure B.1 shows the complete optical layout of the squeezed-light laser, including auxiliary optics. A detailed discussion of the setup is provided in Chapter 3, the phase-locked loop to the main GEO 600 laser is discussed in Section 5.2. For an explanation of the pictograms used in Fig. B.1, please see the Glossary. The size of the pictograms is not scaled to the physical size of the components used.

B. Optical layout of the squeezed-light laser

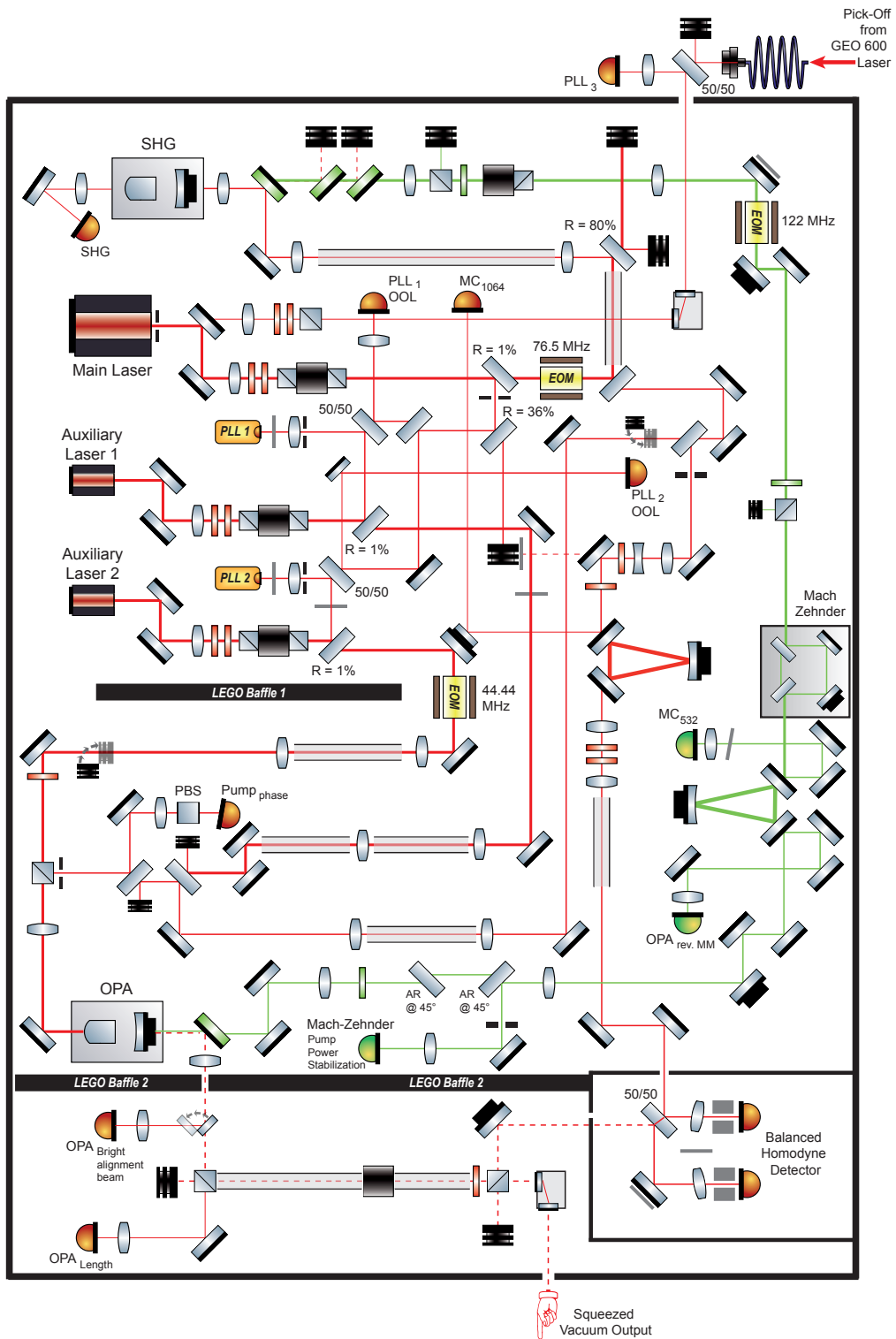


Figure B.1.: Optical layout of the squeezed-light laser.

Bibliography

- [Abadie+11] J. Abadie *et al.*, “A gravitational wave observatory operating beyond the quantum shot-noise limit”, *Nature Phys.* **7** (2011) 962–965
- [Abbott+09] B.P. Abbott *et al.*, “LIGO: the Laser Interferometer Gravitational-Wave Observatory”, *Rep. Prog. Phys.* **72** (2009) 076901
- [Acernese+08] F. Acernese *et al.*, “Status of Virgo”, *Class. Quantum Grav.* **25** (2008) 114045
- [AD-DDS] “Analog Devices”, <http://www.analog.com>
- [ALLEGRO] M.P. McHugh *et al.*, “Calibration of the ALLEGRO resonant detector”, *Class. Quant. Grav.* **22** (2005) S965–S973
- [Arai+09] K. Arai *et al.*, “Status of Japanese gravitational wave detectors”, *Class. Quantum Grav.* **26** (2009) 204020
- [ATF] “Advanced Thin Films”, <http://www.atfilms.com>
- [Aufmuth+05] P. Aufmuth and K. Danzmann, “Gravitational wave detectors”, *New Jour. Phys.* **7** (2005) 202
- [AURIGA] A. Vinante and the AURIGA Collaboration, “Present performance and future upgrades of the AURIGA capacitive readout”, *Class. Quant. Grav.* **23** (2006) S103–S110
- [Bachor+04] H.-A. Bachor and T. C. Ralph, “A guide to experiments in quantum optics” (Wiley-VCH, Weinheim 2004)
- [Ballardin+01] G. Ballardin *et al.*, “Measurement of the VIRGO superattenuator performance for seismic noise suppression”, *Rev. Sci. Instrum.* **72** (2001) 3643–3652
- [Black01] E. D. Black, “An introduction to Pound-Drever-Hall laser frequency stabilization”, *Am. Jour. Phys.* **69** (2001) 79–87
- [Blair+12] D. G. Blair and E. J. Howell, “Sources of gravitational waves”, in: D. G. Blair, L. Ju, C. Zhao and E. J. Howell (editors), “Advanced gravitational wave detectors” (Cambridge University Press, announced for April 2012)

- [Bowen+02] W.P. Bowen *et al.*, “Recovery of continuous wave squeezing at low frequencies”, *J. Opt. B* **4** (2002) 421–424
- [Boyd08] R. W. Boyd, “Nonlinear optics” (Elsevier Academic Press, Amsterdam 2008)
- [Burgay+03] M. Burgay, N. D’Amico and A. Possenti, “An increased estimate of the merger rate of double neutron stars from observations of a highly relativistic system”, *Nature* **426** (2003) 531–533
- [Braginsky+01] V. B. Braginsky and S. P. Vyatchanin, “Frequency fluctuations of nonlinear origin in self-sustained optical oscillators”, *Phys. Lett. A* **279** (2001) 154–162
- [Braginsky+92] V. B. Braginsky, F. Ya. Khalili and K. S. Thorne (editor), “Quantum measurement” (Cambridge University Press, Cambridge 1992)
- [Caves81] C. M. Caves, “Quantum-mechanical noise in an interferometer”, *Phys. Rev. D* **23** (1981) 1693–1708
- [Caves+85] C. M. Caves and B. L. Schumaker, “New formalism for two-photon quantum optics. I. Quadrature phases and squeezed states”, *Phys. Rev. A* **31** (1985) 3068–3092
- [Chelkowski+05] S. Chelkowski *et al.*, “Experimental characterization of frequency-dependent squeezed light”, *Phys. Rev. A* **71** (2005) 013806
- [Chelkowski+07] S. Chelkowski *et al.*, “Coherent control of broadband vacuum squeezing”, *Phys. Rev. A* **75** (2007) 043814
- [Chelkowski-PhD] S. Chelkowski, “Squeezed light and laser interferometric gravitational wave detectors”, Dissertation (Gottfried Wilhelm Leibniz Universität Hannover 2007)
- [Chickarmane+98] V. Chickarmane *et al.*, “Squeezed light in a frontal-phase-modulated signal-recycled interferometer”, *Phys. Rev. A* **57** (1998) 3898–3912
- [Cohen-Tannoudji+99] C. Cohen-Tannoudji, B. Diu and F. Laloë, “Quantenmechanik” (de Gruyter, Berlin 1999)
- [Crooks+04] D. R. M. Crooks *et al.*, “Experimental measurements of coating mechanical loss factors”, *Class. Quantum Grav.* **21** (2004) S1059–S1065
- [Cutler+02] C. Cutler and K. S. Thorne, “An overview of gravitational wave sources”, in: N. T. Bishop and S. D. Maharaj (editors), “Proceedings of the 16th international conference on General Relativity and gravitation” (World Scientific 2002) 72–111
- [Drever+83] R. W. P. Drever and J. L. Hall, “Laser phase and frequency stabilization using an optical resonator”, *Appl. Phys. B* **31** (1983) 97–105
- [Degallaix+09] J. Degallaix *et al.*, “Commissioning of the tuned DC readout at GEO 600”, *J. Phys. Conf. Ser.* **228** (2010) 012013
- [Deich+96] W. T. S. Deich and S. R. Kulkarni, “The masses of the neutron stars in M15C compact stars in binaries”, in: J. van Paradijs, E. P. J. van den Heuvel and E. Kuulkers (editors), “Compact stars and binaries. Proceedings of the 16th symposium

- of the International Astronomical Union” (Kluwer Academic 1995) 279–285
- [Eberle+10] T. Eberle *et al.*, “Quantum enhancement of the zero-area Sagnac interferometer topology for gravitational wave detection”, *Phys. Rev. Lett.* **104** (2010) 251102
- [Einstein05] A. Einstein, “On the electrodynamics of moving bodies”, *Ann. Phys.* **17** (1905) 891
- [Einstein15] A. Einstein, “On the general theory of relativity”, *Sitzungsber. Preuss. Akad. Wiss. Berlin* (1915) 778
- [Einstein16] A. Einstein, “Approximative integration of the field equations of gravitation”, *Sitzungsber. Preuss. Akad. Wiss. Berlin* (1916) 688
- [Einstein18] A. Einstein, “On gravitational waves”, *Sitzungsber. Preuss. Akad. Wiss. Berlin* (1918) 154
- [EPICS] “Experimental Physics and Industrial Control System (EPICS)”, <http://www.aps.anl.gov/epics/>
- [ET] ET Science Team, “Einstein gravitational wave telescope. Conceptual design study”, Internal report ET-0106C-10 (2011)
- [EXPLORER/NAUTILUS] P. Astone *et al.*, “Methods and results of the IGEC search for burst gravitational waves in the years 1997–2000”, *Phys. Rev. D* **68** (2003) 022001
- [Faulkner+04] A. J. Faulkner *et al.*, “PSR J1756-2251: a new relativistic double neutron star system”, *Astrophys. J.* **618** (2005) L119–L122
- [FINESSE] A. Freise, “FINESSE (Frequency domain INterferomETER Simulation SoftwarE) 0.99.8”, <http://www.gwoptics.org/finesse/>
- [First Contact] “First Contact”, <http://www.photoniccleaning.com>
- [Flanagan+05] É. É. Flanagan and S. A. Hughes, “The basics of gravitational wave theory states”, *New Jour. Phys.* **7** (2005) 204
- [Forward78] R. L. Forward, “Wideband laser-interferometer graviational-radiation experiment”, *Phys. Rev. D* **17** (1978) 379–390
- [Franzen+06] A. Franzen, B. Hage, J. DiGuglielmo, J. Fiurášek and R. Schnabel, “Experimental demonstration of continuous variable purification of squeezed states”, *Phys. Rev. Lett.* **97** (2006) 150505
- [Franzen-PhD] A. Franzen, “Präparation von destillierten und purifizierten gequetschten Zuständen”, Dissertation (Gottfried Wilhelm Leibniz Universität Hannover 2008)
- [Fritschel+12] P. Fritschel on behalf of the LIGO Scientific Collaboration, “LIGO: The Laser Interferometer Gravitational-Wave Observatory”, in: D. G. Blair, L. Ju, C. Zhao and E. J. Howell (editors), “Advanced gravitational wave detectors” (Cambridge University Press, announced for April 2012)

- [General Standards Corporation] “General Standards Corporation”,
<http://www.generalstandards.com>
- [GEO-Sens] <https://intranet.aei.uni-hannover.de/geo600/geohflogbook.nsf>
- [Gerry+06] C. C. Gerry and P. L. Knight, “Introductory quantum optics” (Cambridge University Press, Cambridge 2006)
- [Gertsenshtein+63] M. E. Gertsenshtein and V. I. Pustovoit, “On the detection of low-frequency gravitational waves”, *Soviet Journal of Experimental and Theoretical Physics* **16** (1963) 433–435
- [Goda-PhD] K. Goda, “Development of techniques for quantum-enhanced laser-interferometric gravitational-wave detectors”, Dissertation (Massachusetts Institute of Technology 2007)
- [Goda+08a] K. Goda *et al.*, “Generation of a stable low-frequency squeezed vacuum field with periodically poled KTiOPO4 at 1064 nm”, *Opt. Lett.* **33** (2008) 92–94
- [Goda+08b] K. Goda *et al.*, “A quantum-enhanced prototype gravitational-wave detector”, *Nature Phys.* **4** (2008) 472–476
- [Gräf-Diploma] C. Gräf, “PPKTP-Quetschlichtquelle und Twin-Signal Recycling”, Diploma thesis (Gottfried Wilhelm Leibniz Universität Hannover 2008)
- [Grote+08] H. Grote (for the LIGO Scientific Collaboration), “The status of GEO 600”, *Class. Quantum Grav.* **25** (2008) 114043
- [Grote+10] H. Grote (for the LIGO Scientific Collaboration), “The GEO 600 status”, *Class. Quantum Grav.* **27** (2010) 084003
- [Grote+11] H. Grote and D. H. Reitze, “First-generation interferometric gravitational-wave detectors”, in: D. G. Blair, L. Ju, C. Zhao and E. J. Howell (editors), “Advanced gravitational wave detectors” (Cambridge University Press, announced for April 2012)
- [Harms+03] J. Harms *et al.*, “Squeezed-input, optical-spring, signal-recycled gravitational-wave detectors”, *Phys. Rev. D* **68** (2003) 042001
- [Heisenberg27] W. Heisenberg, “Über den anschaulichen Inhalt der quantentheoretischen Kinematik und Mechanik”, *Zeitschrift f. Physik A* **43** (1927) 172–198
- [Heurs-PhD] M. Heurs, “Gravitational waves in a new light: Novel stabilisation schemes for solid-state lasers”, Dissertation (Universität Hannover 2004)
- [Hild-PhD] S. Hild, “Beyond the first generation: extending the science range of the gravitational wave detector GEO 600”, Dissertation (Gottfried Wilhelm Leibniz Universität Hannover 2007)
- [Hild+07] S. Hild *et al.*, “Demonstration and comparison of tuned and detuned signal recycling in a large-scale gravitational wave detector”, *Class. Quantum Grav.* **24** (2007) 1113-1523

-
- [Hild+09] S. Hild *et al.*, “DC-readout of a signal-recycled gravitational wave detector”, *Class. Quantum Grav.* **26** (2009) 055012
- [Hobden+66] M. V. Hobden and J. Warner, “The temperature dependence of the refractive indices of pure lithium niobate”, *Phys. Lett.* **22** (1966) 243–244
- [Hulse+75] R. A. Hulse and J. H. Taylor, “Discovery of a pulsar in a binary system”, *Astrophys. J.* **195** (1975) L51–L53
- [Hulse94] R. A. Hulse, “The discovery of the binary pulsar”, *Rev. Mod. Phys.* **66** (1994) 699–710
- [Hygrosens] “SEMI833ET NTC” by Hygrosens Instruments, <http://www.hygrosens.com>
- [InnoLight] “Mephisto series” by InnoLight GmbH, <http://www.innolight.de>.
- [Jaeckel+90] M. T. Jaeckel and S. Reynaud, “Quantum limits in interferometric measurements”, *Europhys. Lett.* **13** (1990) 301–306
- [Ju+12a] L. Ju *et al.*, “Gravitational waves”, in: D. G. Blair, L. Ju, C. Zhao and E. J. Howell (editors), “Advanced gravitational wave detectors” (Cambridge University Press, announced for April 2012)
- [Ju+12b] L. Ju *et al.*, “Thermal noise, suspensions and test masses”, in: D. G. Blair, L. Ju, C. Zhao and E. J. Howell (editors), “Advanced gravitational wave detectors” (Cambridge University Press, announced for April 2012)
- [Kimble+01] H. J. Kimble, “Conversion of conventional gravitational-wave interferometers into quantum nondemolition interferometers by modifying their input and/or output optics”, *Phys. Rev. D* **65** (2001) 022002
- [Kuroda+10] K. Kuroda (on behalf of the LCGT Collaboration), “Status of LCGT”, *Class. Quantum Grav.* **27** (2010) 084004
- [Lastzka-PhD] N. Lastzka, “Numerical modelling of classical and quantum effects in non-linear optical systems”, Dissertation (Gottfried Wilhelm Leibniz Universität Hannover 2010)
- [Leonhardt97] U. Leonhardt, “Measuring the quantum state of light” (Cambridge University Press, Cambridge 1997)
- [Lightman05] A. P. Lightman, “The discoveries: great breakthroughs in twentieth-century science, including the original papers” (Pantheon books, New York 2005)
- [LIGO-CDS] “LIGO Control and Data System (CDS)”, <http://www.ligo.caltech.edu/~rolf/>
- [LIGO-Fil01] R. Abbott and J. Heefner, “Advanced LIGO anti-aliasing and anti-image filter function”, *Internal LIGO report* LIGO-T070038-00-C (2007)
- [LIGO-Fil02] J. Heefner, “AdL AA and AI filter board”, *Internal LIGO report* LIGO-D070081-v1 (2009)
- [LIGO-Sens] http://www.ligo.caltech.edu/~jzweizig/distribution/LSC_Data

- [Liu+00] Y. T. Liu and K. S. Thorne, “Thermoelastic noise and homogeneous thermal noise in finite sized gravitational-wave test masses”, *Phys. Rev. D* **62** (2000) 122002
- [Livas+86] J. Livas *et al.*, “The MIT gravitational wave detector”, in: R. Ruffini (editor), “Proceedings of the fourth Marcel Grossmann meeting on General Relativity” (Elsevier 1986) 591–597
- [Lück+10] H. Lück *et al.*, “The upgrade of GEO 600”, *J. Phys. Conf. Ser.* **228** (2010) 012012
- [McKenzie-PhD] K. McKenzie, “Squeezing in the audio gravitational wave detection band”, Dissertation (Australian National University 2008)
- [McKenzie+04] K. McKenzie *et al.*, “Squeezing in the audio gravitational-wave detection band”, *Phys. Rev. Lett.* **93** (2004) 161105
- [McKenzie+05] K. McKenzie *et al.*, “Quantum noise locking”, *J. Opt. B* **7** (2005) S421–S428
- [Meier-PhD] T. Meier, “High-power cw green lasers for optical metrology and their joint benefit in particle physics experiments”, Dissertation (Gottfried Wilhelm Leibniz Universität Hannover 2011)
- [Mehmet+10] M. Mehmet, H. Vahlbruch, N. Lastzka, K. Danzmann and R. Schnabel, “Observation of squeezed states with strong photon-number oscillations”, *Phys. Rev. A* **81** (2010) 013814
- [Mehmet+11] M. Mehmet *et al.*, “Squeezed light at 1550 nm with a quantum noise reduction of 12.3 dB”, *to be published*
- [MiniGRAIL] A. de Waard *et al.*, “Preparing for science run 1 of MiniGRAIL”, *Class. Quant. Grav.* **23** (2006) S79–S84
- [Misner+73] C. Misner, K. S. Thorne, J.A. Wheeler, “Gravitation” (Freeman, San Francisco 1973)
- [Newton+86] G. P. Newton *et al.*, “Some improvements to the Glasgow gravitational wave detector”, in: R. Ruffini (editor), “Proceedings of the fourth Marcel Grossmann meeting on General Relativity” (Elsevier 1986) 599–604
- [Newton87] I. Newton, “Philosophiae naturalis principia mathematica” (London 1687)
- [NIOBE] D. G. Blair *et al.*, “High sensitivity gravitational wave antenna with parametric transducer readout”, *Phys. Rev. Lett.* **74** (1995) 1908–1911
- [O’Connell82] R. F. O’Connell, “The Wigner distribution function—50th birthday”, *Foundations of Physics* **13** (1982) 83–92
- [Ott09] C. D. Ott, “Probing the core-collapse supernova mechanism with gravitational waves”, *Class. Quantum Grav.* **26** (2009) 204015
- [Pereira+88] S. F. Pereira *et al.*, “Generation of squeezed light by intracavity frequency doubling”, *Phys. Rev. A* **38** (1988) 4931–4934
- [PIa] “P016.00H ring actor” by PI, <http://www.physikinstrumente.de>

-
- [PIb] “P-025.20H PICA-Thru Piezoaktor” by PIceramic GmbH,
<http://www.piceramic.com>
- [Pirani56] F. A. E. Pirani, “On the physical significance of the Riemann tensor”, *Acta Physica Polonica* **15** (1956) 389
- [Rowan+05] S. Rowan, J. Hough and D. R. M. Crooks, “Thermal noise and material issues for gravitational wave detectors”, *Phys. Lett. A* **347** (2005) 25–32
- [Rüdiger11] A. Rüdiger, “Shot noise calculations”, *Internal AEI note* (Garching 2005 and München 2011). Here, an error in Reference [Saulson94] (p. 74, Eq. (5.10), being a factor $\sqrt{2}$ too large), resulting from a calculation for mid-fringe operation, is corrected.
- [Saulson94] P. Saulson, “Fundamentals of interferometric gravitational wave detectors” (World Scientific, Singapore 1994)
- [Schenberg] O. D. Aguiar *et al.*, “The Brazilian gravitational wave detector Mario Schenberg: status report”, *Class. Quant. Grav.* **23** (2006) S239–S244
- [Schnabel+04] R. Schnabel, J. Harms, K. A. Strain and K. Danzmann, “Squeezed light for the interferometric detection of high-frequency gravitational waves”, *Class. Quantum Grav.* **21** (2004) S1045–S1051
- [Schnabel+10] R. Schnabel, N. Mavalvala, D. E. McClelland and P. K. Lam, “Quantum metrology for gravitational wave astronomy”, *Nature Communications* **1** (2010) 121
- [Schnupp88] L. Schnupp, “Internal modulation schemes”, European Collaboration Meeting on Interferometric Detection of Gravitational Waves, Sorrento, Italy, 2. Oct. 1988
- [Schutz09] B. F. Schutz, “A first course in General Relativity” (Cambridge University Press, Cambridge 2009)
- [Scully+02] M. O. Scully and M. S. Zubairy, “Quantum optics” (Cambridge University Press, Cambridge 2002)
- [Shoemaker+88] D. Shoemaker *et al.*, “Noise behavior of the Garching 30-meter prototype gravitational-wave detector”, *Phys. Rev. D* **38** (1988) 423–432
- [Slusher+85] R. E. Slusher *et al.*, “Observation of squeezed states generated by four-wave mixing in an optical cavity”, *Phys. Rev. Lett.* **55** (1985) 2409–2412
- [Somiya11] K. Somiya, *Personal communication* (2011), correcting an error in Reference [Saulson94] (p. 78, Eq. (5.17), being a factor $\sqrt{2}$ too small).
- [Spero+86] R. Spero *et al.*, “The Caltech laser-interferometric gravitational wave detector”, in: R. Ruffini (editor), “Proceedings of the fourth Marcel Grossmann meeting on General Relativity” (Elsevier 1986) 615–620
- [Stairs+02] I. H. Stairs *et al.*, “Studies of the relativistic binary pulsar PSR B1534+12. I. Timing analysis.”, *Astrophys. J.* **581** (2002) 501–508

- [Takahashi+04] R. Takahashi and the TAMA Collaboration, “Status of TAMA 300”, *Class. Quantum Grav.* **21** (2004) S403–S408
- [Takeno+07] Y. Takeno, M. Yukawa, H. Yonezawa and A. Furasawa, “Observation of -9 dB quadrature squeezing with improvement of phase stability in homodyne measurement”, *Opt. Express* **15** (2007) 4321–4327
- [Taylor94] J.H. Taylor, “Binary pulsars and relativistic gravity”, *Rev. Mod. Phys.* **66** (1994) 711–719
- [Telemeter] “HOT2.0-65-F2A Melcor Element” by Telemeter Electronic, <http://www.telemeter.info>
- [Thorne87] K. S. Thorne, “Gravitational radiation”, in: S. W. Hawking and W. Israel (editors), “300 years of gravitation” (Cambridge University Press, Cambridge 1987) 330–458
- [TMC] “Technical Manufacturing Corporation (TMC)”, <http://www.techmfg.com/>
- [Uehara97] N. Uehara, “Ring mode cleaner for the initial LIGO 10 Watt laser”, *Internal LIGO report* (Stanford University, Stanford, California 1997)
- [Unruh83] W. G. Unruh, “Quantum noise in the interferometer detector”, in: P. Meystre and M. O. Scully (editors), “Quantum optics, experimental gravitation, and measurement theory” (Plenum Pr., New York 1983) 647–660
- [Vahlbruch+06] H. Vahlbruch *et al.*, “Coherent control of vacuum squeezing in the gravitational-wave detection band”, *Phys. Rev. Lett.* **97** (2006) 011101
- [Vahlbruch+07] H. Vahlbruch, S. Chelkowski, K. Danzmann and R. Schnabel, “Quantum engineering of squeezed states for quantum communication and metrology”, *New J. Phys.* **9** (2007) 371
- [Vahlbruch+08] H. Vahlbruch *et al.*, “Observation of squeezed light with 10-dB quantum-noise reduction”, *Phys. Rev. Lett.* **100** (2008) 033602
- [Vahlbruch+10] H. Vahlbruch *et al.*, “The GEO 600 squeezed light source”, *Class. Quantum Grav.* **27** (2010) 084027
- [Vahlbruch-PhD] H. Vahlbruch, “Squeezed light for gravitational wave astronomy”, Dissertation (Gottfried Wilhelm Leibniz Universität Hannover 2008)
- [Virgo-Sens] “Virgo sensitivity curves”, <https://www Cascina.virgo.infn.it/DataAnalysis/Calibration/Sensitivity/>
- [Wald84] R. M. Wald, “General Relativity” (Univ. of Chicago Press, Chicago 1984)
- [Weber60] J. Weber, “Detection and generation of gravitational waves”, *Phys. Rev.* **117** (1960) 306–313
- [Weber69] J. Weber, “Evidence for discovery of gravitational radiation”, *Phys. Rev. Lett.* **22** (1969) 1320–1324
- [Weber70] J. Weber, “Anisotropy and polarization in the gravitational-radiation experiments”, *Phys. Rev. Lett.* **25** (1970) 180–184

-
- [Weiss72] R. Weiss, “Electromagnetically coupled broadband gravitational antenna”, *Quarterly progress report of the Research Laboratory of Electronics of the Massachusetts Institute of Technology* **105** (1972) 54 (unpublished)
- [Wenzel] “Wenzel Associates Inc.”, <http://www.wenzel.com>
- [Wiechmann+93] W. Wiechmann *et al.*, “Refractive-index temperature derivatives of potassium titanyl phosphate”, *Optics Lett.* **18** (1993) 1208–1210
- [Wigner32] E. Wigner, “On the quantum correction for thermodynamic equilibrium”, *Phys. Rev.* **40** (1932) 749–759
- [Willke+98] B. Willke *et al.*, “Spatial and temporal filtering of a 10-W Nd:YAG laser with a Fabry-Perot ring-cavity premode cleaner”, *Optics Lett.* **23** (1998) 1704–1706
- [Willke+02] B. Willke *et al.*, “The GEO 600 gravitational wave detector”, *Class. Quantum Grav.* **19** (2002) 1377–1387
- [Willke+06] B. Willke *et al.*, “The GEO-HF project”, *Class. Quantum Grav.* **23** (2006) S207–S214
- [Winkler+07] W. Winkler *et al.*, “The GEO 600 core optics”, *Opt. Commun.* **280** (2007) 492–499
- [Wu+87] L.-A. Wu, M. Xiao and H. J. Kimble, “Squeezed states of light from an optical parametric oscillator”, *J. Opt. Soc. Am. B* **4** (1987) 1465–1475
- [Yamada+93] M. Yamada, N. Nada, M. Saitoh and K. Watanabe, “First-order quasi-phase matched LiNbO₃ waveguide periodically poled by applying an external field for efficient blue second-harmonic generation”, *Appl. Phys. Lett.* **62** (1993) 435–436
- [Yuen+83a] H. P. Yuen and V. W. S. Chan, “Noise in homodyne and heterodyne detection”, *Opt. Lett.* **8** (1983) 177–179
- [Yuen83b] H. P. Yuen, “Contractive states and the standard quantum limit for monitoring free-mass positions”, *Phys. Rev. Lett.* **51** (1983) 719–722

Bibliography

List of publications

The publications directly related to the results presented in this thesis are highlighted.

— 2011 —

1. | **A. Khalaidovski**, H. Vahlbruch, N. Lastzka, C. Gräf, K. Danzmann, H. Grote and R. Schnabel, “Status of the GEO 600 squeezed-light laser”, submitted to *JPCS*, arXiv:1112.0198
2. | **A. Khalaidovski**, H. Vahlbruch, N. Lastzka, C. Gräf, K. Danzmann, H. Grote and R. Schnabel, “Long-term stable squeezed vacuum state of light for gravitational wave detectors”, *submitted to Class. Quantum Grav.*, arXiv:1109.3731
3. | **A. Khalaidovski**, H. Vahlbruch, N. Lastzka, C. Gräf, K. Danzmann and R. Schnabel, “A squeezed-light source for the gravitational wave detector GEO 600”, in: T. Damour, R.T. Jantzen and R. Ruffini (editors), “Proceedings of the 12th Marcel Grossmann Meeting on recent developments in theoretical and experimental General Relativity, astrophysics and relativistic field theories” (World Scientific, Singapore, announced for 2011) 1729–1731
4. | J. Abadie, ..., Z. Keresztes, **A. Khalaidovski**, F.Y. Khalili, ..., J. Zweizig, “A gravitational wave observatory operating beyond the quantum shot-noise limit”, *Nature Phys.* **7** (2011) 962–965
5. | J. Abadie, ..., Z. Keresztes, **A. Khalaidovski**, F.Y. Khalili, ..., J. Zweizig, “All-sky Search for Periodic Gravitational Waves in the Full S5 LIGO Data”, arXiv:1110.0208
6. | J. Abadie, ..., D.G. Keppel, **A. Khalaidovski**, F.Y. Khalili, ..., A.M.J. Wijers, “Implementation and testing of the first prompt search for electromagnetic counterparts to gravitational wave transients”, arXiv:1109.3498

- 7.] B. P. Abbott, . . . , D. G. Keppel, **A. Khalaidovski**, F. Y. Khalili, . . . , J. Zweizig, “Directional limits on persistent gravitational waves using LIGO S5 science data”, arXiv:1109.1809
 - 8.] J. Abadie, . . . , D. G. Keppel, **A. Khalaidovski**, F. Y. Khalili, . . . , K. Yamaoka, “Beating the spin-down limit on gravitational wave emission from the Vela pulsar”, *Astrophys. J.* **737** (2011) 93
 - 9.] J. Abadie, . . . , D. G. Keppel, **A. Khalaidovski**, F. Y. Khalili, . . . , J. Zweizig, “Search for gravitational waves from binary black hole inspiral, merger, and ring-down”, *Phys. Rev. D* **83** (2011) 122005
 - 10.] J. Abadie, . . . , D. G. Keppel, **A. Khalaidovski**, F. Y. Khalili, . . . , K. Yamaoka, “Search for gravitational wave bursts from six magnetars”, *Astrophys. J.* **734** (2011) L35
 - 11.] J. Abadie, . . . , D. G. Keppel, **A. Khalaidovski**, F. Y. Khalili, . . . , J. Zweizig, “Search for gravitational waves associated with the August 2006 timing glitch of the Vela pulsar”, *Phys. Rev. D* **83** (2011) 042001
- 2010 —
- 12.] H. Vahlbruch, **A. Khalaidovski**, N. Lastzka, C. Gräf, K. Danzmann and R. Schnabel, “The GEO 600 squeezed-light source”, *Class. Quantum Grav.* **27** (2010) 084027
 - 13.] J. Abadie, . . . , D. G. Keppel, **A. Khalaidovski**, F. Y. Khalili, . . . , J. Zweizig, “Calibration of the LIGO gravitational wave detectors in the fifth science run”, *Nucl. Instrum. Meth. A* **624** (2010) 223–240
 - 14.] J. Abadie, . . . , D. G. Keppel, **A. Khalaidovski**, F. Y. Khalili, . . . , J. Zweizig, “First search for gravitational waves from the youngest known neutron star”, *Astrophys. J.* **722** (2010) 1504–1513
 - 15.] J. Abadie, . . . , D. G. Keppel, **A. Khalaidovski**, F. Y. Khalili, . . . , J. Zweizig, “Search for gravitational waves from compact binary coalescence in LIGO and Virgo data from S5 and VSR1”, *Phys. Rev. D* **82** (2010) 102001
 - 16.] J. Abadie, . . . , D. G. Keppel, **A. Khalaidovski**, F. Y. Khalili, . . . , J. Zweizig, “Sensitivity to gravitational waves from compact binary coalescences achieved during LIGO’s fifth and Virgo’s first Science Run”, arXiv:1003.2481
 - 17.] J. Abadie, . . . , D. G. Keppel, **A. Khalaidovski**, F. Y. Khalili, . . . , J. Zweizig, “Predictions for the rates of compact binary coalescences observable by ground-based gravitational-wave detectors”, *Class. Quantum Grav.* **27** (2010) 173001

-
- 18.] J. Abadie, . . . , D.G. Keppel, **A. Khalaidovski**, F.Y. Khalili, . . . , J. Zweizig, “All-sky search for gravitational-wave bursts in the first joint LIGO-GEO-Virgo run”, *Phys. Rev. D* **81** (2010) 102001
- 19.] J. Abadie, . . . , D.G. Keppel, **A. Khalaidovski**, F.Y. Khalili, . . . , J. Zweizig, “Search for gravitational-wave inspiral signals associated with short Gamma-Ray Bursts during LIGO’s fifth and Virgo’s first science run”, *Astrophys. J.* **715** (2010) 1453–1461
- 20.] B.P. Abbott, . . . , D.G. Keppel, **A. Khalaidovski**, F.Y. Khalili, . . . , B. Stappers, “Searches for gravitational waves from known pulsars with S5 LIGO data”, *Astrophys. J.* **713** (2010) 671–685
- 21.] B.P. Abbott, . . . , D.G. Keppel, **A. Khalaidovski**, F.Y. Khalili, . . . , J. Zweizig, “Search for gravitational-wave bursts associated with gamma-ray bursts using data from LIGO Science Run 5 and Virgo Science Run 1”, *Astrophys. J.* **715** (2010) 1438–1452
- 2009 —
- 22.] A. Khalaidovski, A. Thüring, H. Rehbein, N. Lastzka, B. Willke, K. Danzmann, and R. Schnabel, “Strong reduction of laser power noise by means of a Kerr nonlinear cavity”, *Phys. Rev. A* **80** (2009) 053801
- 23.] B.P. Abbott, . . . , D.G. Keppel, **A. Khalaidovski**, F.Y. Khalili, . . . , J. Zweizig, “An Upper Limit on the Stochastic Gravitational-Wave Background of Cosmological Origin”, *Nature* **460** (2009) 990–994
- 24.] B.P. Abbott, . . . , D.G. Keppel, **A. Khalaidovski**, F.Y. Khalili, . . . , J. Zweizig, “Search for Gravitational Waves from Low Mass Compact Binary Coalescence in 186 Days of LIGO’s fifth Science Run”, *Phys. Rev. D* **80** (2009) 047101
- 25.] B.P. Abbott, . . . , D.G. Keppel, **A. Khalaidovski**, F.Y. Khalili, . . . , J. Zweizig, “Einstein@Home search for periodic gravitational waves in early S5 LIGO data”, *Phys. Rev. D* **80** (2009) 042003
- 26.] B.P. Abbott, . . . , D.G. Keppel, **A. Khalaidovski**, F.Y. Khalili, . . . , J. Zweizig, “Search for gravitational wave ringdowns from perturbed black holes in LIGO S4 data”, *Phys. Rev. D* **80** (2009) 062001
- 27.] B.P. Abbott, . . . , D.G. Keppel, **A. Khalaidovski**, F.Y. Khalili, . . . , J. Zweizig, “Search for gravitational-wave bursts in the first year of the fifth LIGO science run”, *Phys. Rev. D* **80** (2009) 102001
- 28.] B.P. Abbott, . . . , D.G. Keppel, **A. Khalaidovski**, F.Y. Khalili, . . . , J. Zweizig, “Stacked Search for Gravitational Waves from the 2006 SGR 1900+14 Storm”, *Astrophys. J.* **701** (2009) L68–L74

- 29. | B. P. Abbott, . . . , D. G. Keppel, **A. Khalaidovski**, F. Y. Khalili, . . . , J. Zweizig, “Search for High Frequency Gravitational Wave Bursts in the First Calendar Year of LIGO’s Fifth Science Run”, *Phys. Rev. D* **80** (2009) 102002
- 30. | B. P. Abbott, . . . , D. G. Keppel, **A. Khalaidovski**, F. Y. Khalili, . . . , F. Robinet, “First LIGO search for gravitational wave bursts from cosmic (super)strings”, *Phys. Rev. D* **80** (2009) 062002
- 31. | B. P. Abbott, . . . , D. G. Keppel, **A. Khalaidovski**, F. Y. Khalili, . . . , J. Zweizig, “Search for Gravitational Waves from Low Mass Binary Coalescences in the First Year of LIGO’s S5 Data”, *Phys. Rev. D* **79** (2009) 122001
- 32. | B. P. Abbott, . . . , D. G. Keppel, **A. Khalaidovski**, F. Y. Khalili, . . . , J. Zweizig, “All-Sky LIGO Search for Periodic Gravitational Waves in the Early Fifth-Science-Run Data”, *Phys. Rev. Lett.* **102** (2009) 111102
- 33. | B. P. Abbott, . . . , D. G. Keppel, **A. Khalaidovski**, F. Y. Khalili, . . . , J. Zweizig, “LIGO: The Laser Interferometer Gravitational-Wave Observatory”, *Rep. Prog. Phys.* **72** (2009) 076901

— 2007 —

- 34. | **A. Khalaidovski**, “Der optische Kerr-Effekt im Fabry-Perot Interferometer”, Diploma thesis (Gottfried Wilhelm Leibniz Universität Hannover 2007)

Curriculum Vitae

Personal Details

Aleksandr Khalaidovski
Celler Strasse 36
30161 Hannover
Germany

Email: alexander.khalaidovski@aei.mpg.de

Date of birth: 16th of January 1982

Place of birth: Kiev (Ukraine)

Married, no children

Education and University Studies

02/2011 - 04/2011	Academic stay at LIGO-Hanford Gravitational Wave Observatory.
08/2008 - present	Scientific assistant, University of Hannover (LUH).
08/2007 - present	Doctoral studies in Physics, University of Hannover (LUH).
08/2007 - present	Member of the International Max Planck Research School (IMPRS) on Gravitational Wave Astronomy.
03/2007	Diploma thesis, University of Hannover (LUH). Title: “The optical Kerr effect in a Fabry-Perot interferometer”. Grade: “with distinction”.
09/2003–07/2004	Year abroad at the <i>Università degli Studi di Milano</i> , Italy as part of the degree course.
2002–2006	Scholarship from the <i>Studienstiftung des deutschen Volkes</i> .
09/2001	Physics studies, University of Hannover (LUH).
06/2001	Graduation (Abitur) from the Ricarda-Huch-Schule (Hannover) as best in class.